Study of the Synchronous Operation of an Annular Field Reversed Configuration Plasma Device

by

David E. Kirtley

A dissertation submitted in partial fulfillment
of the requirements for the degree of
Doctor of Philosophy
(Aerospace Engineering)
in The University of Michigan
2008

Doctoral Committee:

Professor Alec D. Gallimore, Chair
Professor Iain D. Boyd
Associate Professor John E. Foster
Deputy Chief James M. Haas, Air Force Research Laboratory

ACKNOWLEDGEMENTS

Funding for this work was provided by the National Science Foundation, Air Force Research Laboratory, and the University of Michigan's Horace H. Rackham School of Graduate Studies.

TABLE OF CONTENTS

LIST OF FIGURES

Figure

LIST OF TABLES

Table

NOMENCLATURE

SYMBOL	DEFINITION
A_c	Annular chamber cross section area $[m^2]$
A_p	Collection area of a Langmuir probe $[m^2]$
A_p	Annular plasma cross section area $[m^2]$
B	Magnetic field $[T]$
B_{LO}	Lift-off reversed magnetic field $[T]$
B_p	Effective magnetic field in a plasma, probe magnetic field $[T]$
B_v	Vacuum magnetic field $[T]$
B_z	Peak axial magnetic field $[T]$
B_θ	Toroidal magnetic field $[T]$
C	Capacitance $[F]$
e_{ion}	Ionization threshold energy $[eV]$
E_{in}	Total energy input into discharge chamber $[J]$
E_{ion}	Energy required to ionize plasma within separatrix $[J]$
$E_{kinetic}$	Plasma kinetic energy within separatrix $[J]$
E_p	Plasma thermal energy within separatrix $[J]$
E_{rad}	Energy loss to radiation within discharge chamber $[J]$
E_{UB}	Inductive, magnetic energy stored in the discharge coil $[J]$
E_θ	Azimuthal cylindrical electric field $[V/m]$
F	Geometrical uniformity constant derived from Equation 2.9 $[-]$
f_{max}	Circuit frequency $[Hz]$
$\bar{I}$	Radiation intensity $\left[\frac{W}{m^2}\right]$
I	Current $[A]$
I_{esat}	Electron saturation current $[A]$
I_{ionsat}	Ion saturation current $[A]$
I_p	Current collected by Langmuir probe $[A]$
I_2	Current collected by a triple probe $(P_1 - P_2)$ $[A]$
I_3	Current collected by a triple probe $(P_1 - P_3)$ $[A]$

J_i	Ion current density $\left[\frac{A}{m^2}\right]$
K_n	Knudsen number $[-]$
L	Inductance, in a circuit, of a single layer solenoidal coil $[H]$
l	Width of the B-dot probe $[m]$
l_1	Axial discharge coil length, $l_0 = 0.307$ $[m]$
l_1	Distance between the inner coil faces of a Helmholtz coil $[m]$
l_2	Distance between the outer coil faces of a Helmholtz coil $[m]$
n	Average plasma density [quasineutral] $\left[m^{-3}\right]$
N	Number of complete turns of a magnetic coil/circuit $[-]$
nA	Magnetic flux constant $[m^2]$
n_e	Local average electron plasma density $\left[m^{-3}\right]$
n_i	Local average ion plasma density $\left[m^{-3}\right]$
N_e	Total electron content within separatrix $[-]$
P	Plasma pressure $\left[\frac{J}{m^3}\right]$
P_M	Maximum plasma pressure $\left[\frac{J}{m^3}\right]$
P_0	Neutral pressure $[mTorr]$
P_1	Positive triple probe tip $[-]$
P_2	Negative triple probe tip $[-]$
P_3	Negative triple probe tip $[-]$
r	Average radius of a B-dot probe $[m]$
R	Resistance $[\Omega]$
R	Chamber radius, quartz radius $[m]$
R_{eff}	Effective coil resistance $[\Omega]$
R_0	Input impedance $[\Omega]$
r_c	Average coil radius $[m]$
r_l	Flux loop radius $[m]$
r_p	Langmuir probe tip radius $[m]$
r_s	Separatrix radius $[m]$
$r_{\delta\phi}$	Excluded flux radius $[m]$
r_1	Helmholtz coil inside radius $[m]$
r_2	Helmholtz coil outside radius $[m]$
r_w	Inner radius of the discharge coil $[m]$
s	Triple probe tip separation $[m]$
t	Time $[s]$
T	Average plasma temperature $T = T_i + T_e$ $[K]$
T_e	Electron temperature $[eV]$
T_i	Ion temperature $[eV]$

v_a	Alfvén speed $\left[\frac{m}{s}\right]$
v_d	Diamagnetic drift velocity $\left[\frac{m}{s}\right]$
v_i	Ion thermal velocity $v_i = \left(\frac{T_i}{m_i}\right)^{1/2}$ $\left[\frac{m}{s}\right]$
V	Bulk plasma velocity $\left[\frac{m}{s}\right]$
V_{bp}	B-dot probe induced voltage $[V]$
V_f	Plasma floating potential
V_{rp}	Rogowski coil induced voltage $[V]$
V_p	Plasma potential
V_0	Background bias potential $[V]$
V_{12}	Triple probe potential, P1-P2 $[V]$
V_{13}	Triple probe potential, P1-P3 $[V]$
z	Atomic mass $[amu]$

GREEK

β	Ratio of the magnetic pressure to plasma particle pressure [-]
Δ	Experimental length scale $[m]$
λ	Conductor area ratio for a Helmholtz Coil (2.14) $[m]$
λ_c	Collisional length scale $[m]$
λ_d	Debye length $[m]$
λ_{Le}	Electron gyro-radius $[m]$
λ_{Li}	Ion gyro-radius $[m]$
μ	Dielectric permeability $\left[\frac{N}{A^2}\right]$
ν_a	Plasma Alfvén speed $\nu_a = \frac{B}{\mu_0 n_i m_i}$ $[m/s]$
ϕ	Magnetic flux $[weber]$
$\delta\phi$	Magnetic probe phase delay $[rad]$
ϕ_l	magnetic flux at axial center $[weber]$
ϕ_p	Effective plasma magnetic flux $[weber]$
ϕ_v	Effective vacuum magnetic flux $[weber]$
ρ	Conductance $\left[\frac{\Omega}{m^2}\right]$
τ	Time constant, 1/e $[s]$
τ	Average plasma lifetime $[s]$
τ_a	Plasma Alfvén time $\tau_a = \frac{r_s}{\nu_a}$ $[s]$
τ_f	Average plasma formation time $[s]$

CONSTANTS

e	Electron charge, $e = 1.602 \times 10^{-19} \quad [C]$
k_B	Boltzmann constant, $k_B = 1.38 \times 10^{-23} \quad \left[\frac{J}{K}\right]$
m_e	Electron mass, $m_e = 9.11 \times 10^{-31} \quad [kg]$
m_i	Ion mass, $m_i = z \times 1.67 \times 10^{-27} \quad [kg]$
μ_0	Vacuum permeability, $\mu_0 = 4\pi \times 10^{-7} \quad \left[\frac{N}{A^2}\right]$
π	Pi, $\pi = 3.141...$

ACRONYMS

AFRC	Annular Field Reversed Configuration
AFRL	Air Force Research Laboratory
CCD	Charge Coupled Device [Detector]
CT	Compact Toroid
CTOR	Compact Toroid Fusion Reactor
CSS	Coaxial Slow Source
DAQ	Data Acquisition [System]
DICAM	Intensified Digital Camera
DSO	Digital Storage Oscilloscope
Edwards AFB	Edwards Air Force Base, California
EMI	Electro-Magnetic Interference
FRC	Field Reversed Configuration
FRCHX	Field Reversed Configuration Heating Experiment
FWHM	Full-Width at Half-Maximum
GPIB	General Purpose Interface Bus [IEEE488]
HD	High Density [Probe]
LANL	Los Alamos National Laboratories
LD	Low Density [Prob]
LSX	Large S FRC Experiment
MP	Mega-Pixel
MTF	Magnetized Target Fusion
NEP	Noise Equivalent Power
NIST	National Institute of Standards and Technology
OML	Orbital Motion Limited
PHD	Pulsed High Density Experiment

PI	Pre-Ionization
PPI	Pre- Pre-Ionization
RF	Radio-Frequency, defined as 0.1-100 MHz
RMF	Rotating Magnetic Field
RZSS	Air Force Research Laboratory Spacecraft Propulsion
SAFRC	Synchronous Annular Field Reversed Configuration
Si/PIN	Silicon Positive-Intrinsic- Negative [Diode]
USB	Universal Serial Bus
VI	Virtual Instrument
XOCOT	Experimental Coaxial Field Reversed Configuration Thruster

CHAPTER 1

Background and Approach

1.1 Theta Pinch Theory

The thetatron, or theta pinch [6], consists of a cylindrical coil surrounding an insulated discharge chamber and connected to a high-energy capacitive discharge system. A large, high-speed current pulse is then driven through the azimuthal coil generating a high-speed transient longitudinal magnetic field within the discharge chamber, which in turn from Ampere's Law, Equation 1.1, generates a large azimuthal electric field. When a neutral gas is injected into the chamber, the large electric field ionizes the gas and generates significant diamagnetic current within the discharge chamber. The diamagnetic current interacts with the longitudinal applied magnetic field to generate a radial compression Lorentz force, Equation 1.2, on the plasma. At the timescales of a typical theta pinch, on the order of 1 μs, the plasma is super-sonically accelerated inward creating high-speed efficient shock heating, ionizing, then heating and compressing of the plasma. Within a microsecond the plasma has been compressed and heated by the magnetic field such that a high plasma beta, β, condition is reached in which the interior plasma pressure is balanced by the external magnetic pressure, as shown in Equation 1.3, at which time the extreme pressure tends to drive the plasma along the longitudinal magnetic field lines out of the discharge chamber [6], [7], [22]. Theta pinches were originally used to investigate early

magnetic compression fusion, and quickly led to the creation of very high-density laboratory pulsed-plasmas. This in turn led to the discovery of field reversed theta pinches, an evolution of the azimuthal theta pinch concept in which the discharge is performed slower, on the order of 10 μs allowing the applied current to fully reverse and the diamagnetic current to fully disconnect from the applied field coils.

$$\nabla \times \mathbf{B} = \mu_0 \mathbf{J} + \epsilon_0 \mu_0 \frac{\partial \mathbf{E}}{\partial t} \tag{1.1}$$

$$\mathbf{F} = q(\mathbf{E} + \mathbf{v} \times \mathbf{B}) \tag{1.2}$$

$$\beta = \frac{P_n}{P_B} = \left(\frac{2\mu_0 n k_B T}{B^2} \right) \tag{1.3}$$

1.2 Field Reversed Configuration Overview

The primary characteristic of a field reversed configuration plasma is the lack of magnetic field lines linking the generation coils to the plasma. This property leads to a plasma that is formed in a high β configuration, namely the external applied magnetic pressure balances the interior plasma particle pressure, a unique and highly desirable condition for efficient containment and energy deposition of plasmas. These plasmas are collectively known as CT, or Compact Toroids [16], [15] and include both FRCs (Field Reversed Configuration), an elongated configuration where the axial magnetic field dominates the azimuthal, $B_z \gg B_\theta$ [19] and Spheromaks, with $B_z \approx B_\theta$ [27]. Figure 1.1 describes an ideal FRC after reversal. [64]

The study of FRCs has primarily been for magnetically confined fusion, with the goal of compression and heating of an FRC for sufficient $n\tau$ (Lawson criterion for fusion initiation) to begin $D - T$ or $D - He_3$ fusion [64]. There have also been ex-

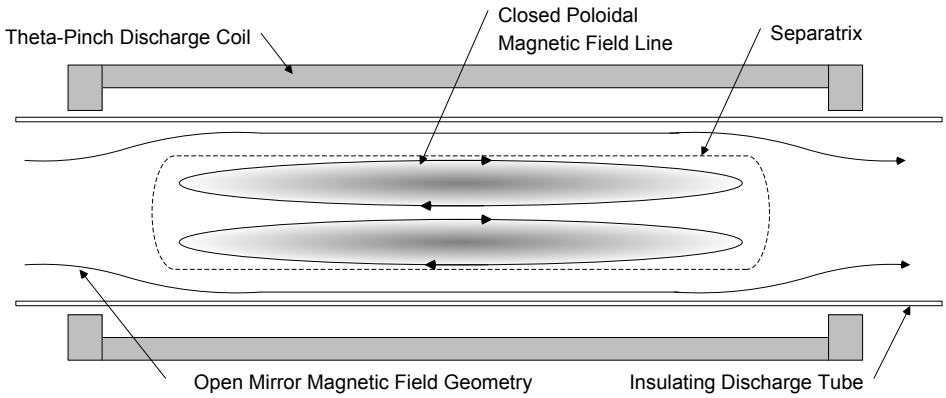

Figure 1.1: A Field Reversed Configuration

Typical FRC Properties	
Diameters	0.15-0.90 m
Peak Magnetic Field	0.1-1.3 T
β	0.5-1
Ion density	$10^{13} - 10^{16}$ $\left[cm^{-3}\right]$
Electron temperature	$100 - 1000\ eV$
FRC lifetime, τ	10-500 μs

Table 1.1: Typical Field Reversed Configuration plasma characteristics

periments using the unique translational nature of FRCs to either impinge multiple FRCs on each other [21], or to allow translation through an adiabatic magnetic compression nozzle to further heat and compress the FRC after formation [47]. Finally, more recent experiments in Magnetized Target Fusion (MTF) have targeted the goal of translating a deuterium FRC into an imploding magnetic liner that acts to further heat and compress. [26]

Typical FRC experimental characteristics are shown in Table 1.1.

1.2.1 FRC History

Tuszewski provides a complete history of FRC research through the mid-1990's in "Field Reversed Configurations" [64] a selection of which is also summarized in Table 1.2. This author has updated Table 1.2 to show the recent (and current) status of FRC research in the United States.

1.2.2 Typical Field Reversed Configuration Operation

Figure 1.2 demonstrates a typical FRC discharge using the geometry as outlined by Figure 1.1 and the operational parameters by Table 1.2, showing graphically a cross section of those steps with the final FRC translating out of the device due to magnetic field non-uniformity.

> "At the exit of the FRC reactor is a compressed, relatively non-diffuse neutral toroidal plasma with a self-consistent magnetic field and large poloidal currents (relative to the toroidal plasma currents). It has been noted that forming efficient FRCs is a very empirical process of electrical circuit characteristic development; however, once a valid discharge scheme (and pre-ionization method) has been developed these [reactors] are very robust and repeatable. This pre-ionization stage should be a major focus of any FRC development process and is a major focus of this ... investigation." [64]

1.2.3 State-of-the-Art Field Reversed Configuration Theory

Pre-ionization is accomplished in a variety of methods including microwaves [64], pulsed laser ionization [13], ringing-multi poles [15], and theta-ringing [60]. Theta-ringing has been accepted as the most widely, and usually simplest, pre-ionization method, as it utilizes the existing coil geometry with only minor additional electronics. A typical theta ringing ionization is a 1-kA, 1-MHz decaying RF-type discharge [64]. Extensive testing has shown that pre-ionization is the most critical and often poorly performing phase in FRC formation; without uniform or sufficient pre-ionization the large discharge current does not couple with the plasma and FRC formation is poor or nonexistent [60]. Several of the newer FRC concepts actually

Year	Experiment	Lab	Length (cm)	Diameter (cm)	B_{Peak} (kG)	Po (mTorr)	τ (μs)	Main studies
1959	-	NRL	10	6	100	100	2	Annihilation
1962	Scylla I	LASL	11	5	55	85	3	Annihilation
1962	Scylla II	LASL	19	8	125	85	4	Rotation
1964	0-P	Garching	30	5	53	100	1	Tearing
1965	Pharos	NRL	180	17	30	60	30	Confinement
1967	Centaur	Culham	50	19	21	20	15	Confinement
1967	Julietta	Jiilich	128	11	27	50	15	Tearing
1971	E-G	Garching	70	11	28	50	25	Tearing
1979	TOR	Kurchatov	150	30	10	5	100	Formation
1979	FRX-A	LASL	100	25	6	5	30	Confinement
1981	FRX-B	LANL	100	25	13	25	60	Confinement
1982	STP-L	Nagoya	150	12	10	9	30	Rotation
1983	FRX-c	LANL	200	50	8	15	300	Confinement
1984	TRX-I	MSNW	100	25	10	10	150	Formation
1985	HBQM	U Wash	300	22	5	5	30	Formation
1986	TRX-2	STI	100	24	13	10	100	Confinement
1987	CSS	U Wash	100	45	3	40	60	Slow-formation
1988	FRXC	LANL	200	70	6	5	450	Formation
1990	LSX	STI	500	90	8	3		Stability
1998	TRAP	U Wash	200	27	1	20		Translation
1999	STX	U Wash	300	40	0.1*	0.4	400	Propulsion
2003	TCS**	U Wash	260	80	5			RMF Formation
2004	PHD	U Wash		18	7			Translation
2005	PTX	NASA	7	8.3	1.0	40		Propulsion
2006	MAP**	MSNW		20				Propulsion
2007	XOCOT**	AFRL	30	40	1.5	14	100	Propulsion
*	RMF							
**	On-Going							

Table 1.2: Summary of FRC experiments

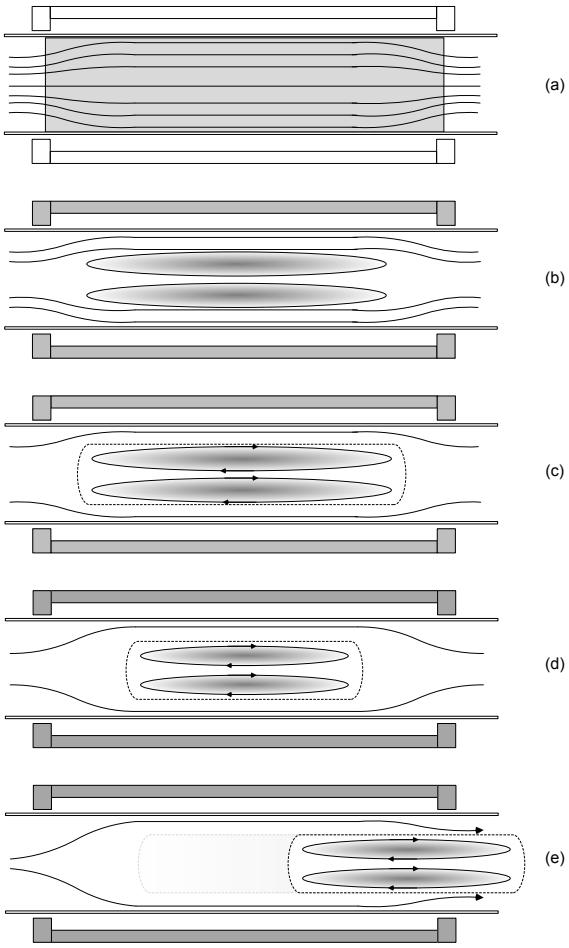

(a) Fill coil with gas and low level flux

(b) Pre-Ionize to trap and freeze plasma to field lines

(c) Force field reversal to tear and internally reconnect field lines

(d) Fully formed self-consistent FRC at this point

(e) Continue pulse to radially compress, or destabilize to translate axially

Figure 1.2: Typical FRC discharge evolution

utilized several of the pre-ionization techniques simultaneously to create not only denser starting plasmas, but also more uniform. Combining an axial DC glow discharge with a ringing radial field has been shown to create a plasma that is more uniformly distributed in the axial direction.

The energy deposition into the plasma during FRC formation appears to have two main modes, the so-called 'snowplow' and 'ohmic-resistive' heating modes [5] as a function of diffusion and compression timescales. For high voltage, fast timescale discharges, the plasma currents are located, as expected, primarily in a thin exterior shell of the plasma and the rapid compression of this well-defined boundary heats the internal plasma. General equations of non-collisional shock formation and compression yield surprisingly accurate predictions of final plasma temperature and geometry. For slower plasma discharges, the currents appear to diffuse internally into the plasma, generating far less compression but comparable energy deposition due to ohmic heating of this colder, more resistive, and more diffuse plasma. While classical heating is too low to account for the measured diffusive heating, the large density gradients tend to drive anomalous resistivity and thereby drastically increase heating and energy deposition into the plasma [52]. Typical FRC devices have a combination of these two modes, usually an initial shock heating that then transitions into a slower ohmic heating to continue to heat and compress (i.e. deposit energy) the plasma on longer timescales. Also as expected, the plasma diffusion into the chamber walls appears to be coupled with the heating mechanism and discharge timescales, with the slower resistive mode more susceptible to major Bohm diffusion losses [53].

Plasma translation has been demonstrated in excess of 250 km/sec in deuterium and in a separate experiment cohesive plasma has been maintained for 15 m (chamber geometry was the only limitation) [20]. The CTOR (Compact Toroid Fusion

Reactor) modeling program demonstrated the potential of > 100 m coherent FRC translation with a low-magnitude, flux-conserving guide field [66]. The actual translation mechanism is also not completely understood, although acceleration of the plasma out of the FRC is believed to be primarily a function of magnetic pressure, as it is in a high-β configuration. There has been repeatable empirical evidence that the kinetic energy of the ejected cool FRC is equal to the enthalpic energy of the hot, contained plasma as in Equation 1.4.

$$\mathbf{V_z} = \sqrt{\frac{5k_BT_e}{m_i}} \tag{1.4}$$

This mechanism is best understood as the magnetic pressure driving the plasma translation, that is driven by the particle pressure, and subsequently the thermal energy of the compressed plasma [64]. Translation does not appear to be a direct function of dB/dt [47], although that is an important driver in heating, compression, and magnetic pressure. Also, the translational instability requires an initial asymmetry in the magnetic field or particle pressure. Of note, one of the original FRC fusion concepts was to eject an FRC into a magnetic compression nozzle such that the adiabatic compression and FRC resonance times provided sufficient $n\tau$ for fusion [20].

1.2.4 Field Reversed Configuration Applications

The primary applications of a field reversed configuration plasma have been outlined earlier in Section 1.2, and will be explored in more detail in the following Sections in order of decreasing FRC energy.

1.2.4.1 Kinetic Heating and Fusion

Most reactor studies and experiments have been along the vein of a pulsed/translating reactor that utilizes some of the most attractive benefits of an FRC plasma: the high

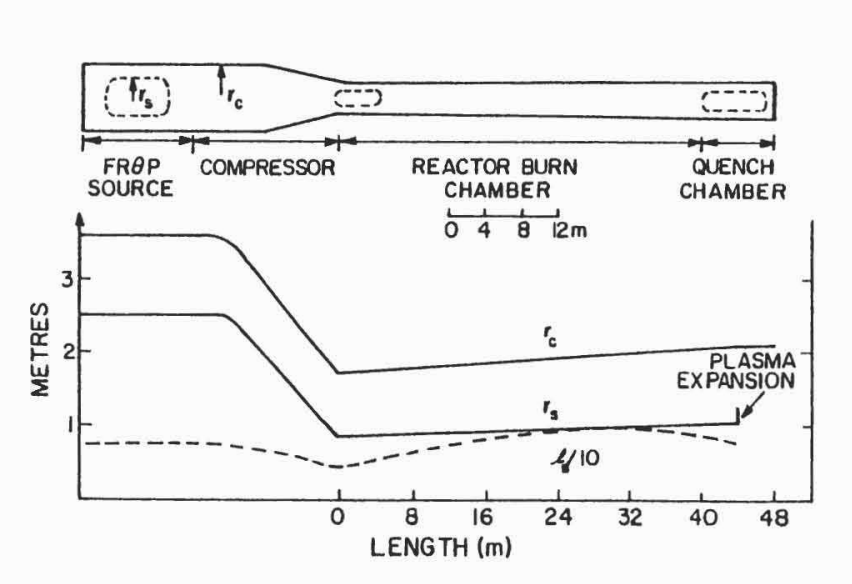

Figure 1.3: Schematic of the CTOR translating compact toroid reactor [66]

plasma beta, power density, compactness, and ease of translation. Typically, a reactor will have three main stages: the FRC formation, the adiabatic compression, and main burn chamber as shown in the simplified diagram from CTOR, Figure 1.3. One of the largest benefits of this technique is that it allows a separation of the acceleration and burn regions to help protect a real reactor. A more recent concept, the FIREBIRD, [66] continued the evolution of this concept.

The FIREBIRD consisted of a 1 m radius, 50 m long vacuum chamber with formation, compression, and burn regions. It was designed for a peak field strength of 3-5 Tesla, and an initial plasma formation energy of 100 MJ. Using the unique translational nature of FRCs, a high-energy density plasma is formed and accelerated to a compression nozzle where energy is then added adiabatically (through a convergence of the guiding magnetic field) until fusion temperatures are reached in the burn chamber. Peak expected temperature and density was 10 keV and $5 \times 10^{21}\ m^{-3}$ and FRC velocity was 400 m/s. Once in the burn chamber, the FRC would then expel neutrons into the liner/breeder blanket and finally travel to the quench cham-

ber [47], [33], [1]. A modern experimental investigation of this technique gases on creating smaller, low energy FRCs and then accelerating them with multiple acceleration coils to much higher kinetic energies [56]. The Pulsed High Density Experiment (PHD) has yielded FRCs with $n_e = 10^{21}\ m^{-3}$, $T_e = 500\ eV$ with a peak velocity of 1×10^6 m/s.

1.2.4.2 Magnetized Target Fusion

Another unique approach that utilizes the translational nature of the FRC is the Magnetized Target Fusion (MTF) concept, specifically utilizing imploding metal liners. In this concept there are two compression capacitor banks, the first creates a low energy FRC that is translated into a small aluminum (or lithium) cylindrical liner, see Figure 1.4. The metal liner is then compressed with a much higher energy capacitor bank, ideally compressing and heating the field reversed plasma to fusion temperatures and energies. In the AFRL/LANL MTF experiment (FRCHX) [14], [26], [62] an initial FRC is formed at a density of $10^{23}\ m^{-3}$, temperature 100 to 300 eV, length 30 cm, and separatrix radius 2.5 cm using a 750-kJ capacitor bank. This FRC is then translated into the 30-cm-long, 5-cm initial radius, 0.11-cm-thick Aluminum liner that is imploded with an 11-MA, 10-MJ Shiva Star capacitor bank at AFRL-Kirtland. As of the publishing of this work, the FRCHX experiment is still underway.

1.2.4.3 Tokamak Refueling

Additionally, the fact that FRC devices create small, self-consistent (B-field), high-speed plasmas is useful for other fusion devices, namely for Tokamak refueling [23]. By forming FRCs at low temperatures and then accelerating them into the closed field lines of a stable Tokamak it may be possible to re-fuel an operating Tokamak without major disturbances in the stability. The TRAP experiments [58] demon-

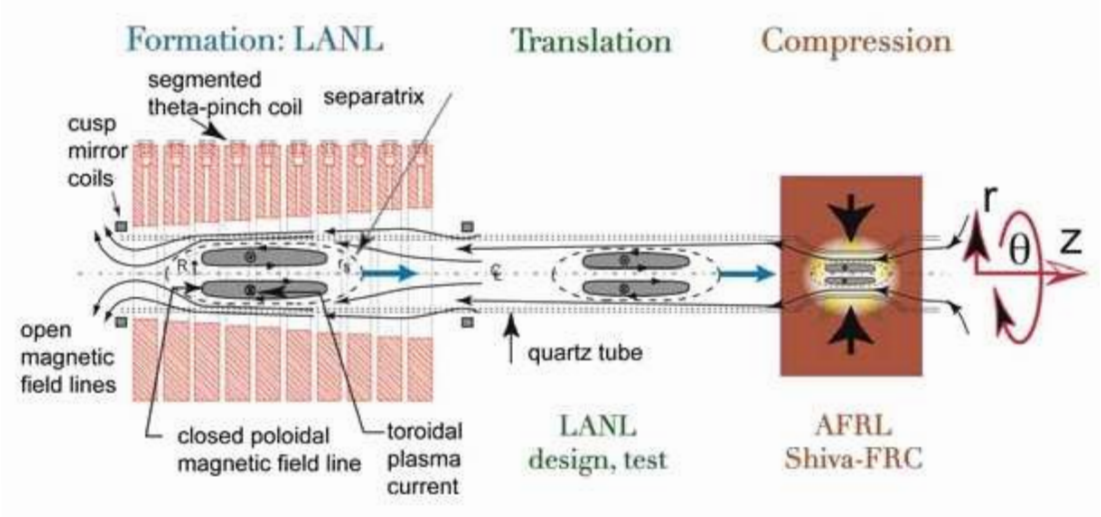

Figure 1.4: Schematic of the AFRL/LANL MTF experiment [26]

strated the utility of creating low-temperature ($< 50\ eV$), high-density ($10^{22}\ m^{-3}$) deuterium plasmas and accelerating them to sufficient velocities ($2 \times 10^5\ m/s$) to penetrate a large, Tokamak-like, transverse magnetic field structure.

1.2.5 Field Reversed Configuration Applications to Electric Propulsion

Field reversed configuration plasmas also appear to have usage in the propulsion field. At the exit of an FRC device is a highly compressed, relatively high-density plasma that has been formed efficiently (low energy, trapped flux, neutral propellant loss) and then translated out of the device by magnetic field pressure (and the time changing electric field that can be derived therein) [47]. Additionally, in this configuration the magnetized plasma is not connected to the coils by magnetic field lines and consists of a relatively stable, closed field configuration that lends itself to ejection with very little divergence and momentum loss. Several programs have been active within the United States in the last decade to explore FRCs as propulsion devices [32], [31], [57] all aiming to develop lower energy (than the experiments in

Table 1.2) FRC formation and translation, typically with higher atomic mass gases. The heavier atomic gases allow greater kinetic energy input and lower FRC exit velocities to the typically desired propulsive exit velocities (10^4 m/s).

1.3 Annular Field Reversed Configuration Theory

Traditional FRC devices have demonstrated high-velocity translation and high-efficiency compression. However, they also have some inherent disadvantages, namely high voltages (20-200 kV) and fast discharge times leading to complicated propellant feed and switching. A possible solution to these issues is the Coaxial Slow Source FRC concept (CSS) developed at the University of Washington by Vlases, Brooks, and Pierce for deuterium fusion [42]. This concept is derived from several annular, slow-formation, AFRC concepts developed previously [40]. An annular, coaxial FRC has two, coaxial discharge coil that are each used for generating magnetic fields and flux within the annular region. The CSS concept has demonstrated FRC formation and translation (in excess of 100 km/s with deuterium) at coil voltages of less than 1000 volts and discharge times longer than 250 μs. The CSS has approximately 500-2000 V discharge voltages, 10-60 mTorr propellant pressures, and 100-500 μs discharge times. It successfully demonstrated results similar to traditional FRC concepts (LSX etc.), however the temperatures were insufficient for fusion, and there was some evidence of the rotational n=2 instabilities that do not appear to be present in traditional FRCs. There was also evidence of excessive radiation losses due to the long discharge time and oxygen impurities. However, as our primary interest is FRC formation and immediate translation, these instabilities are of substantially less importance. The majority of the studies on the CSS device were on the so-called programmed discharge mode (asynchronous) and are described in Section 1.3.1.1, while this study focuses on a similar geometry device operating in synchronous discharge mode also known as the

tearing formation mode. The AFRL/UM XOCOT concept geometry is based upon the general geometry of the CSS device, but is scaled to incorporate lower discharge voltages. Upgrades in capacitor technologies, switching, and general device scaling have been done with the goal of re-tooling this general concept into one focused on lower voltages and internal diagnostics.

1.3.1 Annular Field Reversed Configuration Analysis and Operation

There are two main benefits of an annular coaxial FRC discharge: slow-formation and flux addition. Typical FRC discharges as described in the previous Sections have discharge timescales on the order of an Alfven time, τ_a, typically a few microseconds. Forcing the discharge on this timescale leads to significant technological challenges and required driving voltages that are very large (>50 kV), and the required switching is expensive and technologically limited. A simple, LRC circuit model clearly shows the requirements for driving an over- damped pulsed discharge system, as described in the ignitron (the pulsed switching that we are using for this experiment) applications notes from GE [43]. Pulse discharge characteristics are further explored in Section 2.1.2 and Equations 2.1-2.4. Regardless, for many applications the ability to operate at lower voltages with longer lifetime switches is very useful. Secondly, traditional explosive timescale FRCs are limited by the amount of trapped initial bias flux in the discharge region. FRC lifetimes, and possibly total energy content, are limited by the amount of initial bias flux. A slower diffusive timescale FRC formation allows us the continuous addition of flux during compression and reversal periods of the discharge. Theoretically this should allow for longer lifetime and more stable FRC plasmas. Slow-formation is characterized by a formation time much greater than the radial Alfven translation time ($\tau_f \gg \tau_a$) which, leads to plasma formation and heating at resistive-diffusive timescales ($\tau_f > 50\ \mu s$). Slow-formation FRCs were

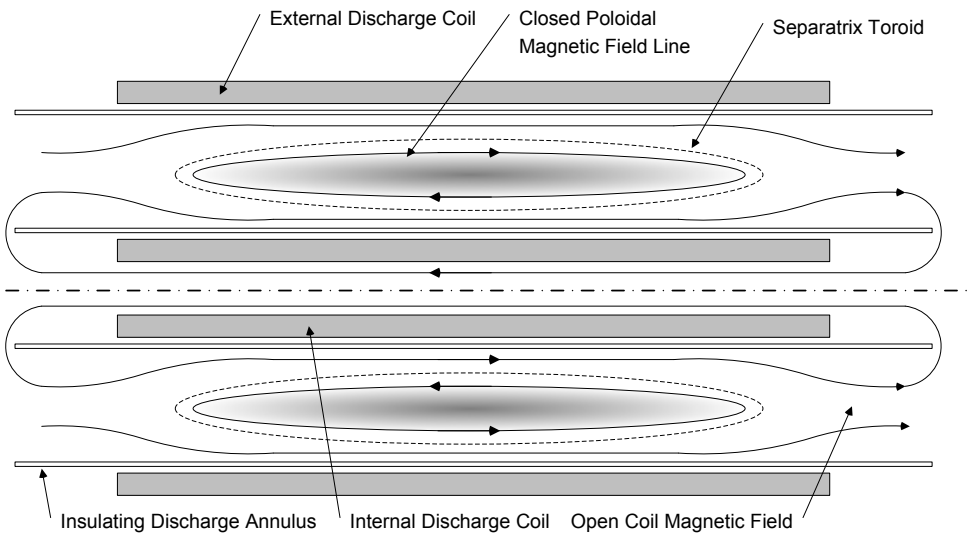

Figure 1.5: An Annular Field Reversed Configuration

first suggested by Philips [40] and later developed to several interesting formation concepts: the coaxial-coil theta pinch (CSS) [42], multi-pole geometry (Extrap) [35], and rotating magnetic field (Rotamak) [24]. In total, developing a lower voltage higher efficiency and longer lifetime field reversed configuration plasma is a valuable goal and the primary objective in this dissertation.

1.3.1.1 Asynchronous/Program Mode

Asynchronous or programmed mode field reversed configuration discharges utilize the two discharge coils separately to provide initial flux bias, plasma heating compression, additional internal flux, and possibly final translation by operating the coils in sequence with one another. The primary study for the coaxial slow source research was done by Brooks, Vlases, and Smith [42], [44]. Figure 1.6 details the formation process.

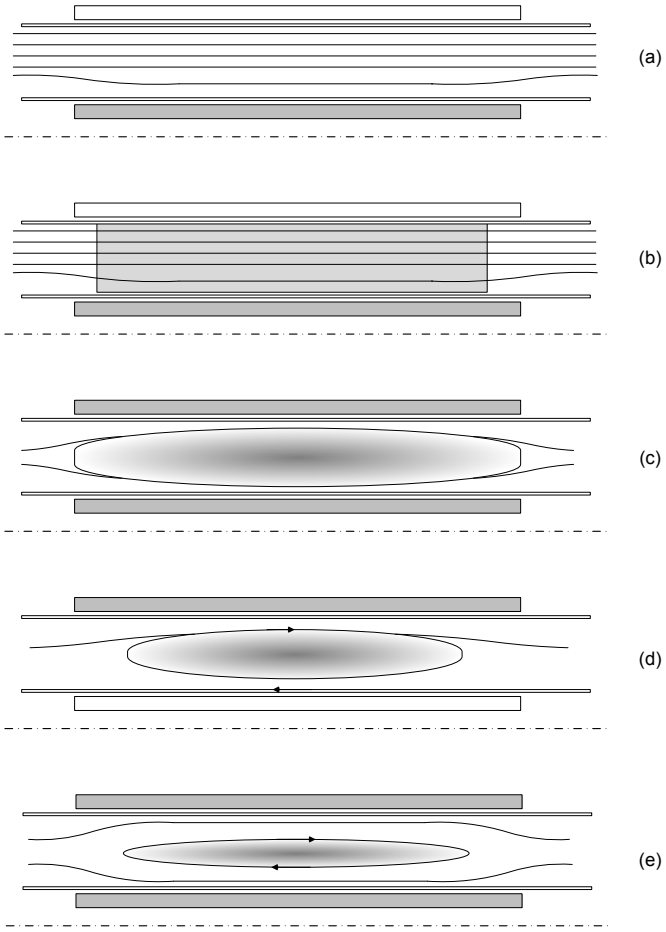

(a) Fill coil low level flux from inner coil

(b) Pre-ionize to freeze flux lines

(c) Initiate external field to generate diamagnetic current

(d) As the inner current reverses the plasma current disconnects from the coils and becomes self-consistent

(e) Continue pulse to radially compress, or destabilize to translate axially

Figure 1.6: Progression of asynchronous operation of an Annular Field Reversed Configuration

The CSS team had reasonable success with operating in asynchronous mode demonstrating FRC compression and heating at less than 1 kV and on timescales greater than 100 μs. Additionally, peak densities appear to have reached 10^{21} m^{-3} on deuterium. While operating in an independent mode allows a vast amount of parameter space optimization, the increased operational options may not be beneficial as the main negative and one of the primary conclusions of the independent CSS studies was that driving coils and an independent mode tends to lead to an unbalanced flux situation that drives the bulk plasma into the walls, which leads directly to the study of synchronous or parallel coil operation in an annular field reversed configuration plasma device.

1.3.1.2 Synchronous/Tearing Mode

Parallel operation of an annular field reversed configuration plasma is the primary study for this experimental dissertation. Parallel coil operation allows for a low-voltage, long-timescale FRC formation with a self-balancing radial flux profile, creating efficient high-density, low impurity AFRC plasmas. Figure 1.7 details the formation process.

The coaxial slow source was upgraded in 1994 [41] to incorporate parallel operation and a four turn coil to their design. The limited results were quite promising, creating a balanced high temperature (10 eV) high-density plasma formation and compression, however it appeared to still have significant issues, in regards to lifetime and turbulence. The current parallel operation discharge experiment was designed to incorporate changes in order to attempt to mitigate those concerns. Firstly, the inner coil radius was increased in order to decrease the area between the coils, and increase the amount of flux available to the inner layer of the field reversed configuration. Secondly, the parallel configuration is highly susceptible to axial instabilities

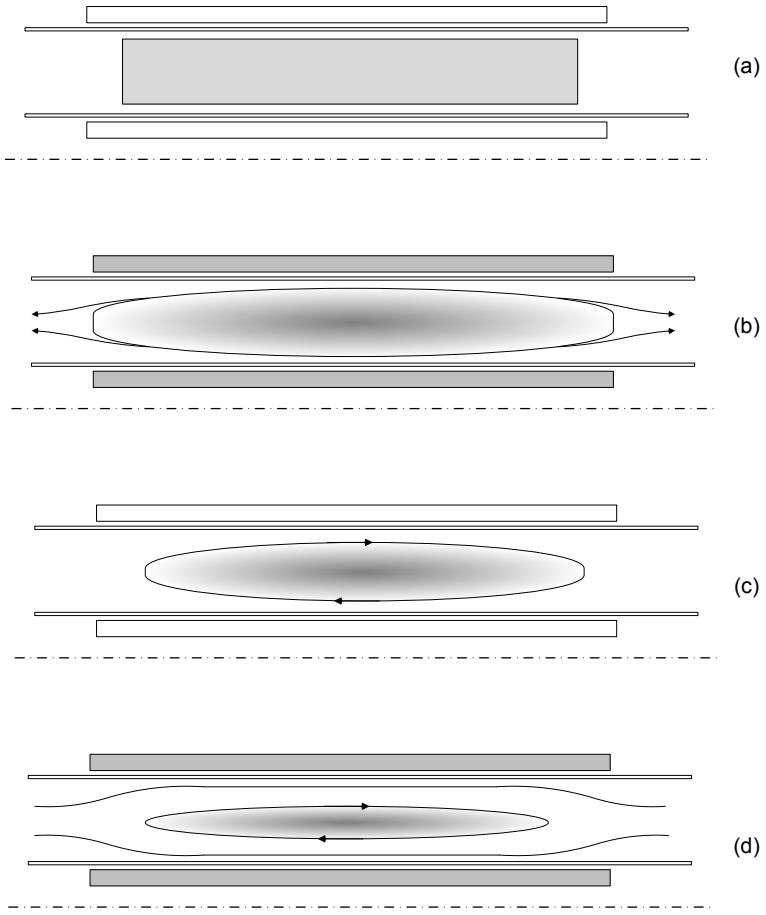

(a) Pre-ionize gas with no initial bias

(b) Initiate external field to generate diamagnetic current and internal field to further provide bias flux

(c) After some nominal relaxation time, the plasma naturally tears and forms a self-consistent structure

(d) Continue to compress and heat or translate plasma with detached field lines.

Figure 1.7: Progression of synchronous operation of an Annular Field Reversed Configuration

and translation prior to full magnetic compression. In order to reduce this translation, the CSS team suggested adding mirror coils to the annular geometry. In order to decrease complexity a non-uniform current distribution was chosen, which will naturally form a minor mirror configuration and is created entirely by the asymmetric distribution of current into and out of the far axial extremes of the inner and outer discharge coils. Finally, one concern is that the device is mismatched to the gyroradius of the primary ions in the annular discharge chamber. Specifically, the ion gyroradius is much too small for the 40 cm coil on deuterium. The discharge experiment described in this dissertation was performed on higher molecular weight noble gases in order to increase the gyroradius and more properly match the discharge geometry, with the peak field values given in Table 1.3. Another important note is that it should be expected that each major current reversal should also yield a similar flux and plasma reversal. In fact, it should be expected that with an existing uniform background gas density a major reversal (i.e., not a start-up, but a true current reversal from negative to positive bias flux) should yield a superior FRC with higher initial flux distribution than the natural relaxing case given in Figure 1.7.

1.3.2 The XOCOT Discharge Experiment Overview and Design Parameters

Table 1.3 summarizes the operation and geometric characteristics explored in this experimental investigation [30], [31]. In later chapters these discharge parameters are referenced and discussed in detail.

Coil	Outer Coil		Inner Coil	
Turns	1		1	
Length	30.7 cm		30.7 cm	
Inner Diameter	43.5 cm		10.6 cm	
Outer Diameter	51.3 cm		15.8 cm	
Coil Inductance [3]	0.38 μH		0.03 μH	
Parallel Coil Inductance	28 nH		28 nH	
Calculated Coil DC Resistance	3.2 $\mu\Omega$		1.3 $\mu\Omega$	
Discharge Period	450 μs	250 μs	185 μs	
Bank Capacitance	2000 μF	488 μF	480 μF	
Approximate Bank Inductance	0.2 μH	0.4 μH	0.05 μH	
Total Circuit Inductance	0.85 μH	1 μH	0.6 μH	
Discharge Current (1 kV)	75 kA	39 kA	28 kA	
Stored Energy (1 kV)	1 kJ	244 J	244 J	
Peak Field Strength (1 kV)	0.29 T	930 G	680 G	
Quartz Insulator			Pre-Ionization	
Inner Tube OD	197 mm		DC Glow Voltage	3-5 kV
Inner Tube Wall Thickness	7 mm		DC Glow Current	0.5-1 mA
Outer Tube ID	406 mm			
Outer Tube Wall Thickness	6 mm		Theta-Ringing	
Tube Length	152 cm		Capacitance	0.1 μF
			Peak Current	0.5 kA
			Peak Voltage	0.5 kV
			Discharge Period	4 μs

Table 1.3: XOCOT discharge experiment parameters

	Testing Goal
(I)	Create a high energy, pulsed discharge facility, diagnostics, and plasma experiment to investigate theta pinches
(II)	Explore the discharge parameter space for a Synchronous Annular Field Reversed Configuration Plasma S(AFRC)
(III)	Characterize and quantify the optimal operation parameters for a low-voltage, diffusive timescale magnetized discharge
(IV)	Experimentally characterize the radial scaling parameters for efficient FRC formation and compression
(V)	Preliminarily quantify translational and downstream plasma properties for an AFRC

Table 1.4: XOCOT discharge study goals

1.4 Study Goals

The XOCOT discharge study that is expounded upon in the following Chapters (and Sections) seeks to explore the electrical, plasma discharge, and efficient operation of an Annular Field Reversed Configuration Plasma operated in a Synchronous (or Parallel) discharge configuration. As described in Section 1.2, there are numerous, important applications of an efficient, high-energy density, magnetized plasma as formed by a field reversed theta pinch. More specifically, the ability to create this type of plasma configuration on longer timescales, with additional flux addition, and at much lower operational voltages is worth exploring in significant detail. Finally, this study has focussed on heavier atomic mass gases (argon, xenon) in order to explore the utilization of FRCs for advanced fuel cycle and space propulsion applications. The primary goals of this experimental dissertation are outlined in Table 1.4 and are the programmatic progression required to fully explore the creation of an Annular Field Reversed Configuration Plasma.

1.5 Contribution to the Field

Field reversed configuration plasmas have been investigated in the past, with eleven modern, full-scale experiments investigating a wide range of discharge con-

ditions and parameters. However, very little work has been done with plasma discharges lasting greater than 20 μs, and only two major experiments investigating FRCs of less than 1 kJ (or even 10 kJ). One of those experiments, the CSS, an annular FRC, showed significant promise in creating long-lived, efficient FRCs and was tested quite extensively in an asynchronous mode. It was discovered that the asynchronous mode induced significant inefficient asymmetries and very preliminary work suggested that they could be eliminated in a synchronous operation. Additionally, it was suggested that investigating a shorter, lower total volume FRC would benefit the radiation and instabilities issues. At the conclusion of this study, the author will expand the understanding and utility of field reversed configuration plasmas to include synchronous operation of Annular Field Reversed Configuration devices. This understanding will advance the application of low-voltage, annular FRCs to the various fusion and propulsion applications outlined in Section 1.2.4. More specifically, this study provides a comprehensive look at the synchronous operation of AFRC at three discharge periods, 450 μs, 250 μs, and 150 μs and discharge energies ranging from 50 J to 1100 J. This represents approximately a 4-fold increase in discharge rate (peak dI/dt) and an even greater range of discharge energy than has been studied previously. The internal and external probe diagnostics will yield unprecedented real-time internal plasma measurements and the ability to make quantitative measurements of plasma energy input efficiency and loss as well as optimal discharge pressures and energies for this geometry.

1.6 Study Approach

The study presented in this dissertation is comprised of five main parts. Firstly, a historical and theoretical treatment of field reversed configuration devices is presented above in order to provide a context for the past experimental work and applications of FRCs. A complete description has been provided of the formation processes for traditional, cylindrical FRCs and the two forms of annular FRCs. Secondly, a complete description of the experimental setup and discharge procedures is given in Chapter 2. This experimental hardware setup represents a completely new facility and pulse discharge network at the Air Force Research Laboratory at Edwards AFB. Chapter 2 also contains a detailed description of the diagnostics used in this experiment, their theoretical operation, real limitations and operational circuitry, and data analysis techniques. Chapter 3 outlines zero-dimensional energy modeling work done early in the experimental procedure as well as a useful empirical energy model to investigate discharge efficiencies real-time. Chapter 4 is a complete study of the pre-ionization techniques used in the XOCOT discharge experiment, as well as a full optimization program. The PPI (pre- pre-ionization glow discharge) and PI (pre-ionization RF ringing discharge) systems were optimized for neutral gas pressures, input voltages, input energies, and geometries with a focus on optimal creation of a high-density magnetized plasma. Finally, Chapters 5-7 detail the creation and testing of FRC discharges at 450 μs, 250 μs, and 185 μs at various discharge pressures, energies, and neutral gases. An internal triple probe was utilized to map the interior of the annular discharge region and various optical diagnostics were used to observe plasma formation, heating, and translation. Chapter 8 serves to provide a concise summary and final analysis of data and calculations presented in this study.

CHAPTER 2

Facilities, Apparatus, and Techniques

Fundamental to the design of any empirical study is the experimental hardware, experimental procedure, and diagnostics used. The XOCOT discharge experiment was a completely new test facility, pulsed-power distribution and storage network, and pulsed-plasma diagnostic platform. Chapter 2 describes the annular vacuum facility and data acquisition (DAQ) system that was constructed to enable the precise and high-speed testing of a highly-repeatable, but single shot annular FRC. A complete capacitive storage system, low-inductance transmission lines, safety network, and EMI shielding were constructed to test kJ energy pulsed plasmas operating on the 100-1000 μs discharge timescale. Additionally, the high-current pulsed switching systems for the pre-ionization and main bank discharges will be discussed from both a theoretical and practical standpoint. Chapter 2, Section 2.4 contains a detailed summary of the theoretical operation and limitations, construction techniques, and operational regimes of the diagnostics used in this experiment. Several optical diagnostics were utilized, including cameras and photometers to investigate the formation and compression of magnetized plasma by optical emissions. Also externally, magnetic field probes and flux loops were used to measure diamagnetic current, resultant magnetic fields, and the radial location of the annular plasma. Finally, Section 2.5

describes a high-speed, current-mode triple probe that was designed and used for internal measurements of plasma density, temperature, and position.

2.1 Discharge Experiment Overview

The discharge experiment was designed to investigate the discharge, heating, and compression of an annular FRC without the complications of non-uniform and pulsed neutral gas distributions. The experimental setup consisted of two annular quartz chambers that were backfilled with a neutral, cold gas to a specified pressure with the external, annular inductive electrodes that were discharged at atmospheric pressure around this annular chamber.

2.1.1 Vacuum Facility Design and Construction

The vacuum system was constructed in order to support a completely vertical setup, with the express goal to alleviate stress concerns that would be due to two cantilevered (and the center unsupported) 60-in. quartz tubes. The chamber itself consists of two 60-in., approximately 7-mm thick quartz tubes, of 40.6- and 19.7-cm outer diameters that are sealed with a 60-cm diameter, 3-cm-thick polycarbonate top seal and a stainless steel adapter flange on the bottom. Both ends are then sealed with custom L-gaskets. This height was chosen to allow for 1 coil length below, and 3 coil lengths downstream of the main discharge coils, both to alleviate interference between the adapater flange and allow sufficient downstream distance to observe translation. An image of the stainless steel adapter flange is given in Figure 2.1; the flange was designed to accommodate both quartz tubes and 7, 2.75 $in.$ ConFlat flange adapters for pressure sensors, feed system, and internal probe mounts. The main pumping system is a Varian VHS-6, 6 in. diffusion pump backed by a Varian DS 602 rotary vane roughing pump. The propellant is fed via a Unit UFC-8160 mass flow controller and Unit DX-5 digital controller. Figure 2.2 shows a generalized

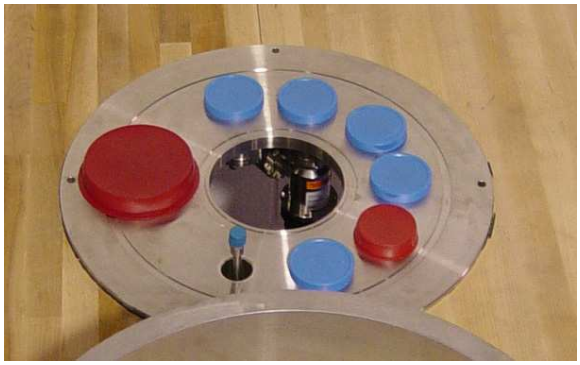

Figure 2.1: Photograph of the stainless steel adapter flange

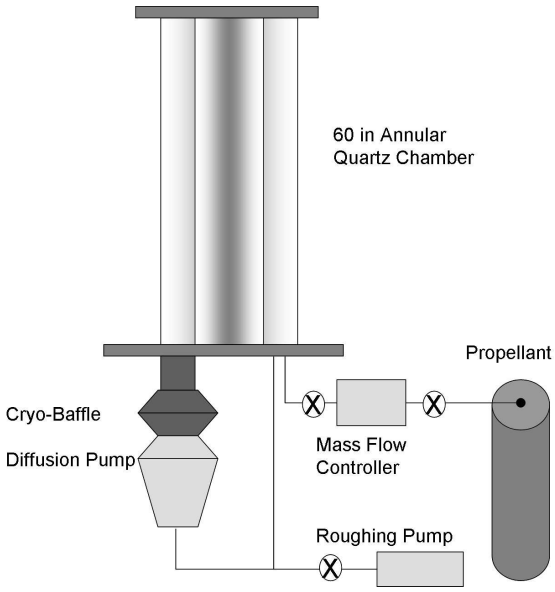

Figure 2.2: Schematic of annular vacuum pumping system

schematic of the annular vacuum chamber, pumping system, and propellant feed system.

This system has a pumping speed of 1930 L/s on argon and a base pressure of 10^{-7} Torr.

2.1.2 Energy Transmission System Design and Hardware

The key hardware in a pulsed plasma discharge experiment are the components of the pulsed energy transmission network. These include a fast acting switch, a low inductance transmission line, an energy storage system, and all associated safety mechanisms. The timing of a pulse energy discharge network is given, to first order, by the decay constants of a simple, overdamped LRC circuit, namely $\omega = \sqrt{LC}$, and $\tau = \frac{R}{L}$. For the 450-μs discharge case, a total capacitance value of 2000 μF was used, and for the 250-μs case a capacitance value of 488 μF was used by utilizing various combinations of high-energy Maxwell (General Atomic) capacitors. The capacitor network has two important safety features that must be included on all high-energy pulsed power systems. First, a permanent bleed and balance network was permanently connected across each capacitor (approximately 50 kΩ) in order to slowly discharge the capacitors in the event of a switch failure as well as to maintain a voltage balance between the capacitors in the event of a capacitor failure. Secondly, a gravity dump switch automatically (in the case of power failure) discharges the capacitors across a 5-kJ, 14 Ω electrolytic resistor network [2] in order to quickly empty the capacitors in the event of a misfire or other significant system failure. Additionally, a smaller set of 0.1 μF capacitors were used for the 250 kHz pre-ionization discharges.

The main switching was accomplished using two 100-kA mercury discharge ignitrons (model NL-7703) [43], pulse isolation transformers, and high-voltage insulation. These ignitrons were triggered via fiber optics and a Northstar ignitron trigger generator, yielding a turn-on-time much less than 1 μs and very low ripple. The pre-ionization discharge however, requires a faster switch and therefore a 15-kV, 1.5-kA thyristor switch designed and built by ABB semiconductors (5SPP 0921 01), was

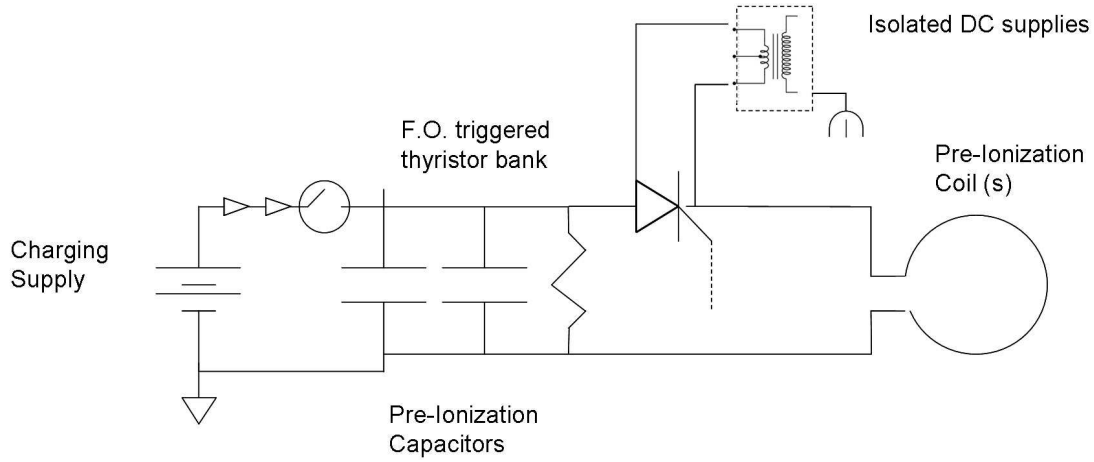

Figure 2.3: Discharge circuit for a typical pre-ionization discharge

used, and was also fiber-optically triggered. The circuits are shown in Figures 2.3 and 2.4.

By observing the ringing frequency (2-4 kHz), the input capacitance, and an approximation for the inductance of the switching, a coil inductance of 70 nH was determined.

Reference [43] provides an excellent description of the discharge conditions for an overdamped pulsed ringing discharge. Using a simple LRC discharge circuit, an assumption of initial charge voltage before discharge, and a damped sinusoidal solution, Equations 2.1-2.4 and Figure 2.5 describe the resultant operational parameters.

$$f = \frac{1}{2\pi\sqrt{LC}} \tag{2.1}$$

$$I_p = 1.57C\frac{dV}{dt} \tag{2.2}$$

$$\Delta E = \frac{1}{2}C\left(V_p^2 - V_0^2\right) \tag{2.3}$$

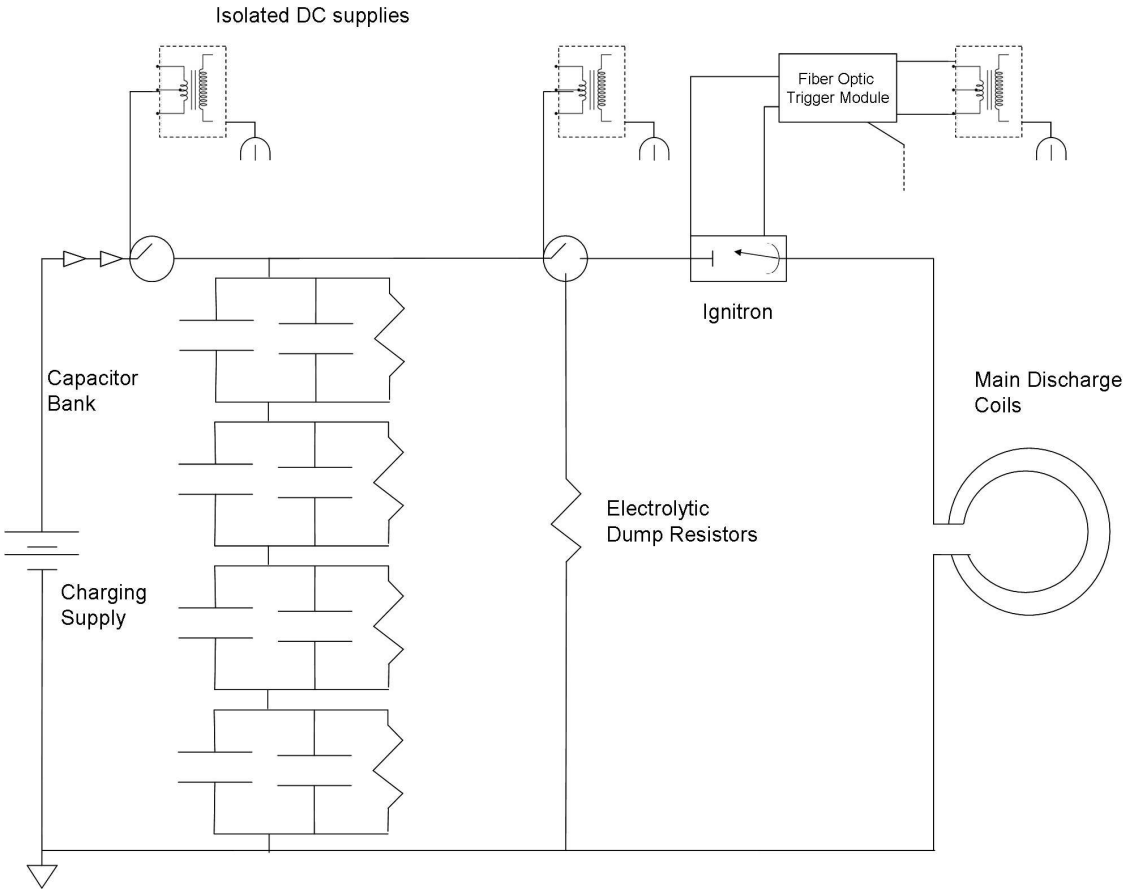

Figure 2.4: Discharge circuit for a typical main bank discharge

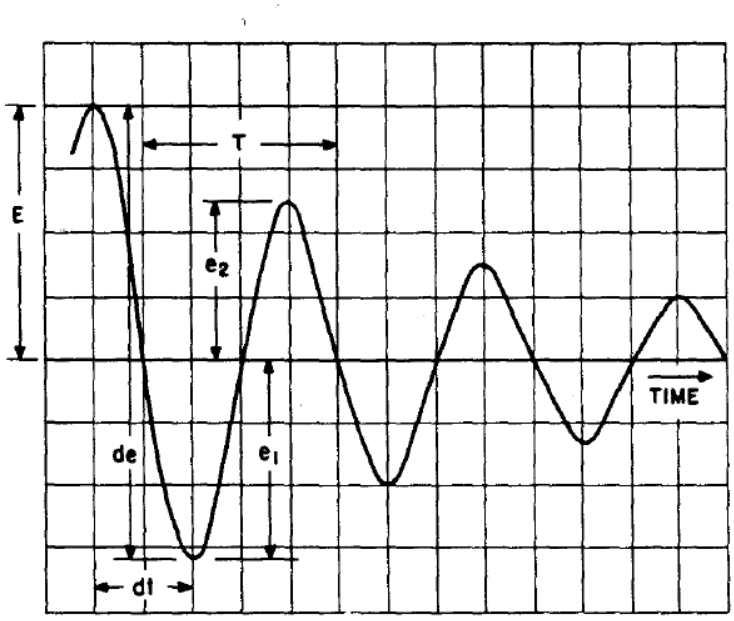

Figure 2.5: Simple LRC pulsed discharge in an overdamped condition from Reference [43]

$$\frac{I_2}{I_1} = e^{\left(\frac{-R}{L}\right)\frac{1}{2f}} \tag{2.4}$$

2.2 Circuit Designs for the Discharge Networks

Figure 2.4 shows the general electrical circuitry and discharge hardware for the first set of XOCOT experimental discharge testing described in Chapter 5. This pulse network was constructed to have a 2000 μF capacitance and a peak voltage rating of 1000 Volts. This first bank was constructed with existing AFRL capacitors at the expected discharge parameters. Unfortunately, the system setup as constructed at AFRL (Figure 2.10) had higher than expected line and ignitron inductance. That yielded a significantly longer discharge period than initially desired. Additionally, at the peak operating voltages, bank-voltage was within 10 % of the peak capacitor voltages. Chapter 5 details the testing that was performed on this 450-μs period capacitor bank.

In order to examine higher dI/dt discharges and operate within the voltage limits

of the capacitors, a new capacitor bank was constructed using higher-voltage, modern capacitors. Figure 2.6 shows the schematic diagram for the 250-μs discharge period capacitor bank. Additionally, Table 1.3 shows the fundamental operating conditions for the 250-μs, 500-μF discharge. The higher dI/dt discharge periods were expected to increase compression and initial heating by the applied, reversed currents. Additionally, the previous data on asynchronous AFRC discharges and very small amount of previous data on synchronous operation was at 150-200 μs, necessitating a longer discharge period to be able to compare the results of using heavy-ion gases. The capacitor bank tested has a rated maximum voltage of 4000 Volts.

During the studies in Chapter 6, significant challenges in capacitor lifetime were discovered. Specifically, running 4 high-energy capacitors in series and therefore balancing both the voltage across each individual capacitor as well as the bulk current through them was a significant challenge and all capacitors must be highly uniform and de-rated. At the higher coil voltages (1000 V) the peak current output per capacitor was reached and intermittent failure would occur. The experimental results shown in Chapter 6 were completed before the capacitor failure began. In order to mitigate this effect, newer, lower-capacitance capacitors were installed that were both in parallel (load balancing and peak current become non-issues) as well as significantly derated. Chapter 7 details experimental investigations with the 185-μs period capacitor bank. Figure 2.7 shows the new circuit setup. Instead of 4, 2000-μF capacitors in series (resultant measured capacitance of 487 μF), 2 parallel 225-μF capacitors (measured bank capacitance of 480 μF) are used, which should yield a similar discharge value on capacitance alone. However, as the capacitor inductance is a contributing portion of the total circuit inductance it must be taken into account. An individual capacitor has approximately 100 nH inductance. The circuit in Figure

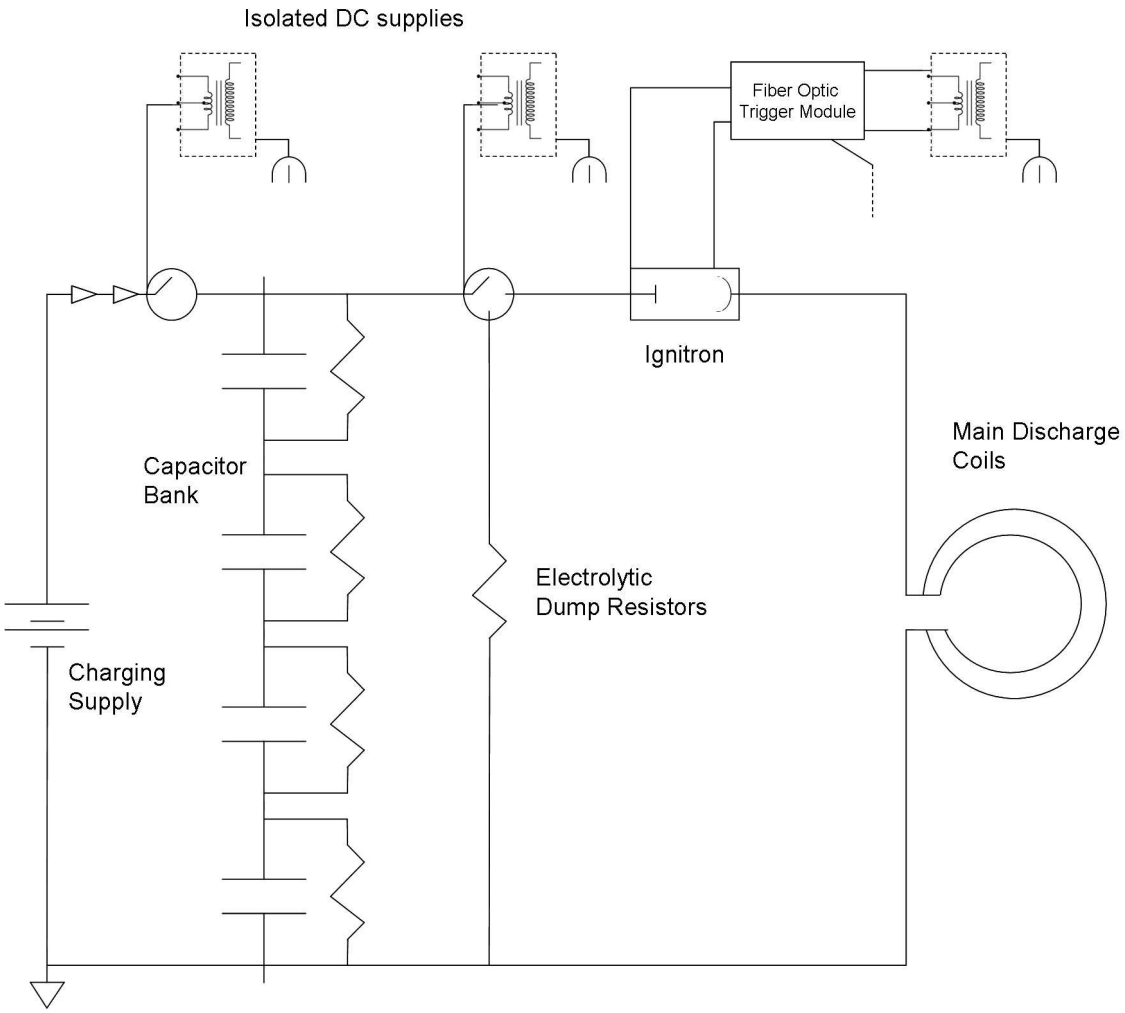

Figure 2.6: Discharge circuit for a typical 250-μs main bank discharge

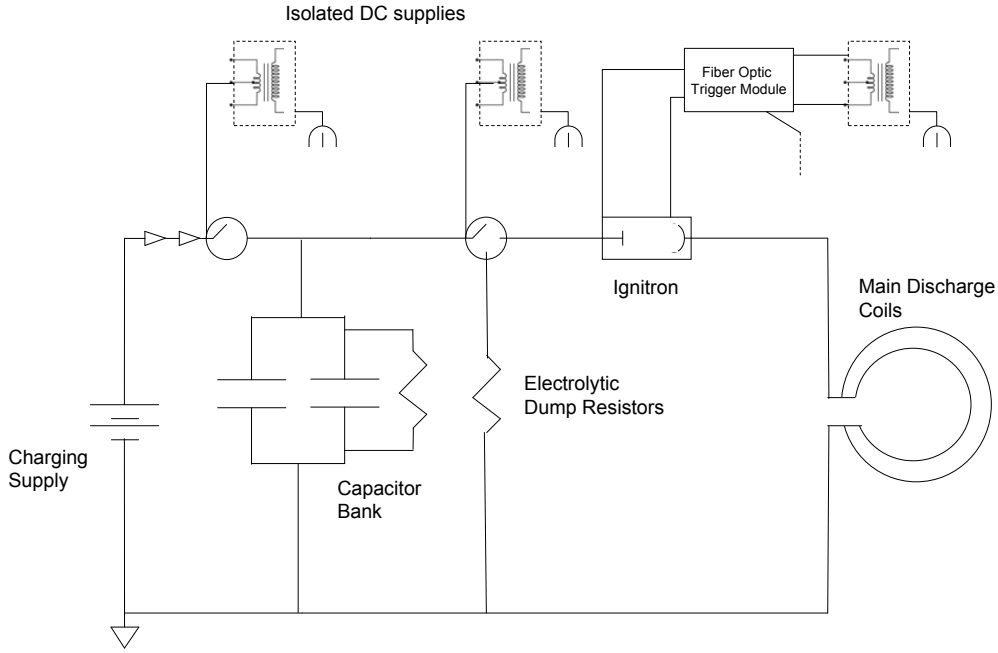

Figure 2.7: Discharge circuit for a typical 185-μs main bank discharge

2.4 has 400 nH inductance, while Figure 2.7 has 50 nH. As in Equation 2.1 this will have a significant effect on circuit discharge period and thus a third discharge period data point can be obtained. Additionally, this data point can yield an empirical calculation of the total effective circuit impendence without the capacitors of 0.6 μH.

In total, three capacitor bank networks were constructed and enabled the testing of 450-, 250-, and 185-μs period discharges.

2.2.1 XOCOT Discharge Experimental Setup

The XOCOT discharge experiment utilizes the pulsed energy distribution network and annular vacuum chamber to investigate high-energy density pulsed plasma experiments, specifically an annular field reversed configuration theta pinch. The experimental setup utilized for the following discharge testing is described in Figure 2.9 and Table 1.3. Inserted through the bottom flange, shown in Figure 2.8, are the propellant feed line (1/4 in. swagelock), the internal probe assembly (detailed further in Section 2.5.3.1), manual vent valve, diffusion pump gate valve, and manual roughing pump valve. Additionally, the flange connects to a MKS Series 910 Dual Trans combination Micro Pirani/Piezo Pressure Transducer that is accurate from 10^{-5} to 10^{3} Torr. Finally, the bottom flange serves as a feedthrough for the triple probe assembly, which is shown in detail in Figure 2.45, and the PPI (pre- preionization seed plasma) DC glow discharge electrode. The PPI discharge electrode is a thoriated tungsten electrode, 3-mm in diameter, and 21-mm-length in exposed cylindrical electrode fed through an isolated high-voltage, high-current feedthrough. The PPI electrode is located on the bottom, steel interface flange and is biased with respect to the bottom flange.

The main discharge coil consists of a 43.5-cm inner-diameter, 51.3-cm outer-diameter aluminum outer discharge coil connected in parallel with 4/0 copper cabling to an inner 10.6-cm inner-diameter, 15.8-cm outer-diameter discharge coil. Figure 2.11 shows the discharge coil and Table 1.3 details the geometric characteristics used for these experiments. Aluminum was chosen as the discharge coil due to its low-magnetic and low-density properties as compared to other highly-conductive metals.

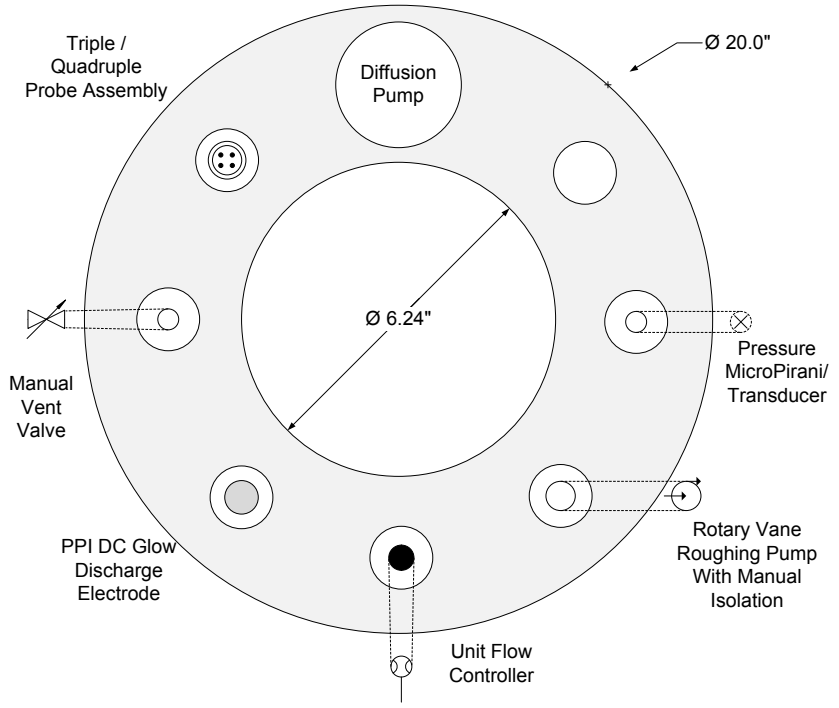

Figure 2.8: Schematic of bottom flange adapters, feedthroughs, and electrodes

	Procedure Description
(Ia)	Rough chamber to 10 mTorr pressure
(Ib)	Backfill argon to 200 mTorr
(Ic)	Apply 1500 V differential to alternating triple probe leads until steady, DC heating ion impact glow
(Id)	Maintain glow heating for 10 seconds to remove contamination
	Triple probe cleaning procedure
(IIa)	Engage Diffusion pump and purge chamber at $< 10^{-5}$ Torr for 30 minutes
(IIb)	Backfill chamber with argon, xenon flow to a stable 5-20 mTorr
(IIc)	Charge main capacitor bank to operation voltage
(IId)	Charge pre-ionization bank
(IIe)	Disengage main bank power supply
(IIIa)	Initiate PPI pre-ionization glow discharge
(IIIb)	Trigger discharge sequence
(IVa)	Disengage power supplies, PPI
	Repeat from IIc with new operational voltage

Table 2.1: XOCOT discharge testing procedure

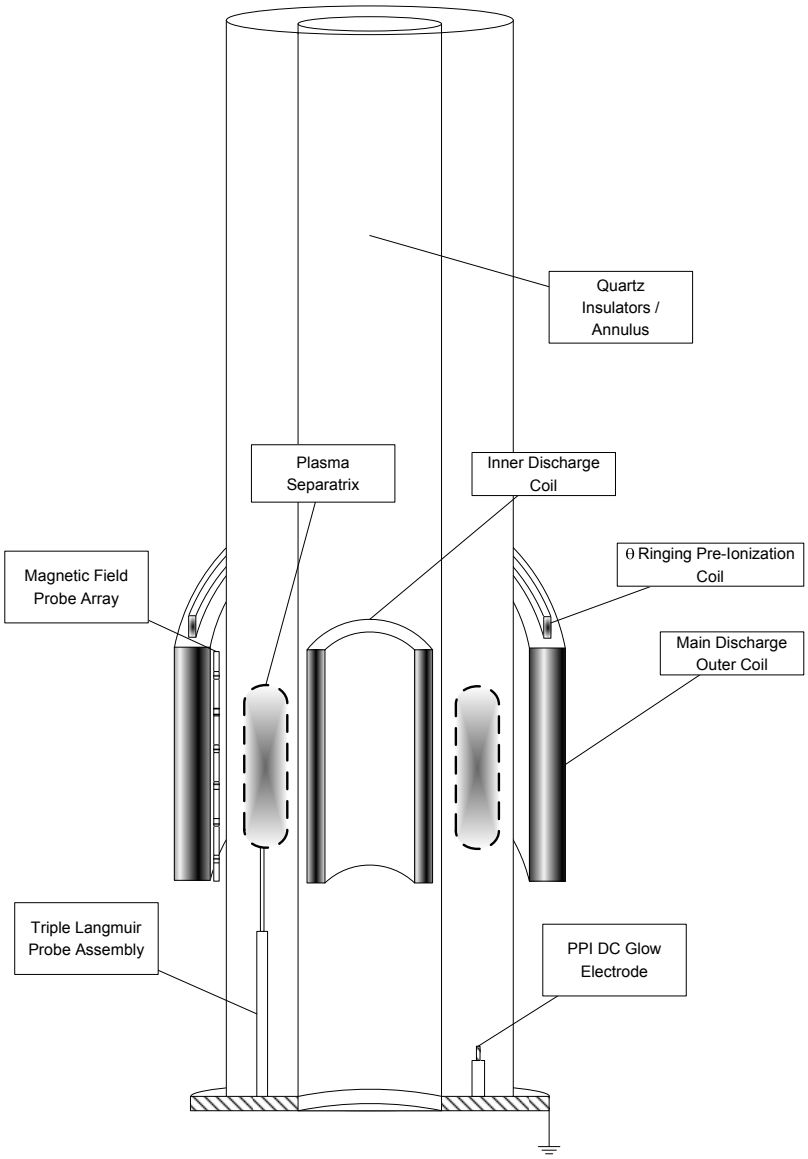

Figure 2.9: Schematic of system setup and coil schematic

Figure 2.10: Photograph of the annular chamber, test setup, and current transmission cables

	Procedure Description
(IIIa)	Initiate PPI pre-ionization glow discharge
(IIIb)	Manually trigger discharge sequence with pulse generator
(IIIc)	Pulse generator triggers DICAM triggers initialization
(IIId)	Pulse generator triggers data acquisition recording on oscilloscopes
(IIIe)	Pulse generator triggers data acquisition recording on spectrometer (for 3 ms)
(IIIf)	Pulse generator triggers preionization thyristor stack via fiber optics
(IIIg)	Pulse generator triggers main bank switch via fiber optics
(IIIh)	Main bank switch triggers high current thyristor to discharge bank
(IIIi)	Large scale compression and heating begins
(IIIj)	DICAM is switched via internal timing circuits

Table 2.2: XOCOT discharge testing timeline

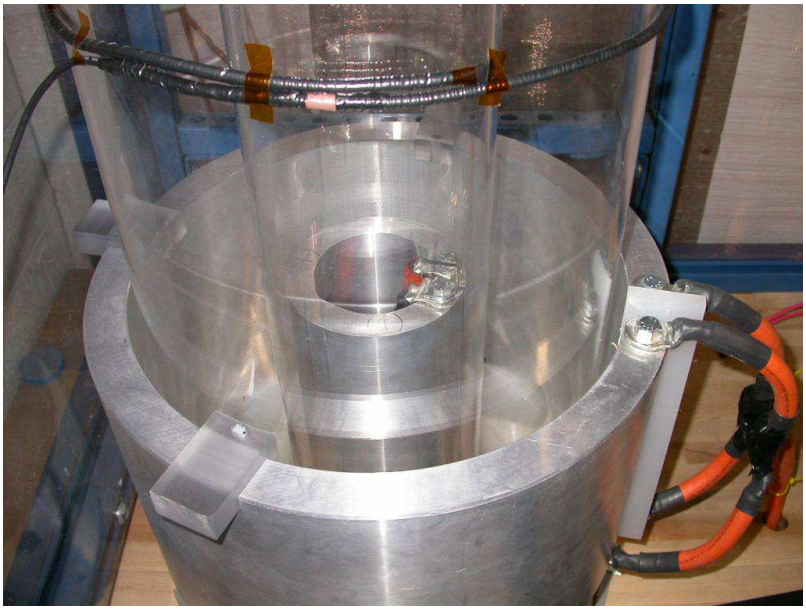

Figure 2.11: Annular Discharge Coil used in the discharge experiment

2.2.2 EMI Mitigation

In pulsed discharge systems, the electromagnetic interference (EMI) is a significant complication for data collection and analysis. Interference can be due to several sources, mitigation of which has been taken into consideration at all levels of experimental design. First, and most prominently, noise due to ground interference can be present when large magnitude or high-frequency currents are driven through the building or data ground lines. Two main techniques were used [30] to mitigate these effects: as described in Section 2.1.2 isolation of main pulsed discharge lines and the data acquisition system through both optical (triggering lines), isolation transformers on the power lines (for the charging power supplies), and physical isolation of the data acquisition systems. The triggering, digital data acquisition, and oscilloscopes were powered via Tripplite 1500 VA backup power supplies that were physically isolated from the 120 V power and building ground power networks. Secondly, a dedicated earth ground was installed and bonded to the main power ground line to more adequately sink the spurious ground currents. Additionally, the radiated E/M radiation must be considered, both the electrostatic and electromagnetic coupling. The primary technique to reduce this effect is shielding by copper and stainless steel mesh [17] to absorb both the kHz (main discharge) and MHz (pre-ionization ringing discharge) radiated electric and magnetic fields. A grounded Faraday-cage type shielding system was used for the main discharge chamber and pulsed switching system as well as the main capacitor bank. Additionally, UV and physical shielding was provided by 0.25 *in.* and 0.125 *in.* polycarbonate sheets surrounding the annular discharge chamber, the capacitor bank, and the entire assembly as can be seen in Figure 2.10.

2.3 Data Acquisition

Data acquisition and pulse generation are tied together closely with the main triggering pulse generator also triggering a main bank initiation and discharge. As shown in the complete data acquisition (DAQ) diagram in Figure 2.12, data acquisition is accomplished primarily by a bank of digital oscilloscopes, a DSO (Digital Storage Oscilloscope), and a workstation. The scopes used are two, four-channel Tektronix TDS640 digital oscilloscopes and one four-channel TDS400 digital oscilloscope that are interfaced to the Dell workstation via GPIB and GPIB to USB connectors. Additionally, an eight-channel Sigma 100 DSO is used to collect 12-bit and 14-bit magnetic field probe data, with data being collected via a USB port to the workstation. The workstation runs National Instruments LabVIEW 7.0 with a virtual instrument (VI) that is responsible for data collection, collation, and saving from the scopes, but not the high-speed triggering necessary to capture the full pulse width. Data from the Sigma 100 are stored internally and later accessed via USB and used as a remote hard drive to the workstation. All four scopes are hardware triggered via their auxiliary trigger inputs. The Ocean Optic's spectrometer described in Section 2.4.6 is connected via USB to the workstation and is operated with Ocean Optics' OOIBASE32 data acquisition software. The software is triggered with a hardware trigger that directly ties the pulse generator to the Ocean Optics hardware itself. The DICAM high-speed camera is driven by an external DAQ and trigger module that provides $< 10\ ns$ trigger delay and image processing. The camera's DAQ module is connected to a DOS-compatible computer (for driver compatibility) and the data are copied to the main DAQ workstation by removable disk.

The various data are then imported into a data analysis package, IGOR 5.0, that is subsequently used for all data processing and graph generation. Appendix

A contains the IGOR code utilized to analyze the triple probe and magnetic field probe data.

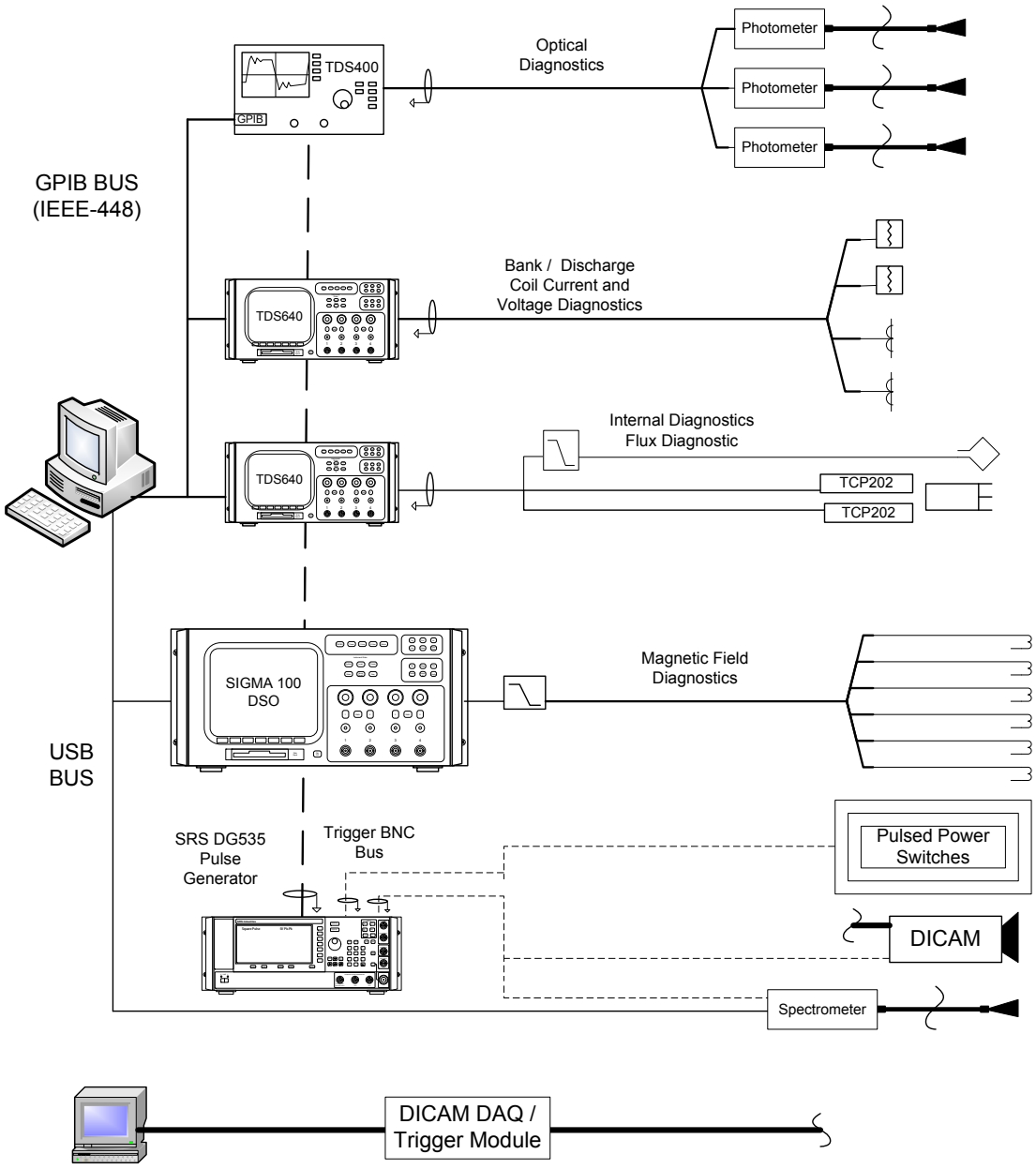

Figure 2.12: Schematic of data acquisition and electrical setup for the discharge experiment

2.4 External Diagnostics

In order to fully characterize the FRC discharges in real time, a collection of internal and external diagnostic were employed. Firstly, the external diagnostics served to explore the instantaneous formation, compression, heating, and translation of the created magnetized plasmas. To that end several broad characterizations of external diagnostics were designed, developed, and implemented. Optical diagnostics are extremely useful in realtime characterization of generalized plasma properties and are more free from noise, complicated plasma interaction, and contamination of the discharge itself. For these experiments, high-speed photometers were used to take both point and spatially generalized, real-time measurements of the broadband optical emission of the plasma. A mega-pixel (MP) camera was used to explore the spatially resolved and instantaneous broadband emission of the plasma to characterize the compression and heating effects during the various stages of the experiment. A spectrometer was used to gather wavelength resolved, but spatially and temporally averaged plasma data from the center (axially) of the discharge experiment. Secondly, magnetic diagnostics were implemented to record the flux and field emissions of the high-density magnetized plasma. Arrays of magnetic field probes (in this experiment they have been B-dot flux probes) were used to simultaneously record instantaneous plasma position and magnetization at multiple locations simultaneously. Also, flux and current probes (flux loops and Rogowski coils) were used to gain further bulk plasma information, real-time. These diagnostics were all positioned outside of the discharge annulus and have very little impact on plasma formation and compression during the course of a typical discharge (the inductance of the probes used was very low and provided little impedance insertion loss). Finally, several internal plasma

probes were inserted into the plasma, both at single points and also swept through the plasma to gain spatially and temporally resolved plasma magnetic field, temperature, density, and energy distribution information. However, all internal plasma probes have a profound effect on the plasma itself, both through a cooling effect (cold sputtered ions and secondary electron emission) and electrical effects (sheaths, magnetic interaction, and internal current collection) which will be explored further in later Sections.

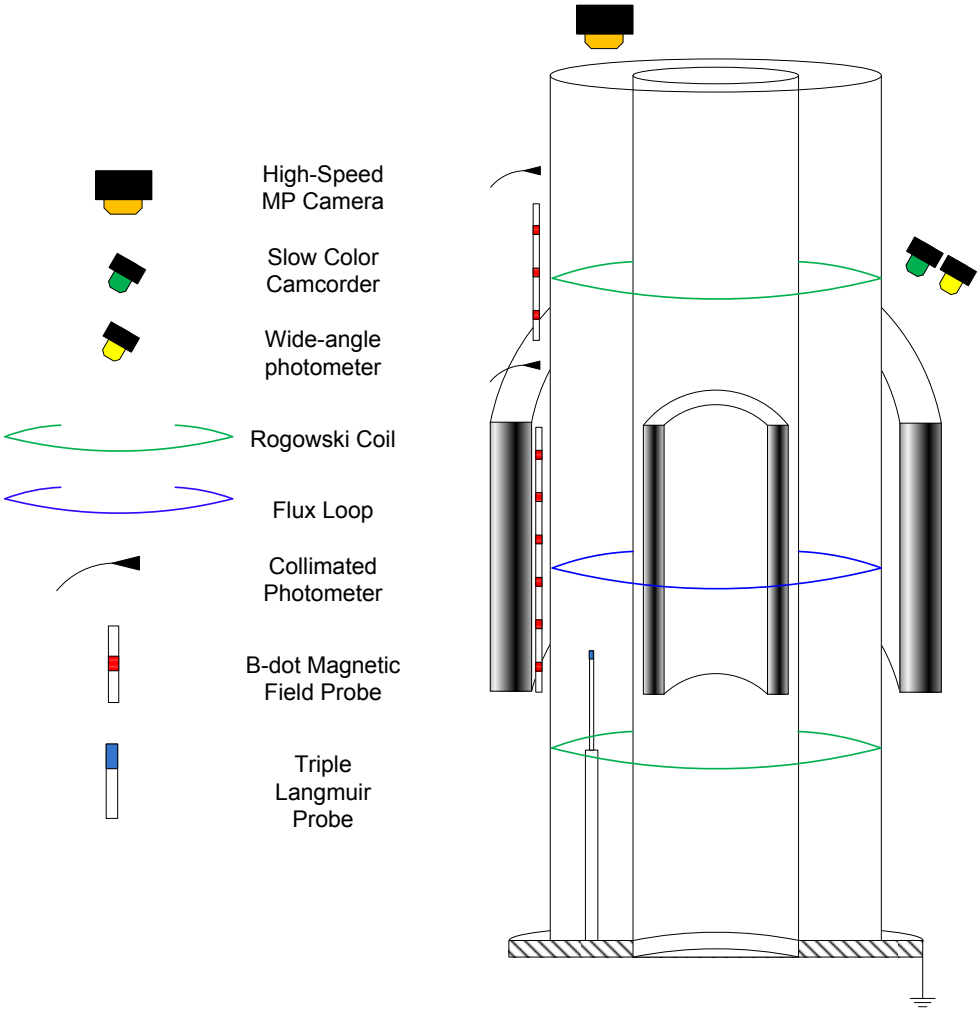

Figure 2.13: Schematic of external and internal diagnostics used in the discharge experiment

2.4.1 Photometers

Two photometers were used in the XOCOT discharge experiment: New Focus 2031 large-area photometer and New Focus 2051 variable-gain photometer, whose operational specifics are given in Tables 2.3 and 2.4, respectively. The 2031 photometer was positioned as the wide-angle photometer in Figure 2.13 to observe the bulk plasma content during a typical discharge. The New Focus 2031 was used as a generalized measure of how well the discharge was creating and heating plasma content. The collimated photometers are connected by fiber-optic cabling with transmission spectra given in Figure 2.15 to low-dispersion collimator lenses. A general relation between the broadband emission and bulk plasma content is given by Equation 2.5, as a function of electron temperature, T_e, and plasma density n_e. This approximation does not distinguish between individual frequency emission or the photometers' inherent absorption spectrum (Figure 2.14), however, it does give a good reference comparison for different discharge parameters and bulk plasma content (or in this case the *density* $\times$ *temperature* product).

$$I \propto n_e e^{\frac{-1}{T_e}} \tag{2.5}$$

Model 2031	Specifications	
Wavelength Range	400-1070 nm	
Detector Material/Type	Silicon/PIN	
Detector Diameter	8 mm	
Typical Max. Responsivity	0.6 A/W (at 900 nm)	
Maximum Power Density	10 mW/mm^2	
Gain Settings	'Low'	'Medium'
Bandwith (kHz)	1000	150
Transimpedance Gain (V/A)	2×10^3	1×10^5
Saturation Power (at 900 nm)	4 mW	83 μW
Typical Min. NEP ($pW/\sqrt{Hz}$)	43	1.3
Output Impedance	100 Ω	
Electrical Output Connector	BNC	

Table 2.3: Specifications for the New Focus 2031 high-speed, Large Area Photometer

Model 2051	Specifications	
Wavelength Range	300-1070 nm	
Detector Material/Type	Silicon/PIN	
Detector Diameter	1.0 mm	
Typical Max. Responsivity	0.5 A/W	
Maximum Power Density	20 mW/mm^2	
Gain Settings	'Medium'	'High'
Bandwith (kHz)	6000	250
Transimpedance Gain (V/A)	2×10^5	6×10^6
Saturation Power (at 900 nm)	21 μW	0.7 μW
Typical Min. NEP ($pW/\sqrt{Hz}$)	136	0.68
Output Impedance	100 Ω	
Electrical Output Connector	SMA	

Table 2.4: Specifications for the New Focus 2051 Adjustable Photometer

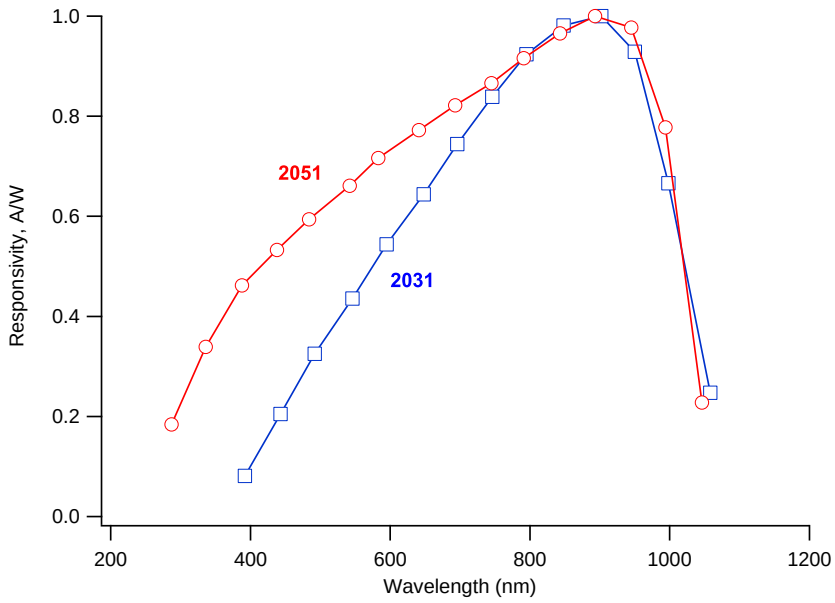

Figure 2.14: Spectral responsivity for NewFocus 2051, 2031 high-speed photometers

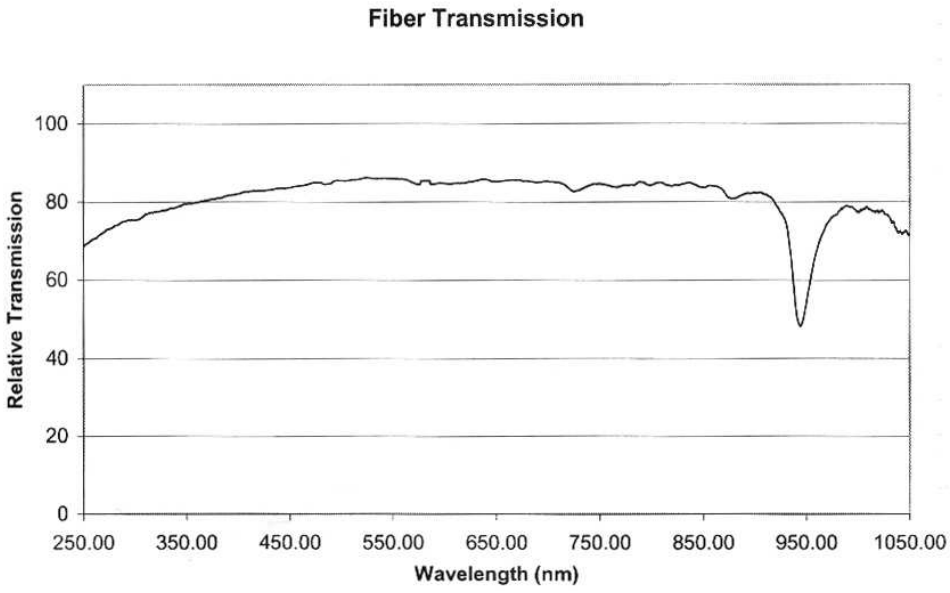

Figure 2.15: Fiber optic transmission spectrum for the high-speed photometer

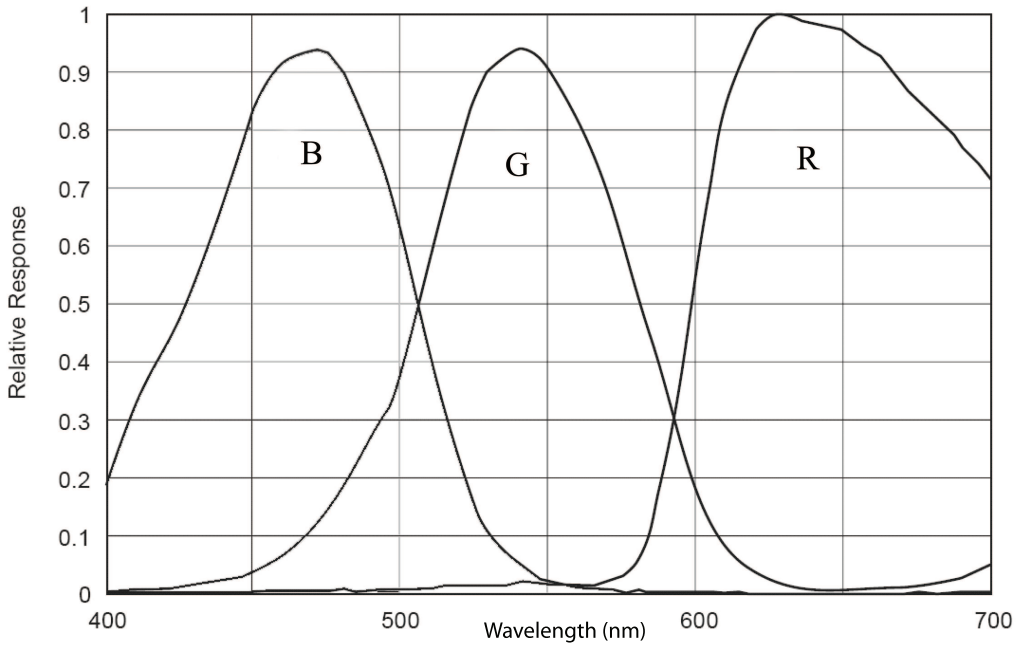

Figure 2.16: DICAM II spectral response

2.4.2 DICAM II

The DICAM II was one of the key diagnostics for observing plasma uniformity and some indication of plasma compression heating during the formation and then downstream translation of an FRC. The DICAM II is a one megapixel, sub-microsecond single-photograph camera in visible wavelengths. The DICAM wavelength response is as shown in Figure 2.16 and was triggered in accordance with trigger diagram Figure 2.12. The DICAM is an 3-chip (Red, Green, Blue) intensified CCD camera which is externally triggered and data is subsequently downloaded by parallel data cable. Data from the DICAM have been shown to be invaluable in understanding the nonuniformities of the formation plasma. Data using this camera are used throughout Chapters 5–7.

The DICAM was outfitted with a 105-mm Nikkor 3.5 lens, with the aperture set at f/11. This aperture setting was optimized to focus on the plasma region and

ignore the EMI shielding that is in the viewplane. The DICAM was positioned approximately 5 m away from the discharge coil, with an incident mirror to allow the imaging of the discharge area from above. Figure 2.17 (a) shows the typical view of the DICAM, with an amplification setting of 6.0 (as opposed to the typical 4.0), an integration time of 900 μs, and two large 1-kW halogen lights illuminating the target region. As can be clearly seen, both the desired imaging area and its reflection can be seen due to the geometry of imaging from this distance. Figure 2.17 (b) shows a typical FRC discharge case and the reflections seen there. In the figures presented later in this dissertation, a white circle will be drawn at the approximate location of the quartz insulators at the approximate axial center of the discharge coil, helping to separate the plasma from the reflection. The photographs in Figures 2.18 (a) and (b) show the resultant effect.

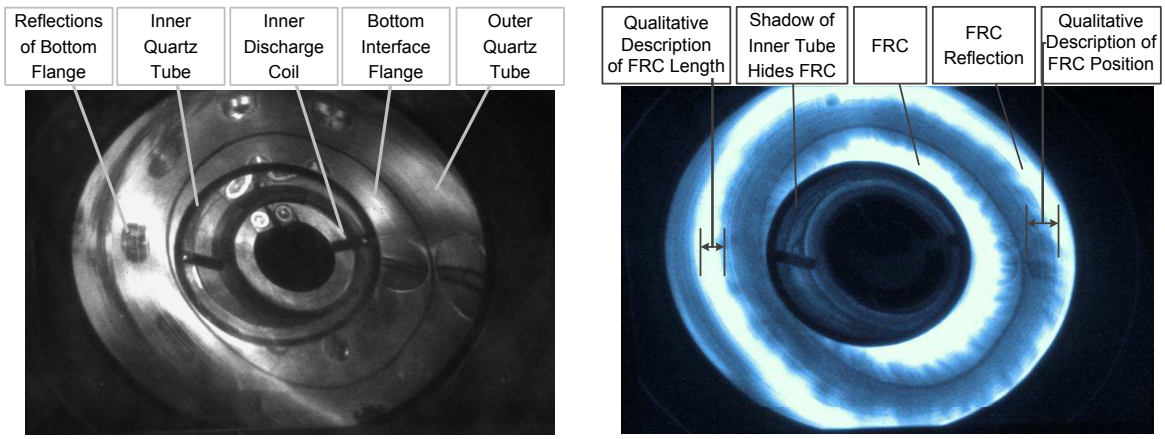

(a) (b)

Figure 2.17: (a) DICAM background image, (b) DICAM FRC image

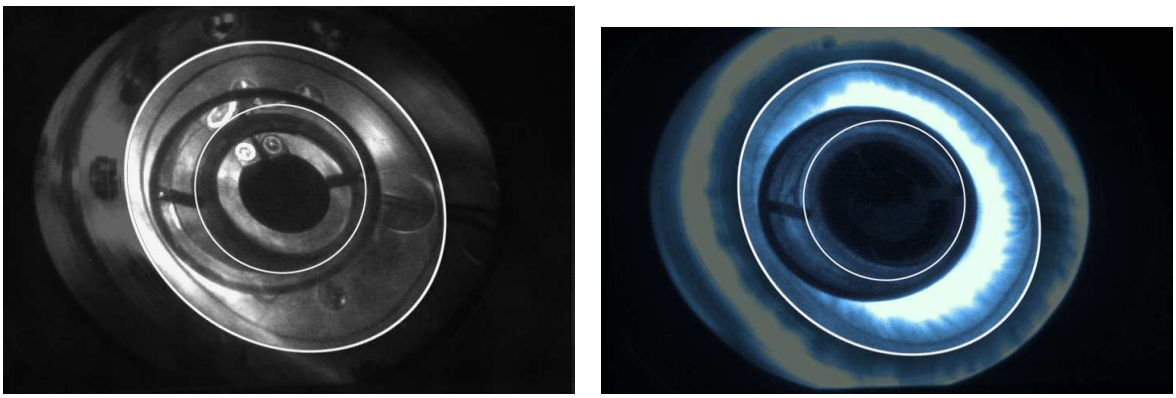

(a) (b)

Figure 2.18: (a) DICAM background image with enhancement, (b) DICAM FRC image with enhancement

2.4.3 Magnetic Field Probe

The primary external diagnostic for magnetized inductive plasmas is the magnetic field probe. For these tests a B-dot probe is used to collect high-resolution magnetic flux derivative measurements that are subsequently electronically integrated to give magnetic field. In this case an array of B-dot probes were used; 12 high-accuracy 2-axis B-dot probes were constructed and calibrated for use along the exterior coils, 12 3-axis B-dot probes were also constructed for the internal measurements of the XOCOT coils. Fundamentally, B-dot probes convert changing magnetic field flux contained within a flux loop into applied voltage on the probe in accordance with Equation 2.6. Using this derivative data of the magnetic field the time-varying magnetic field average at the spatial location of the flux loop can be determined for various directional vectors of that loop.

$$V_{bp} = nA\frac{dB_p}{dt} \tag{2.6}$$

$$B_p(t) = \int \frac{V_{bp}(t)dt}{nA} + V_{0-DC} \tag{2.7}$$

Equations 2.6 and 2.7 show the derivative and integral results for magnetic field probes respectively, with V_{bp}, B_p, n, A as the voltage on the probe, the magnetic field contained within the probe, and nA as the turn-loop area product, respectively. The design of magnetic field probes is highly sensitive to the frequency response desired. For this application, the magnetic field probes were designed to fully capture a 500-μs discharge, yielding a necessary frequency response of 2 kHz. A baseline response frequency of 2 kHz, coil dimensions, and the maximum magnetic field then set the operational parameters for the design of the B-dot probes. Luckily, at those frequencies, more complicated effects such as capacitive pickup and circuit self-resonance

stop being a major concern. Therefore the design of these B-dot probes becomes a function of Equations 2.6, 2.8, 2.9, and 2.10 showing the nA product required to satisfy the inductance, frequency response, and magnitude requirements. Figure 2.19 shows a photograph of the 3-axis internal probes used to measure the vacuum magnetic field inside of the discharge coils.

$$\tau = \frac{L}{R_0} \tag{2.8}$$

$$L = \frac{r^2 N^2 \pi}{l}\left(1 - \frac{8w}{3\pi} + \frac{w^2}{2} - \frac{w^4}{4} + O\left(w^6\right)\right) \quad , w = \frac{l}{r} \tag{2.9}$$

$$L = \frac{F N^2 r^2}{l} \quad \mu H \tag{2.10}$$

$$N = \sqrt{\frac{R_0}{f_{max}(MHz) F r}} \tag{2.11}$$

In the equations above L is the inductance of the single layer solenoidal magnetic field coil, r is the average radius of the probe, N is the number of complete turns, l is the width of the probe (for example a 4-turn coil would have a width of 4 wire diameters, and F is the geometrical uniformity constant in Equation 2.11 that is derived from Equation 2.9).

Physically, the size of the individual B-dot probes was set by the spacing between the quartz tube and the discharge coil, approximately 1.25 cm. The probe forms consist of square cross section, nylon rods 0.63 cm in width, wound with 0.25-mm-diameter magnet wire, and twisted/shielded leads. Figures 2.20–2.22 show the magnetic field probes to scale and installed within the discharge coils.

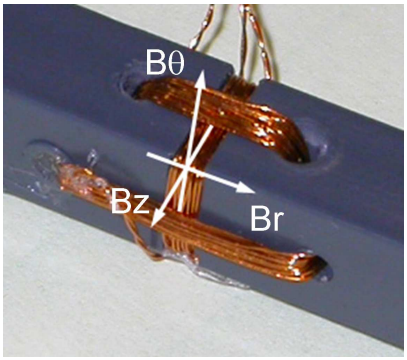

Figure 2.19: Photograph of internal magnetic field probe

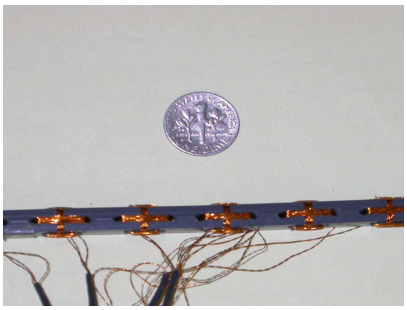

Figure 2.20: Final probe design shown with scale

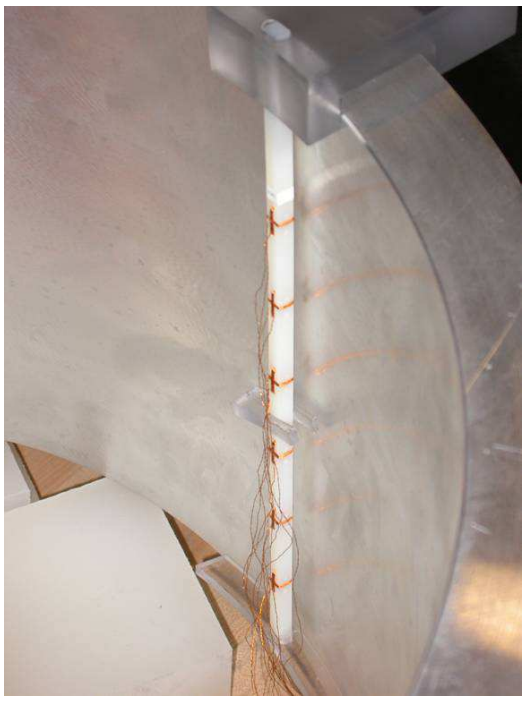

Figure 2.21: External magnetic field probe inserted in position in outer coil

Figure 2.22: 3-axis internal field probe setup testing coil discharge uniformity

2.4.3.1 Magnetic Field Probe Calibration

$$d\mathbf{B} = \frac{\mu_0}{4\pi}\frac{Id\mathbf{l} \times \hat{\mathbf{r}}}{r^2} \tag{2.12}$$

The calibration of the magnetic field probes required several steps. First, the construction of a high-frequency Helmholtz coil in order to calibrate the magnetic field probes and secondly calibration of the Helmholtz coil with DC fields in order to validate the nA product of the coil. An additional requirement is that the calibration procedure can calibrate all three axes for the internal probes at operational voltages. Much of the B-dot probe calibration work was conducted by fellow University of Michigan graduate student, Daniel Brown at AFRL in the summer of 2003 [30]. A Helmholtz coil is a parallel pair of identical circular coils spaced one radius apart with constructively adding magnetic fields. A magnetic field profile from a Helmholtz coil has a very uniform magnetic field between the magnetic field coils (due to the $1/R$ fall-off of a magnetic solenoid). From [37] "The primary purpose of this device is to provide a uniform, low frequency magnetic field for susceptibility testing of electronic equipment." The real magnetic field in between the coils on the $(x = 0)$ axis can be solved from the Biot-Savart law (Equation 2.12) as:

$$B = \left(\mu_0 \sqrt{\frac{P\lambda}{r_1 \rho}}\right) \left(\sqrt{\frac{1}{2\pi\left(\alpha^2 - 1\right)\left(\beta_2 - \beta_1\right)}} \left[\beta_2 ln \frac{\alpha + \sqrt{\alpha^2 + {\beta_2}^2}}{1 + \sqrt{1^2 + {\beta_2}^2}} - \beta_1 ln \frac{\alpha + \sqrt{\alpha^2 + {\beta_1}^2}}{1 + \sqrt{1^2 + {\beta_1}^2}}\right]\right) \tag{2.13}$$

$\alpha = \frac{r_2}{r_1} \qquad \beta_1 = \frac{l_1}{2r_1} \qquad \beta_2 = \frac{l_2}{2r_2}$

For the ideal case (square coil cross section, average separation is the average radius), Equation 2.13 simplifies to:

$$B = \left(\frac{4}{5}\right)^{3/2} \frac{\mu_0 n I}{R} \tag{2.14}$$

In Equation 2.14, B is the magnetic field on the axis of the coil, r_1 is the inside radius of the coil pair, r_2 is the outside radius of the coil pair, l_1 and l_2 are the distances between inner and outer coil faces, respectively, P is the total power consumed by the coil pair, in watts, λ is equal to (*conductor cross section area*)/(*coil cross section area*), ρ is the conductor resistivity, and R is the average coil radius. The Helmholtz coil used consists of two coils with a radius of 2.92 cm and 36 turns each, and was calibrated using a DC gaussmeter to validate the B/I curve for the real geometry and non-ideal behavior. Figure 2.23 shows the results of DC calibration of the Helmholtz coil, which was calibrated to 5 % of its predicted value, $B = 11.08I$. The experimental geometric constant for the Helmholtz calibration coil was 11.65.

Figure 2.24 is a photograph of the actual Helmholtz calibration setup used to test the B-dot probe assemblies. Note the two coils, 3-axis calibration access, and nylon guide structure. Further considerations must be paid to frequency response of the Helmholtz coil system. In order to test the magnetic field probes at their requisite frequencies, the Helmholtz coil must also be able to operate at at least 2 kHz. At this frequency the dielectric constant of the nylon ceases to become a significant issue, but the inductance of a 36-turn coil is significant. The frequency response of the

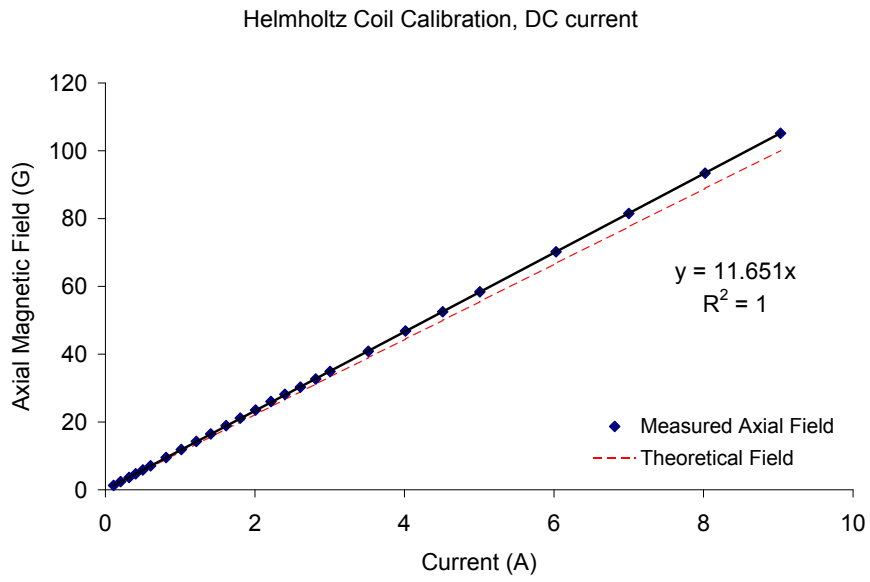

Figure 2.23: Helmholtz coil DC calibration

Helmholtz coil system is given by Equations 2.8,2.9 and yields a 5 kHz maximum operating frequency for the given dimensions [25].

The magnetic field probes are calibrated by the procedure below using the circuit in Figure 2.24:

1. Estimate nA constant

   For the Axial External Probes $nA = 6.75 \times 10^{-4}$ $\left(\frac{V-s}{T}\right)$

   For the Radial External Probes $nA = 9.90 \times 10^{-5}$ $\left(\frac{V-s}{T}\right)$

2. Drive a kHz-frequency sinusoidal signal through a Kepco amplifier at various voltages and frequencies

   4, 10 kHz and 4, 6, 8, 10 Volts

3. Record sinusoidal output of B-dot probes and sinusoidal voltage on the current

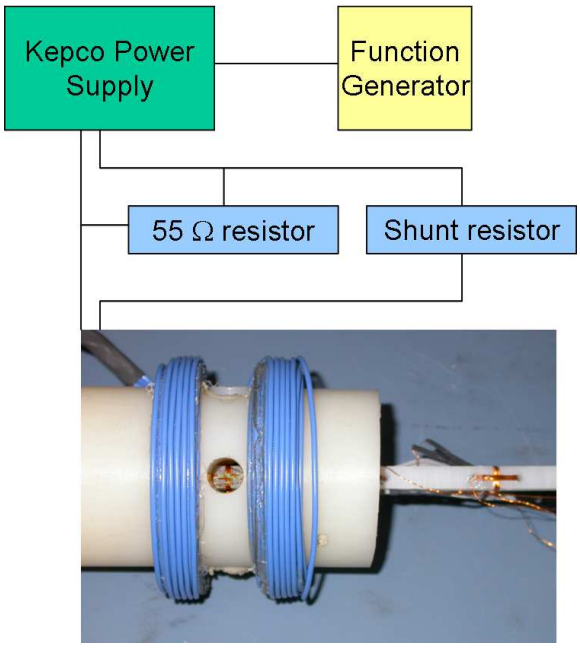

Figure 2.24: Helmholtz testing circuit setup

shunts

4. Using the recorded current, nA of the Helmholtz coil, V_{pp}, f_0, measure nA and $\delta\phi$ for the magnetic field generated as in Figure 2.25

The above calibration technique yielded a calibration constant for every orientation and location for both external probes, as well as the internal 3-axis probes. The magnetic field probes that are used for most of the data in this dissertation are described in Table 2.5. The variation from expected value can be attributed to variability in the nylon cross section and wire wrapping non-symmetries.

2.4.3.2 Magnetic Field Probe Noise Correction

The B-dot probes were connected as in Figure 2.26 with the return path grounded to the oscilloscope and data acquisition ground. The magnetic field probe data were recorded on the 12-bit Sigma 100 DSO yielding a 4000:1 resolution. As the B-dot probe collects derivative magnetic field results, any small, but fast, transients yield a large, high-speed signal in the voltage resolution of the magnetic field data. There-

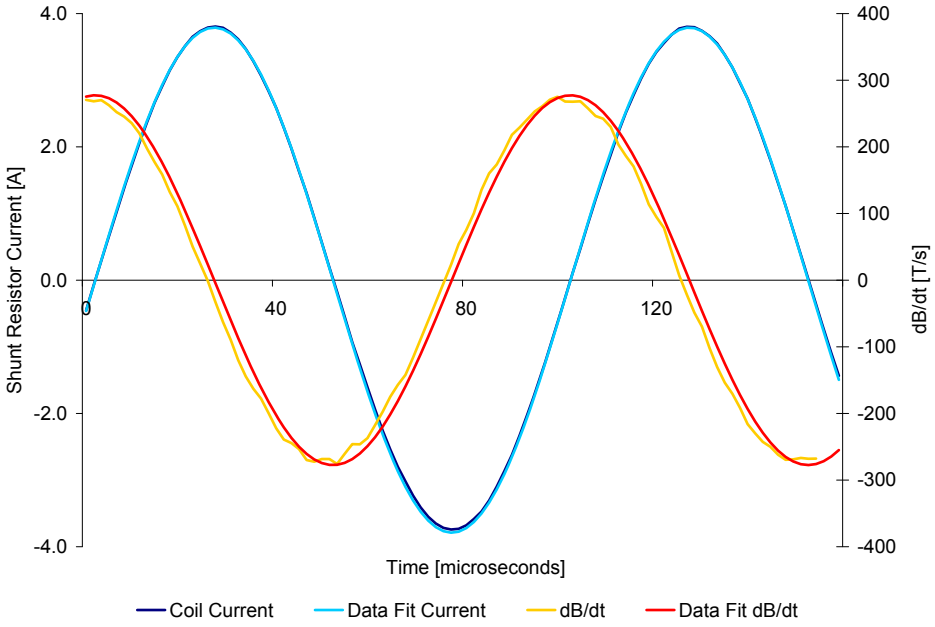

Figure 2.25: Characteristic B-dot probe calibration curve

Position	Orientation	nA	Deviation from expected
1	Axial	6.89×10^{-4}	2.1 %
2	Axial	6.70×10^{-4}	−0.7 %
3	Axial	7.32×10^{-4}	8.4 %
4	Axial	7.45×10^{-4}	10.4 %
5	Axial	6.83×10^{-4}	1.2 %
6	Axial	6.55×10^{-4}	−3.0 %
1	Azimuthal	1.06×10^{-3}	7.1 %
2	Azimuthal	1.11×10^{-3}	12.1 %
3	Azimuthal	1.14×10^{-3}	15.2 %
4	Azimuthal	1.06×10^{-3}	7.1 %
5	Azimuthal	1.13×10^{-3}	14.1 %
6	Azimuthal	1.09×10^{-3}	10.1 %

Table 2.5: External magnetic field probe calibration constants

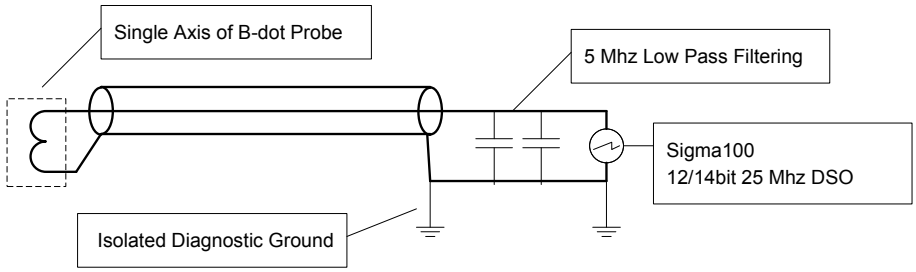

Figure 2.26: Magnetic field probe circuit configuration

fore, as shown in Figure 2.27, a binomial smoothing was applied digitally in IGOR, the equivalent of a Gaussian low pass filter with a cutoff frequency (1/2 transmission magnitude) of 370 kHz. This procedure preserves high-speed pre-ionization and magnetic field events 1-μs-long and greater. Magnetic field data utilized further in this dissertation are pre-filtered with this type of Gaussian filter.

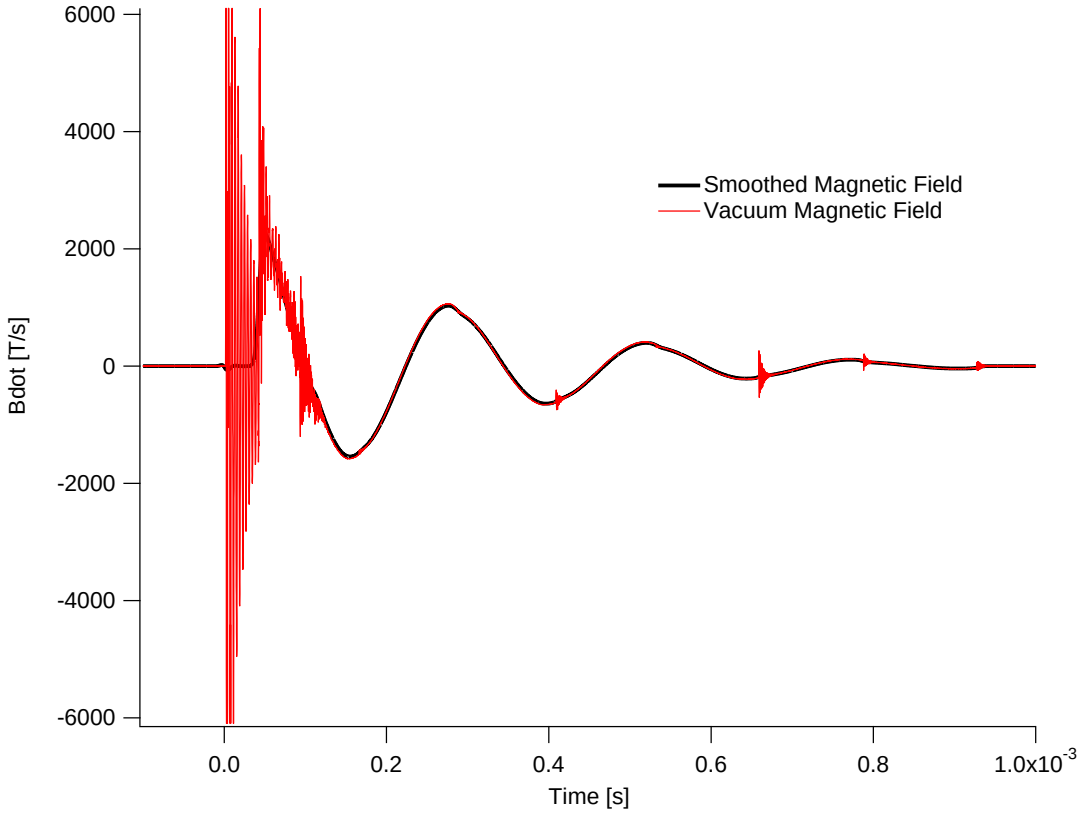

Figure 2.27: Raw B-dot probe data and filtered data for a 900-V, 250-μs discharge

Using the Gaussian filtered data, a direct comparison of the derivative magnetic field data can be shown and a qualitative measure of plasma interference can be investigated as in Figure 2.28. This analysis is particularly useful in seeing the temporal locations of plasma interaction with the compression coils. Equations 2.6 and 2.7 describe the ideal voltage and magnetic field response of a B-dot probe. In reality there is a non-zero term that is introduced by the oscilloscope resolution itself which must be accounted for by re-zeroing the data based off of the pre-trigger scope data. Equation 2.15 shows that non-zero term (V_{bp0}) and how it can create a large, non-real function when the V_{bp} data are electronically integrated. Figure 2.29 shows how simply this correction is made.

$$B_p(t) = \int \frac{V_{bp}(t)dt}{nA} + \frac{V_{bp0}}{nA}t(t) + V_{0-DC} \tag{2.15}$$

Finally, simple calculus dictates that the integral of the differences in the resultant magnetic field data is the same as the difference of the integrals if the terms are linear and unique. Figure 2.30 shows the integrated vacuum and plasma magnetic field data, and Figure 2.31 shows that indeed it is the case that the two magnetic deficit calculations are correct. For future calculations, the raw B-dot probe plasma data will be subtracted from the raw vacuum data before filtering and integration (in order to preserve as many real high-speed transient details as possible while reducing oscilloscope noise with the procedure above). Notice in Figure 2.31, the pre-ionization ringing still appears in the difference data due to the clipping of the B-dot probe data on the scope for data acquisition focusing on the main bank discharge. Equation 2.16 defines magnetic deficit as the change in magnetic field (integrated derivative field) between identical discharge cases, one with a neutral gas and magnetized plasma and one case with no neutral gas and no magnetized plasma. This magnetic deficit

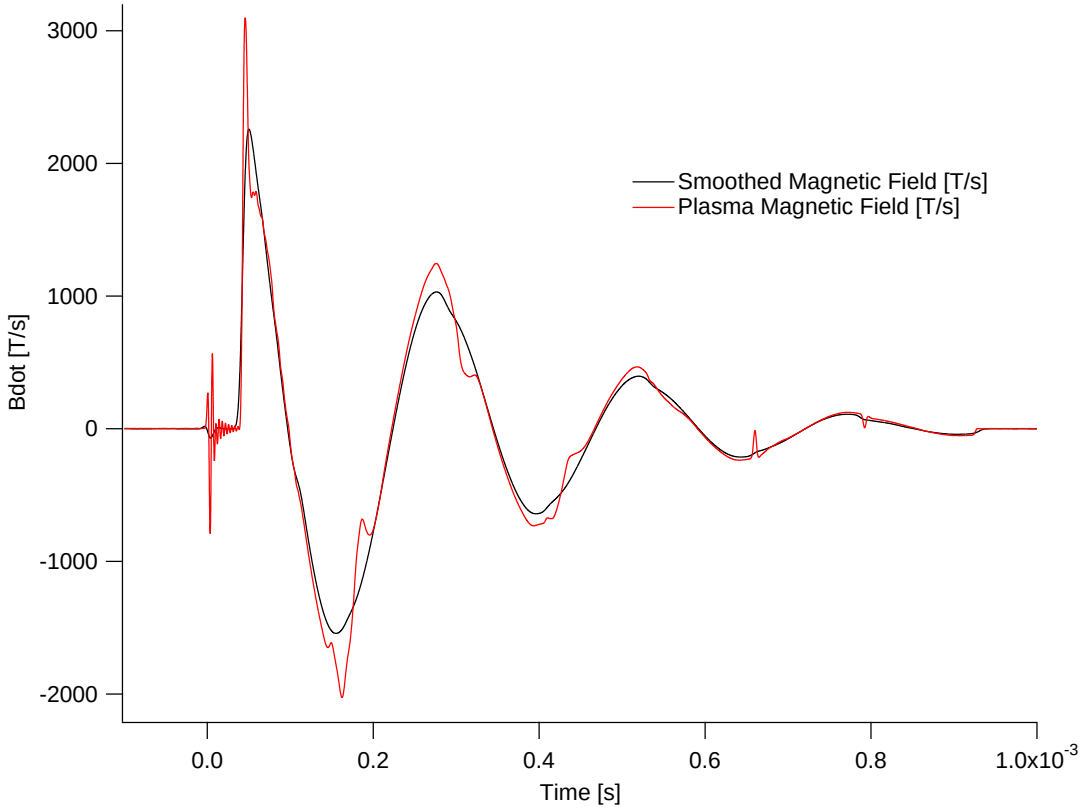

Figure 2.28: Raw vacuum and plasma B-dot probe data a 900-V, 250-μs, 12-mTorr discharge

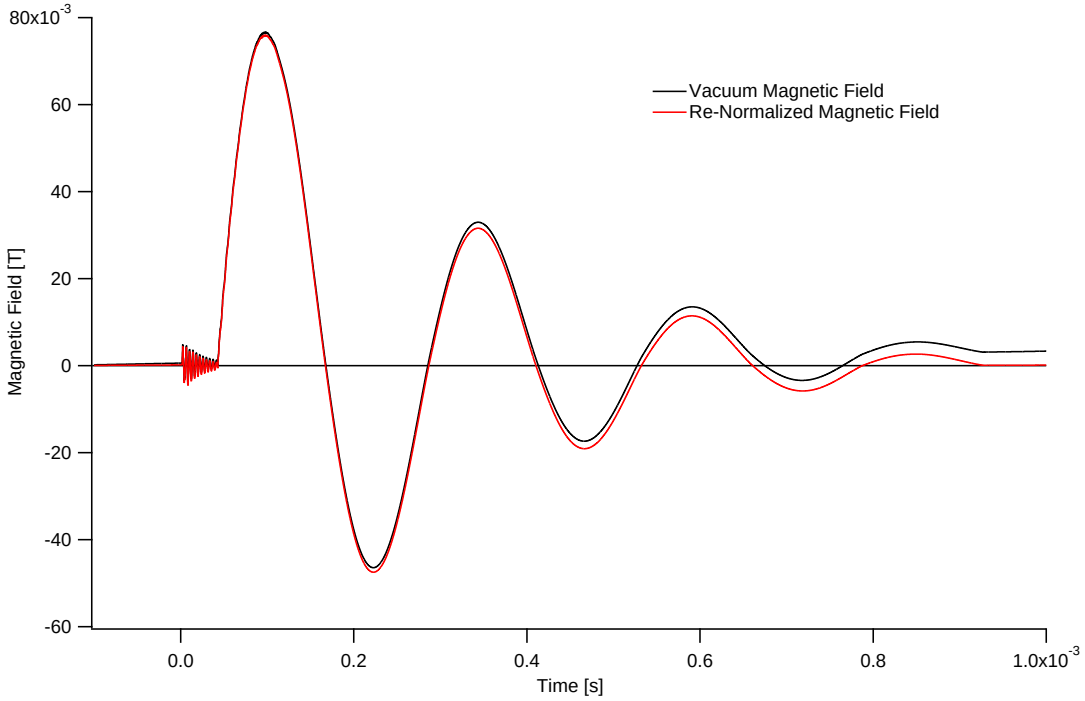

Figure 2.29: Filtered and compensated vacuum B-dot probe data for a 900-V, 250-μs discharge

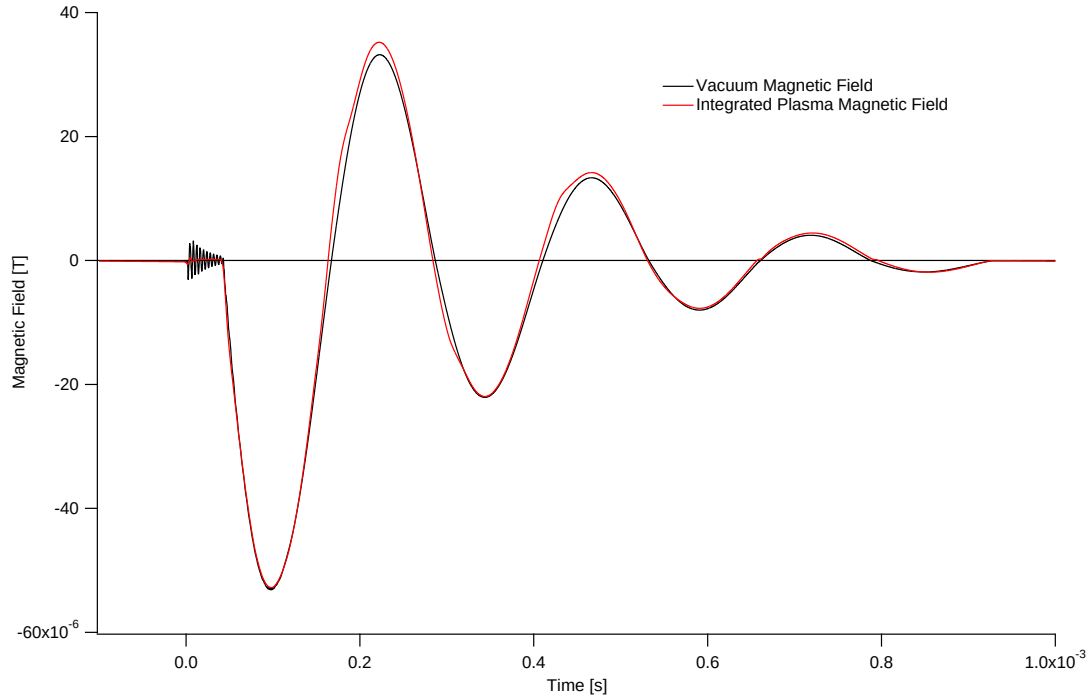

Figure 2.30: Vacuum and plasma B-dot probe data for a 900-V, 250-μs discharge

is a result of the interaction between the applied coil current (the vacuum case) and the diamagnetic current in the plasma within the discharge annulus. The diamagnetic current generates an opposing magnetic field that is measured at the probe location between the coil and the plasma separatrix (location of the outer edge of the diamagnetic current) to be a deficit in the vacuum field. This can be interpreted as a measurement of both the location of the diamagnetic current, and for a weakly-magnetized plasma as the fraction of magnetization. Section 2.4.5.1 details the analysis for detailed geometric analysis of the separatrix as a function of the change in magnetic field.

$$B_{deficit} = B_{plasma} - B_{vacuum} \tag{2.16}$$

Figures 2.32 and 2.33 show the same analysis and results for a 15-mTorr discharge. These data are fully analyzed in Section 6.3.

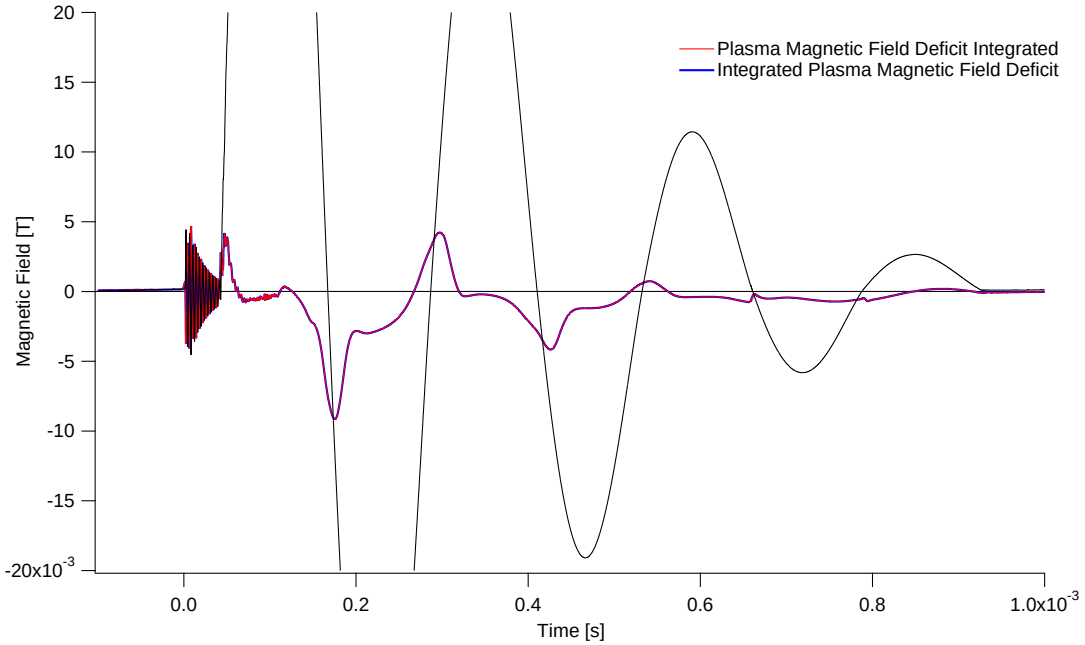

Figure 2.31: Integrated vacuum and deficit B-dot probe data for a 900-V, 250-μs discharge at 12 mTorr. A partial trace of the integrated vacuum magnetic field is shown to show current reversal

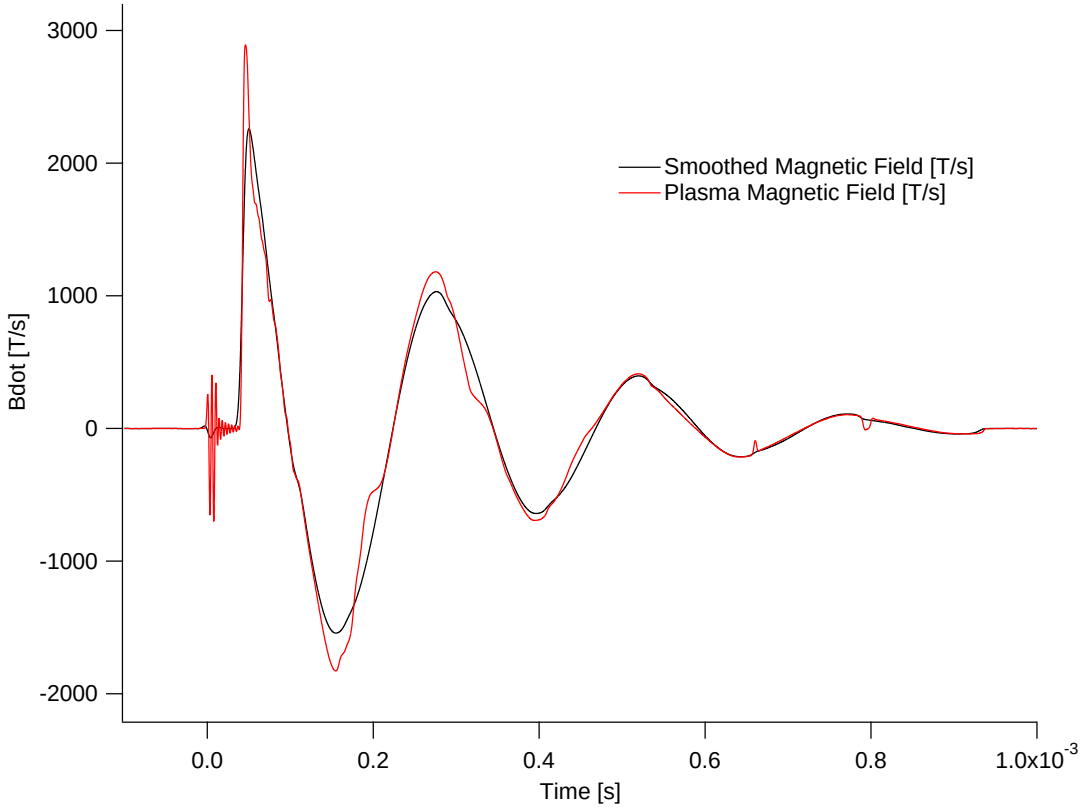

Figure 2.32: Raw vacuum and plasma B-dot probe data a 900-V, 250-μs, 15-mTorr discharge

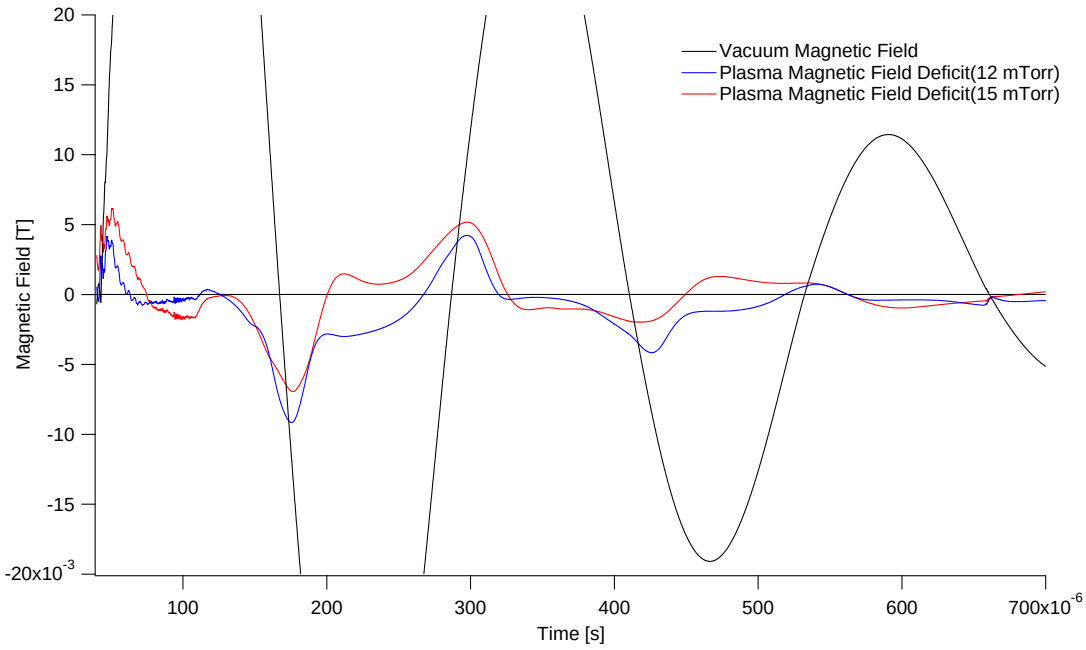

Figure 2.33: Integrated vacuum and deficit B-dot probe data for a 900-V, 250-μs discharge at 12 and 15 mTorr. A partial trace of the integrated vacuum magnetic field is shown to show current reversal

2.4.4 Rogowski Coils

A Rogowski coil operates under a similar principle as a B-dot magnetic field probe, only the flux loops are arranged perpendicular to the main direction of interest forming a toroidal flux collection area rather than just circular, and as a current passes through the toroidal coil, the voltage induced in the coil is I-dot, the change in current passing through the coil as shown in Equation 2.17 [46], [45], [48].

$$V_{rp} = \mu_0 n A \frac{dI_{rp}}{dt} \tag{2.17}$$

Additionally, the design of the Rogowski coil is even more sensitive to frequency response and the inductance and capacitance of the coil itself. Equations 2.18 and 2.19 enumerate the cut-off frequency and phase response of a Rogowski coil for a given number of turns and geometry. The Rogowski coils were designed and built to monitor plasma translation out of the main discharge coils.

$$f = \frac{1}{2\pi\sqrt{LC'}} \tag{2.18}$$

$$F(\theta) = \frac{1}{1 + \frac{jL\omega}{R_d} - \omega^2 LC'} \tag{2.19}$$

This diagnostic is particularly useful for pinch and Tokamak type devices in which there are large, internal magnetized diamagnetic currents that can be measured and give an indication of plasma content. Also, specifically for translating plasmas, this diagnostic can be utilized to observe bulk axial plasma translation in the form of pulsed currents in addition to the azimuthal currents in the plasma toroid.

2.4.5 Diamagnetic Flux Loop

Another primary magnetic flux diagnostic is the diamagnetic flux loop, primarily utilized for the excluded flux analysis in Section 2.4.5.1. The simple flux loop fully contains the discharge area and measures the real time axial magnetic flux passing through the flux loop as in Equation 2.20. In a plasma without large diamagnetic currents the diamagnetic flux loop would be an indirect measurement of the V_θ on the coil. However, in this experimental case it provides a measure of how the diamagnetic current acts to oppose the generated flux in the coil.

$$\frac{d\Phi_D}{dt} = \int_{\partial C} \frac{d\mathbf{B}}{dt} \cdot d\mathbf{s} \tag{2.20}$$

2.4.5.1 Diamagnetic Excluded Flux Analysis

The diamagnetic excluded flux analysis has been used extensively on past FRC experiments and the theory was updated in 1983 [65] to incorporate one or fewer flux loops, using magnetic field probes, and flux loops. At a specific axial location the excluded flux radius can be defined as in Equation 2.21 for a given magnetic flux (B),

and field value (ϕ) at the vacuum and plasma conditions, respectively. This technique is applicable for a highly magnetized plasma and is limited only by experimental accuracy that ϕ and B can be measured in real time. Additionally, R is the radial location of the magnetic and flux probes, and r_w is the inner radius of the discharge coil, approximating the external radius of the quartz insulator. The advancement introduced by Tuszewski [65] was in recognizing that the magnetic field of FRCs are approximately axial uniform near the midplane and that the magnetic flux could then be reconstructed from the real-time magnetic field data using Equation 2.22.

$$r_s = r_w - R\left(1 - \frac{\phi_p}{\phi_v}\frac{B_v}{B_p}\right) \tag{2.21}$$

$$\phi = \phi_l + B\pi\left(r_w^2 - R^2\right) \tag{2.22}$$

2.4.6 Spectrometer

An Ocean Optics USB2000 spectrometer was used to characterize plasma temperature as averaged over an entire discharge. The USB2000 spectrometer is a wide-band spectrometer capable of capturing the spectral emission of the XOCOT discharge from 400-950 nm. Its main operational parameters are described in Table 2.6. By observing the integrated spectra output of a main bank discharge, the average emission line intensities, and more importantly, the average ratio of line intensities can be compared to find the electron temperature of the discharge [38], [10]. This technique can also be used as a qualitative measurement to investigate the average composition of the plasma in terms of relative amounts of ionized species and therefore the percent ionization (or second ionization) in the bulk plasma. Without a high-accuracy calculation of electron temperature this measurement technique is a qualitative investigation rather than quantitative. Spectrometer temperature

Ocean Optics	USB2000
CCD Detector	linear silicon CCD array
Pixels	2048 pixels
Pixel size	14 μm x 200 μm
Signal-to-noise ratio	250:1 (at full signal)
A/D resolution	12 bit
Detector range	400-1100 nm
Focal length	f/4, 42 mm (input); 68 mm (output)
Optical resolution	0.5 nm FWHM
Dynamic range	2000:1 for a single scan
Fiber optic connector	SMA 905
Integration time	3 milliseconds to 65 seconds

Table 2.6: Operational characteristics of an Ocean Optics USB2000 spectrometer

and density techniques can be very high-accuracy, non-intrusive measurements, but require a higher-speed, higher-resolution spectrometer than was available for this investigation. The control spectra are given in Figures 2.35 and 2.36 for argon, helium, and xenon respectively, based on the National Institute of Standards and Technology (NIST) standard spectra database [49].

The spectrometer was connected to an Ocean Optics 3-m, SMA 905 fiber optic cable with a spectral response shown in Figure 2.34 with the end positioned at the location of the collimation photometer (nearer to the discharge coil) as shown in Figure 2.13. The fiber optic probe was left bare, has a half angle of 27.5° and a collection axis of approximately 14 cm providing a wide-angle plasma collection area.

Two modeling studies have been used to correlate the average collected line ratios to average electron temperatures. For argon, Babic and Akyel developed a model for high-density helicon plasmas in the 1-10 eV temperature range for $\frac{Ar_{II\,480}}{Ar_{I\,750}}$ and $1 - 10 \times 10^{18}\ m^{-3}$ densities [12]. Figure 2.37 shows the correlation. For xenon, Karabadzhak and Dressler have developed a model for xenon Hall thruster plasmas

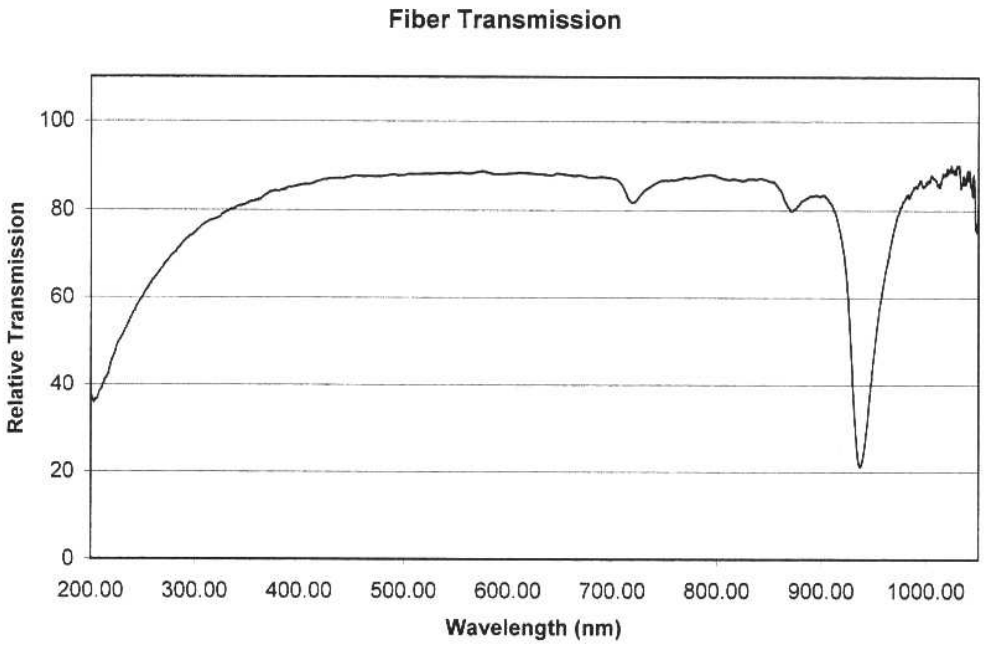

Figure 2.34: Fiber optic transmission spectrum for the spectrometer

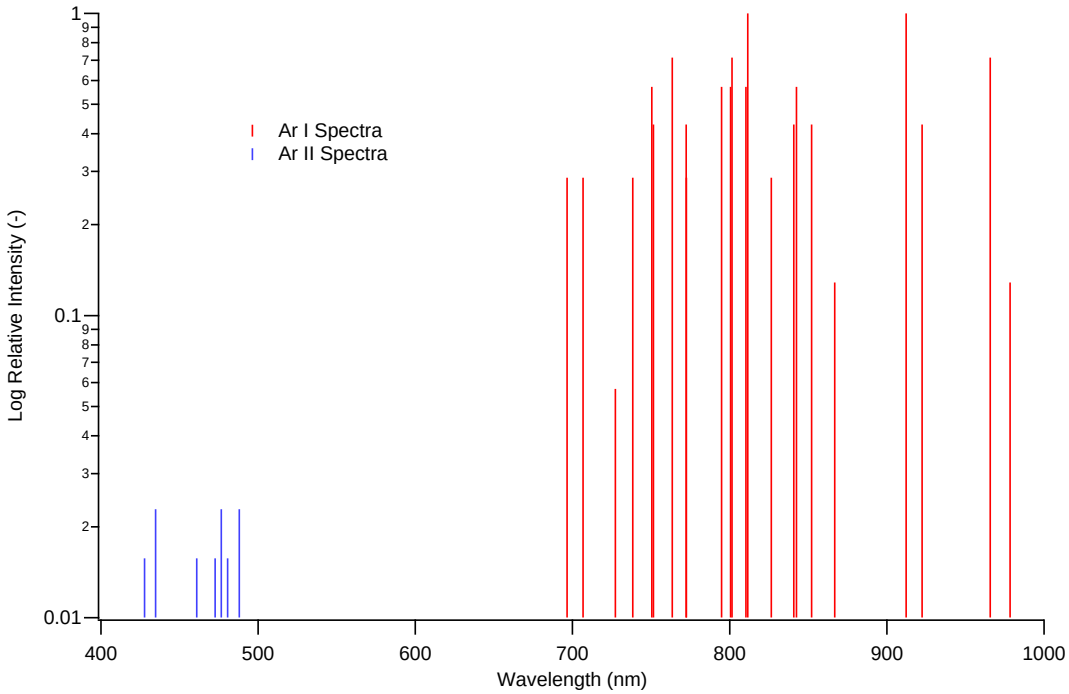

Figure 2.35: NIST argon I, II emission spectra [49]

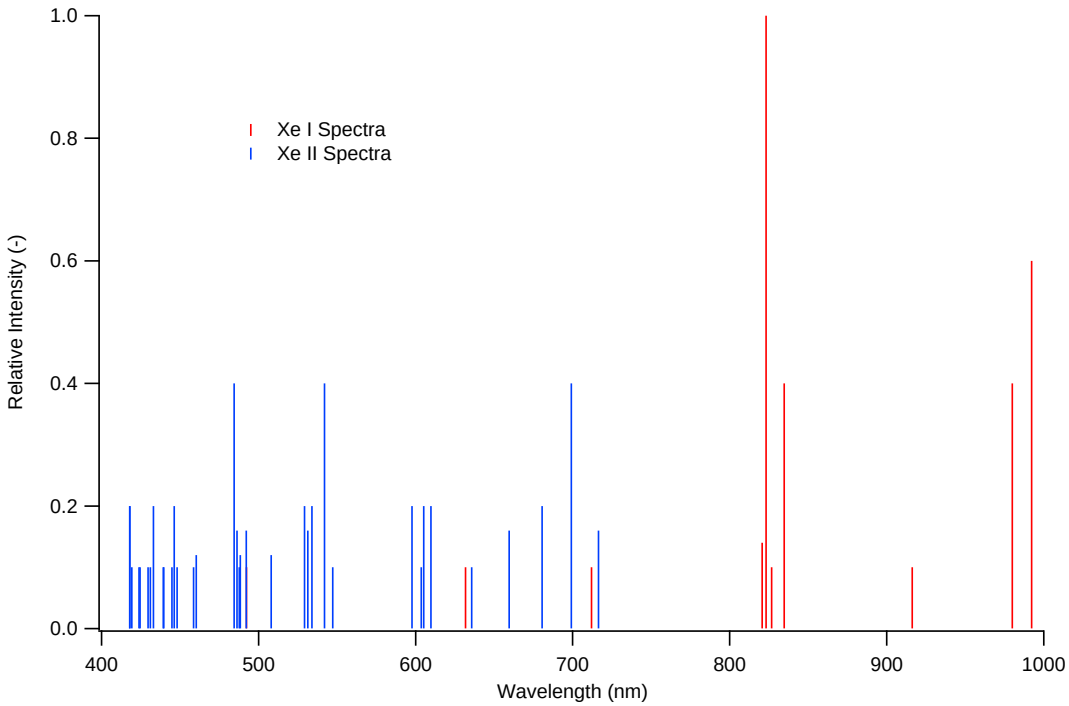

Figure 2.36: NIST xenon I, II emission spectra [49]

at 1-20 eV for $\frac{Xe_{I\,823}}{Xe_{I\,824}}$ and $\frac{Xe_{I\,834}}{Xe_{I\,824}}$. Figure 2.38 shows the correlation. [29]

2.5 Internal Diagnostics

Internal diagnostics are key to providing plasma data, real-time, of the inner workings of the FRC formation, compression, heating, and translation processes. While the physics and electrical noise issues are significantly more complicated than the external probes described earlier (and will be addressed in the following Sections), they provide the most useful actual plasma density and temperature data available for these experiments. In the following Sections (2.5.1-2.5.3) the theory of Langmuir plasma probes will be lightly touched on to give an overview and basis for data solutions and complications, for more detailed derivations see References [8], [9], [36], [25], [39].

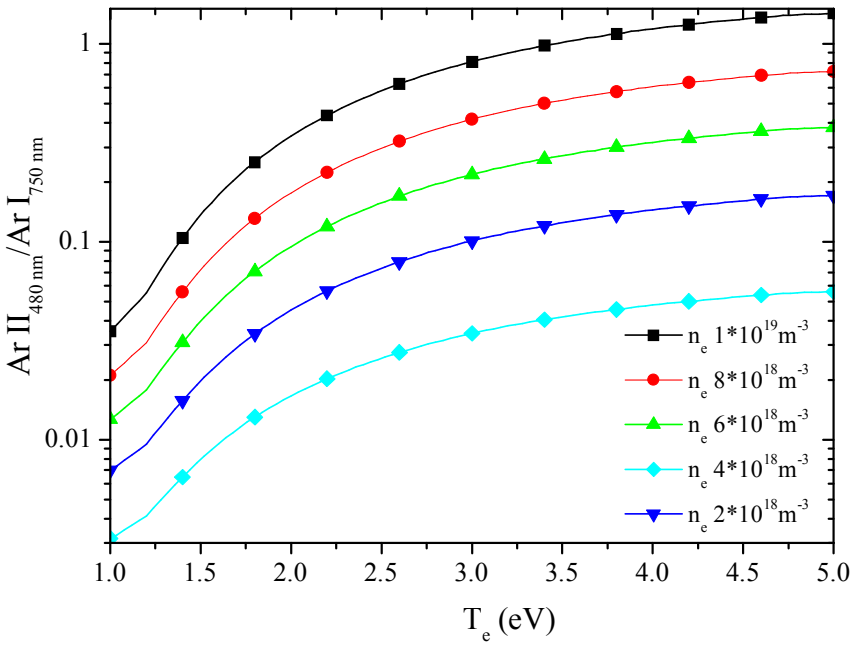

Figure 2.37: Argon collisional-radiative model line-ratio-to-temperature correlations developed for RF/Helicon discharges [12]

2.5.1 Single Langmuir Probe

The single Langmuir probe is the fundamental basis for the more complicated probes used in these experiments. Fundamentally, a single Langmuir probe measures the current collected by an electrode in a plasma as a function of its voltage potential between the high impedance probe and a low conductance, grounded reference probe. By observing the current collected through the sheath around the probe, detailed plasma measurements of electron temperature, electron density, and electron energy distribution can be made. Two complete discussions of Langmuir probe operation (and design) can be found in Chen [9] and Schott [50]. Note, however, that for the discussions in Sections 2.5.1.1 and 2.5.2 the plasma is interpreted as a quiescent, steady-state plasma, while Section 2.5.3 deals with a high-speed, variable plasma and associated probe techniques.

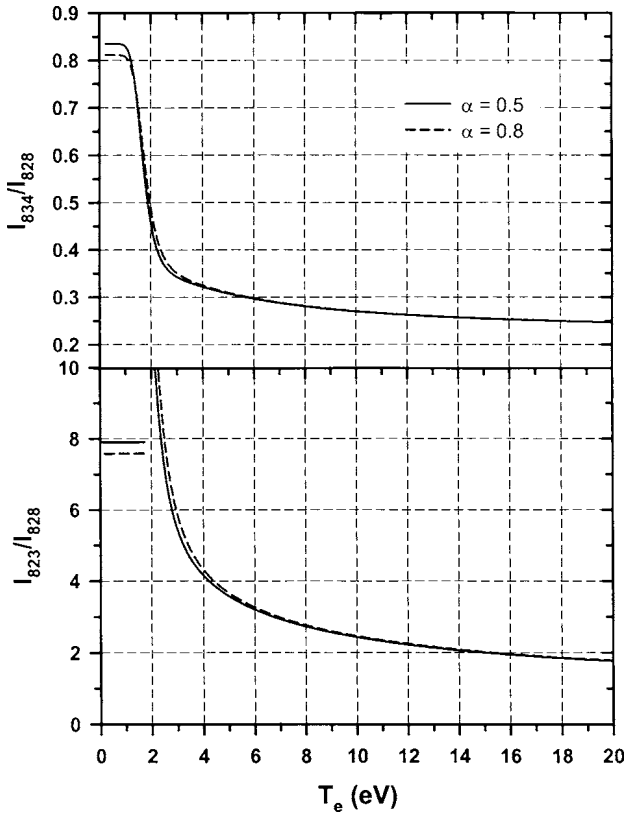

Figure 2.38: Xenon collisional-radiative model line ratio to temperature correlations [29]

2.5.1.1 Theory of Operation

Langmuir probe theory can be separated into several regimes based on two non-dimensional parameters: the Knudsen number (K_n) and Debye length (λ_d). First, the Knudsen number (Equation 2.23) defines whether the plasma has a collisional or collisionless distribution function. In this analysis a collisonless plasma is assumed on the length scale of the plasma probe [25]. Secondly, the plasma probe can operate in a thin or thick, OML (orbital motion limited), sheath based on the relative size of the sheath and probe radii [34]. All of the empirical and theoretic analysis performed was conducted on a cylindrical probe with a probe radius much smaller than the probe length. For a $\frac{r_p}{\lambda_d} < 3$, an OML analysis must be used to correctly correlate collected current with plasma properties. For $\frac{r_p}{\lambda_d} > 10$, a thin-sheath approximation can be used (for the plasma parameters seen in Field Reversed Configuration plasmas, this is primarily the case).

$$Kn = \frac{\lambda}{L} = \frac{k_B T}{\sqrt{2}\pi\sigma^2 P l} \tag{2.23}$$

Figure 2.39 shows a typical voltage-current response of a Langmuir probe and the three main operational regimes. First, in the ion saturation mode a large negative voltage is applied and most of the electrons are repelled. As a result, a positive ion sheath forms around the probe and a small current of positive ions penetrates the sheath to be collected by the probe. At the other end of the I-V curve is the electron saturation region where significantly more electrons reach the probe than ions and a large negative electron sheath develops. In between there are both electrons and ions crossing the sheath, and at the floating voltage, V_f the electron and ion currents balance.

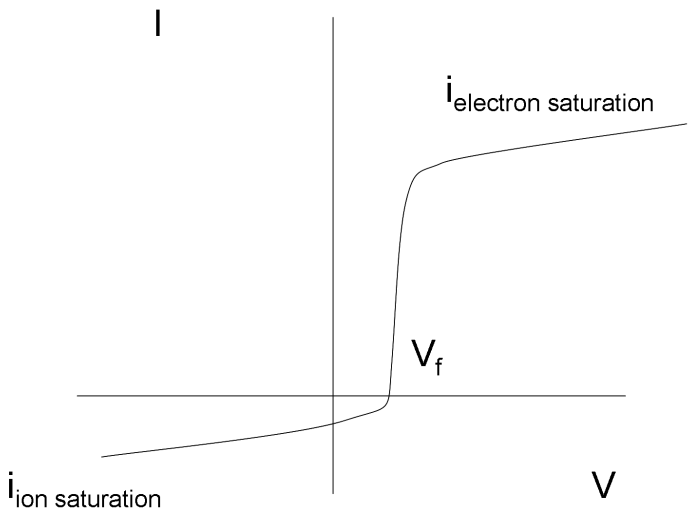

Figure 2.39: Typical I-V curve for a Langmuir plasma probe

$$f(v) = \sqrt{\frac{k_B T_e}{2\pi m_e}} exp\left(-\frac{m_e v^2}{2k_B T_e}\right) \tag{2.24}$$

$$I_{ionsat} = n_e \exp\left(\frac{-1}{2}\right) eA_p \left(\frac{k_b T_e}{m_i}\right)^{(1/2)} \tag{2.25}$$

$$\lambda_d = \sqrt{\frac{k_b T_e}{4\pi n_e e^2}} \tag{2.26}$$

$$\frac{d(\ln(I_p))}{dV} = \frac{e}{k_b T_e} \tag{2.27}$$

In the electron retarding region, the increase in collected current is affected by the local electron temperature, which can be calculated using Equation 2.27. After the electron temperature has been determined, the Bohm sheath criterion can be exploited to determine the electron number density from Equations 2.25 and 2.26. While the theory is relatively well understood, practical implementation of the Langmuir probe as a useful diagnostic is significantly more complicated. First, most of

the plasmas encountered in this experiment are fast pulsed plasmas with an average timescale of less than 1 ms. Therefore, sweeping the I-V curve in the limited time available leads to a significant decrease in resolution of the time evolution of the plasma itself. Moreover, there are several higher order effects that must be taken into account. The ion saturation current is not constant with increasing negative voltage. In fact, the area of the ion sheath increases linearly with the increasing negative voltage applied to the probe [11]. Therefore increasing voltage leads to a square of increasing ion saturation current. This phenomenon can become a significant issue on the selection of where in the ion saturation region ion current is measured, and is further addressed in the double probe and triple probe design techniques Sections. Moreover, current collected in the electron saturation region is also not constant with increasing voltage and the problem is grossly amplified for a high-speed and RF plasmas [39]. Finally, there are the physical effects due to the placement of an electrode in an electrical plasma, namely current collection and the local non-neutral plasma, and ion depletion due to that electrode collecting current, as well as the physical interaction of a cold metallic wall on a hot plasma. These issues are typically assumed to be small, as long as probe lifetime is sufficient to survive unaffected during plasma operation.

2.5.2 Double Langmuir Probe

Double Langmuir probes have three distinct advantages over single Langmuir probes. First, they minimize plasma perturbation by the probe as they use two oppositely biased probe tips to collect current and in total draw no net current [59]. Current flows between the two probes if the differential potential voltage is greater than zero, and as the voltage becomes larger, the negatively biased probe enters the ion saturation region. Secondly, they are typically used in an environment with

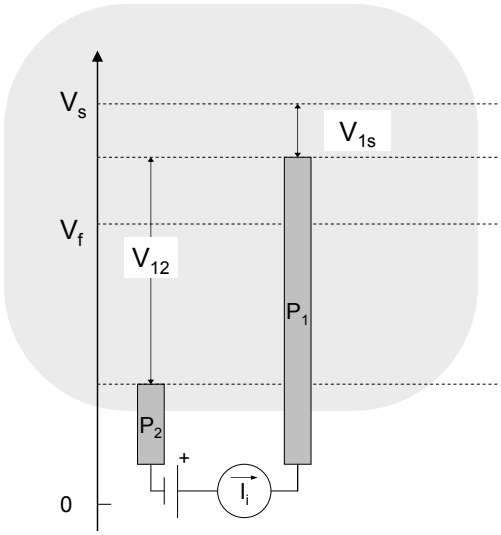

Figure 2.40: Schematic of a double probe design

no distinct electrical ground as they float with plasma changing potential and only reference the voltage difference between the two probe tips, which has benefits for both noise as well as response time in a time-varying plasma. A symmetric double probe (as both the double and triple Langmuir probes used) have two closely spaced identical electrodes that are biased and the current is measured between the probes, as in Figure 2.40 [36].

By taking the thin sheet approximation for a single Langmuir probe and applying a differential voltage between two cylindrical electrodes with balanced collected currents in the ion saturation regime, yields Equation 2.28 which when fitted to an experimental I-V curve can be used to obtain I_i, T_e and therefore, plasma density.

$$I = I_{sat} tanh\left(\frac{V}{2T_e}\right) + \frac{V}{R} + I_0 \tag{2.28}$$

2.5.3 Triple Langmuir Probe

The double Langmuir probe still requires a voltage sweep, which limits its usefulness to data acquisition of plasma phenomena with a frequency of a few kilohertz. The solution employed in this experiment is a triple Langmuir probe using a third electrode to gather high-speed floating-point data on the plasma enabling the collection of plasma characteristics without the need to sweep or switch voltages. This allows the collection of instantaneous plasma density and temperature at frequencies close to the intrinsic resonance frequencies of the probe itself. The techniques of Chen and Sekiguchi [28], [54], [55], and [51] allow for the instantaneous collection and display of plasma properties real-time in an experimental setup. The analytical solution for a double Langmuir probe is used to validate and calibrate the triple Langmuir probes. Most of the quantitative plasma data collected in this experiment was done with triple probes, additionally, triple probes share the same unique property of double probes and in that way collect no net current thereby minimizing plasma interference and ion depletion near the probe. The traditional triple probe circuit diagram is shown in Figure 2.41, showing two symmetric electrodes biased by an applied potential, V_{12}, with one probe in the ion saturation region and the other probe above the floating potential but below the plasma potential. A third electrode is floating with a high impedance to ground (and the other two electrodes) at the plasma floating potential. By validating the criteria in Equations 2.31, 2.32, and 2.33, 2.34, the plasma density and temperature can be instantaneously determined from Equations 2.29 and 2.30 using the Langmuir thin sheath approximations. The following criteria are used to verify that the probe and sheath dimensions satisfy the thin sheath approximation, that the probe tip separation is sufficient such that the individual probe sheaths do not interact, and the overall probe dimensions are such

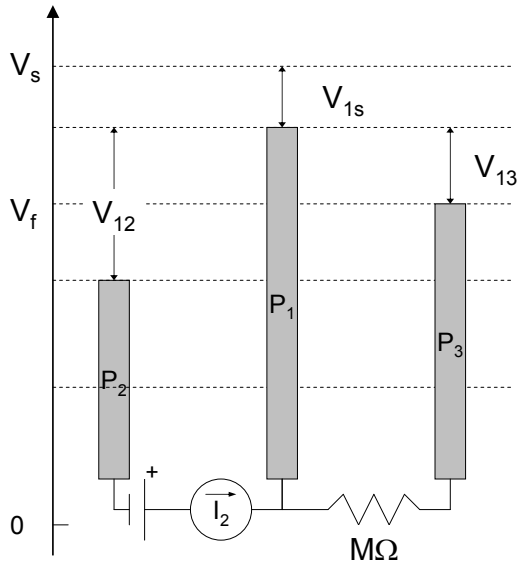

Figure 2.41: Triple Langmuir probe schematic shown in a floating probe configuration

that the probe sees a locally uniform plasma. Additionally, the same approximations as a single Langmuir probe also apply: the plasma is quasineutral, the electron velocity distribution is Maxwellian, and all ions entering the probe sheaths are collected by the probe and not affected by collisional and magnetic field effects.

$$\frac{1-\exp\left(\frac{-eV_{12}}{kT_e}\right)}{1-\exp\left(\frac{-eV_{13}}{kT_e}\right)} = \frac{1}{2} \tag{2.29}$$

$$\frac{I_2}{A_p} = n_e e \left(\frac{kT_e}{2\pi m_e}\right)^{\frac{1}{2}} \tag{2.30}$$

$$r_{Li} >> r_{Le} >> \lambda_d \tag{2.31}$$

$$r_p > 100\lambda_d \tag{2.32}$$

$$r_p << \lambda_c \tag{2.33}$$

$$\lambda_d << s << \Delta \tag{2.34}$$

2.5.3.1 Current Mode Triple Langmuir Probe

The final incarnation of the Langmuir probe and triple probe as described earlier, is the current mode triple probe used in pulsed plasma thrusters [18]. This technique utilizes the fact that the ion saturation region is not constant, and has two probes in the ion saturation region and one probe above the plasma floating-point, as shown in Figure 2.42. By measuring the two ion saturation currents collected by probes P_2 and P_3 the instantaneous plasma density and temperature can be measured without the need for the plasma floating point potential. This has all of the advantages of a floating triple probe, but with one distinct superiority: in high-speed plasmas the capacitive coupling of high-frequency noise to a high-impedance floating probe is commonly extremely difficult to filter out. This high-speed noise tends to distort electron temperature values derived from the floating electrode. In the current mode triple probe there is no high-impedance low-current probe to collect noise, only two low-impedance paths between probes P_1, P_2, and P_3.

Using equations 2.35, 2.36,2.37, the time resolved traces of plasma density and temperature at the probe tip location can be determined. This technique has been used through the following work with great, and low noise, success. The probe itself is constructed of tungsten wire (0.02 in. diameter) in a four bore alumina rod (0.25 in. diameter) in order to withstand the density and temperature of the plasmas.

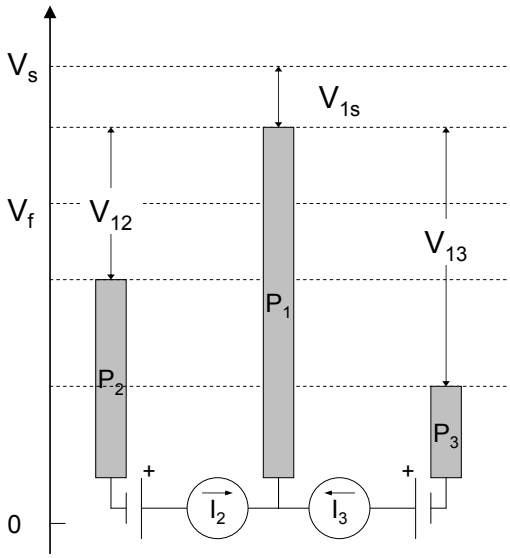

Figure 2.42: Triple Langmuir probe schematic and circuitry in a current collection mode

$$J_i = n_e e \exp\left(-\frac{1}{2}\right)\left(\frac{kT_e}{m_i}\right)^{\frac{1}{2}} \tag{2.35}$$

$$J_i = \frac{1}{A_p}\frac{I_3 - I_2 \exp\left(-\frac{e(V_{13}-V_{12})}{kT_e}\right)}{\exp\left(-\frac{e(V_{13}-V_{12})}{kT_e}\right) - 1} \tag{2.36}$$

$$\frac{1 - \exp\left(\frac{-eV_{12}}{kT_e}\right)}{1 - \exp\left(\frac{-eV_{13}}{kT_e}\right)} = \frac{I_1 - I_2}{I_1 - I_3} \tag{2.37}$$

The triple probes were typically operated with $V_{12} = 12.75\ V, V_{13} = 38.1\ V$, driven by high current, floating lantern batteries, although variations in these parameters can be seen in the actual data. Figures 2.43 and 2.44 and Schematic 2.45 show the actual triple probe used in the experimental tests in Chapter 7. These driving voltages are found by examining the double probe analysis (for non-symmetries) in Chapter 5. Shown are 4 electrodes in a 4-bore alumna tube. This configuration

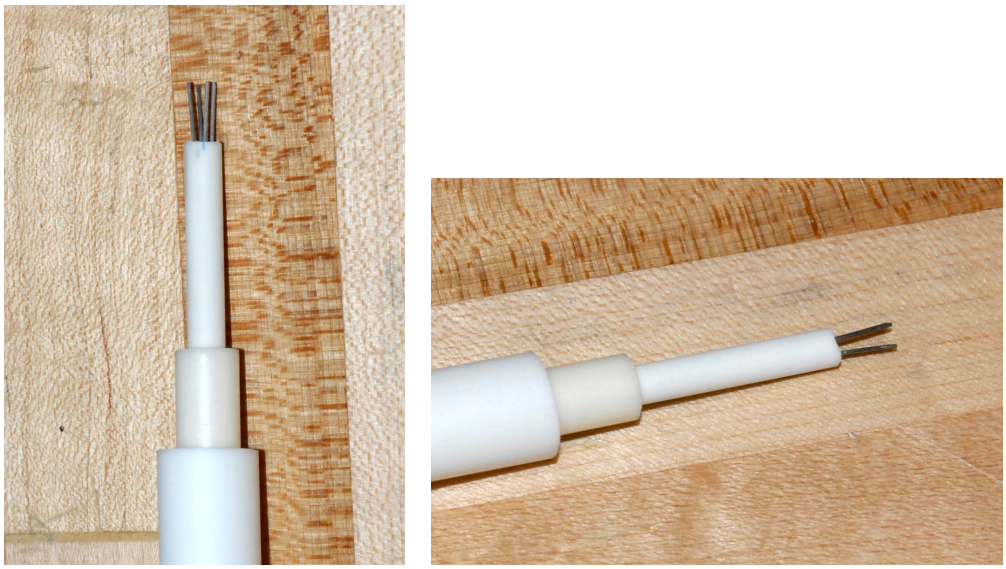

Figure 2.43: Photographs of the triple probe tips used for the XOCOT discharge experiment

Figure 2.44: Photograph of the triple probe used for the XOCOT discharge experiment

Probe	HD 1	HD 2	LD 1
Diameter	0.50 mm	0.50 mm	1.40 mm
Number of Probe Tips	4	4	4
Tip Separation	1.78 mm	1.78 mm	5.1 mm
Tip Length	8.4 mm	8.0 mm	14.0 mm
Collection Area	$1.33 \times 10^{-6}\ m^2$	$1.27 \times 10^{-6}\ m^2$	$6.14 \times 10^{-6}\ m^2$
Alumina Radius	4.75 mm	4.75 mm	8 mm
Total Length	25 cm	Variable	46 cm
Low Density Case			
$\frac{r_p}{\lambda_d}$	20	20	56
$\frac{s}{5\times\lambda_d}$	14	14	41
$\frac{r_{li}}{r_p}$	41	41	15
High Density Case			
$\frac{r_p}{\lambda_d}$	150	150	420
$\frac{s}{5\times\lambda_d}$	110	110	310
$\frac{r_{li}}{r_p}$	41	41	15
Low Density Case	$n_e = 1 \times 10^{18}\ m^{-3}$	$T_e = 10$ eV	$B = 0.1$ T
High Density Case	$n_e = 1 \times 10^{20}\ m^{-3}$	$T_e = 20$ eV	$B = 0.1$ T

Table 2.7: Triple Langmuir probe specifications

allows a spare electrode to be used as noise compensation and/or plasma uniformity studies (not described further in this dissertation).

Table 2.7 shows the 3 triple probe configuration used in these experiments, designated HD (high-density, small electrode) and LD (low-density). This table shows the physical, plasma, and theoretical characteristics of each probe geometry.

Chapter 7 utilizes the current-mode triple probe at multiple locations within the discharge annulus. Figure 2.46 details the location of the triple probe tips within the annulus for the various discharge locations. Position 0 is the location of the low density (LD) triple probe used to collect pre-ionization plasma density information in Chapter 4. Additionally, Position 0 is the location of the high density (HD 1) triple

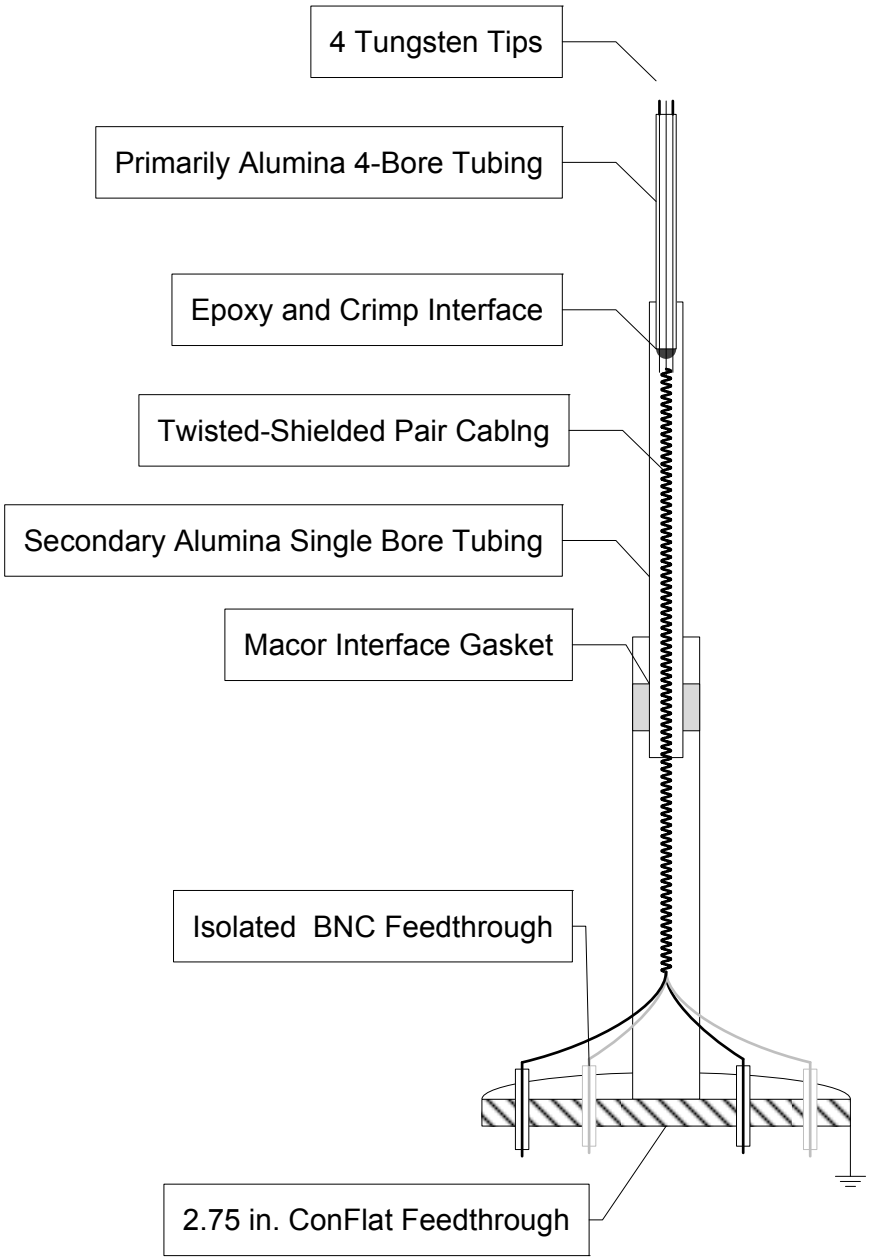

Figure 2.45: Cross-section schematic of a 3-staged scanning triple probe

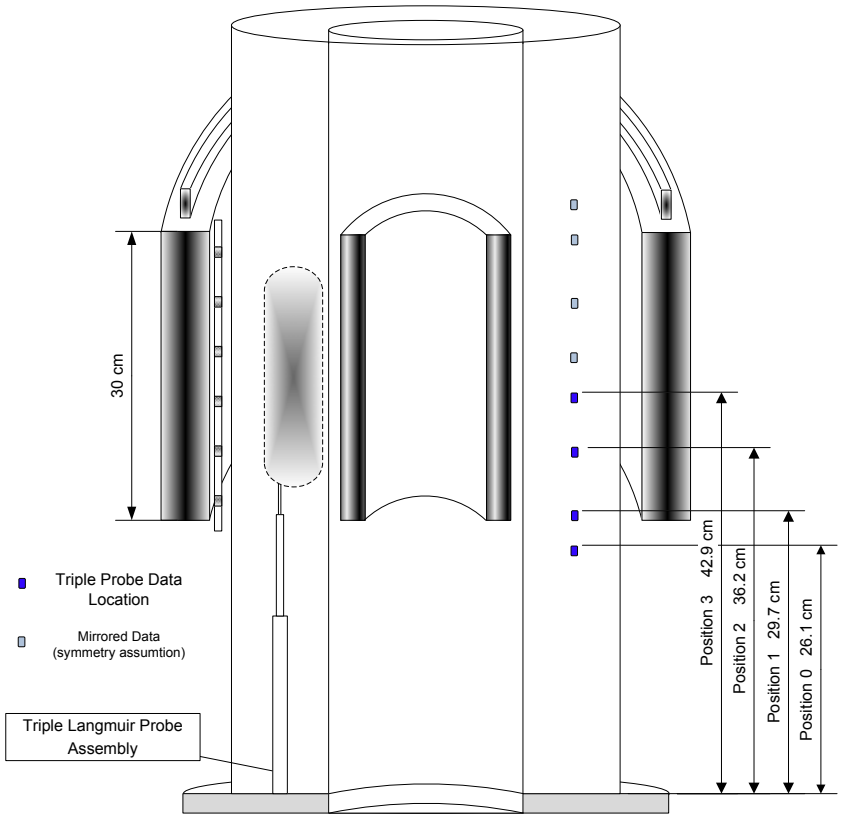

Figure 2.46: Schematic of triple probe locations for the discharge tests described in Chapters 5, 6, and 7

probe used to collect pre-ionization and main bank discharge plasma properties in Chapters 5 and 6. Finally, Positions 1–3 are the axial locations of the high density (HD 2) triple probe described in detail in Chapter 7. All data were collected at a radial location that was centered within the discharge annulus (within 10 %).

2.5.4 Triple Probe Error Analysis

Triple probes have been found to have similar error as Langmuir probes. Several complete analyses [63], [55] have found that the absolute error in electron temperature is less than 30 %, and electron density is less than 50 %. However, just as in

traditional Langmuir probe analysis, the relative error between data points with the same probe, electronics, and plasma conditions (variations from Maxwellian, etc.) is less than 10 %. For the floating triple probe, in a high-speed discharge, the statistical error can be so large that the capacitive current flow can dominate the floating probe collection current and subsequent floating voltage reading. The current mode triple probe has significantly less error associated with electronics: a complete analysis of statistical error (based on collection electronics and repeatability) is included in [18]. For a similar setup, 8-bit oscilloscope, and Tektronix TCP202 current probes the error in collected electron temperature was less than 5 % and for density was less than 15 % for currents above the minimum limits of the current probe (i.e. 2 % of full-scale). Plasma data presented in this dissertation all utilize the above assumptions in error, and although repeatability of pre-ionization discharges and main bank discharges were well below 5 % (peak collected current values), most measurements have to be considered as relative measurements of temperature and density.

CHAPTER 3

Field Reversed Configuration Models

Considerable insight can be gained by investigating bulk energy in an FRC, both in an equilibrium, high-β state as well as from real-time measurements such as those collected in Chapters 4, 5, and 6. Chapter 3 provides a summary of an energy model developed at AFRL to quantify the compressed plasma and discharge coil properties of an annular FRC. Additionally, Chapters 7 and 8 show the real-time energy content contained within the plasma from data measured by the internal high-speed triple probe. The energy equations and analysis required to perform those calculations are shown here.

3.1 Equilibrium Energy Balance

First, a zero-dimensional energy balance model was developed in order to facilitate the development of the initial concept. Dr. James Haas [30] completed most of the following equilibrium analysis, but a summary is provided here for completeness. The model assumes a compressed, equilibrium state plasma with an annular cross section and a separatrix compression yielding to a β of 0.5 (empirically based) to predict the temperature/energy scaling as a function of XOCOT discharge experiment size. It also takes into account the equilibrium energy loss mechanisms (excluding flux/energy loss during formation and reversal) and variations in circuit parameters

in the discharge network and the actual coil geometry. Equations 3.1 and 3.2 detail the definitions of plasma β and the area derivation used in an annular geometry (Equation 3.3) [42]. B_z is the applied compression field, p is the plasma thermal pressure, A_p is the plasma cross sectional area, and A_c is the quartz annulus cross sectional area. Plasma pressure, p, and temperature, $T_e + T_i$ were calculated with Equation 3.5. The main radiation loss mechanism considered was Bremsstrahlung radiation as it dominates Synchrotron radiation for these plasma densities and atomic numbers. Unfortunately, one major source of error in this simple model is the lack of an optical radiation power sink term, as for the electron temperatures that have been found ($< 20\ eV$) simply excited state argon emission will be the dominant radiation mode. The initial models were designed for much higher than 20 eV temperatures and for deuterium where Bremsstrahlung radiation dominates the optical output. As the temperatures (and peak power) were decreased and the molecular weight of the gas increased, optical emission is expected to become the dominant radiation loss term. The coil geometry uses standard inductance and resistance models for a linear, air-cored inductor coil, solid aluminum cylindrical coil, and inductive voltage model. This energy balance model shows that, at the power levels considered (100's kW), ohmic losses in the coils are the main loss mechanisms and that radiation losses do not become a major loss contributor until the AFRC is operated at several orders of magnitude higher discharge power (MW per shot). Results of the energy model are shown in Figure 3.1 for radiation, coil heating, plasma ionization, and plasma heating approximations. This model also predicted (as discussed in AFRC literature) that small increases in coil size would lead to substantial decreases in discharge voltage.

$$p_m = p + \frac{B_e^2}{2\mu_0} = \frac{B_z^2}{2\mu_0} \tag{3.1}$$

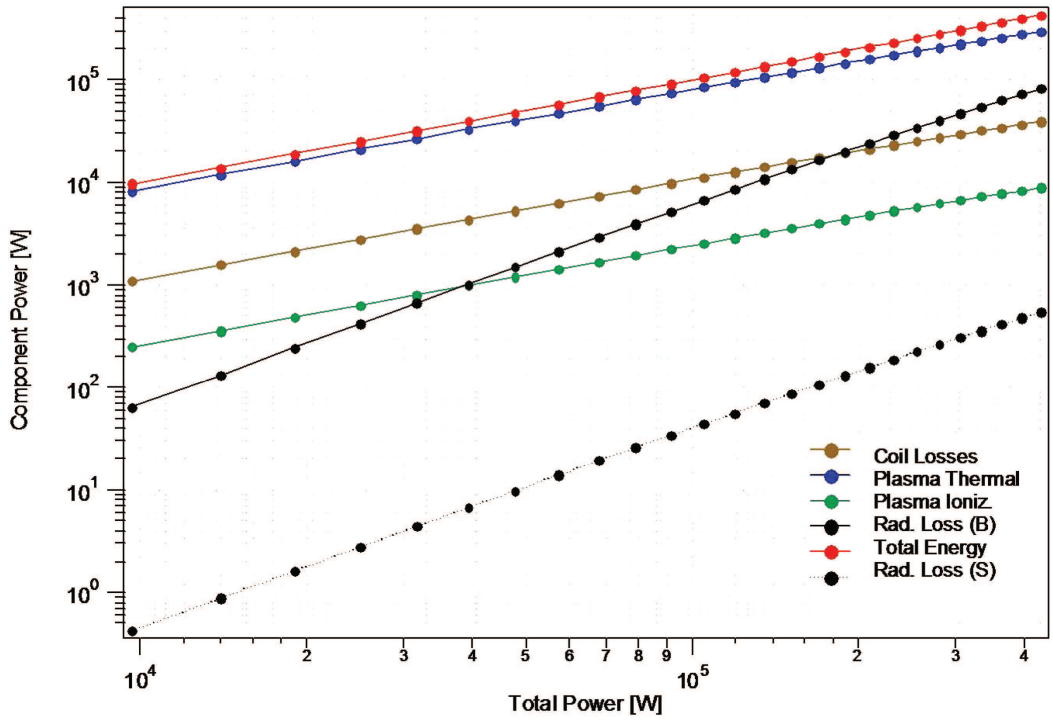

Figure 3.1: Equilibrium model results

$$\langle \beta \rangle = 1 - \frac{1}{2}\frac{A_p}{A_c} \tag{3.2}$$

$$\langle \beta \rangle = \frac{2}{r_s^2}\int_0^{r_s} \frac{p}{p_m} dr \tag{3.3}$$

In Equations 3.1–3.3, r_s is the separatrix radius (later converted to annular plasma area) and B_e is the externally applied magnetic field.

3.2 Energy Analysis

In order to compare with previous, asynchronous AFRC experiments, as well as provide a useful investigation into the operating mechanics of the synchronous FRC, a study of the real-time energy contained in the annular discharge region has been performed. From Reference [4] the total energy balance can be stated as Equation 3.4. This is the energy contained within the annular region at a specific time, for a fully

(and singly) ionized gas. This energy balance contains the instantaneous discharge energy (E_{in}), the thermal energy, ionization energy, and the kinetic/translational energy ($E_{kinetic}$). Equation 3.4 assumes a uniform plasma density within the separatrix region (A_p) which is typically a good assumption. However, the assumption of a constant separatrix area is typically quite poor, as the plasma area is increasing and moving (radially compressing) during a typical discharge and for high accuracy must be measured by magnetic diagnostics. The plasma thermal energy-per-unit-length can be written as Equation 3.5, while the ionization energy is simply Equation 3.6. The ionization energy assumes a uniform plasma density across the region within the separatrix (A_p) which is typically applicable. Finally, again from Reference [4], the energy stored in the magnetic field (coil inductor) per unit length is written as Equation 3.7. Equation 3.8 simply states the power dissipated in the aluminum discharge coils as a function of the effective resistance (from the parallel coil DC resistance and pulsed skin depth resistance), R_{eff}, and the total coil length, l_0. In Equations 3.4 and 3.6, the atomic ionization potential, e_{ion}, is 15.75 eV for argon and 12.12 eV for xenon (assuming singly charged atoms). This analysis is used, and coupled with experimental results, in Section 7.3.4.

$$E_{in} = E_{UB} - N_e k T_e - N_e e_{ion} - E_{rad} + E_{kinetic} \tag{3.4}$$

$$\frac{E_p}{l} = \frac{5}{2}\langle n_e k_B (T_e + T_i) A_p \rangle \tag{3.5}$$

$$\frac{E_{ion}}{l} = n_e \times e_{ion} A_p \tag{3.6}$$

$$\frac{E_U B}{l} = \frac{3}{2}\langle\beta\rangle\frac{B_z^2}{2\mu_0}A_p \tag{3.7}$$

$$\frac{E_{coil}}{l} = \int \frac{I_{coil}^2 R_{eff}}{l_0} dt \tag{3.8}$$

3.3 Energy Analysis Summary

Chapter 3 explored the bulk energy properties of a compressed, annular FRC. It has been shown that for the power levels in the XOCOT discharge experiment an annular FRC can be formed and heated efficiently, with a majority of energy deposited in the plasma, rather than loss through radiation and coil ohmic losses. Additionally, a framework has been provided for analyzing experimental data in terms of total energy content rather than density, temperature, and magnetic field that will be useful in understanding plasma creation and heating efficiency. Finally, Chapter 3 outlined modifications for an annular geometry to the analytic techniques that are commonly employed for cylindrical field reversed configuration plasmas.

CHAPTER 4

Pre-Ionization Studies

Pre-ionization is the first stage in creating a field reversed configuration. Chapter 4 examines the pre-ionization techniques used in this annular field reversed configuration experiment. First, a theoretical survey of the historical and empirical pre-ionization techniques and threshold requirements is conducted. Geometry 1, an isolated, azimuthal pre-ionization coil was tested in order to understand voltage, current, plasma density, and plasma temperature relations for a ringing pre-ionization discharge. A preliminary optimization was then performed in order to maximize the plasma content and ionization fraction. Section 4.3 describes the results for Geometry 2, which utilized the main annular discharge coil as the pre-ionization ringing coil. A complete pre-ionization optimization was done. This Chapter describes the optimization of the PPI (pre- pre-ionization) DC glow discharge which provides a small seed electron population to begin the discharge, in terms of discharge voltage and geometry. Subsequently, testing was done on the optimal pre-ionization and discharge voltages as well as pressures. Finally, a complete time scaling experiment was done, both without the main bank and utilizing a 185-μs discharge (as described in Chapter 7) to investigate the optimal timing and operation of the ringing RF pre-ionization. All experiments in this Chapter were performed with both xenon

and argon propellants. Section 4.4 describes Geometry 3, a $Z-\theta$ ringing discharge which would provide a large pre-ionization load inductance, more axial plasma uniformity, and greater azimuthal pre-ionization plasma density. Chapter 4 ends with a concluding summary of pre-ionization testing results, optimal discharge points, and a description of bulk-, magnetized-plasma initiation.

4.1 Pre-Ionization Theory

Tuszeski and others [64] have said:

> "Preionization is perhaps the most critical and often underestimated phase in FRC formation. Indeed, FRC behavior after formation has often been found to depend profoundly and inexplicably on the details of preionization . . ."

Pre-ionization for FRC plasmas has been accomplished by a variety of means: a pulsed-RF discharge, microwaves [64], pulsed-laser plasmas [13], and more recently arcjet and helicon [61] techniques. For these experiments, an intensive study was undertaken in order to examine and quantify pre-ionization techniques and effectiveness.

There are four primary concerns with a pre-ionization discharge that will have significant effects on the quality and efficiency of an FRC discharge. First, the ionization fraction of the post pre-ionization plasma is a critical parameter in FRC formation as magnetic field diffusion is the primary flux and particle loss mechanism. In any type of theta pinch device, as the magnetic field diffuses through the pre-ionized plasma, it does not efficiently heat, trap, or compress the plasma and as a result particles diffuse through the magnetic field lines and out of the device both axially and radially. Optimally, the initial plasma near the main discharge coils is 100 % ionized so that the discharge current can induce a large diamagnetic current in the plasma to generate compressive forces. Additionally, it would be optimal for

initial pre-ionization energy to only be spent ionizing the neutral gas near the discharge coils as the main compression and diamagnetic current will sufficiently heat the internal annular gas. Unfortunately, the ionization fraction required for efficient FRC compression and heating is a rather empirical number, though in general, it appears a 5-10 % pre-ionization fraction is required and that further ionization due to the main bank (from E_θ in Equation 1.1) will fully ionize the discharge chamber plasma. Secondly, symmetric initial plasma is critical to FRC formation so that the diamagnetic current will penetrate significantly along the full axial region of the FRC chamber and that initial plasma density is uniform so that compression shock formation is uniform. Again, unfortunately, all manner of pre-ionization techniques drive asymmetries whether they are radial or axial nonuniformities. Additionally, the initial neutral gas distribution is also key, for the uniformity reasoning as earlier. Clearly, pre-ionization timing is also critical in a single coil FRC. Pre-ionization during the maximum reverse bias ensures that the maximum amount of flux is trapped for the reversal and therefore leads to larger diamagnetic self-currents in the plasma. In the annular configuration, ionization is initiated prior to main bank discharge and timing is less of an issue and is merely a function of residual plasma ionization fraction, geometrical uniformity, and overall system noise. A parameter study was initiated in Sections 4.2.1, and 4.3.2 in order to optimize input energy and main bank heating. Finally, total system efficiency is a function of how much energy is input for the pre-ionization RF ringing discharge as the absolute minimum amount of energy should be wasted during the initial ionization phase prior to main bank discharge. This is less of a concern in fusion reactor type systems where total energy input by the main bank measures in the megajoules, however it does become a significant issue for low-energy FRC formation. In these experiments, pre-ionization bank energy

was on the scale of 0.1 to 1 % of the main bank discharge energy.

The primary technique used for these experiments is the most widely used technique for FRC pre-ionization, namely an RF azimuthal-ringing discharge around the primary discharge chamber. This initial high-voltage, but low-energy discharge is used to create the pre-ionization seed plasma within the discharge chamber, that the main high-current, high-magnetic-field, and high-energy discharge can do work on. The RF ringing-discharge is called the Pre-Ionization (PI) discharge in this experiment. Several geometries were investigated, both connected and isolated circuits as shown in Figure 4.1, and all discharge parameters were varied in order to fully explore the pre-ionization effectiveness and operational regimes in an annular discharge chamber. In order to minimize initial voltage costs, a seed electron discharge is also used. This is described in the following investigations as a Pre- Pre-Ionization (PPI) or a glow discharge. Both discharge setups and multiple PI discharge geometries are explored in Chapter 2 and Sections 4.2–4.4.

4.2 Pre-Ionization Geometry 1

Figures 4.2–4.4 show a summary of pre-ionization data collected for a single turn inductive coil at the top (as shown in Figure 4.1) of the main discharge coil. Data presented is for a 3-kV case. It is not shown, but density and photometer data all scale monotonically with discharge voltage, and 3 kV was chosen primarily as the functional limit of power supply voltage. Figures 4.2-4.3 show the triple probe data for a single, 10-mTorr discharge with, as expected, a peak of plasma density 20 μs (approximately 5 oscillations) after pre-ionization initiation. The temperature also increases, though the data at less than 10 μs is less accurate as plasma density (and sheath size) is out of the desired range for triple probe operation. Peak electron temperatures of 60 eV and densities of 2×10^{18} m^{-3} have been measured. These

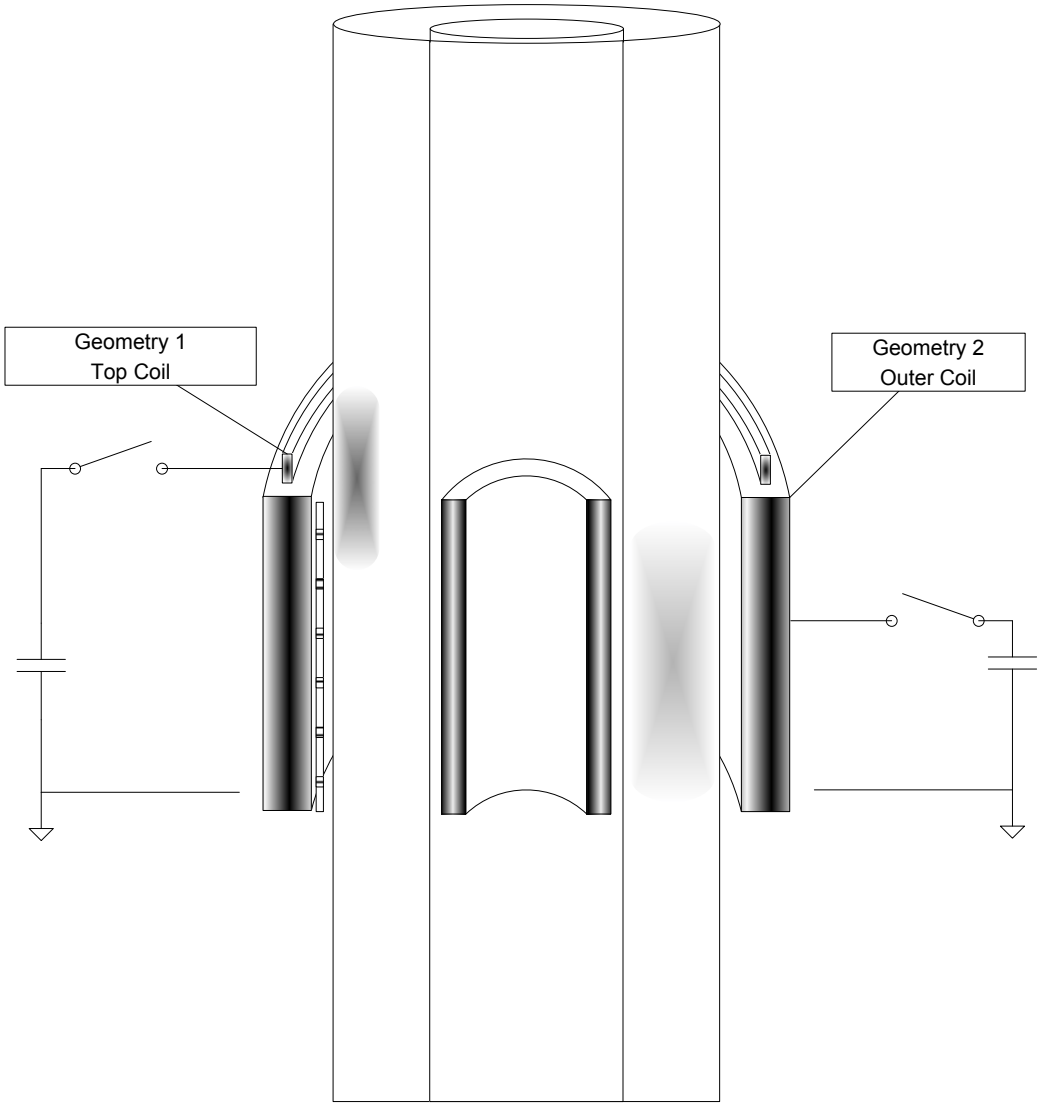

Figure 4.1: Pre-ionization coil schematic for Geometries 1 and 2

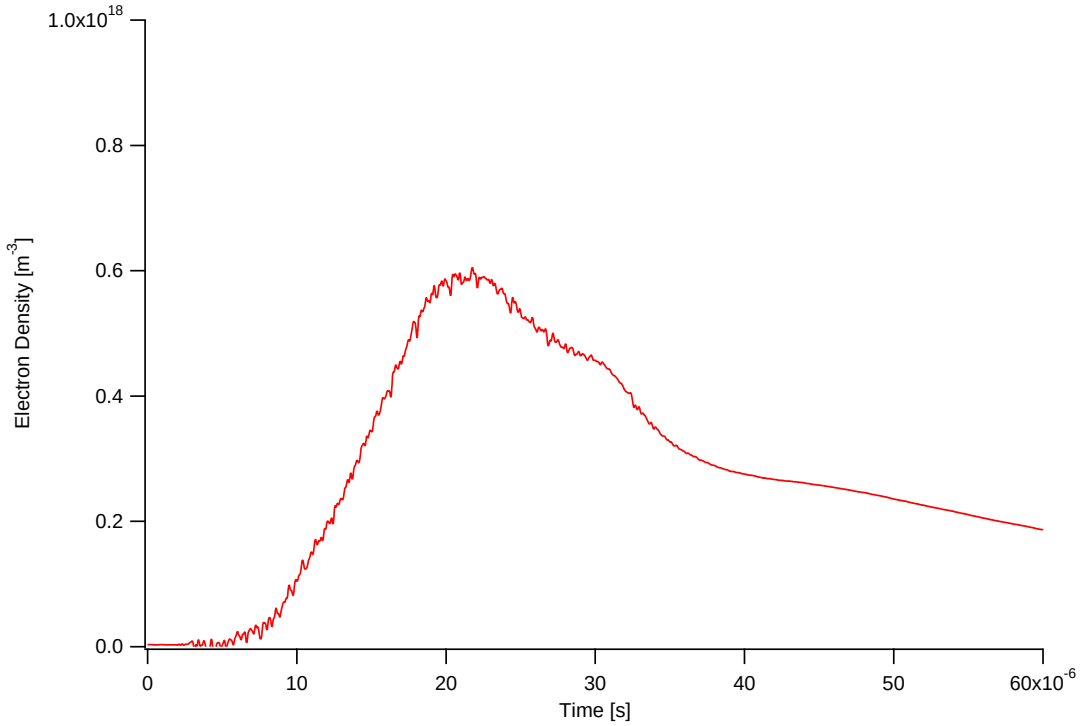

Figure 4.2: Triple probe temperature results for a 3-kV, 10-mTorr pre-ionization discharge

measurements were taken with a low-density triple probe (LD 1) at position 0.

Figure 4.4 shows the variation in pre-ionization results as a function of background neutral propellant density. In general, a peak in plasma production is expected in the 1-10 mTorr range, and indeed, it is seen in the photometer results at 4-7 mTorr suggesting a maximum plasma production (or even an energy efficiency for a given input power). However, those results are not repeated in the measured triple probe density. This suggests that while there is a highly ionized region near the coil, at higher densities (and therefore shorter skin depths) the triple probe is no longer in the region of highest density. That said, the triple probe should still provide a good estimate of average plasma density and temperature in the annular discharge region of the main coil. Using the measured plasma density, percent ionization is shown in Figure 4.5 with peak ionization fraction of 7 %.

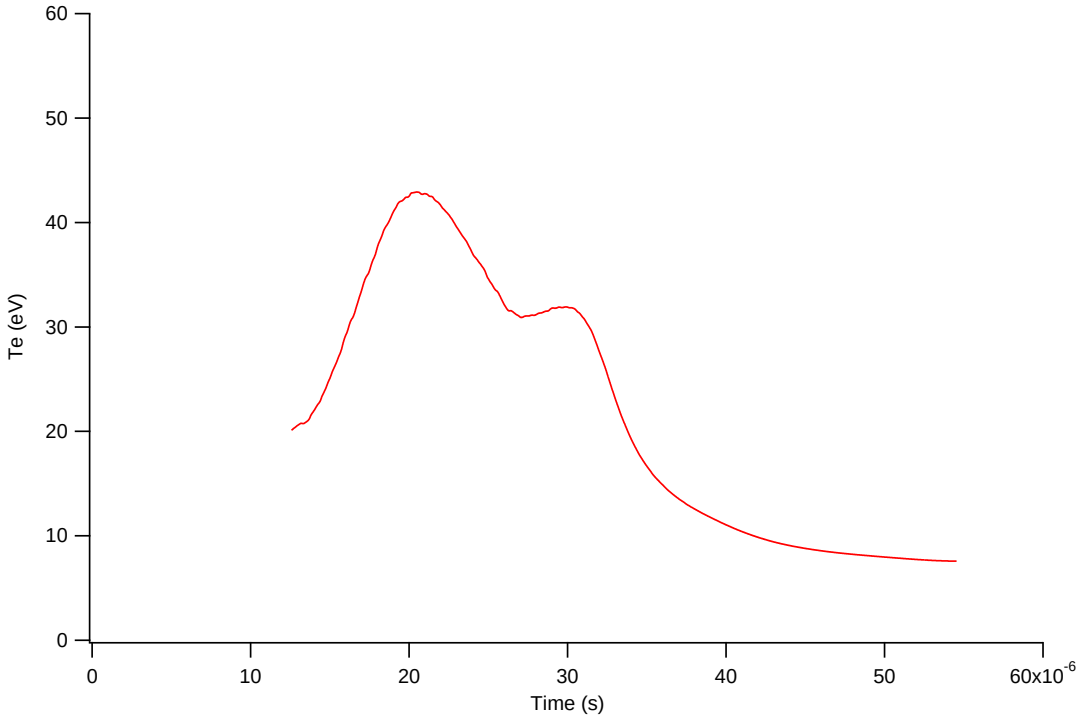

Figure 4.3: Triple probe density results for a 3-kV, 10-mTorr pre-ionization discharge

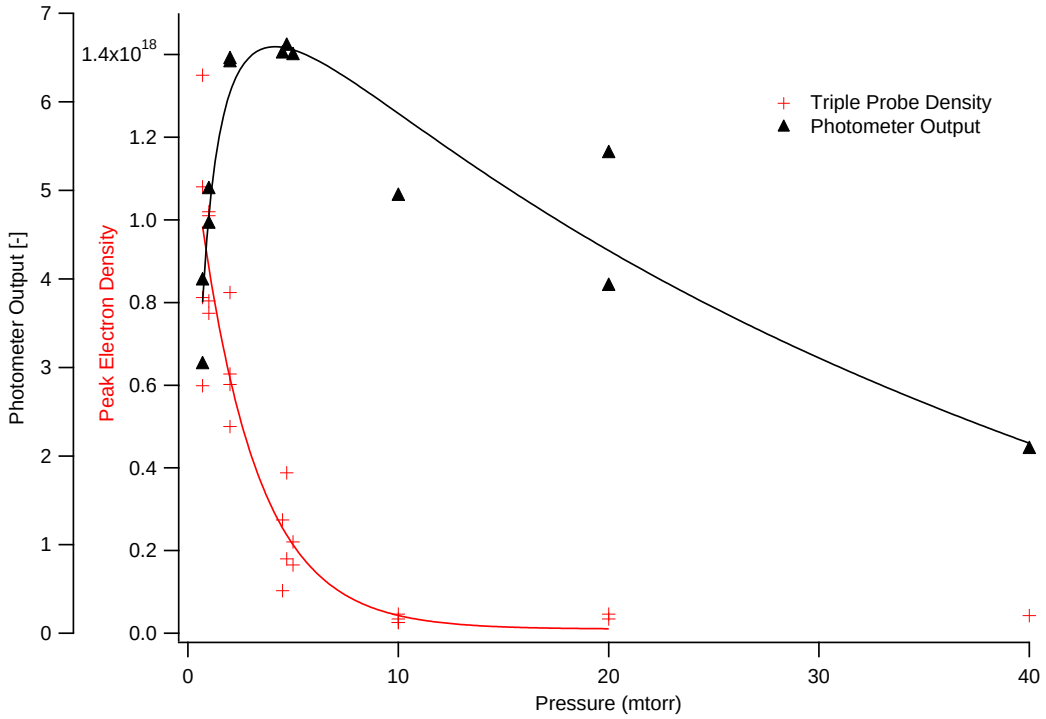

Figure 4.4: Pre-ionization density and photometer results for a range of ionization parameters

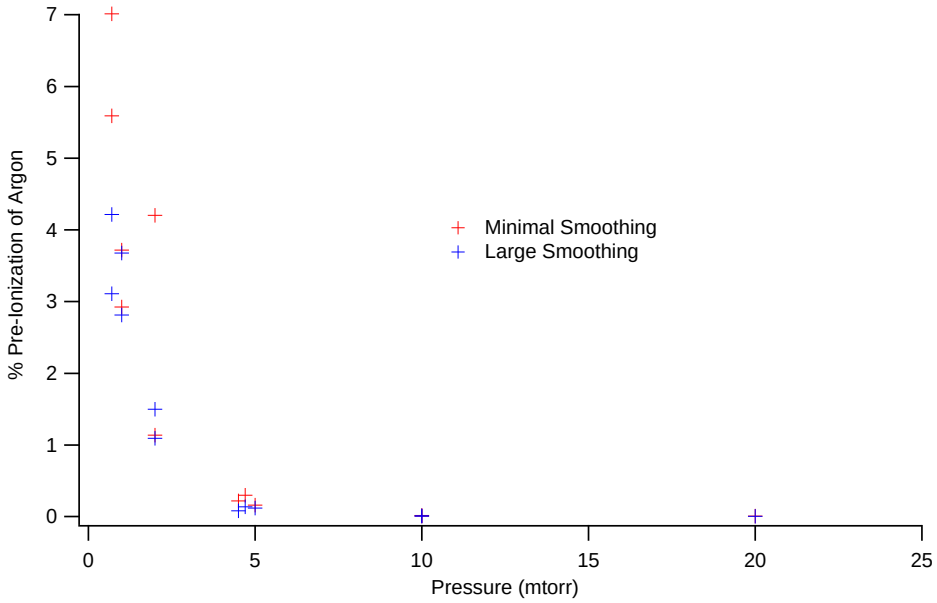

Figure 4.5: Pre-ionization percent ionization results for a range of ionization parameters

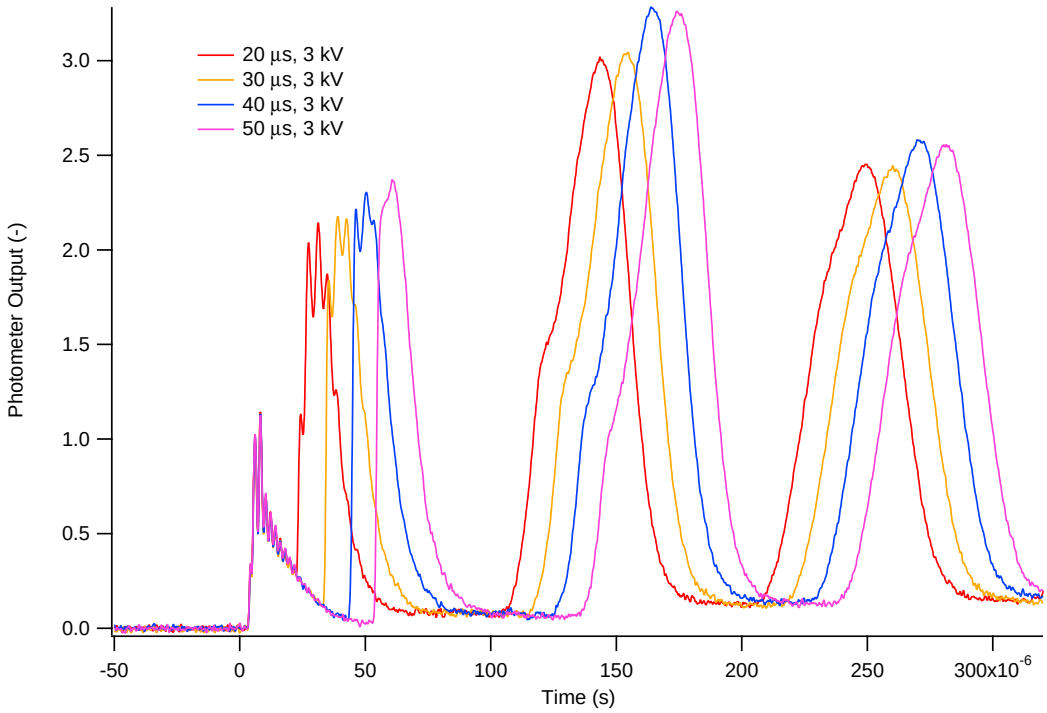

Figure 4.6: Pre-ionization timing study for Geometry 1

4.2.1 Time Scaling Experiments

Not surprisingly, timing of the pre-ionization is a critical parameter in its efficacy. Two conflicting parameters are functions of the pre-ionization timing, namely a peak plasma density and the plasma uniformity in the discharge region. Plasma density peaks during the pre-ionization ringing discharge, however, as the plasma diffuses it more uniformly fills the discharge region. For FRC formation both plasma density and uniformity are critical and so locating the proper timing between the pre-ionization and the main bank discharge becomes an empirical process of multiple ionization discharges, main bank discharges, and the various timings. Figure 4.6 details preliminary efforts to determine pre-ionization timing, at a background pressure of 14 mTorr and a main bank discharge of 500 V with 3 kV on the pre-ionization coil.

Section 4.3.2 provides a more complete analysis of time for scaling Geometry 2

yielding similar results. Results appear to show a local maxima near 60 μs. This value was subsequently chosen as the standard delay in the 450- and 250-μs discharge cases.

4.3 Pre-Ionization Geometry 2

The results for early discharge cases appear to show a significant asymmetry in FRC formation that is attributed to the single pre-ionization coil at the top of the main discharge coil. In order to mitigate this, subsequent testing was performed using the main discharge coils themselves as the pre-ionization coil [31]. Ignitron switching is rated to higher voltages than the pre-ionization discharge, and so is safe to use as isolation of the main bank. Note, however, that using a high current thyristor (with reverse current diode) would be dangerous in this type of discharge configuration. Using the main discharge coil as the pre-ionization coil guarantees an axially symmetric pre-ionization discharge, and while it adds electrical system complexity, the timing study shows that the optimal pre-ionization can exist for up to 100 μs after initiation of pre-ionization discharge and therefore this coil configuration is suitable. Figure 4.1 shows a schematic of the pre-ionization Geometry 2.

4.3.1 Glow Discharge Results

Using pre-ionization Geometry 2, a complete analysis was done studying both the glow discharge and the timing of the main pre-ionization discharge. Figures 4.7–4.11 detail the peak and temporal photometer response for various operating discharge conditions in argon. Each discharge shown uses an identical 3-kV, 250-kHz ringing discharge as the primary ionization technique that was limited by the output of the charging power supply. The glow discharge on a thoriated tungsten electrode (see Figure 2.9) was established 1 second prior to the pre-ionization ringing discharge. It was found that the final product (brightness temperature and density) of the plasma was highly dependent on glow discharge energy and voltage. The pre-ionization discharges in argon yielded very interesting response in that there appears to be a minimum threshold energy in the glow discharge (for various pressures) in order to initiate bulk ionization processes. In addition, increasing energy to the glow discharge increased monotonically the initial pre-ionization magnitude and brightness. Finally, photometer results show that the pre-ionization output is highly dependent on neutral density. Figure 4.10 shows the output response for various background densities at the 6-kV discharge case. The pre-ionization discharges with argon appeared to have a minimum 5 kV glow discharge voltage (1-20 Watts depending on pressure) before primary bulk plasma ignition.

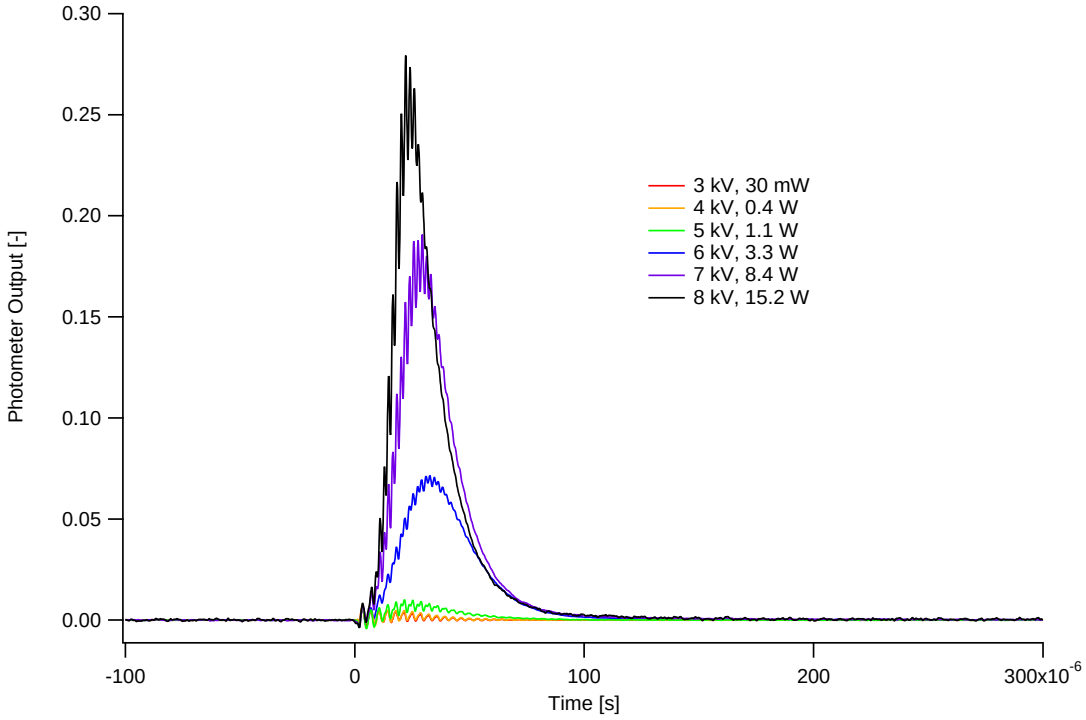

Figure 4.7: Pre-ionization photometer response for an 11-mTorr argon discharge at various PPI glow discharge energies

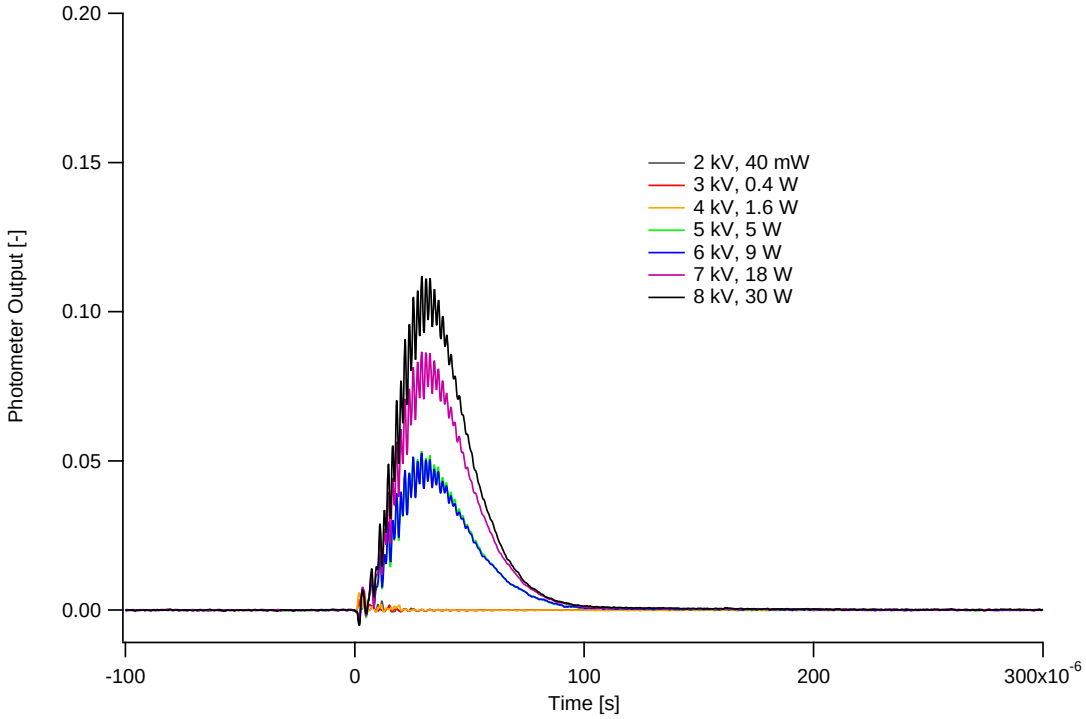

Figure 4.8: Pre-ionization photometer response for a 14-mTorr argon discharge at various PPI glow discharge energies

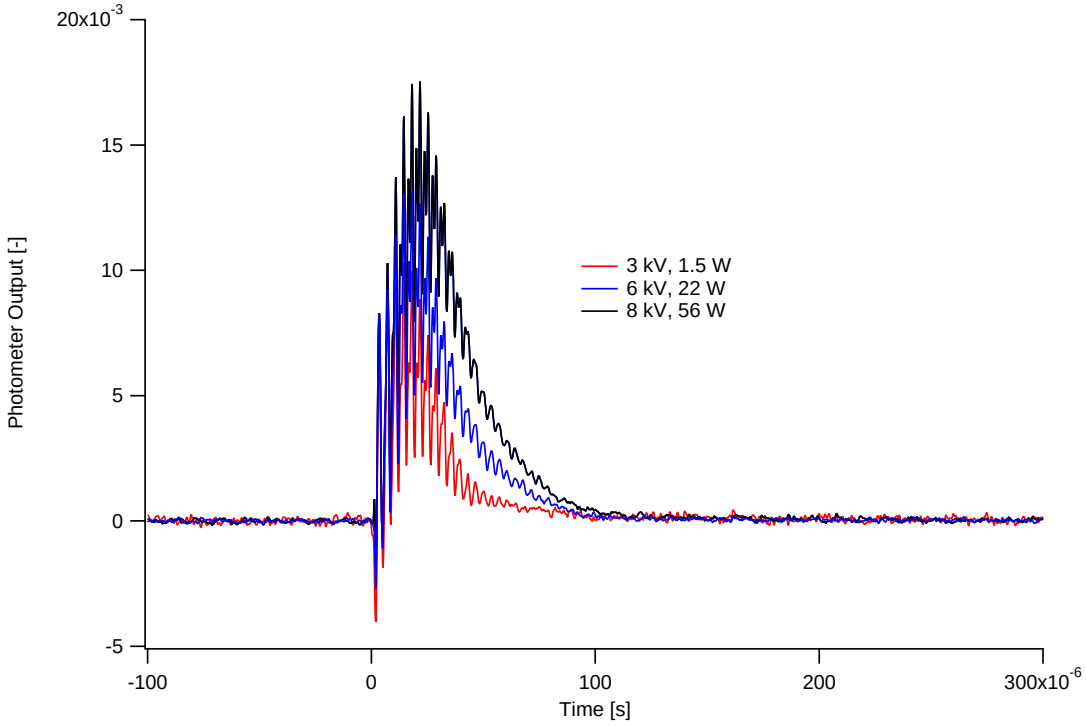

Figure 4.9: Pre-ionization photometer response for a 20-mTorr argon discharge at various PPI glow discharge energies

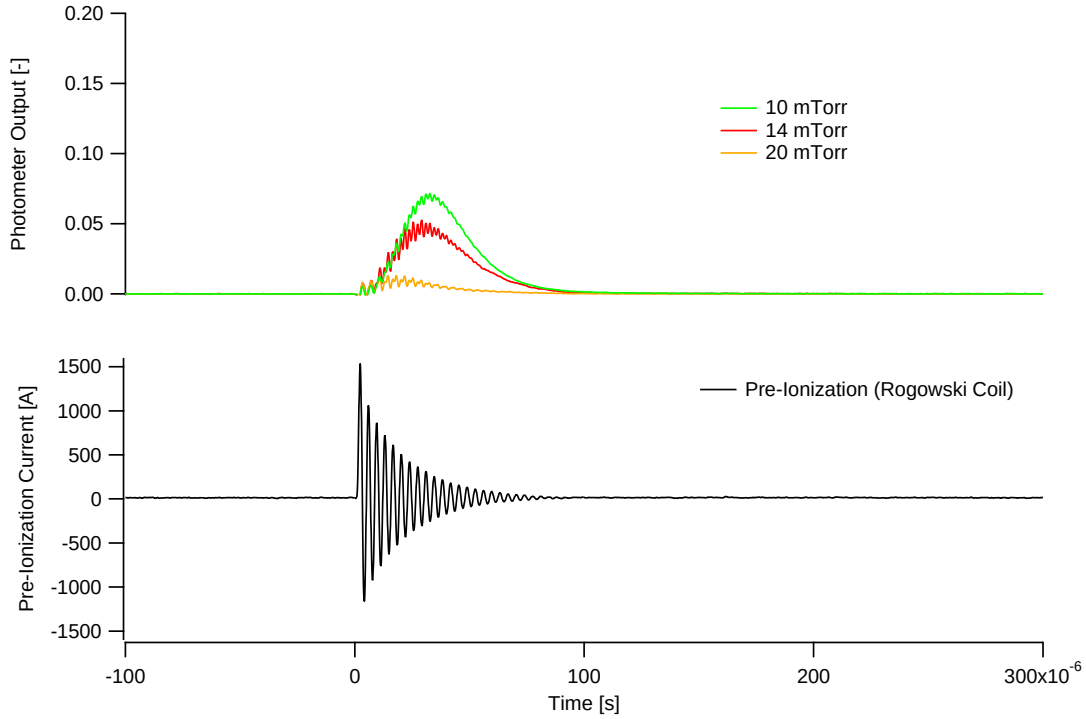

Figure 4.10: Pre-ionization photometer response for a 14-mTorr argon discharge, 6-kV PPI glow discharge as compared to the 250-kHz ringing pre-ionization current

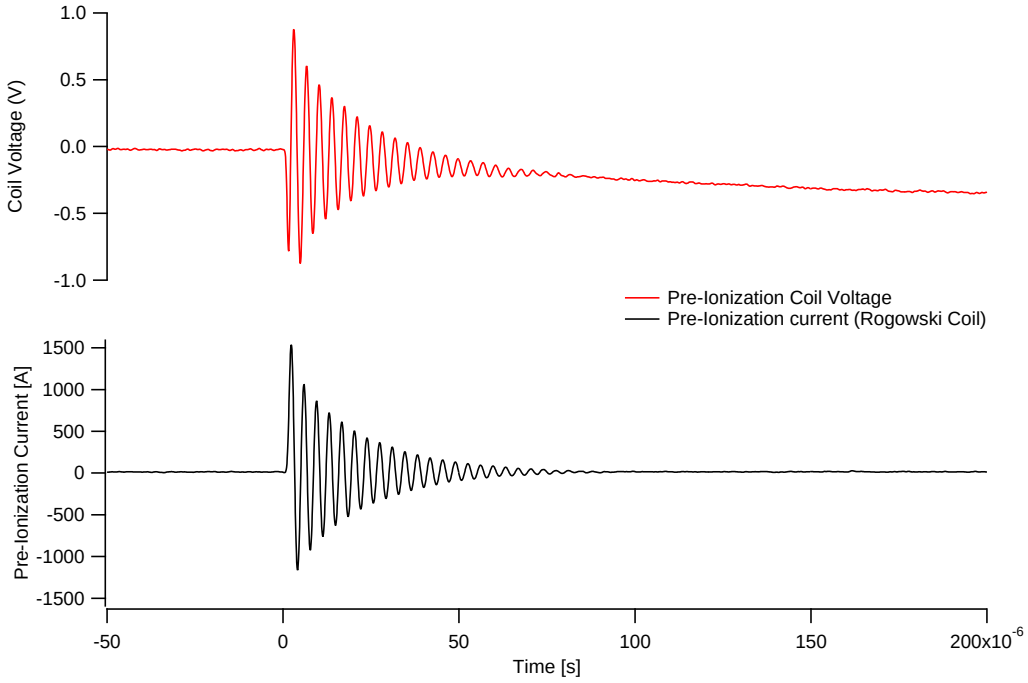

Figure 4.11: Pre-ionization coil current response for a 14-mTorr argon discharge, 6-kV PPI glow discharge as compared to the 250-kHz ringing pre-ionization voltage across the main coil

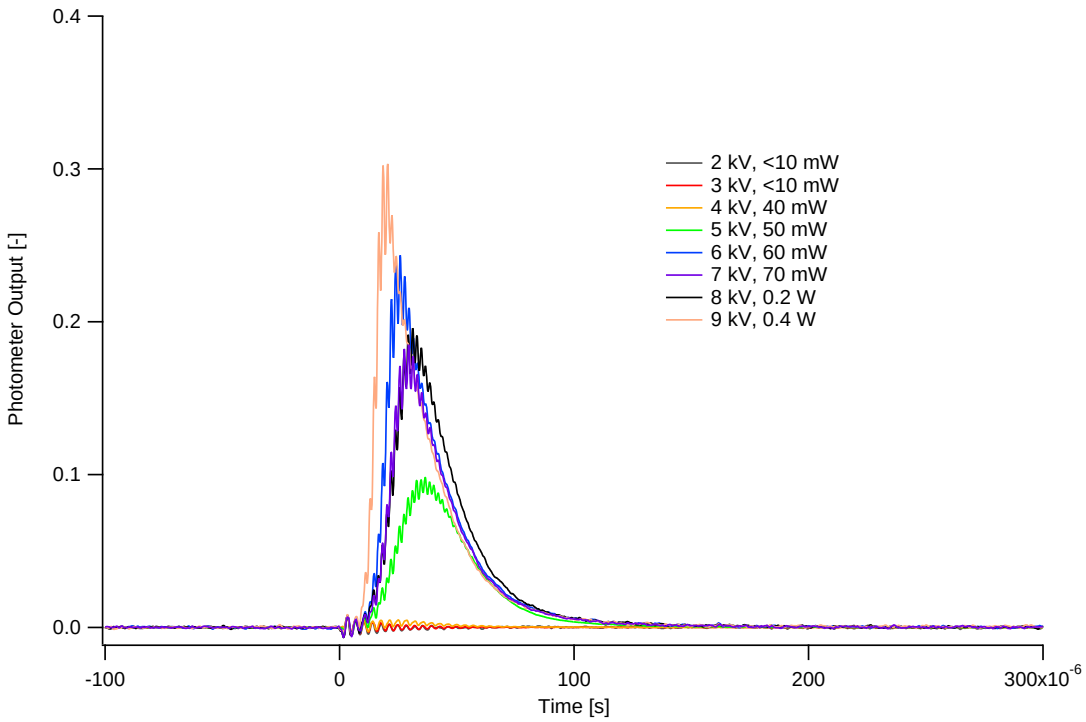

Figure 4.12: Pre-ionization photometer response for a 3-mTorr xenon discharge at various PPI glow discharge energies

Figures 4.12-4.16 show similar results using xenon as the primary operating gas. Xenon, as expected, has a lower initial threshold for bulk ionization (4 kV, 0.5-2 W). Figures 4.15 and 4.16 detail the operating conditions and photometer response of the pre-ionization discharge coil used in the comparison of pre-ionization glow discharge energies.

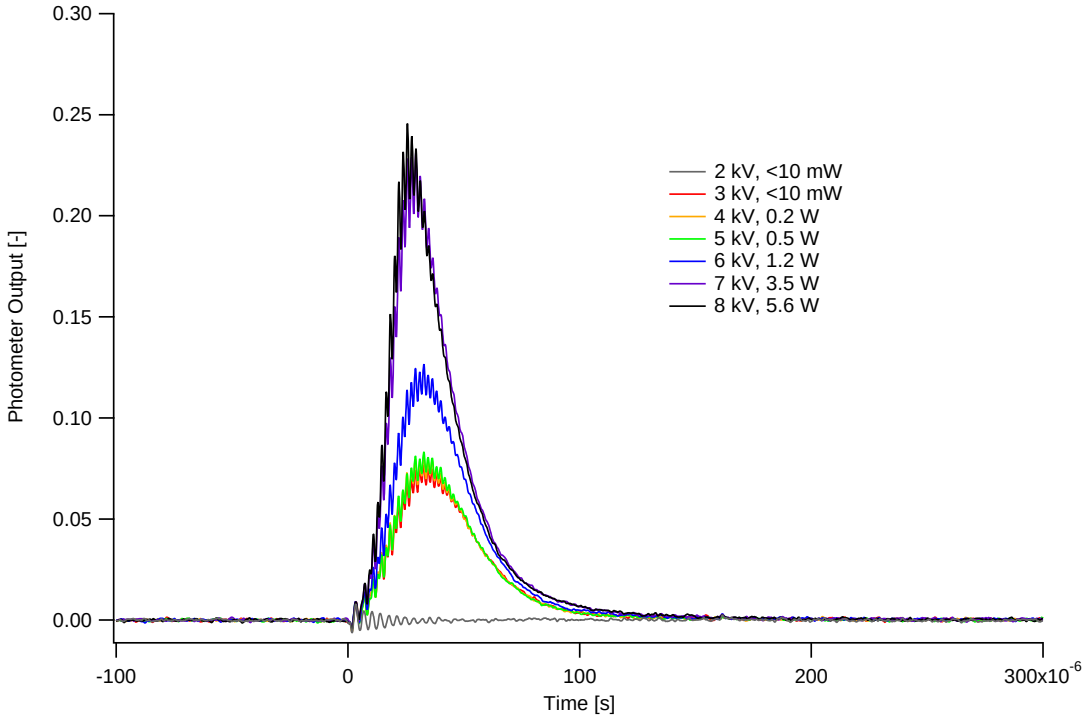

Figure 4.13: Pre-ionization photometer response for a 6-mTorr xenon discharge at various PPI glow discharge energies

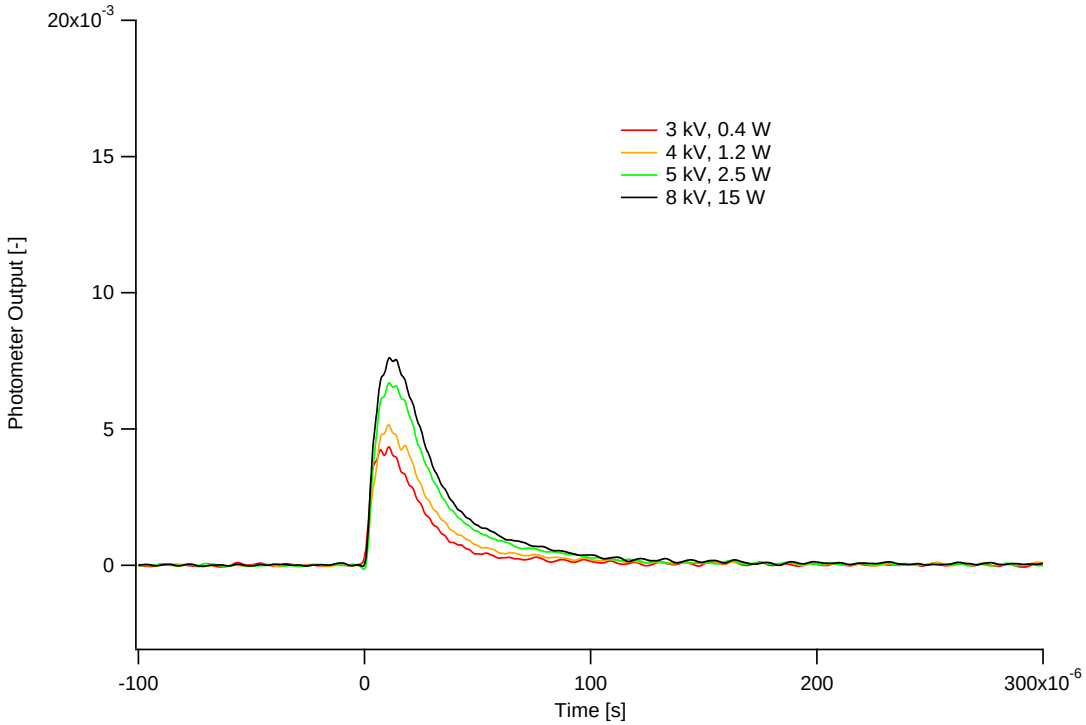

Figure 4.14: Pre-ionization photometer response for a 10-mTorr xenon discharge at various PPI glow discharge energies

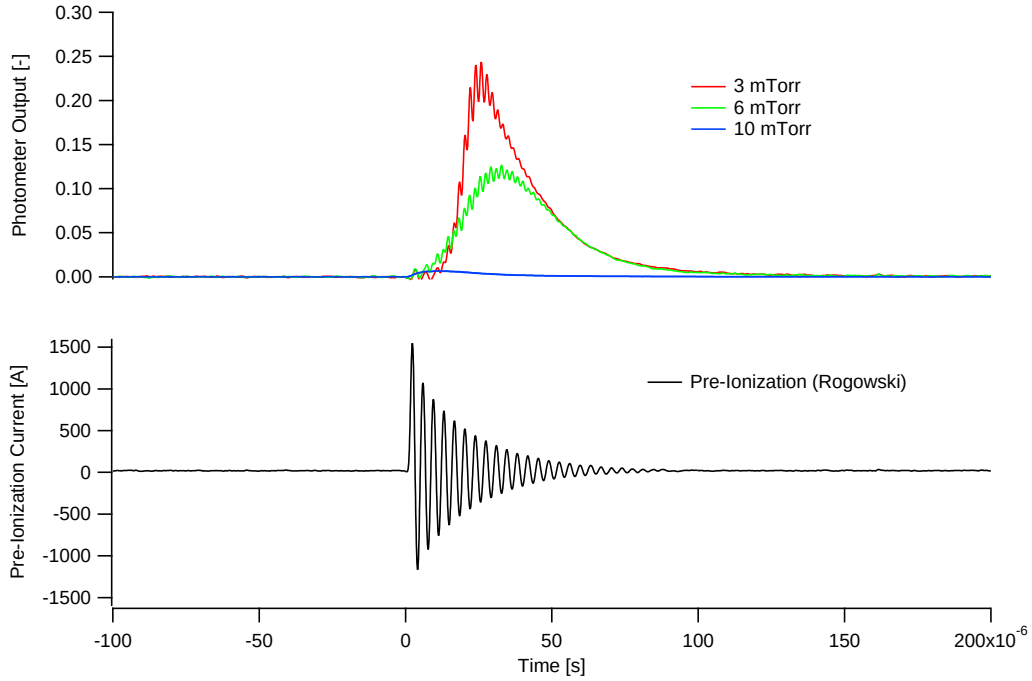

Figure 4.15: Pre-ionization photometer response for a 6-mTorr xenon discharge, 6-kV PPI glow discharge as compared to the 250-kHz ringing pre-ionization current

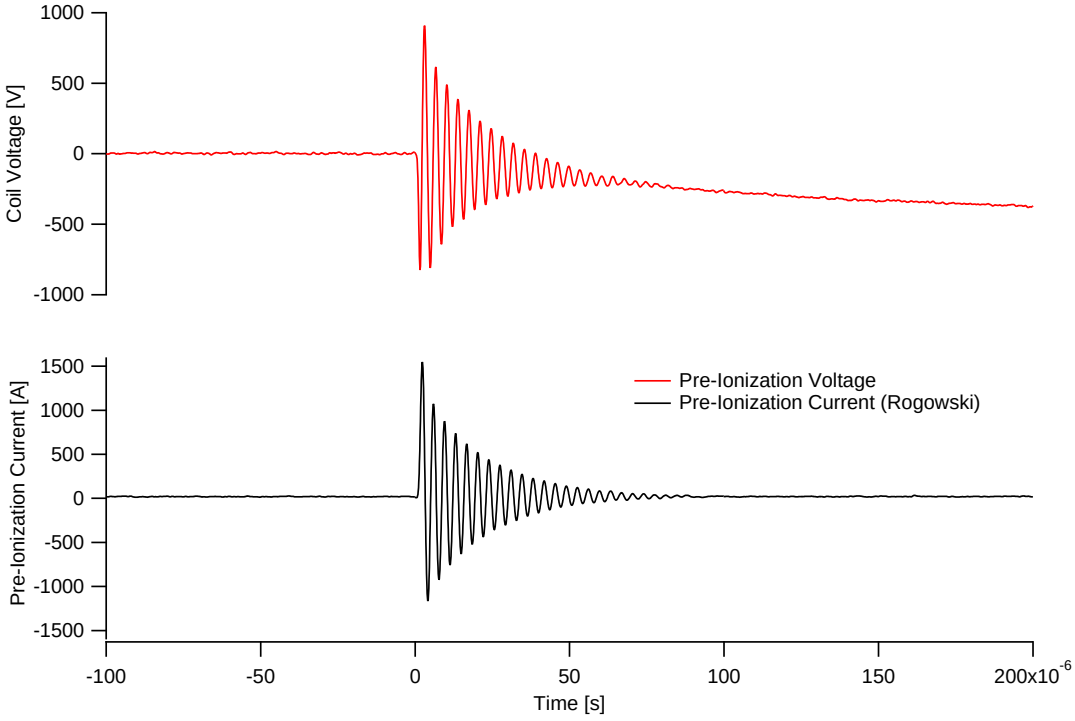

Figure 4.16: Pre-ionization coil current response for a 6-mTorr xenon discharge, 6-kV PPI glow discharge as compared to the 250-kHz ringing pre-ionization voltage across the main coil

It was expected that applying a main bank discharge (for all of the following data an 850-V, 185-μs discharge was utilized) would have little effect on the higher energy plasma and similar results would be found for varying the initial PPI glow discharge energies as shown in the data for the isolated pre-ionization discharge. However, as shown in Figures 4.17 and 4.18 there is an initial turn-on voltage required to initiate a successful pre-ionization and then a successful main bank discharge. In argon the turn-on voltage was found to be around 5 kV DC glow discharge voltage. However, subsequent increases in the pre-ionization glow energy did not have significant increasing effects towards bulk plasma content during a high-energy main bank discharge. In fact, the primary discharge photometer output was essentially constant above 5 kV. The secondary discharge did seem to have some minor effect due to increasing initial glow discharge energy. Figures 4.19 and 4.20 show triple probe current response at Position 1 for the above discharges at various initial pre-ionization glow discharge voltages. Those validate photometer results in showing that the various stages of ionization and plasma current collected by the triple probe during the discharge were essentially minimal until a threshold ionization density and temperature were reached at which point the initial plasma content and temporal structure was uniform. One important note, there appears to be major variability on the subsequent ionization, and plasma structure reaching the triple probe that appears to be primarily due to small variations in the effect of the background pressure and not due to increases in glow discharge. Between individual discharges at the same glow discharge conditions and neutral pressures, the plasma formation and heating is still very uniform (values within 10 % based on photometer data). For these studies, only the initial plasma structure and magnitude was considered and the details and full investigation of plasma response at Position 1 will be explored

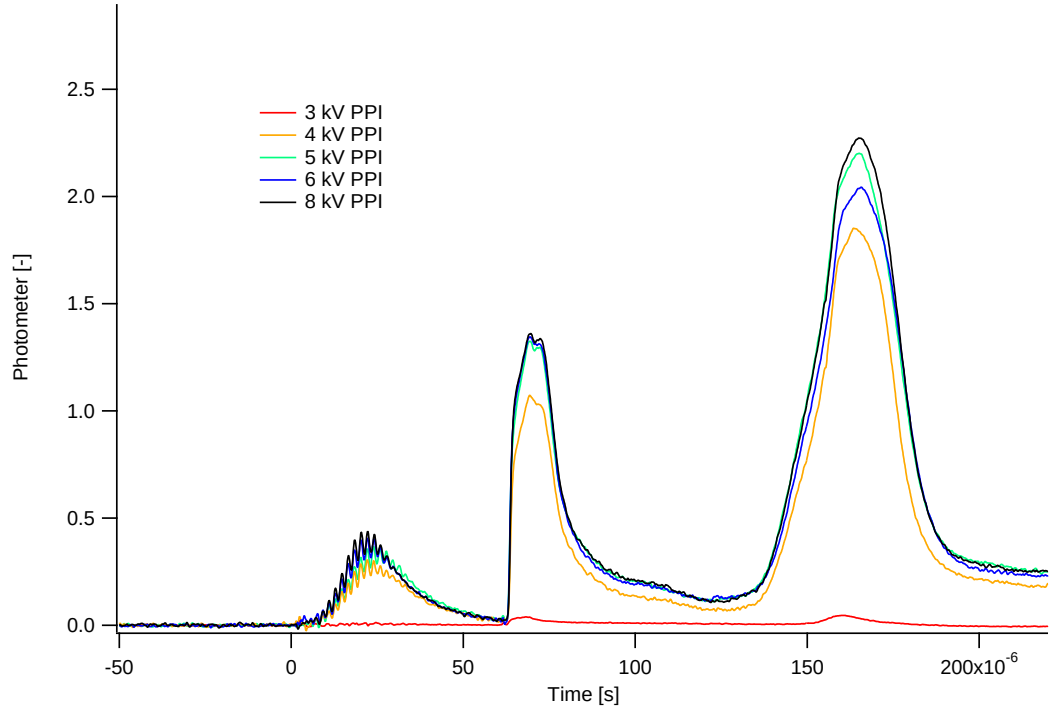

Figure 4.17: Pre-ionization photometer response for a 14-mTorr, 750-V, main bank discharge for various PPI glow discharge voltages

extensively in later Chapters.

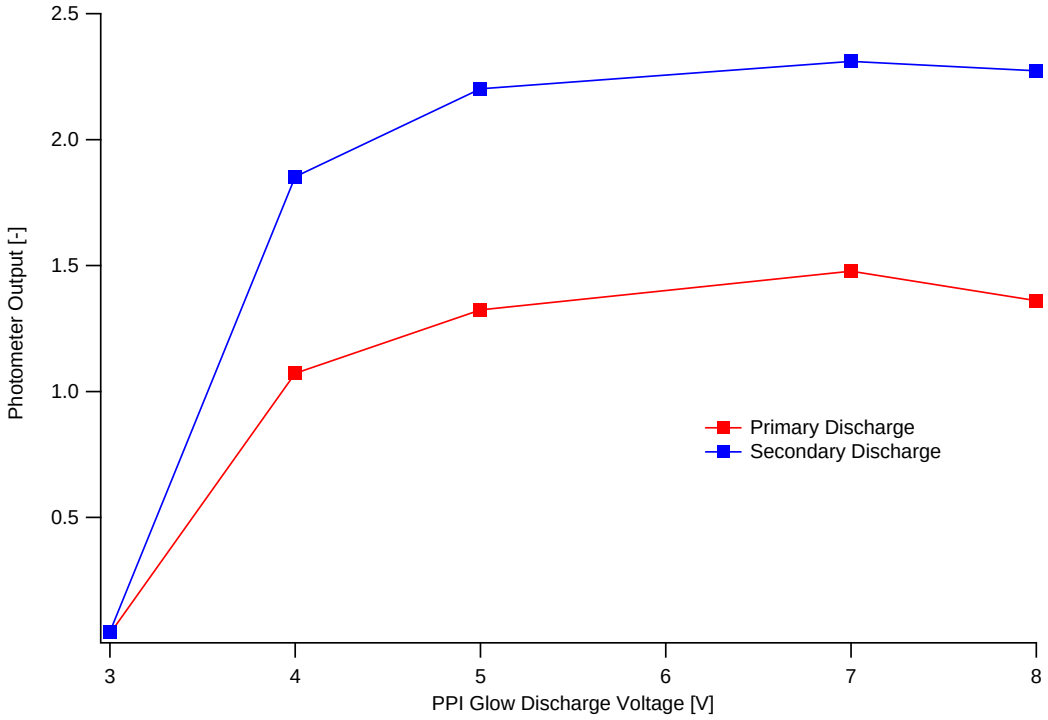

Figure 4.18: Summary of peak photometer data for various PPI glow discharge and 750-V main bank discharges

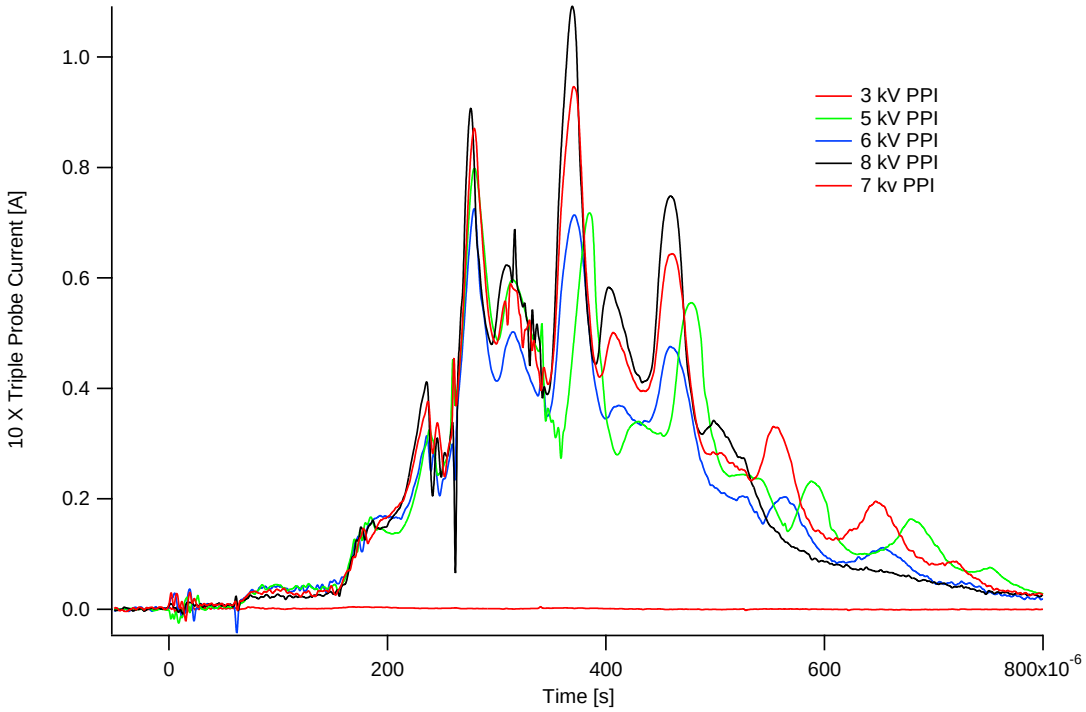

Figure 4.19: Downstream current collection data for a 14-mTorr, 750-V, main bank discharge for various PPI glow discharge voltages

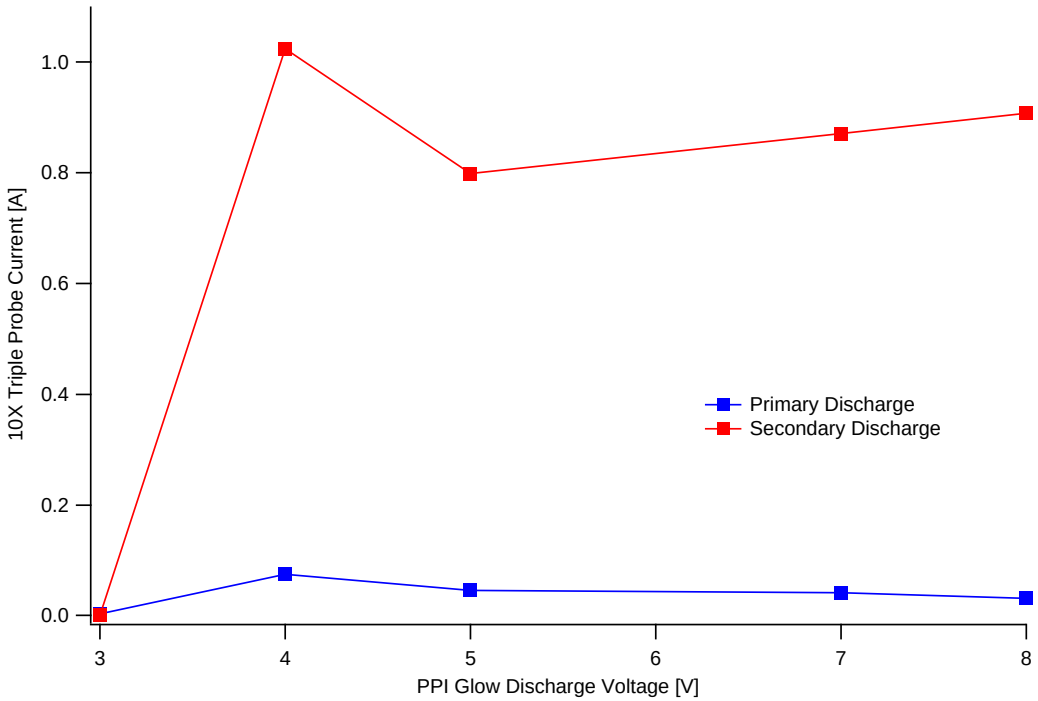

Figure 4.20: Summary of peak downstream current collection data for various PPI glow discharge and 750-V main bank discharges

4.3.2 Time Scaling Experiments

The other primary operating characteristics which must be optimized are the timing delays between the glow discharge initiation, ringing pre-ionization initiation, and the main bank initiation. While fixing a 5-kV glow pre-ionization (PPI) discharge, a 1-second glow discharge initiation time, and the main bank discharge into 14-mTorr argon and 850-V coil voltage discharge, delay time between the pre-ionization discharge and the main discharge was varied utilizing the azimuthal main coil as pre-ionization. It was expected that the optimal discharge would occur at the minimal discharge period, in that a uniform azimuthal and axial ionization plasma will be formed and decay slowly, and the maximum main bank discharge will be at the maximum pre-ionization plasma density and temperature. Additionally, pre-ionization noise must be considered and has not been factored into earlier discussions in terms of optimal discharge delay time. The 250-kHz ringing pre-ionization puts significant electromagnetic noise onto data collection lines and triggering circuits through both radiated EMI and capacitive ground coupling of the large voltage pre-ionization ringing to the low-voltage diagnostic circuits. Therefore, the maximal delay between pre-ionization and main bank discharge is desired for minimizing noise pickup from the pre-ionization discharge. Finally, further extending the delay also reduces the high-speed ringing that is transferred to the high-capacitance, but lower-voltage main bank thereby increasing the lifetime and reliability of the high-energy bank. Figures 4.21, 4.22, and 4.23 show photometer results for varying pre-ionization delay periods from 20 to 500 μs. Surprisingly, pre-ionization delay results seem to show that the optimal delay time is between 60 and 200 μs for the primary discharge and between 20 to 200 μs for the secondary discharge. The logical conclusion is that axial and azimuthal nonuniformities in surface current and initial pre-ionization using the large

azimuthal main coil as the pre-ionization coil still requires a specific delay in order to propagate a more uniform pre-ionization plasma. This does have the beneficial result of suggesting a 100 μs pre-ionization discharge, which will significantly reduce noise and overvoltage concerns in the main discharge. Figures 4.24 and 4.25 show collected triple probe current at Position 1 for various pre-ionization delay periods. Unfortunately, these data are not particularly useful as the complicated structures associated with current collection at Position 1 makes it difficult to pick out clear metrics to use in qualitatively weighing efficacy of the various delay parameters. However, general trends can clearly be seen in that the delay periods greater than 100 μs have significant decrease in resultant plasma density and by analyzing some of the major peak values it can be shown that again a 60 to 100 μs discharge delay is optimal for bulk plasma creation. The individual structures will again be further explored in later Chapters, specifically with internal probe data. One very useful function that can be garnered from this collected current data is that once a threshold value for pre-ionization energy, and glow discharge energy, is reached significant plasma compression and heating will occur for even 500-μs-long discharge periods, and that once a uniform ionization plasma has been created a robust solution of identical structures of collected current are seen for all delay periods (while at different magnitudes).

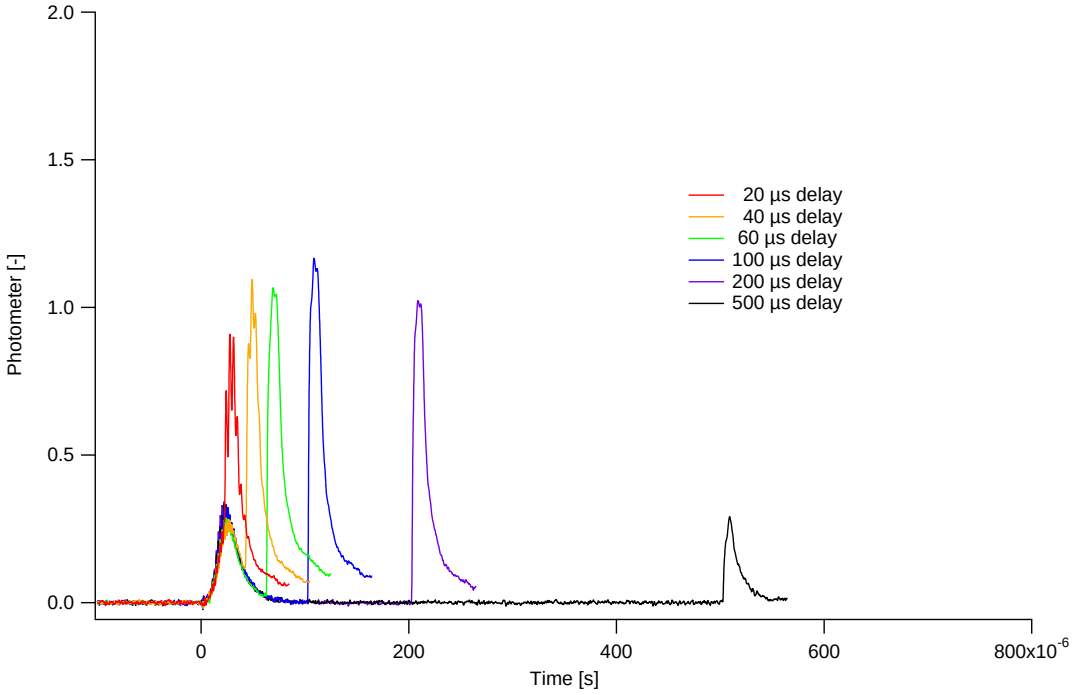

Figure 4.21: Photometer output for multiple 850-V main bank discharges exploring characteristics of variable discharge delays, isolating the primary discharge at 14 mTorr of argon

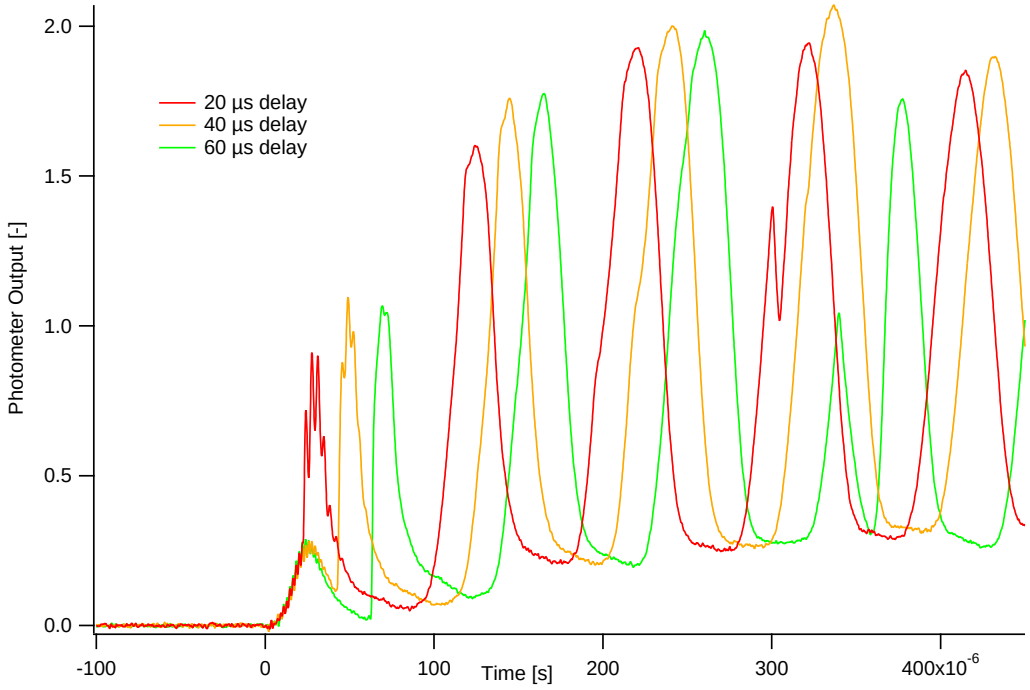

Figure 4.22: Photometer output for multiple 850-V main bank discharges exploring characteristics of variable discharge delays at 14 mTorr of argon

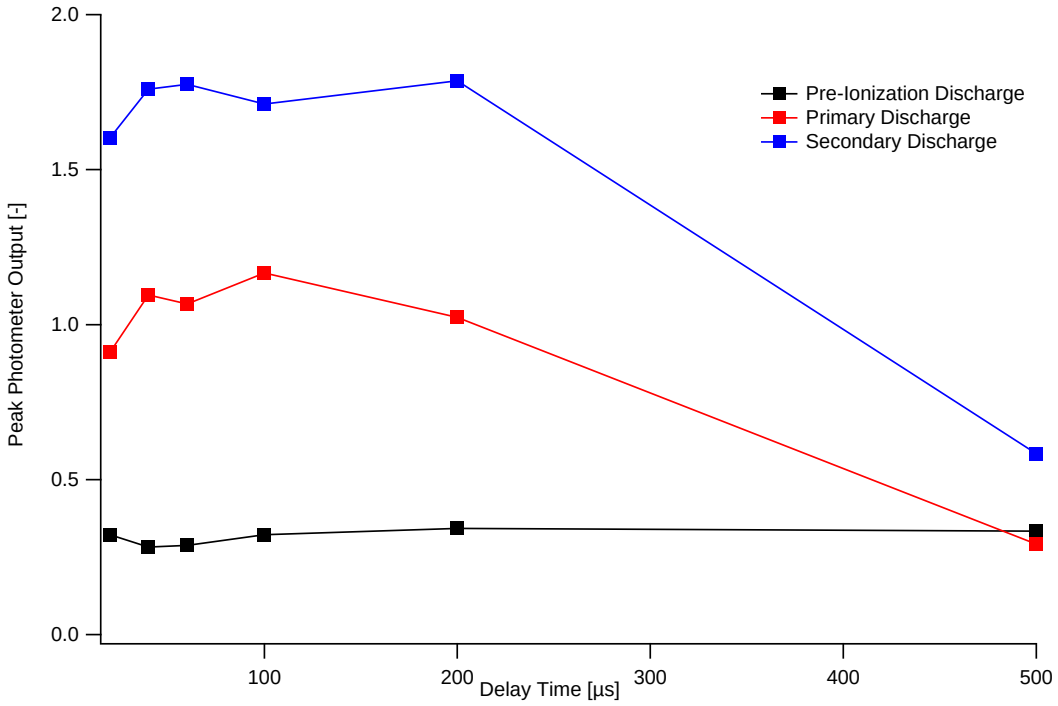

Figure 4.23: Summary of peak photometer discharge results for various delay periods

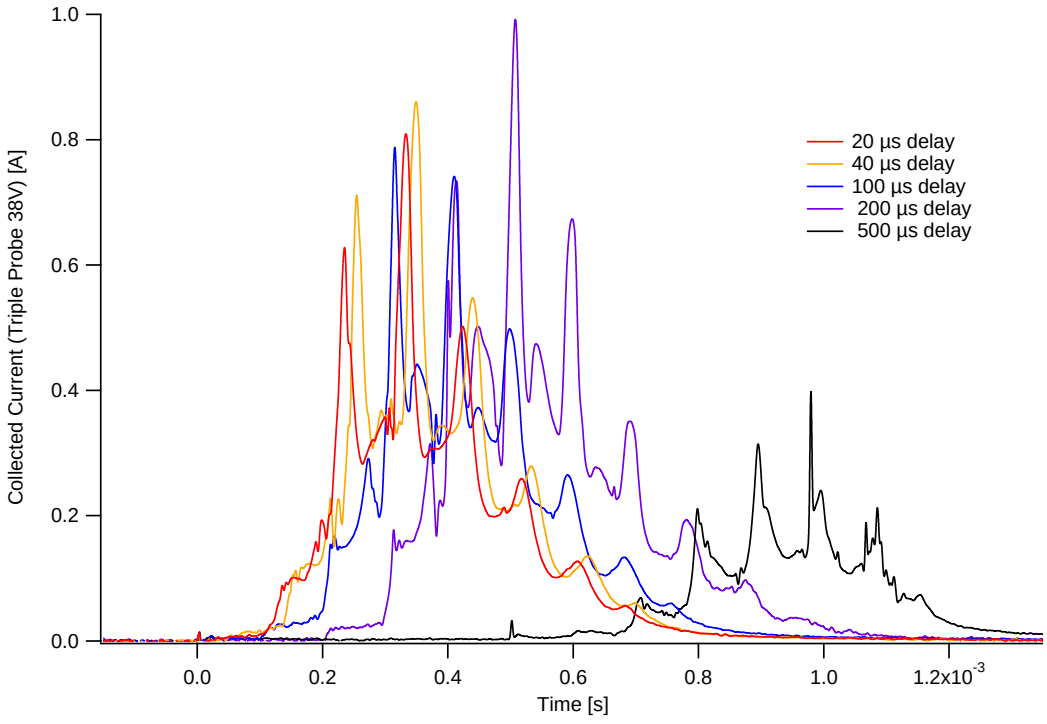

Figure 4.24: Downstream triple probe collected current for multiple 850-V main bank discharges exploring characteristics of variable discharge delays

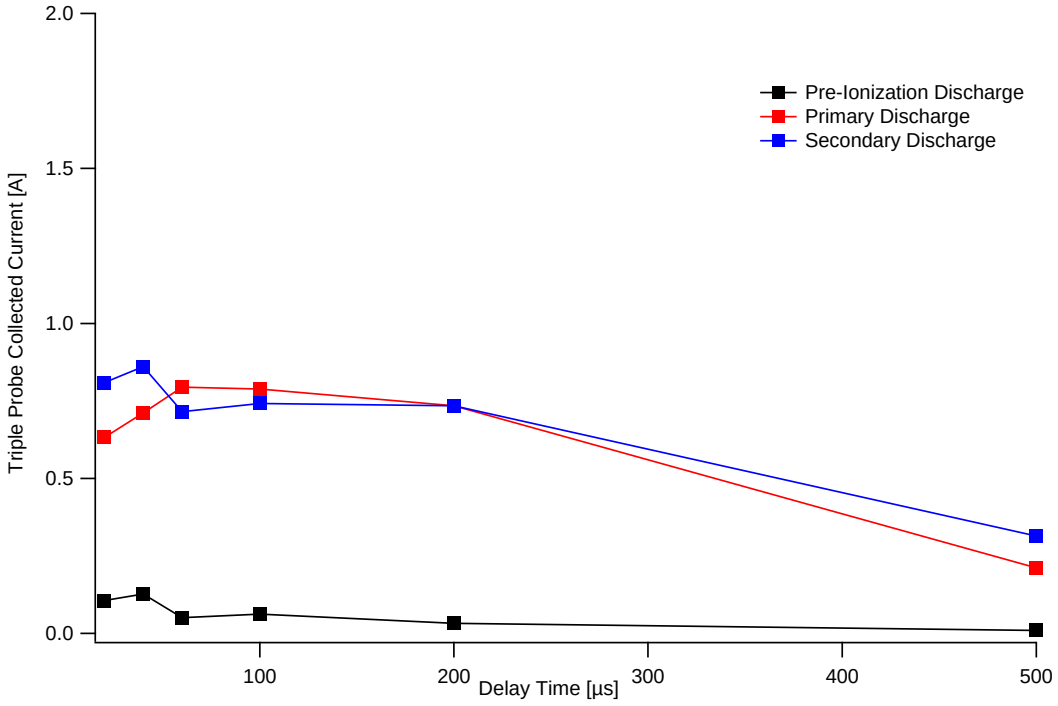

Figure 4.25: Summary of peak triple probe current discharge results for various delay periods

4.4 Pre-Ionization Geometry 3

Figure 4.26 shows a mirror pre-ionization geometry. This coil geometry will decouple the pre-ionization circuitry from the main discharge circuitry as well as create an axially uniform initial plasma content. While this configuration was not tested in this experiment, it remains a high priority for future work. This configuration has two circuitry options; the first and simplest is to have coils in parallel at the same potential, while the second and likely more successful configuration has the coils in series, which sets up both an axial as well as azimuthal voltage differentials between the coils generating even more evenly axially distributed plasma. Additionally, the increased inductance of a two-turn and more distributed coil will increase the coil inductance and therefore decrease path losses in the pre-ionization system.

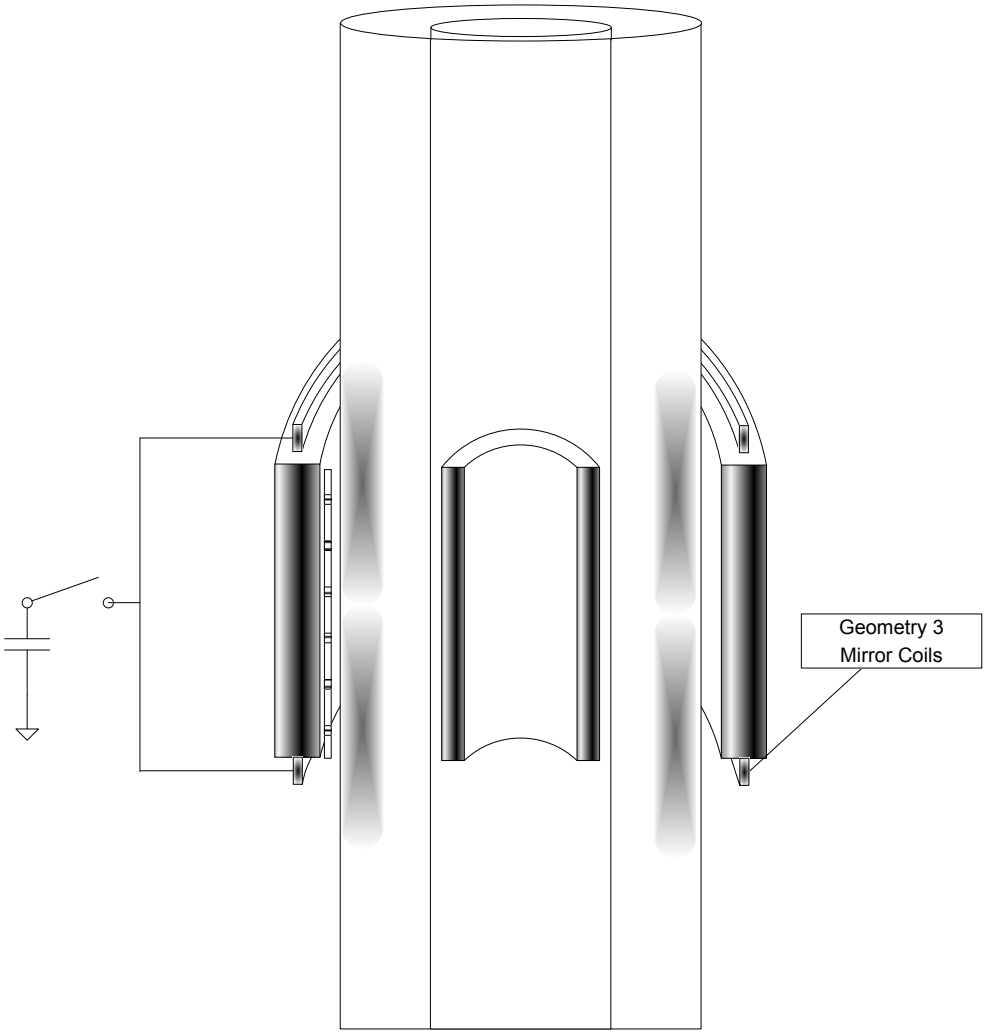

Figure 4.26: Pre-ionization coil schematic for Geometry 3

4.5 Pre-Ionization Conclusions

In summary, two geometries have been investigated in Sections 4.2 and 4.3 and a third proposed in determining an optimal pre-ionization scheme for an annular field reversed configuration discharge. These pre-ionization geometries have been investigated and optimized to determine timing, and energy level requirements for optimized main bank discharge and subsequent plasma compression and heating. For Geometry 1 (used in the 450- and 250-μs discharge cases) a peak plasma density of 2×10^{18} m^{-3} and peak plasma temperature of 50 eV were found for the 1-kV 250-kHz ringing pre-ionization discharge. Additionally, an optimal delay time of 60 μs was used for the data in the Chapters 5 and 6. Following this implementation it was found that the Geometry 1 pre-ionization scheme yielded poor pre-ionization uniformity, and therefore Geometry 2 was selected in order to maximize azimuthal and axial pre-ionization plasma density uniformity. Geometry 2 was investigated in order to optimize the pre-ionization glow discharge energy (Section 4.3.1) and the timing requirements for a pre-ionization discharge system (Section 4.3.2) for various gases, background pressures, and pre-ionization energies. It was found that a minimum glow discharge voltage of 5 kV (approximately 0.5-10 Watts) was required to initiate primary bulk plasma 'turn-on', and a pre-ionization discharge delay of 100 μs yielded optimal main bank plasma creation, compression, and heating. These data configurations are utilized for the majority of testing on the XOCOT discharge experiment and are further detailed in Chapter 7. One final note on pre-ionization discharge, the voltages described here are clearly a function of background pressure and main coil geometry, however, they are also a function of PPI pre-ionization glow discharge geometry. A standard Townsend discharge determines the optimal voltage as a function of pressure and distance between the positive DC glow discharge

electrode and the negative (in this case the ground plane) electrode. An optimized system would seek to minimize the required discharge voltage while maintaining a similar glow discharge energy by optimizing DC glow discharge geometry.

CHAPTER 5

450-μs Discharge Experiments

The first full-scale testing on the XOCOT discharge experiment was utilizing a slow, 450-μs-period main bank discharge. Chapter 5 describes the typical discharge parameters and results for a 4-capacitor bank used in these tests, See Figure 2.4. Tests were performed for discharge voltage and energies of 300 V to 750 V and 180 J to 1.1 kJ. Sections 2.2 and 5.1 outline the operational hardware and typical discharge process. The data investigation continues with analysis using the magnetic field probe to explore the diamagnetic current's shielding effects of the main discharge magnetic field. Section 5.3 describes the utilization of the double Langmuir probe to calibrate the triple Langmuir probe as well as plasma characteristics near the annular discharge coil for a variety of discharge voltages and neutral gas pressures. Finally, an optical study of the radiation emission (400–1000 nm) is described in order to non-intrusively explore the plasma production for the entire operating envelope.

5.1 Typical 450-μs Discharge Parameters

Figures 5.1, 5.2, and 5.3 show data collected for a typical 450-μs discharge (in the detailed data, discharge voltage was 500 V). Shown in Figure 5.1, the DC seed ionization is initiated 1 second before the main discharge. The pre-ionization discharge is triggered, and then 10 μs later (after the majority of the pre-ionization electrical

noise has dissipated) the main bank is discharged. The pre-ionization discharge has a period of 4 μs, while the main bank has a period of 450 μs. Shown are the voltage and current of the inductive coil for a vacuum discharge (with a plasma there are differences in the induced plasma resistance and therefore voltage). It must be noted that actual bank voltages are higher than the coil voltages due to inductive losses in the switches and conductive paths. This is a minor effect for the main bank, but a major effect for the pre-ionization bank, where voltages on the capacitors may be 3-4 times as large as the voltages on the coil.

The three main diagnostics (of the many diagnostics in Figure 2.13) used in this analysis are an optical high-speed mega-pixel DICAM, an array of magnetic field probes, and an internal triple probe located at the edge of the main discharge coil (in order to minimize magnetic field error effects). With coil voltages greater than 200 V and bank discharge periods less than 500 μs, very repeatable results have been achieved, showing multiple magnetized plasma formation and collapse with a single pre-ionization and main bank switching. Figure 5.2 shows plasma density measured at the coil edge and corresponding photometer results for a 500-V, 14-mTorr discharge. Clearly, six plasma intensity increases and density pulses are evident in these charts, though they appear to vary widely in terms of magnitude and instantaneous profiles. These multiple pulse trends are typical and the first two peaks are very repeatable as shown later in Figure 5.14. At this stage it should be noted that the first plasma pulse is quite weak (both in terms of brightness and effluxed plasma), that the second pulse is much brighter than its corresponding effluxed density, and that similar structures exist in both density and photometer results between later pulses. These details will be explored more in later Sections. The pre-ionization discharge is visible in the photometer results of Figure 5.2 as the first brightness

peak during the 0-20 μs period at the beginning of the discharge.

Figure 5.3 continues with the optical exploration of the evolution of these plasma pulses by detailing the formation (and collapse) of a pulse from 200 to 300 μs. Each image is top-down with the same DICAM sensitivity settings (2.5 [-]) and a 5-μs integration/shutter time. Similar analyses in past FRC experiments [64], [44] have shown very similar results with four distinct formation/compression regimes present [30], as shown in Figure 5.3.

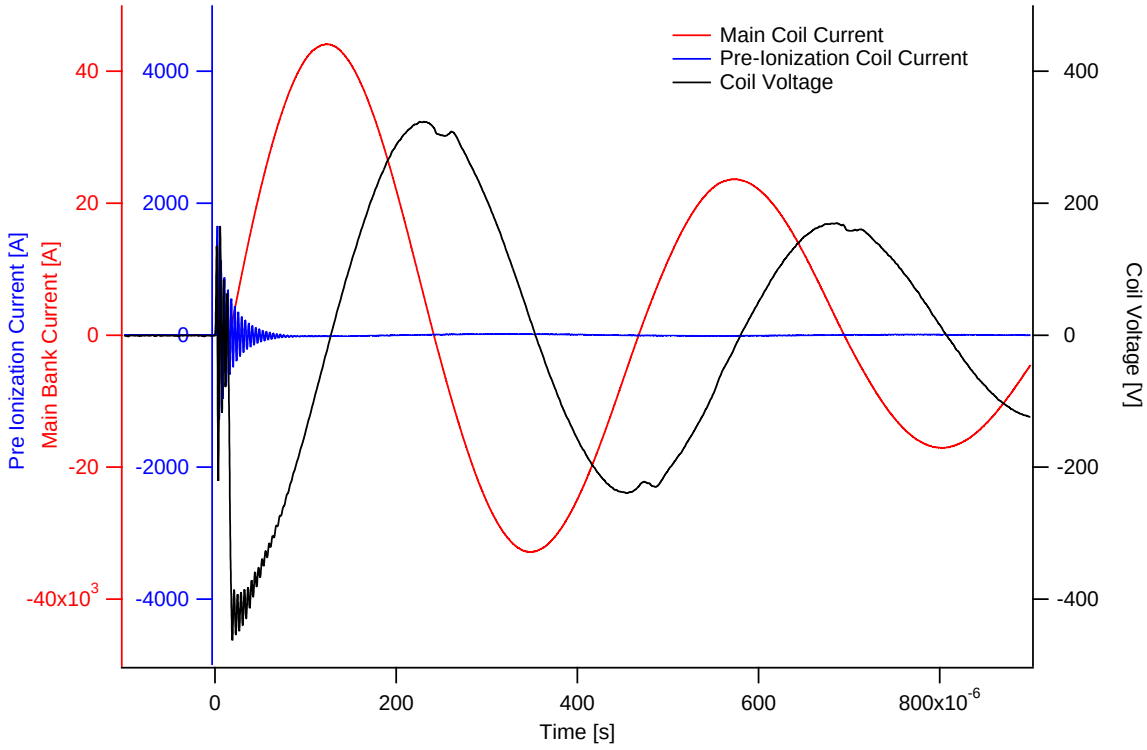

Figure 5.1: A 500-V discharge showing total discharge current (both coils), pre-ionization current, and instantaneous coil voltage for a 450-μs discharge.

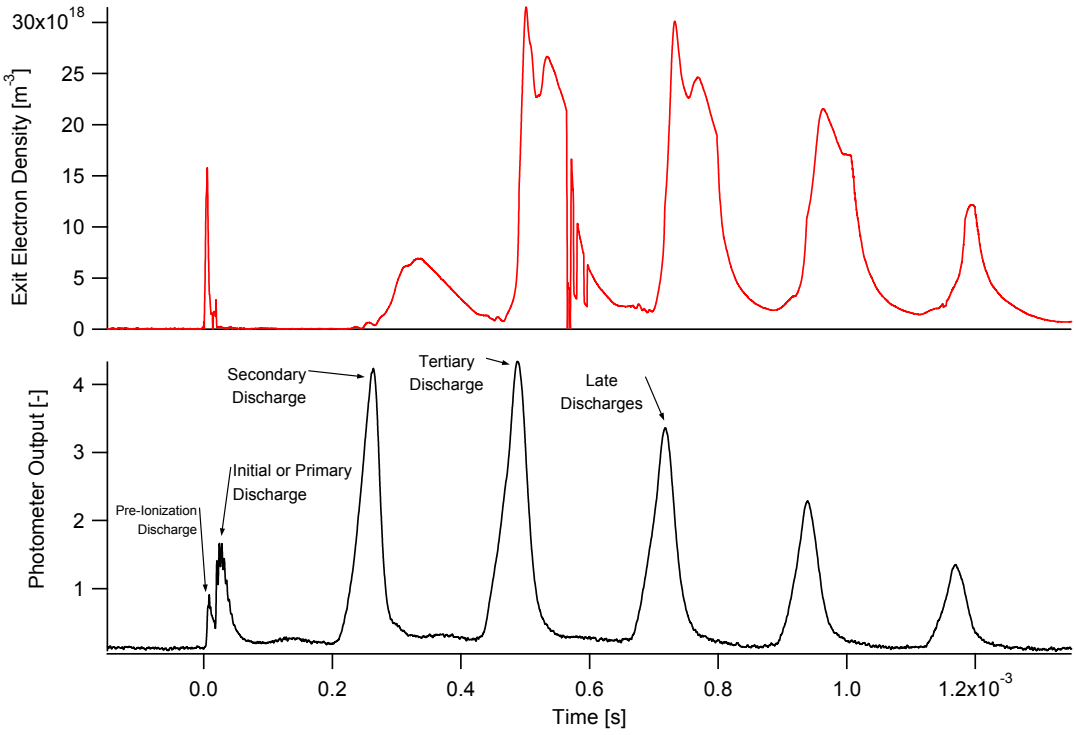

Figure 5.2: Downstream density and photometer results for a 500-V discharge at 14 mTorr.

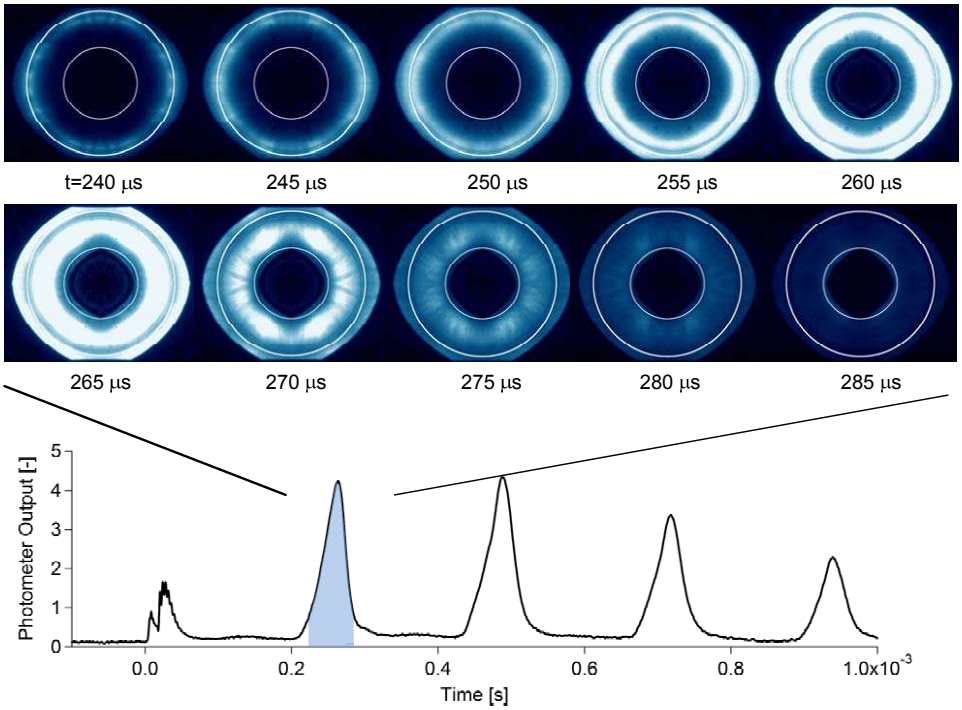

Time	Mode
250-255 μs	Initial formation and reversal
260-265 μs	Radial compression and heating
270-275 μs	Radial compression/Rotational Instability
280-285 μs	Instability leading to radial expansion

Figure 5.3: DICAM photos for a 450-μs, 500-V discharge progression showing plasma evolution

5.2 450-μs Magnetic Field Results

Figures 5.4 and 5.5 show preliminary results from the array of magnetic field probes between the discharge coil and the quartz chamber wall. Figure 5.4 shows the actual B-dot probe results (scaled to Gauss/sec) comparing a vacuum discharge (with no plasma or brightness changes) and a 20-mTorr discharge case that shows the magnitude of magnetic field change due to the magnetized plasma. This change is primarily due to the induced plasma current as the plasma toroid responds to the applied discharge current (and magnetic field) and shows clearly that high-density magnetized plasmas are being formed inside the discharge region. Figure 5.5 shows the digitally-integrated results showing the change of magnetic field as compared to the applied magnetic field resulting from the discharge current. In Figures 5.4 and 5.5 data were taken at position 'AX1' that is 8 cm below the top of the main discharge coil (and pre-ionization discharge coil).

Figures 5.4-5.5 show magnetic field deficits measured (due to the magnetized plasma) for a single discharge. Figure 5.12 details the peak change in magnetic deficit, which can be looked at as the peak magnetic pressure, confinement, or compression of the magnetized plasma along the coil wall for various background fill pressures. From this, it appears that for the earlier plasma pulses the asymmetry in the heating and compression is rather large ($> 50\%$ change in B-field) in the axial direction, with the most magnetized plasma near the pre-ionization discharge coil. For subsequent discharges (Figure 5.7) this is no longer the case, even though average magnetic field is also reduced. Finally, the trend to higher fill pressures continues, with significantly more magnetization, for longer periods at the same discharge energy at higher neutral densities.

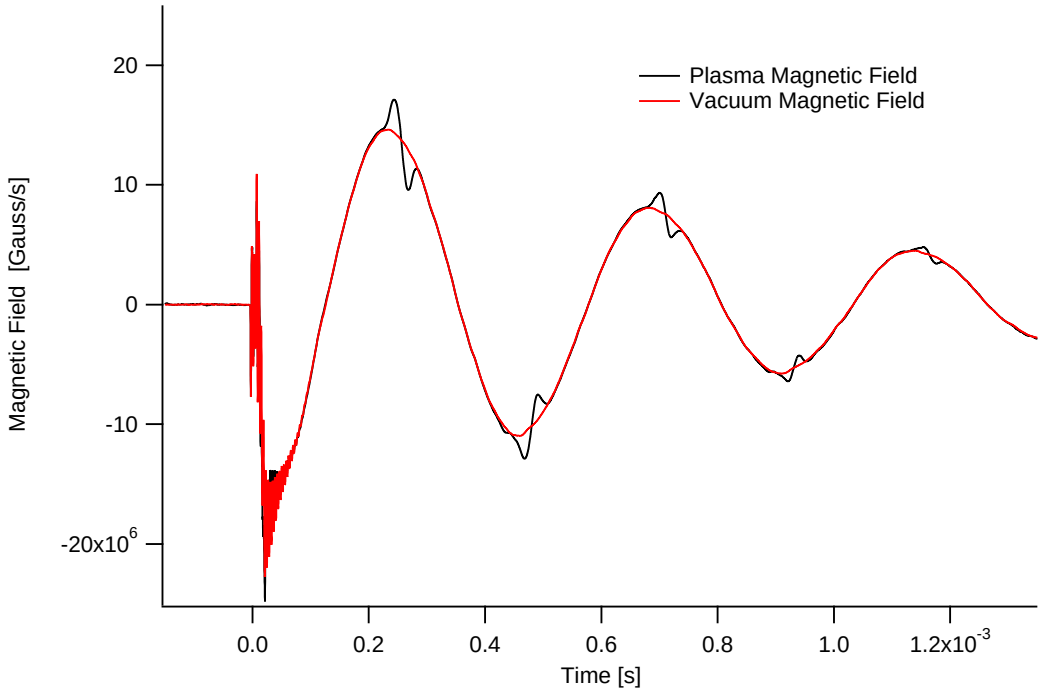

Figure 5.4: Magnetic field probe data for a vacuum and 20-mTorr discharge case with a coil voltage of 500 V

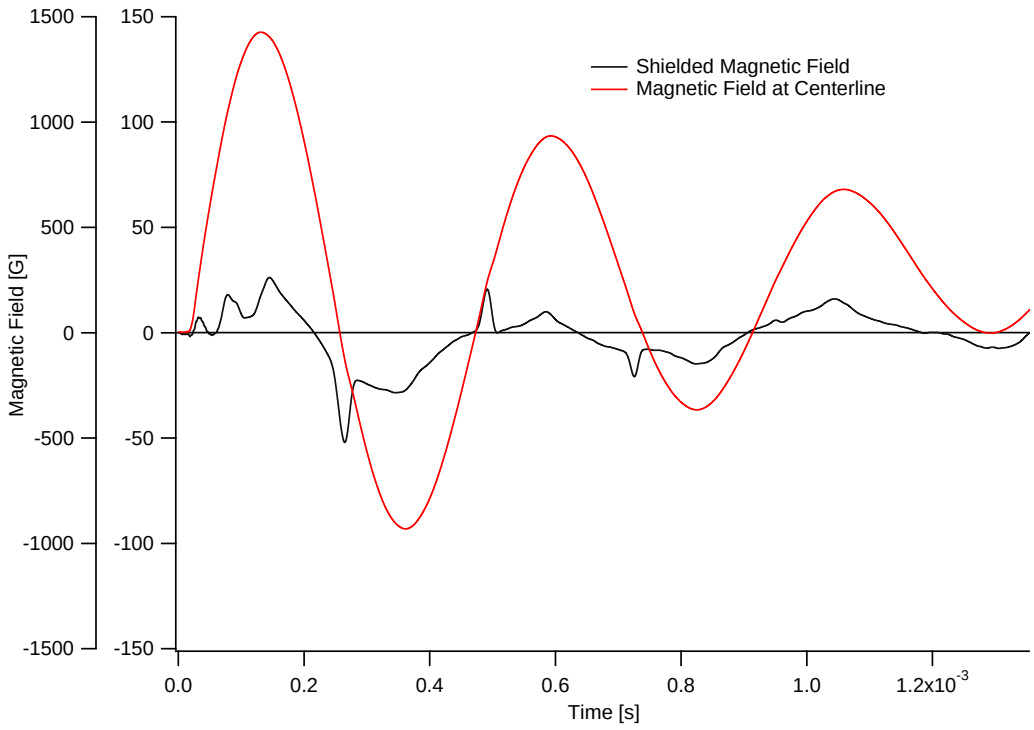

Figure 5.5: Magnetic field deficit for a 500-V, 14-mTorr discharge

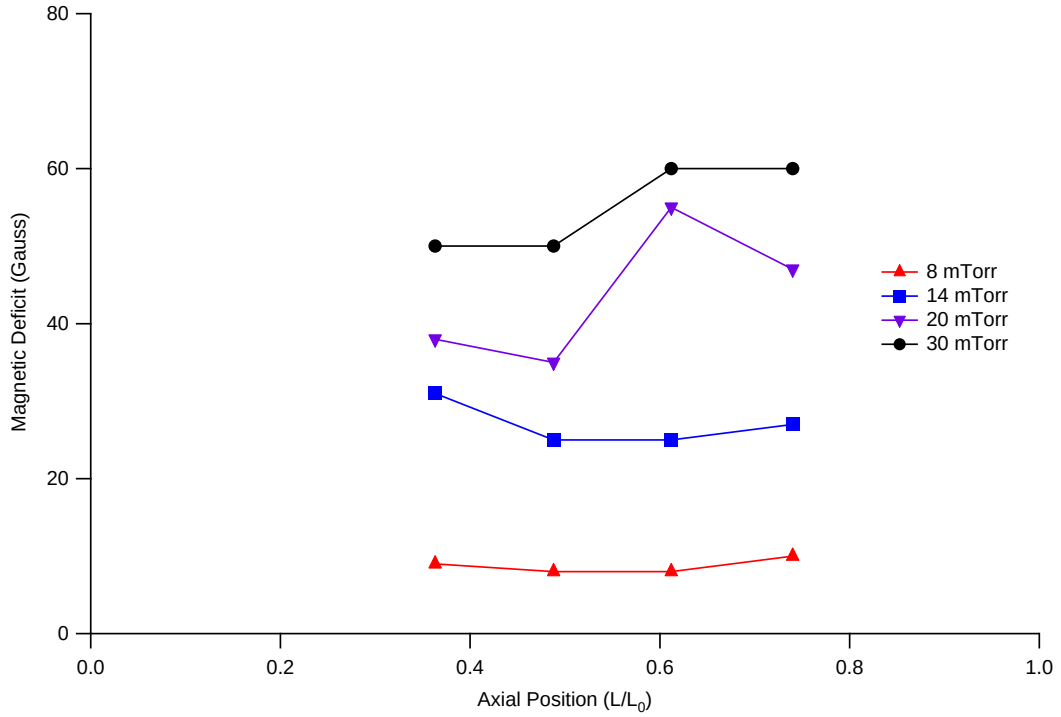

Figure 5.6: Peak magnetic field data for axial locations and various fill pressures. Discharge was 500 V, from 400–600 μs

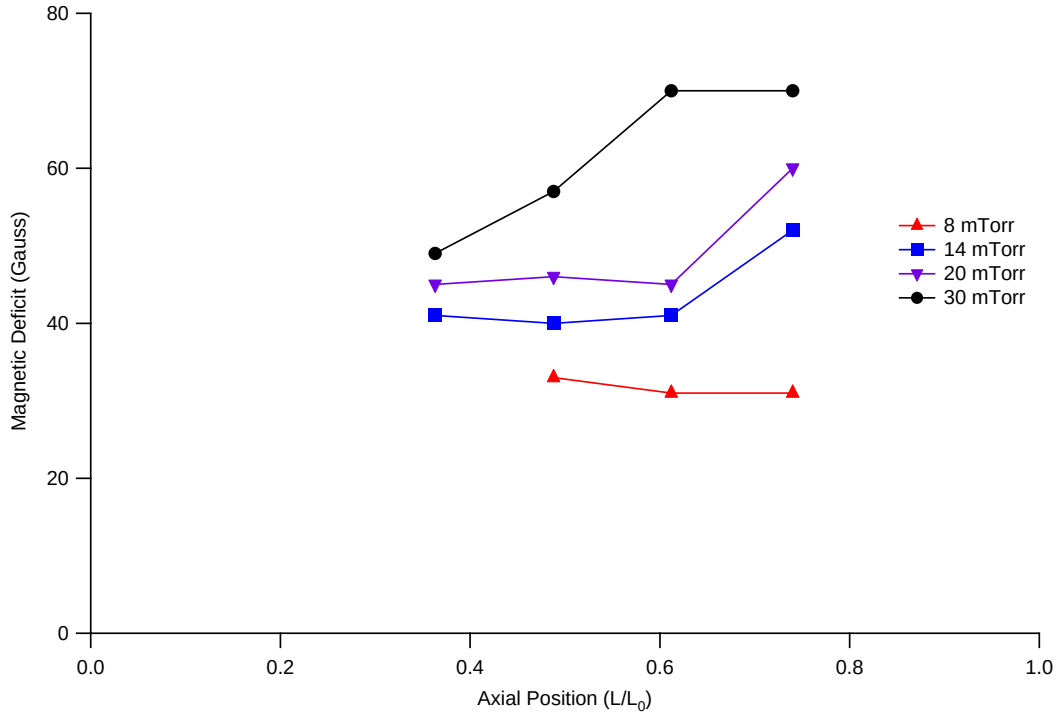

Figure 5.7: Peak magnetic field data for axial locations and various fill pressures. Discharge was 500 V, from 200–400 μs

5.3 450-μs Internal Plasma Properties

5.3.1 Internal Plasma Double Probe Testing and Calibration for the 450-μs Discharge

Plasma density and temperature were measured 4 cm below the bottom edge of the coil (opposite the primary pre-ionization coil). As discussed above this triple probe consists of a biased double probe and a floating plasma potential probe. Multiple discharges were performed and the probe voltage swept in order to attempt to generate a composite set of double probe curves at all points in the discharge. The driving motivation for this process is to calculate electron temperature, which is elucidated in the slope of the linear region of Equation 2.30. Plasma density is primarily dependent on collected current, gas properties, and probe area, and tends to be low in relative error (between data sets for a given electrical setup and probe design). Clearly, this analysis requires the assumption that the discharges are highly repeatable and that the probes satisfy both double- and triple-probe requirements at all points in the discharge. These assumptions only appear to be valid during the first two discharge plasma pulses, and at the higher density conditions, therefore the double probe curves and plasma density and temperature solutions were only generated at these conditions. Figure 5.8 shows the multiple discharge I-V sweeps for a variety of discharge voltages. Figure 5.9 shows the triple probe calculated electron temperature (at a bias voltage of 36 V) compared to several double probe I-V curve calculations of electron temperature. The error bars shown in Figure 5.9 are the errors associated with the curve fit to the double probe data and are representative of error in the data of an individual voltage sweep, not overall relative error that is common to both double and triple Langmuir probes. The results are surprisingly good for the first 500 μs and at the peaks of later data points, with the average electron temperature being very similar; this trend continues across the entire range

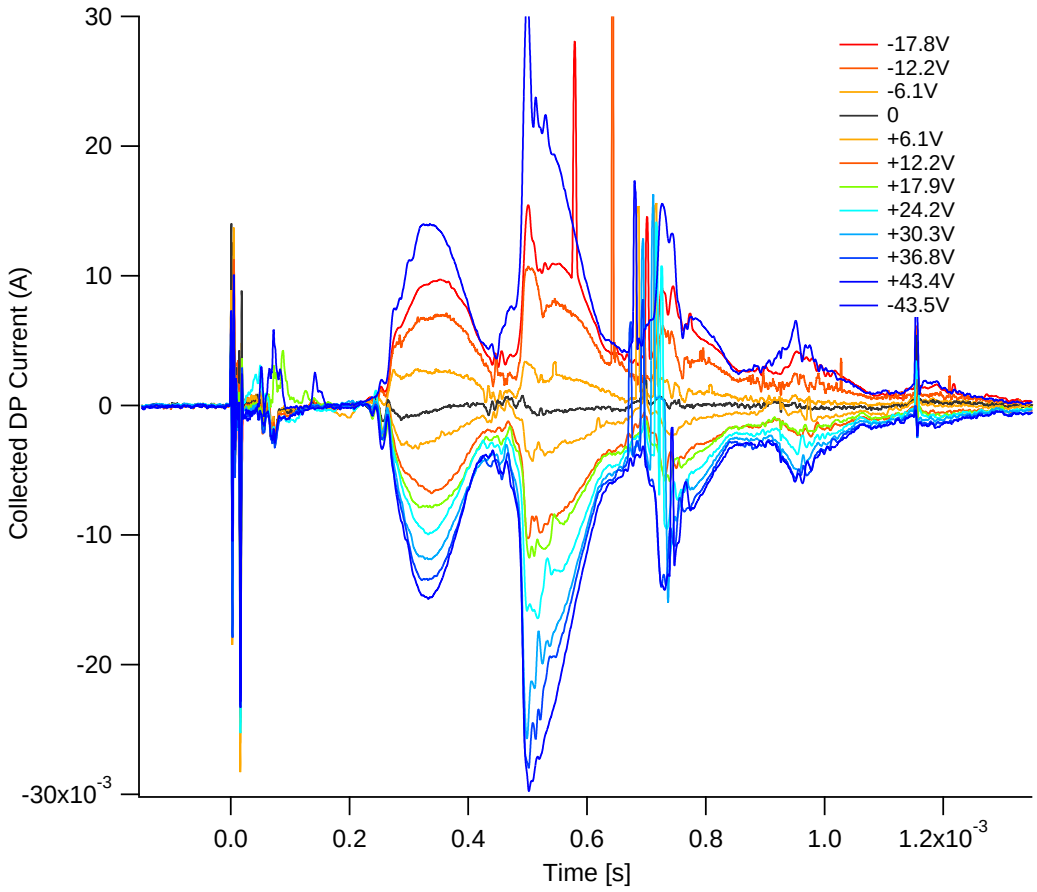

Figure 5.8: Collected current for a double probe for various bias voltages. All discharges performed at 500 V and 14 mTorr

of data taken. There appears to be some lack of symmetry in the double probe sweeps (as shown by the $+/-$ 43 V cases) that is typically due to asymmetries in the plasma on the scale of the double probe electrode separation distance. The triple/double probe result data were then collected at many operating conditions from 175 to 1000 V and 8 to 30 mTorr; Figures 5.2-5.11 show the results of triple probe and photometer results for these tests.

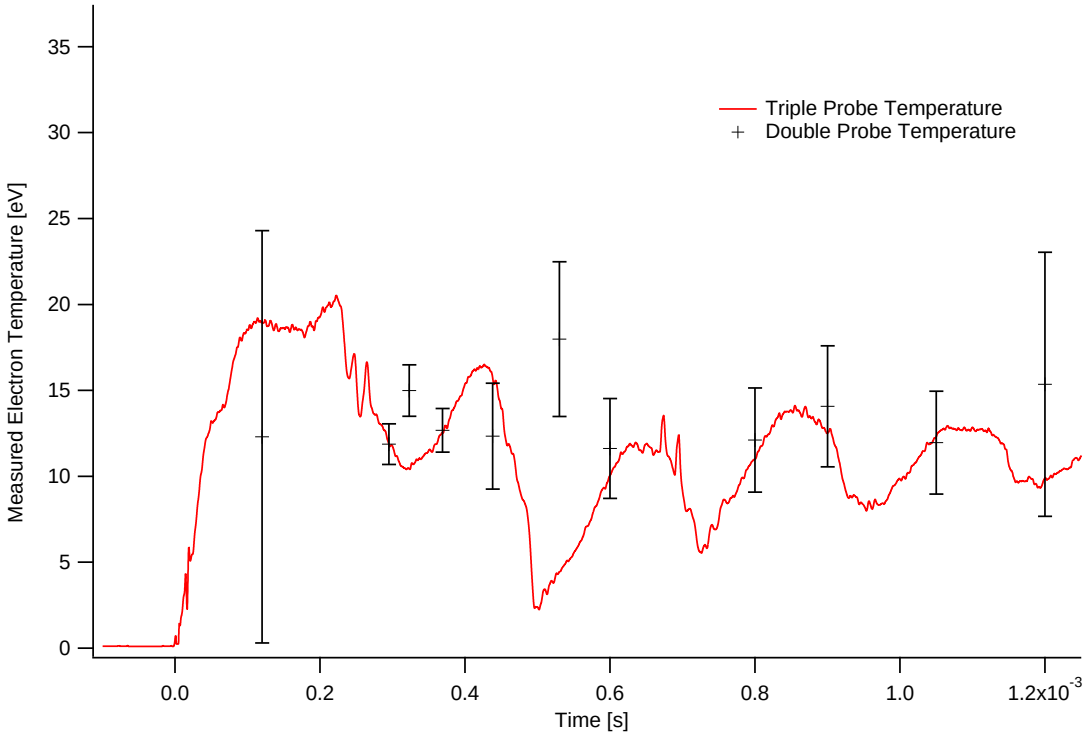

Figure 5.9: Comparison of triple probe T_e to a congregate double probe temperature measurement at the highest confidence points

5.3.2 Internal Plasma Triple Probe Details for the 450-μs Discharge

Figure 5.2 details multiple background neutral densities and has clear trends; as pressure increases the density of each discharge increases as well as broadens. At the highest pressures the second and third major peaks have similar densities. Not shown here, at higher fill pressures, there exist more secondary peaks; 2 defined peaks at 8 mTorr to as many as 8 major plasma peaks at 30 mTorr fill pressure. For Figures 5.10 and 5.11, as expected, with increasing input energy (coil voltage and discharge current) the plasma densities increase, and the intermediate plasma densities stay higher. It also appears that for successively higher powers the temporal peak in density (or when the plasma reaches the triple probe) is delayed, with the exception of the lower pressure, 700-V cases. Why those cases appear to deviate from the trend of the rest of the discharges is still in question, for both the magnitude of the density peaks as well as the timing of the plasma reaching the triple probe. The two most important characteristics in Figures 5.2–5.11 are that the first peak, and expected maximum density and compression, is still quite weak and does not last for very long, and the second peak is much smaller than the subsequent discharges. This is not shown in the photometer results, which indicate that the second peak is much brighter, and for longer times, than any of the rest of the discharge pulses. This implies that the highest plasma content pulse is forming and compressing but not evacuating the chamber below the coil. Downstream data are necessary to confirm that indeed, the first major pulse is effluxing in the downstream axial direction. As shown in detail in Chapter 7, it appears that the second discharge is also much more axially compressed and therefore the photometer is somewhat shielded from the full bulk plasma.

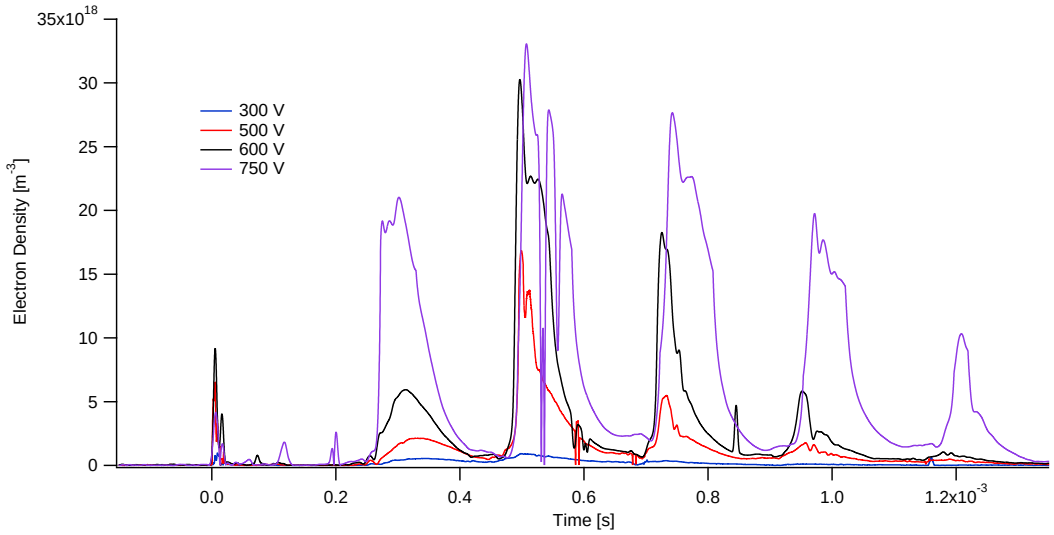

Figure 5.10: Downstream density for multiple discharge energies at 14 mTorr

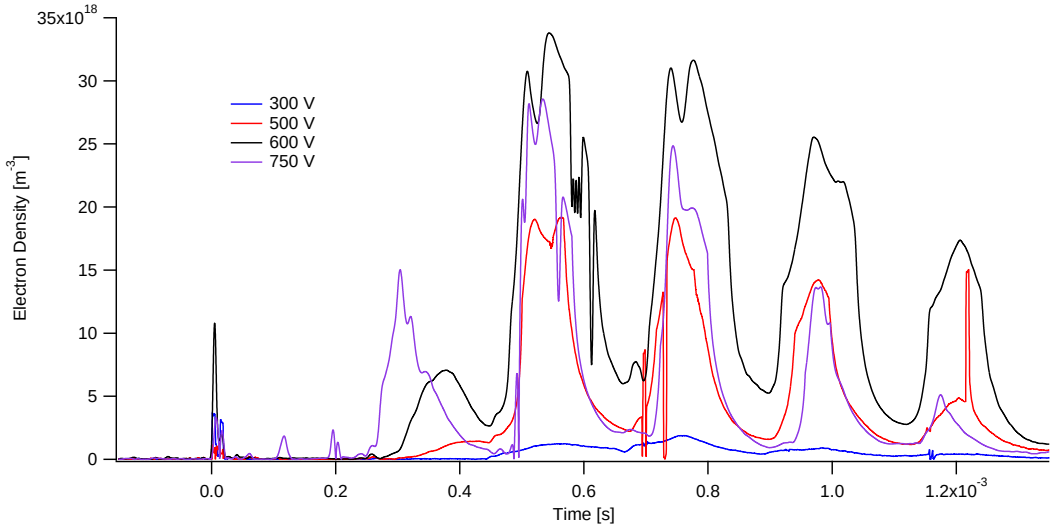

Figure 5.11: Downstream density for multiple discharge energies at 30 mTorr

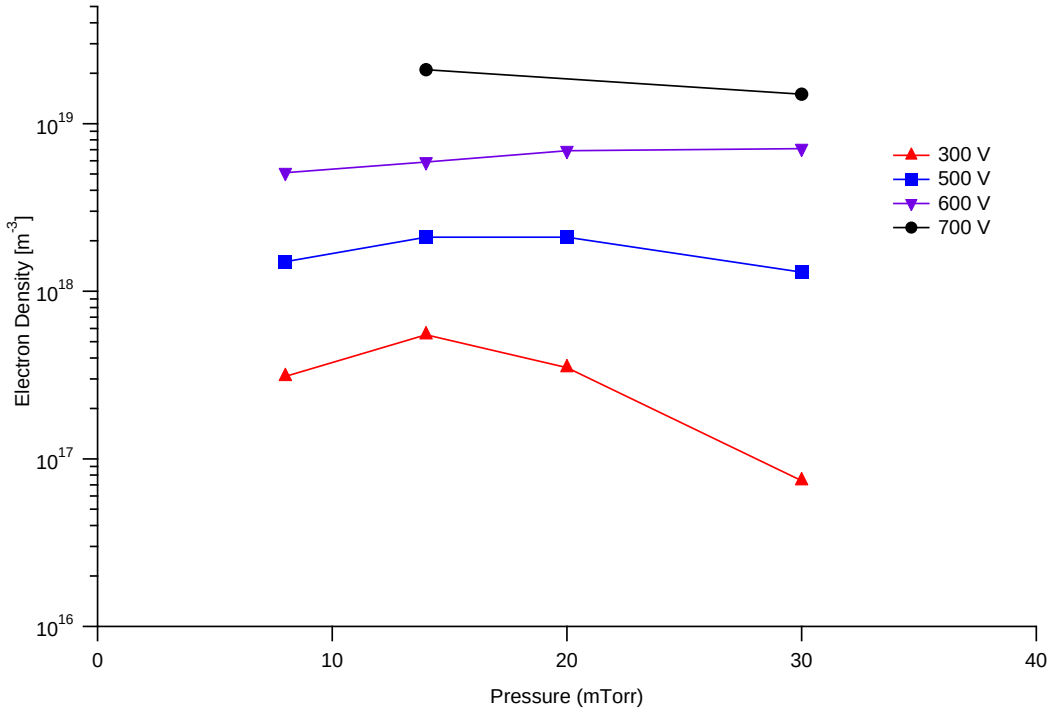

Figure 5.12: Peak Electron densities measured as a function of background pressure for multiple discharge voltages. From 200–400 μs

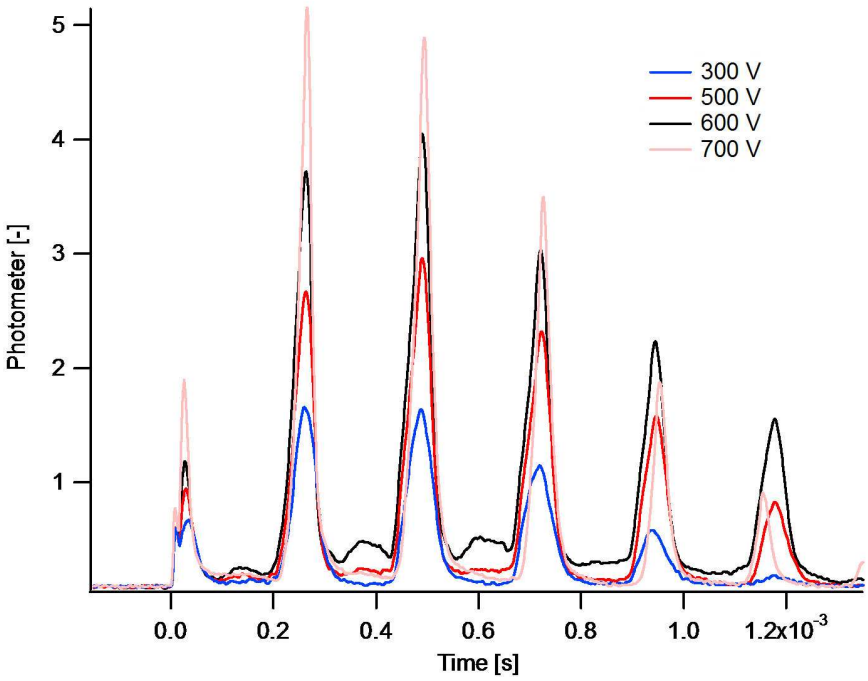

Figure 5.13: Discharge photometer optical emission results for multiple discharge voltages at 14 mTorr

5.4 Optical Details

Indeed, Figures 5.13 and 5.14 show well defined discharge pulses as evidenced by photometer data (including the first two). Also, expected trends are seen seen; with increasing power and/or the optimal fill pressure, the discharge intensity (and the internal plasma density) increases as well as extending for many more pulses. Also, at the higher pressure cases there is more continuous plasma in the annular region.

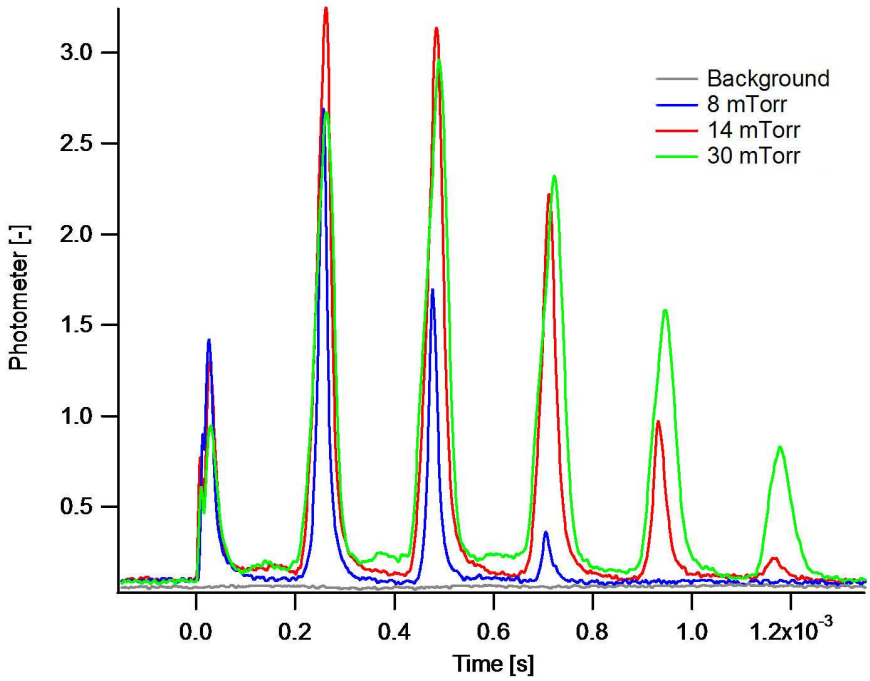

Figure 5.14: Discharge photometer optical emission results for multiple neutral fill pressures at a coil voltage of 500 V

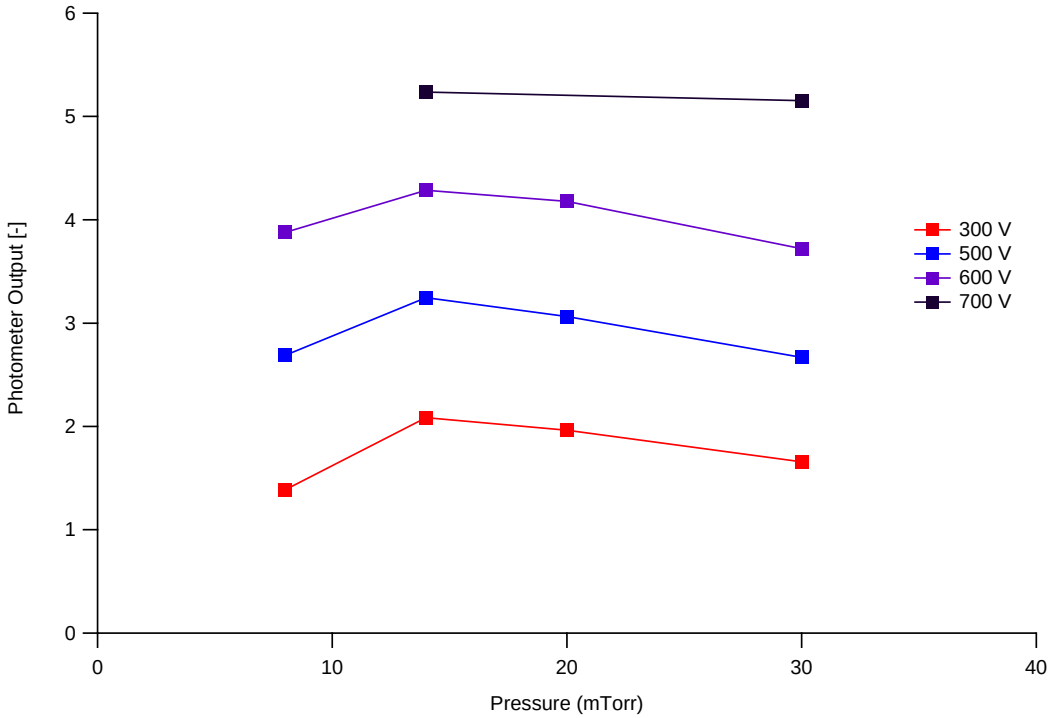

Figure 5.15: Peak photometer results as a function of background pressure for multiple discharge voltages. From 200–400 μs

5.5 450-μs Discharge Conclusions

The initial testing for the XOCOT discharge experiment is shown in Chapter 5. Main bank discharges have successfully yielded high-density magnetized plasmas from 1.5–3.5 $\times$ 10^{19} m^{-3} for 14 and 20 mTorr. A high-speed double probe was designed and tested for multiple bias voltages at a 500-V discharge voltage. This testing enabled the creation of double probe density and temperature measurements of the argon plasma at Position 0 (outside of the main discharge) as well as the calibration and determination of appropriate bias voltage of a high-speed floating-mode triple probe. It has been discovered that even with the successful creation of magnetized plasma, the pre-ionization stage is the most critical for FRC formation. A very weak plasma believed to be entirely an inductive, $<$ 10 % ionization discharge was created for the initial current applied to the annular discharge coils. However, the initial reversal at 225 μs did successfully create a high density, 100 % ionized plasma discharge that translated out of the discharge region and across the triple probe electrodes. Those densities reached 4×10^{17} to 2×10^{19} m^{-3} for 300- and 700-V coil voltages, respectively. It was found that in the backfilled configuration, each subsequent peak dI/dt coil current successfully created magnetized plasma pulses. Comparison of the wide-angle photometer data and the collected external plasma data suggests that the secondary and tertiary discharges (at 200 and 450 μs) may have significantly higher densities and temperature than those measured externally as the peak optical emission happens much sooner in the discharge process than the peak plasma density that leaks out of the compression coil. Finally, magnetic field data suggests that there is a significant axial non-uniformity in plasma creation which is addressed in Chapters 6 and 7.

CHAPTER 6

250-μs Discharge Experiments

Similarly, experiments were performed for a shorter, higher dI/dt, discharge with a period of 250 μs to investigate the effect of higher rise-time on the discharge plasma. A similar analysis to Chapter 5 was performed in Chapter 6. Sections 2.2 and 6.1 outline the discharge and circuit parameters discussed. Figures 6.1 and 6.2 show the typical discharge pattern, with an extended pre-ionization diffusion time that is discussed in Section 4.2.1 (the time between the pre-ionization pulse and the main discharge). Optical measurements were the primary diagnostics used for these tests, Section 6.2 shows high resolution photometer data for multiple plasma discharges contained within each main energy pulse, as well as the inter-discharge plasma. Subsequently, raw B-dot and magnetic field profiles are discussed and the non-uniformities of the pre-ionization systems are elucidated. Finally, Section 6.4 provides summary of internal plasma properties at Position 0 (4 cm below the main discharge coil), shows a representative plasma density and temperature for the discharge as a function of energy and pressure, and initial exploration of the magnetized plasma turn-on and main bank pre-ionization coupling.

6.1 Typical 250-μs Discharge Parameters

Figures 6.1 and 6.2 detail a typical discharge for the 250-μs discharge case, they show the peak voltage of 930-V and 480-V coil voltage cases, respectively, as well as the peak vacuum currents for each discharge condition. Shown in Figure 6.2, the DC, PPI seed ionization is initiated 1 second before the main discharge. The pre-ionization discharge is triggered, and then 60 μs later (after the majority of the pre-ionization electrical noise has dissipated) the main bank is discharged. This timing is a function of the diffusive timescales of the pre-ionization plasma (in order to create a more axial and radially uniform initial plasma condition) and the timing studies discussed in Section 4.2.1. As in the 450-μs case, the pre-ionization discharge has a period of 4 μs, while the main bank has a period of 250 μs. Shown are the voltage and current of the coil for a vacuum discharge (with a plasma there are differences in the induced plasma resistance and therefore voltage). It must be noted that actual bank voltages are higher than the coil voltages due to inductive losses in the switches and conductive paths. Figure 6.3 shows a 3-shot snapshot of the first ionization period of this discharge as well as outlines the primary discharge criteria.

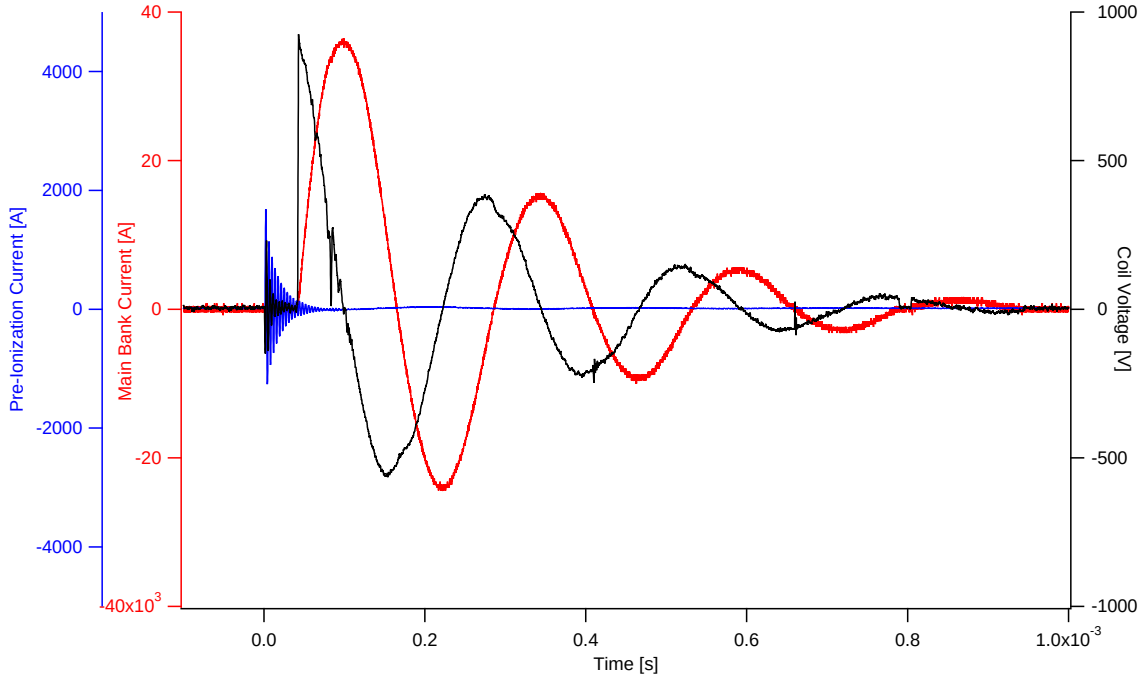

Figure 6.1: A 900-V discharge showing total discharge current (both coils), pre-ionization current, and instantaneous coil voltage for a 250-μs discharge

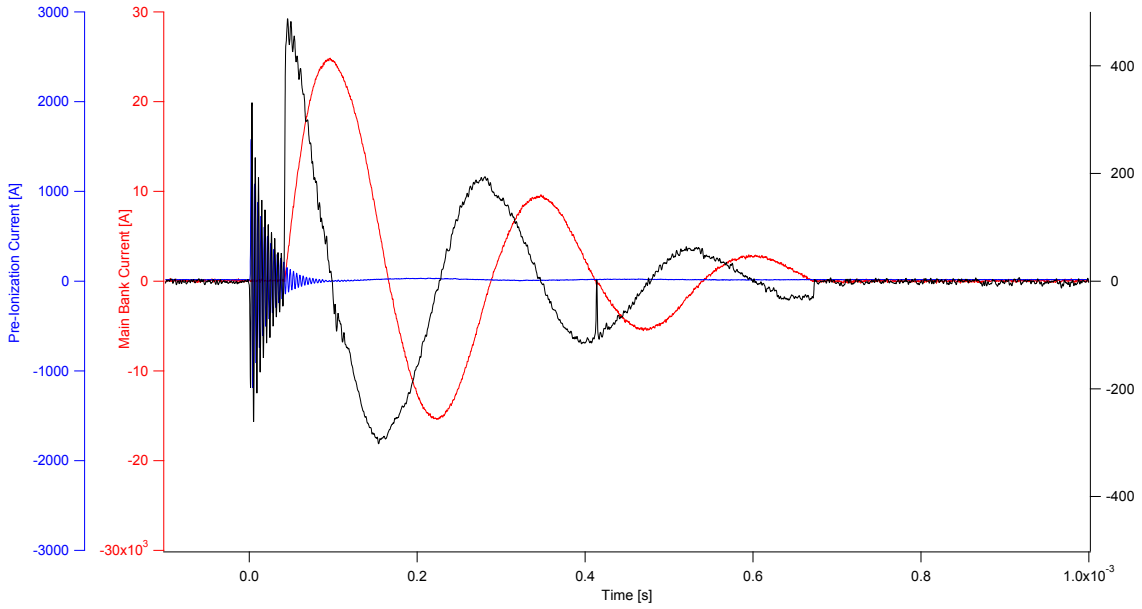

Figure 6.2: A 500-V discharge showing total discharge current (both coils), pre-ionization current, and instantaneous coil voltage for a 250-μs discharge

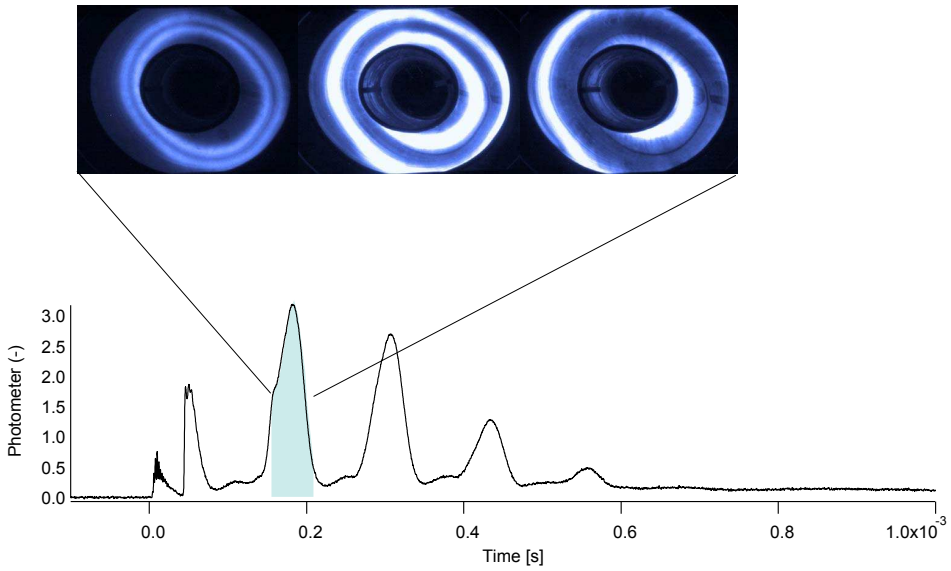

Time	Mode
150-160 μs	Initial formation and reversal
160-190 μs	Radial compression and heating
190-210 μs	Radial compression/rotational Instability

Figure 6.3: DICAM photos and descriptions of typical formation and compression regimes during a 250-μs discharge

6.2 Photometer Results

The photometer results are similar to the 450-μs case, but with some notable, and interesting differences, see Figures 6.4 and 6.5. The peak brightness from the FRC discharge is very repeatable, but less symmetric than for the longer discharge case, with a larger first ionization and wider, secondary ionization. Also, the dark zones interspacing the main re-ionization pulses are brighter and have a larger lead-in to the breakdowns that occur. Moreover, as shown in Figures 6.6 and 6.6, there is greater upstream plasma leakage density than in the 450-μs case, but it occurs at a much later time in the discharge. There is very little of the first two pulses upstream, and instead one large plasma mass that arrives a full 200-μs later than the initial discharge. As the triple probe data taken in these sweeps is unfortunately upstream, rather than downstream in the direction of a moving magnetized plasma toroid, this actually implies that we have little backstreaming plasma and that the measured data are either slow diffusion after compression (and ejection) or, less likely, reflected higher energy plasma. Further tests are conducted in Chapter 7 in order to differentiate the results and explore the internal plasma behavior.

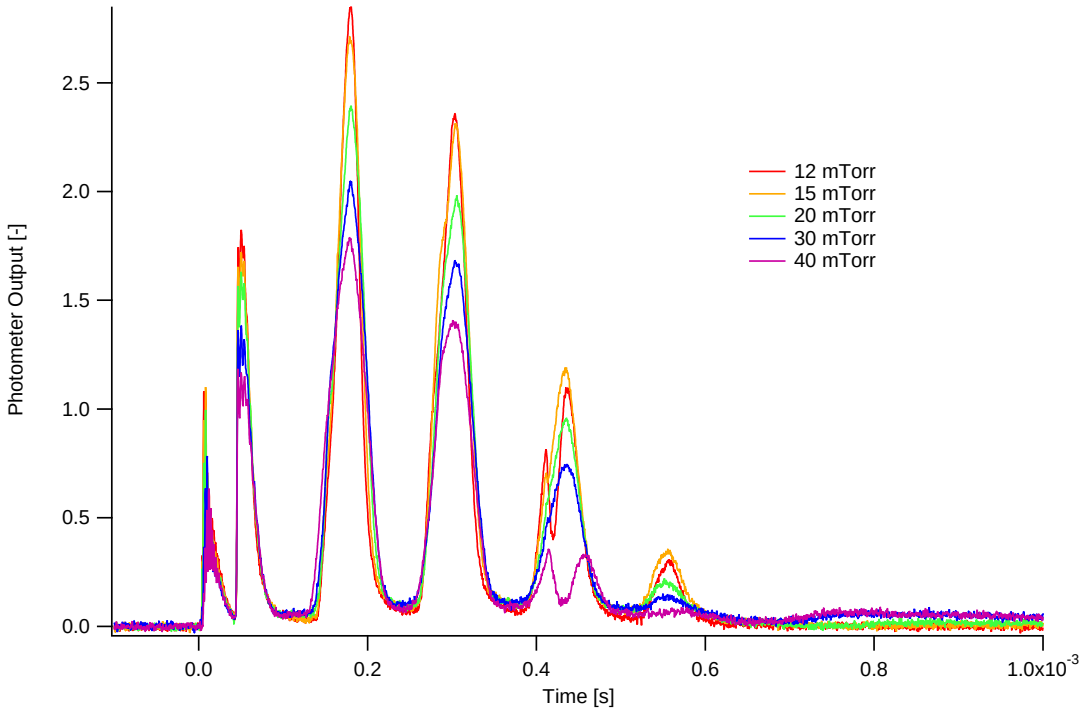

Figure 6.4: A 500-V, 250-μs discharge, with photometer results as a function of neutral plasma density

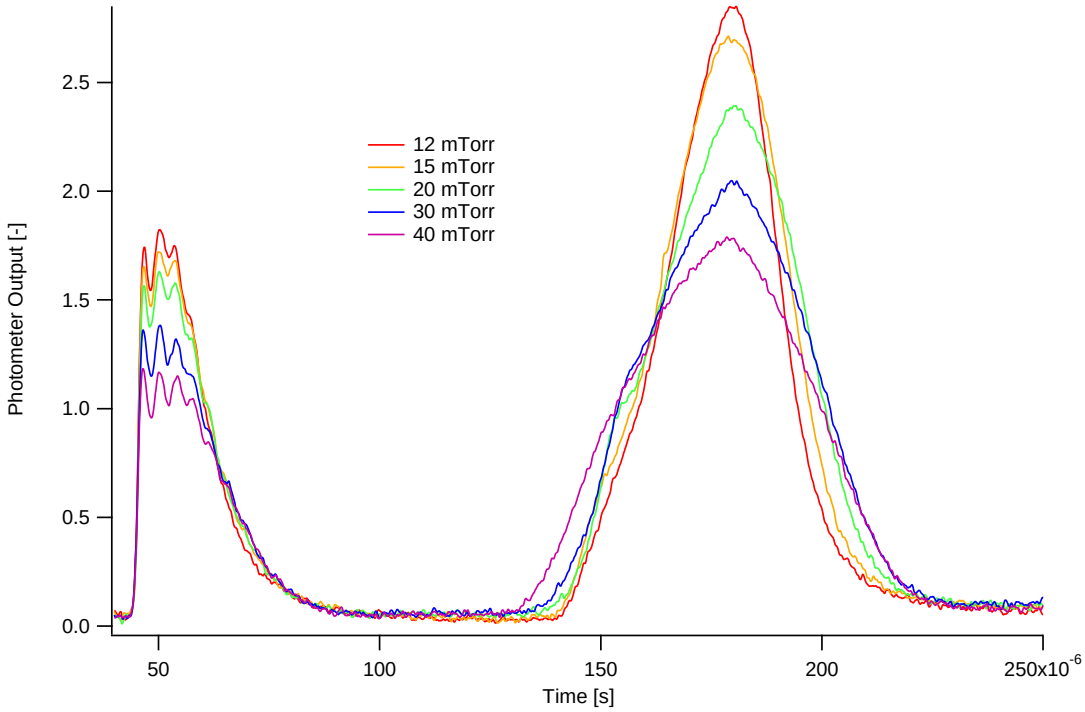

Figure 6.5: Close view of 500-V, 250-μs discharge, with photometer results as a function of neutral plasma density

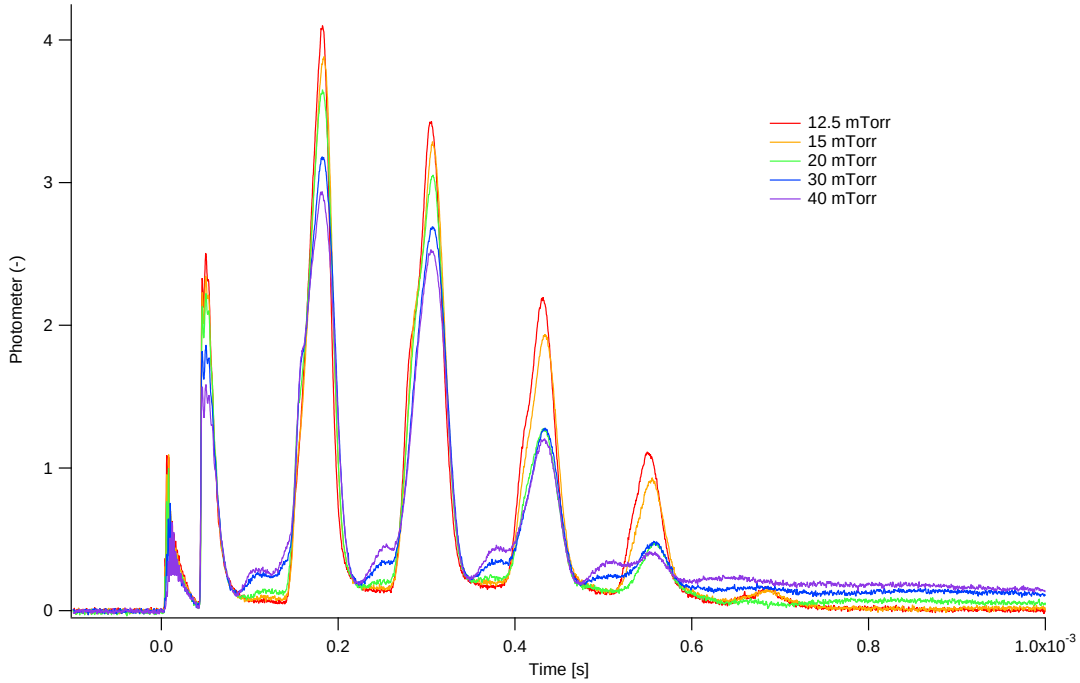

Figure 6.6: A 900-V, 250-μs discharge, with photometer results as a function of neutral plasma density

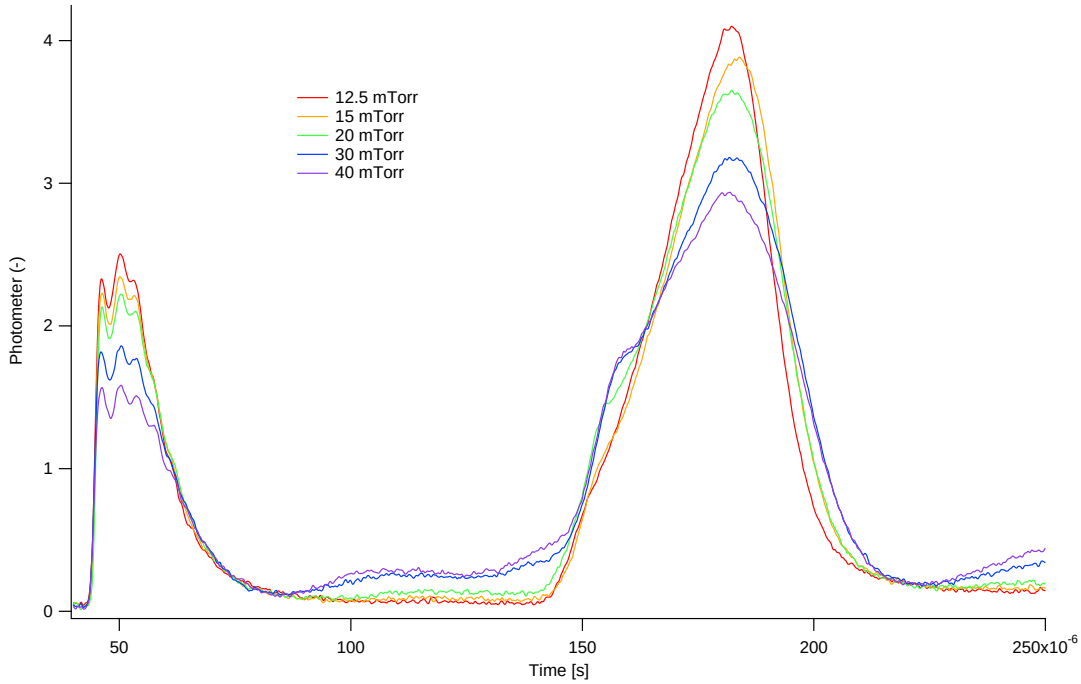

Figure 6.7: Close view of a 900-V, 250-μs discharge, with photometer results as a function of neutral plasma density

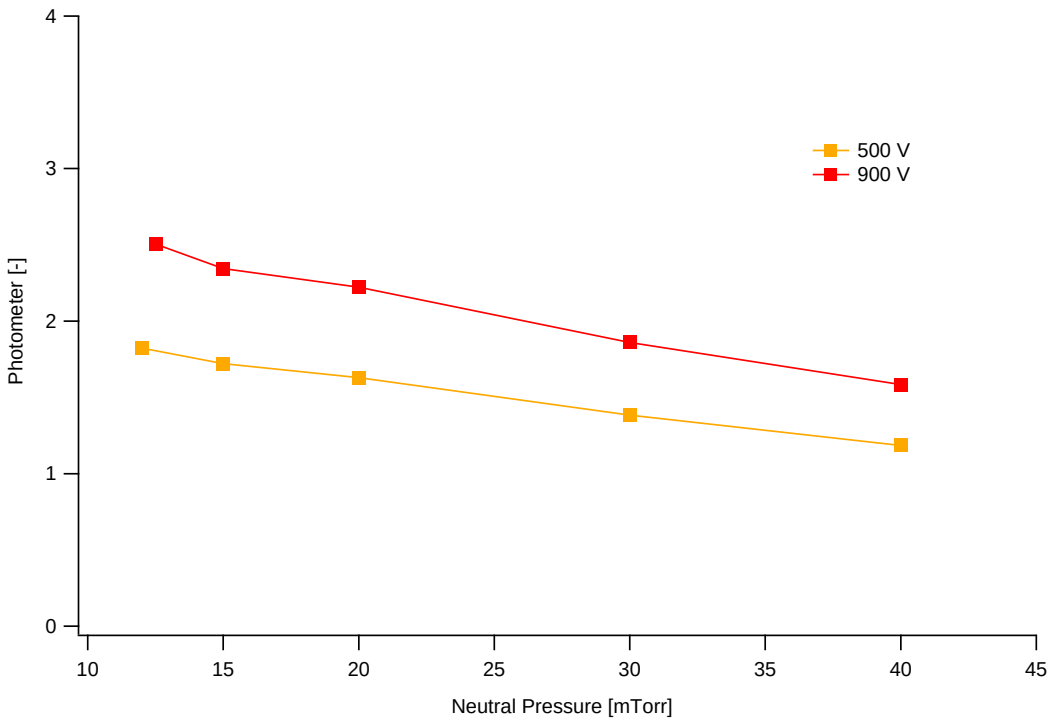

Figure 6.8: Summary of peak photometer results as a function of neutral pressure for the initial plasma discharge

Figures 6.8 and 6.9 show a summary of the peak photometer results for the primary and secondary discharges as functions of coil voltage and neutral discharge pressure. Surprisingly, the 250-μs discharge cases do not appear to have the same photometer trends as the 450-μs cases. The peak plasma optical emission decreases monotonically from 12.5 mTorr. Unfortunately, data were not taken for the 11-mTorr case that has the significant downturn for both the 450- and 185-μs discharge cases and so it can only be surmised as to whether the same trends happen with photometer data.

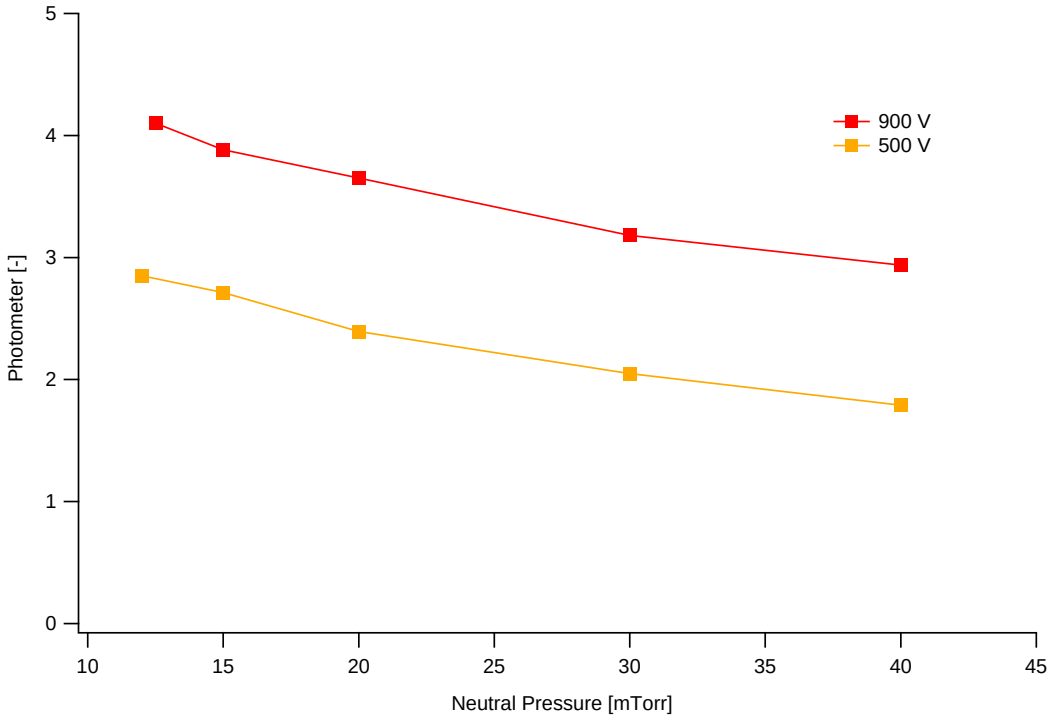

Figure 6.9: Summary of peak photometer results as a function of neutral pressure for the second plasma discharge

6.3 Magnetic Field Results

Figures 6.12 and 6.10 continue the investigation into magnetic field effects. Figure 6.12 shows the magnetic field deficit (as compared to Figure 5.5 for the 450-μs discharge case) with similar trends as before, with higher neutral pressures yielding larger magnetic field shielding and also stronger non-uniformities related to the pre-ionization distributions. Surprisingly, the magnitude of the deficit is 200-300 % larger than with the 450-μs case. This effect is due to the larger dI/dt and induced fields in the plasma. Figure 6.10 shows raw B-dot probe results for multiple pressure discharges. This is explored further in Figure 6.10, however, qualitative results can be garnered by examining the timing and relative magnitude of magnetic field effects. Clearly, there are significant effects compared to the vacuum discharge case (black), and even more significantly there appears to be an increased magnetic deficit due to the larger background pressure cases. This effect becomes more pronounced for the later reversals. Also, we can see that the magnetized plasma starts to become apparent (on the scale of the main discharge) approximately 10 μs before the field zero (10 μs before the largest dI/dt) and continues for 75 μs beyond it.

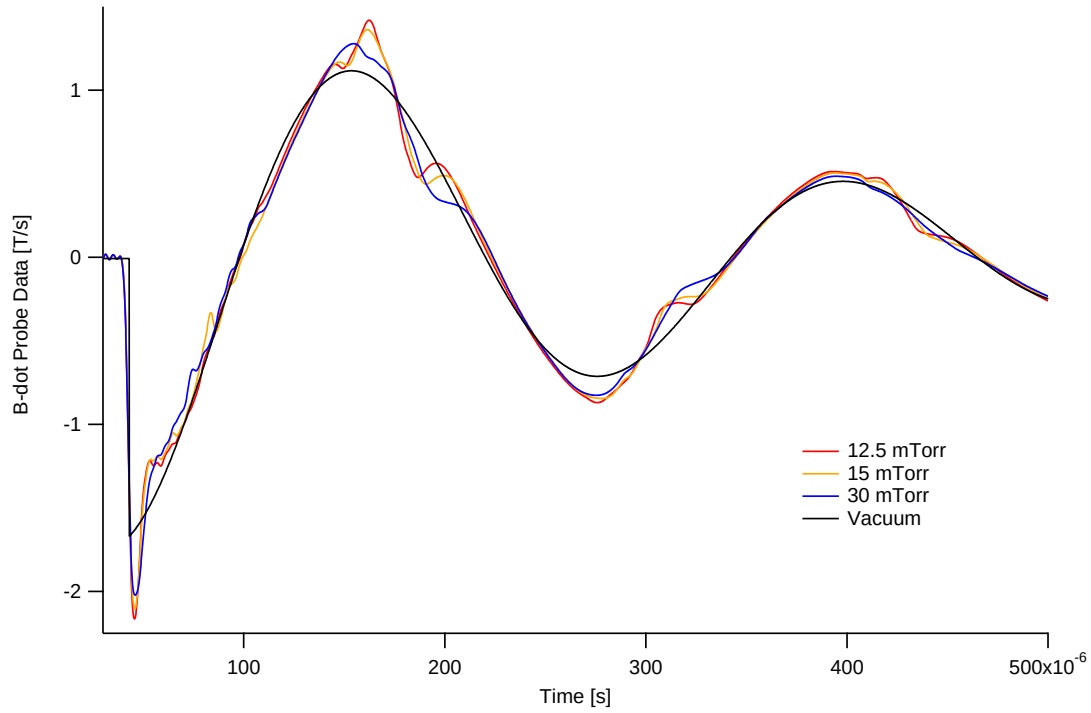

Figure 6.10: B-dot probe results for a 750-V discharge case for various input pressures to examine plasma compression as a function of input neutral density

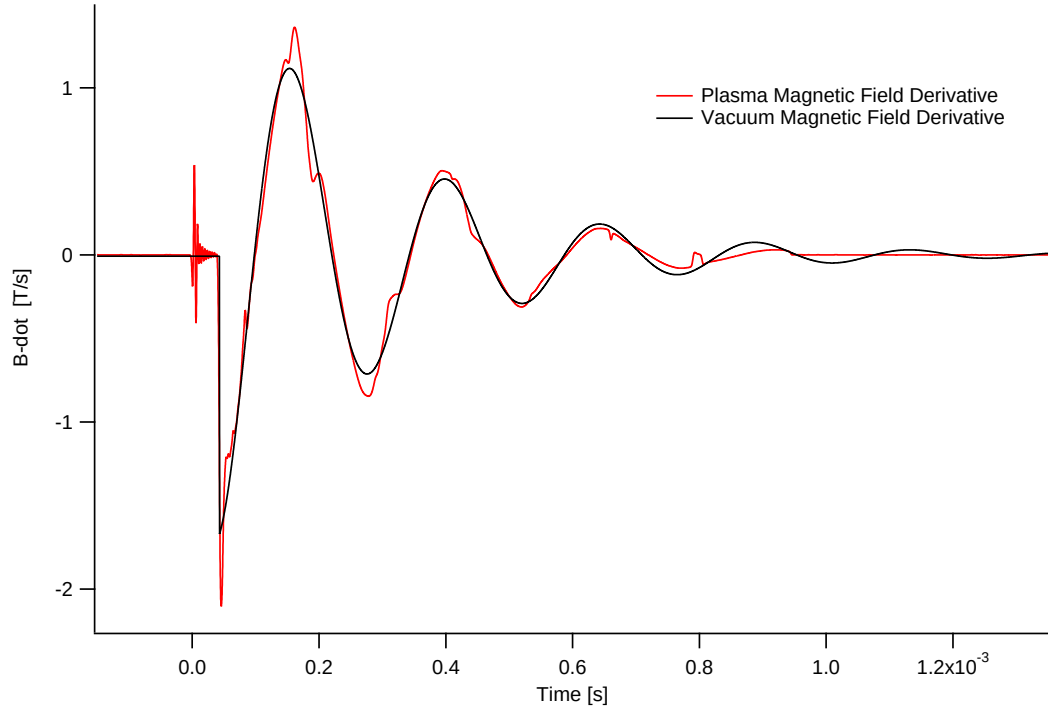

Figure 6.11: Magnetic field data at 14 mTorr comparing derivative magnetic field probe data. Discharge was 900 V

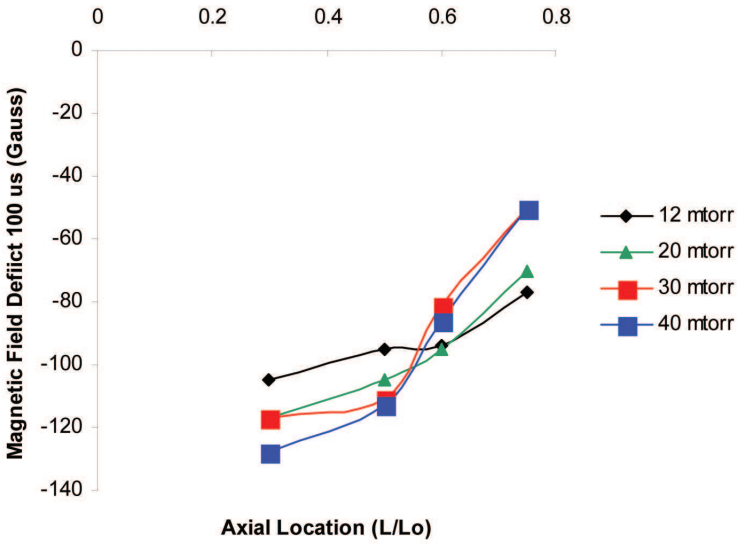

Figure 6.12: Peak magnetic field data for axial locations and various fill pressures. Discharge was 900 V

6.4 Internal Plasma Properties

The fast triple probe was used to collect upstream plasma data at Position 0. This position allows for data collection without seriously interfering with the FRC formation, but does not collect data of the compression at its maximum. These results instead tell a general picture for the residual plasma density and temperature. Figures 6.13–6.18 show plasma properties as collected at Position 0 for a 500-V and 900-V discharge case , respectively. Average electron temperatures of 4.8 and 5.8 eV were recorded for the 500-V and 900-V discharges, respectively. Peak electron densities were recorded at $2.1 \times 10^{19}\ m^{-3}$ for the secondary discharge (at 15 mTorr, 900 V) and as high as $3.2 \times 10^{19}\ m^{-3}$ for the tertiary discharge. No major plasma density was collected during the initial discharge, presumably as it is all contained within the discharge coil itself, and the triple probe does not see plasma density until it has exited the discharge coil. Finally, in the close views, Figures 6.17 and 6.18, it can be seen that the turn-on voltage and pressure for a 900-V discharge with pre-ionization Geometry 2 is 20 mTorr, and higher pressures require significantly more energy input in order to begin the main compression-heating cycle.

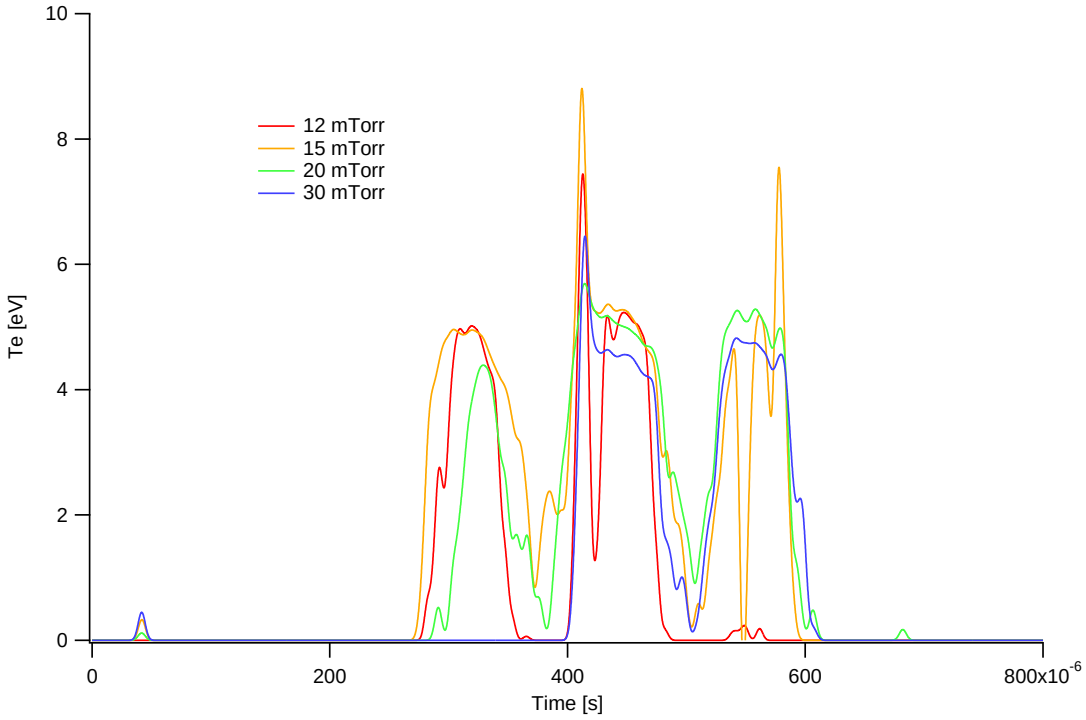

Figure 6.13: A 500-V, 250-μs, 15-mTorr discharge showing electron temperature for various discharge pressures at Position 0

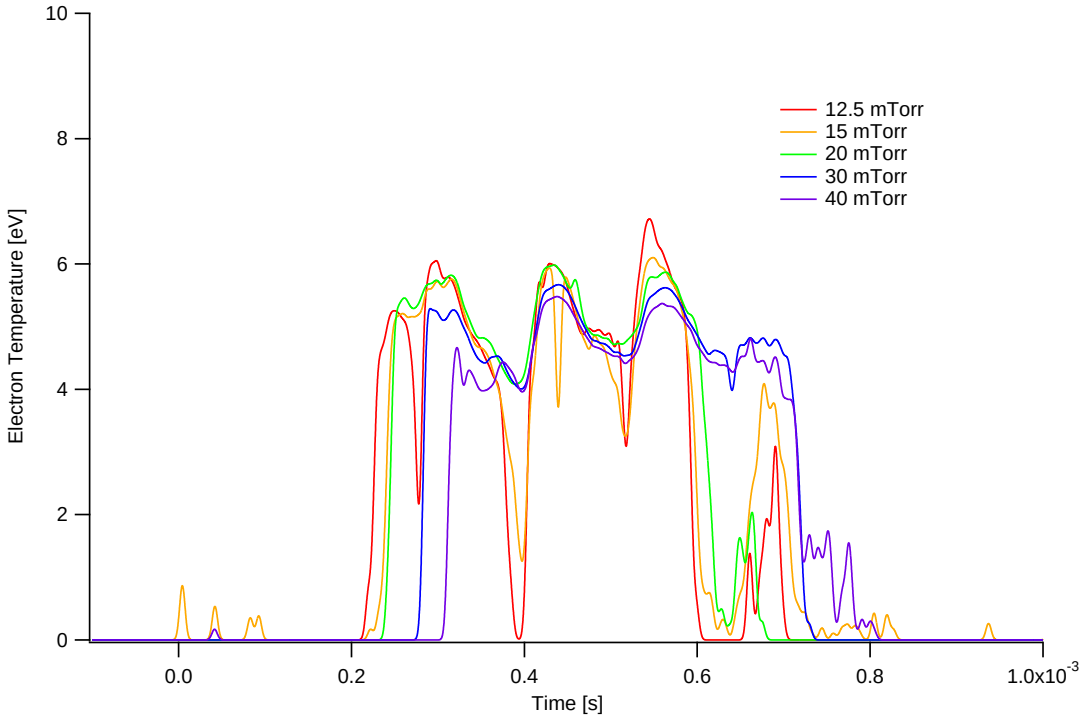

Figure 6.14: A 900-V, 250-μs, 15-mTorr discharge showing electron temperature for various discharge pressures at Position 0

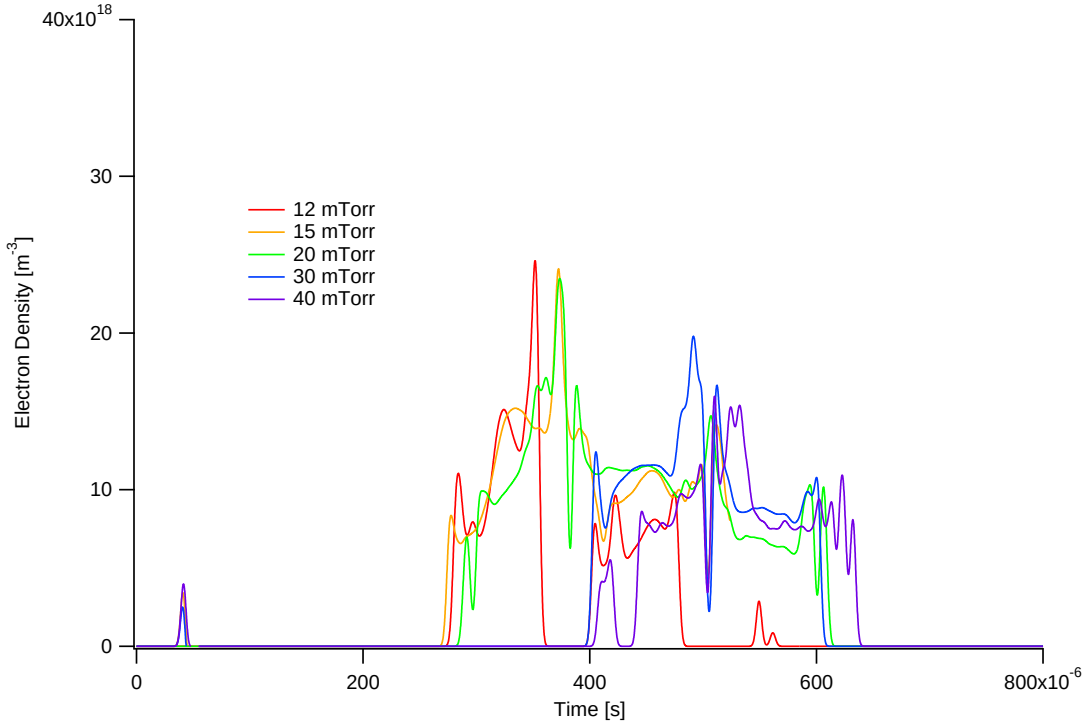

Figure 6.15: A 500-V, 250-μs, 15-mTorr discharge showing electron density for various discharge pressures at Position 0

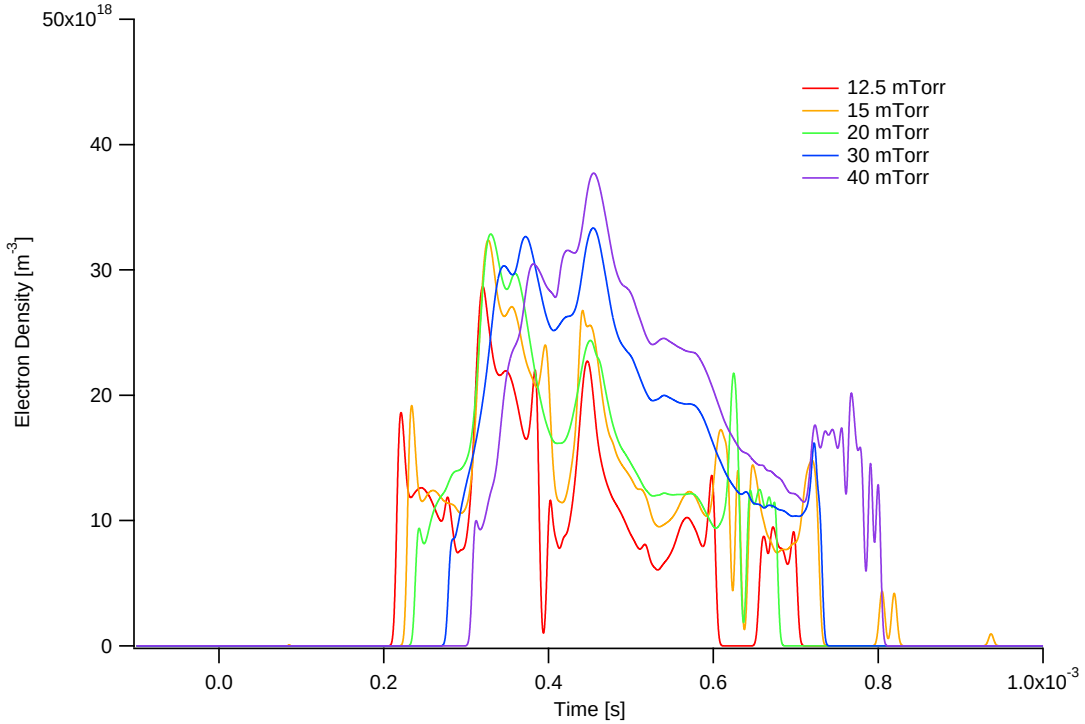

Figure 6.16: A 900-V, 250-μs, 15-mTorr discharge showing electron density at Position 0

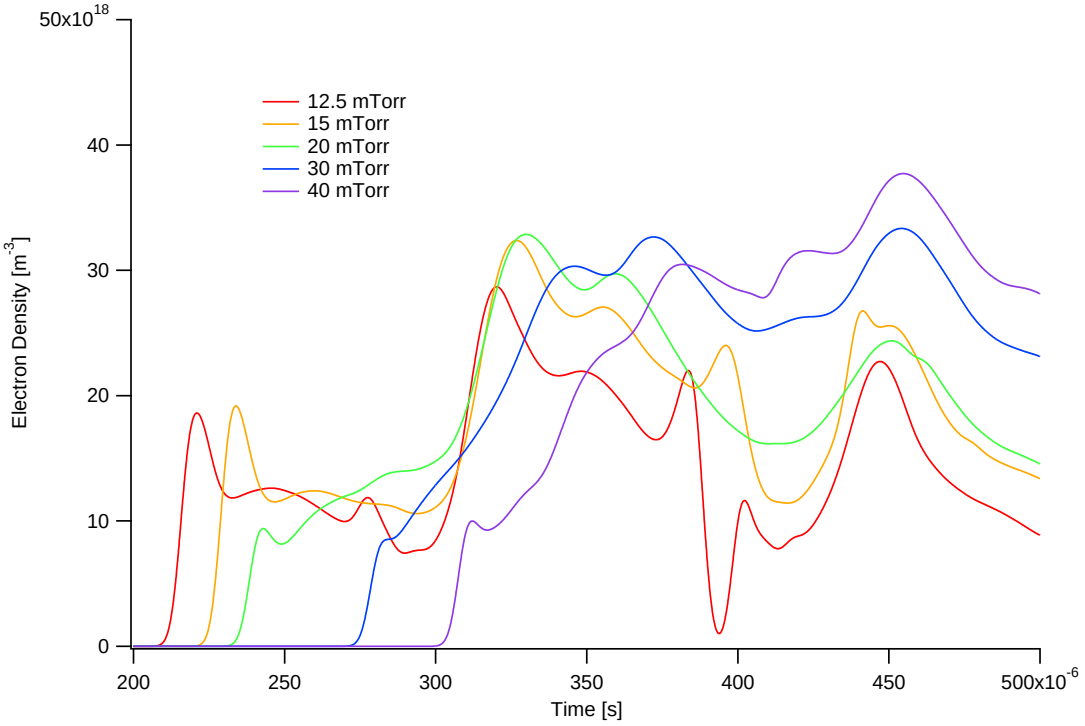

Figure 6.17: Close up of a 900-V, 250-μs discharge showing electron density for various discharge pressures at Position 0

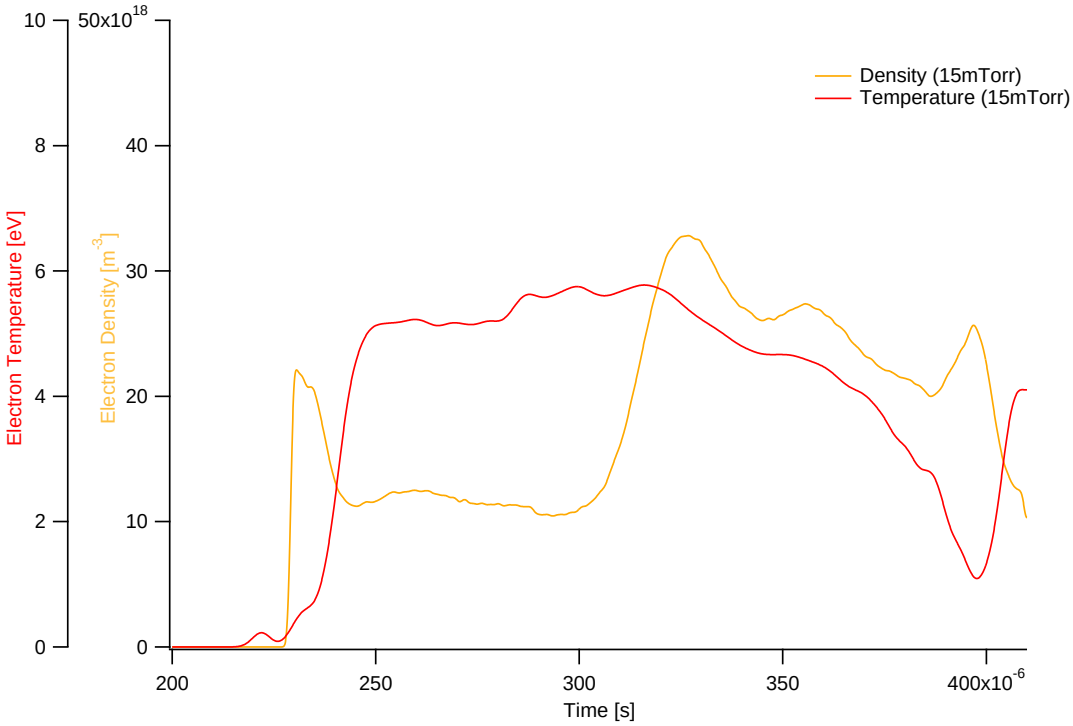

Figure 6.18: A 900-V, 250-μs, 15-mTorr discharge showing simultaneous electron density and temperature for various discharge pressures at Position 0

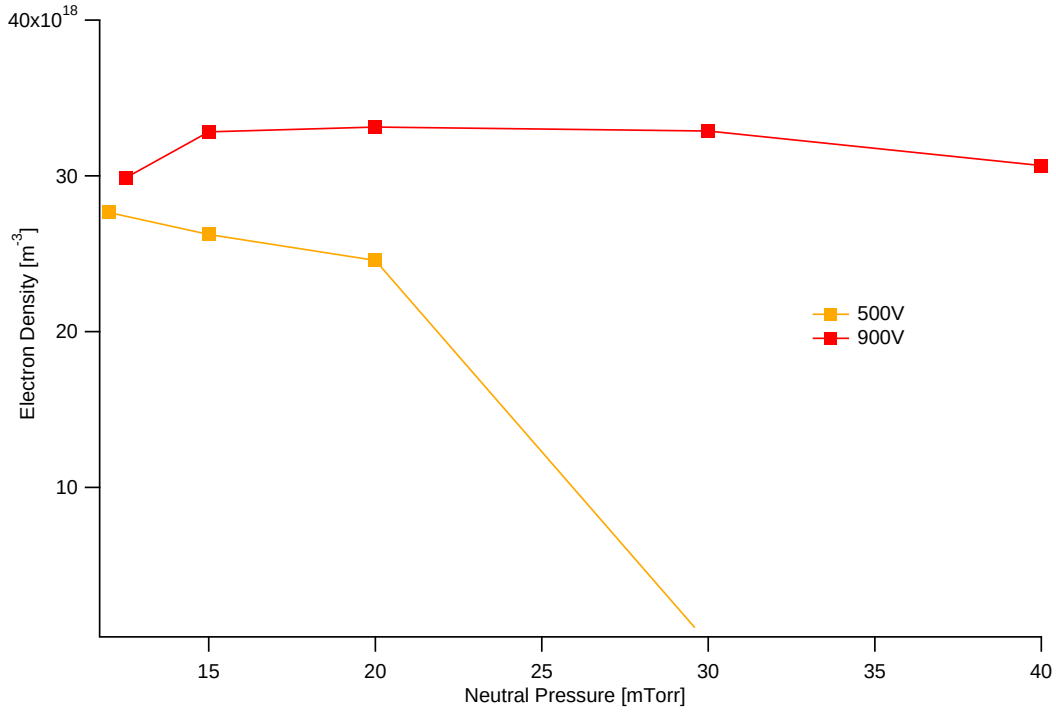

Figure 6.19: Summary of peak density results as a function of neutral pressure for the second plasma discharge at Position 0

The electron density does follow the typical trends seen earlier, with a distinct peak at 12-15 mTorr for the low-voltage cases and a peak density measured at 15–20 mTorr for higher-voltage discharges. Figure 6.19 shows the results for the secondary (first measured) plasma density pulse.

6.5 250-μs Discharge Conclusions

In summary, discharge experimentation was continued for the XOCOT discharge by studying external plasma density, diamagnetic current, and optical emission for a discharge period of 250 μs, argon propellant pressure from 10 mTorr to 50 mTorr, and discharge voltages from 500 V to 1000 V. The results from Chapter 6 led directly to the comprehensive study done in Chapter 7, for a similar energy discharge, but with a higher-current rise-time (shorter discharge period). A 250-μs period successfully creates high-density, fully-magnetized plasmas at less than 1000 V coil voltage. Repeatable discharges have been performed that show, as in the 450-μs cases, the initial ionization without initial reversed bias field is unsuccessful in creating large-scale, magnetized plasma. Photometer results suggest a region of highly compressed, high-temperature plasma is formed for a short time, but is neither translated out of the annulus and onto the triple probe, nor representative of bulk plasma formation along the axis. Similar to the 450-μs cases, when an initial bias is present and the major current reverses, a very bright (see Figure 6.7), dense (see Figure 6.17) plasma is formed and exits the discharge annulus. As can be seen in the DICAM photographs in Figure 6.3 a repeatable, and expected, pattern emerges for FRC formation. During the initial dI/dt compression, just prior to current reversal, pre-ionization and plasma density increase along the outer quartz wall (typically 120–160 μs). After the current reverses the plasma brightness and density increase greatly during the main radial compression phase (around 160–190 μs) at which time the plasma starts to spin and become unstable. There is evidence for a rotational instability as the plasma compresses near to the quartz wall. At that time, the triple probe (that is located at Position 0 outside of the coil) registers the bulk plasma density. From the photometer and triple probe measurements there appears to be a maximum in

energy deposition between 12 and 15 mTorr with peak plasma densities between 2.8×10^{19} and 3.5×10^{19} m^{-3} for 500 V and 900 V respectively. Compared with the results in Chapter 5, similar general trends as well as optimal discharge conditions were found. The primary difference was found in electron temperature. The average temperature at the maximum energy tested (250-J) was approximately 6 eV, while for the 450-μs case peak electron temperature was found to be approximately 15 eV. This implies that the direct effect of increasing discharge energy, regardless of discharge period in an annular configuration, acts to increase compression and peak electron temperature, while maintaining the same peak plasma density that is recorded at Position 0. This immediately implies that the peak density measured in the annulus during the 450-μs discharge would be significantly higher than that in the 250-μs discharge case. Finally, as before, the magnetic field probe data and wide-angle photometer data clearly show an axial non-uniformity. This non-uniformity is subsequently explored and mitigated in Section 4.3 and in Chapter 7.

CHAPTER 7

185-μs Discharge Experiments

During the studies in Chapter 6, significant challenges in capacitor lifetime were discovered. The experimental results shown in Chapter 6 were completed before the capacitor failure began. In order to mitigate this effect, newer, lower capacitance capacitors were installed that were both in parallel (load balancing and peak current become non-issues) as well as significantly derated as described fully in Section 7.1. Chapter 7 details the complete investigation of discharges from 500 V to 1000 V and 60 J to 250 J in both argon and xenon. As in Chapters 5 and 6, Section 7.2 outlines the typical discharge process. Section 7.3 shows the data collected for argon discharges at various discharge pressures and densities. The primary diagnostic used for these experiments was the internal scanning triple probe described in Section 2.5.3.1 to take real-time plasma temperature and density data. Plasma characteristics are explored at Positions 1, 2, and 3 that are located at axial locations of 0, 6.5 cm, and 13.2 cm from the bottom of the axial discharge coil. At each position plasma electron temperature, density, and time-response are taken real-time for multiple neutral background pressures and discharge energies. Finally, using the coil current, plasma temperature, and plasma density a real-time analysis of the energy contained within the plasma and discharge coil is given for data collected at Position

3. Section 7.4 repeats this analysis for xenon, at Positions 1, 2, and 3 and background pressures of 3–10 mTorr. At the conclusion of each Section is an exposition of results and conclusions for each respective gas. Finally, Section 7.5 gives a summary and conclusion for the entire 185-μs discharge study.

7.1 Typical 185-μs Discharge Parameters

Figure 2.7 shows the new circuit setup and the corresponding calculations that yielded a 185-μs discharge period. The triple probe described in Figure 2.45 was constructed to use in this 185-μs discharge configuration in order to insert the probe to fully measure plasma properties along the central axis of the annulus. Figure 7.1 shows the probe locations for Positions 1, 2, and 3 that are used in this Chapter and the following data sets and descriptions. One important note, now that the primary coil is being used as the pre-ionization source it is acceptable in assuming an axial symmetry around the center of the coil and so data were only taken for one half of the full axial length of the coil. This was done primarily to reduce probe interference in the plasma discharge region by limiting it to only the lower half of the discharge coil. As will be described later, even with the minimizations that did occur, probe interference was a significant issue to the pre-ionization explored earlier. In Figure 7.1 Position 0 is the probe location for data collection that was done in Chapters 5 and 6. As there was a significant discharge period change (and diffusion rate, peak field, etc.) there was no quantitative comparative study done between Positions 0 and 1.

A typical discharge curve is shown in Figure 7.2 for a peak 950-V, 28-kA discharge. Additional typical discharge parameters are given in Table 7.1.

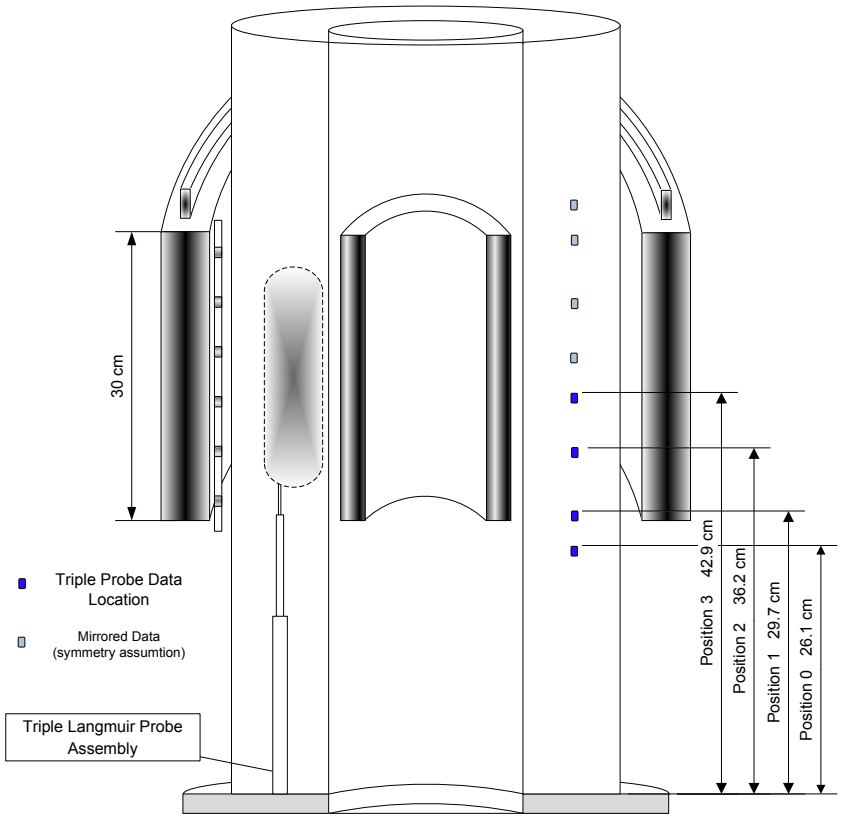

Figure 7.1: Schematic of triple probe locations for the discharge tests described in Chapters 5, 6, and 7

Peak Coil Voltage	Peak Coil Current	Reversal Voltage
550 V	13.0 kA	420 V
750 V	17.7 kA	550 V
850 V	22.5 kA	670 V
950 V	28.0 kA	750 V

Table 7.1: Typical vacuum operational parameters for the 185-μs discharge setup

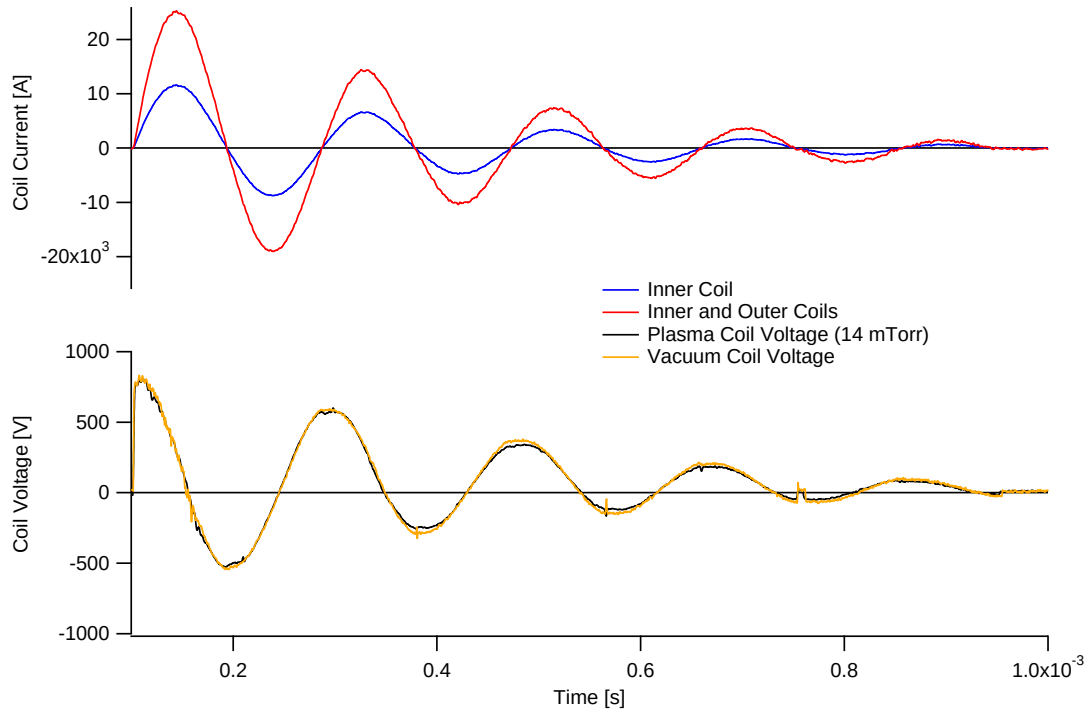

Figure 7.2: A typical 950-V, 185-μs discharge with a peak coil current of 28 kA

7.2 Typical Discharge Results

As explored in Chapters 5 and 6, a neutral fill pressure of 14 mTorr appears to be the optimal for plasma production and energy input. A pressure of 14 mTorr will be the baseline pressure that is explored in the most detail. Figures 7.3–7.6 show some typical operational characteristics for the 185-μs discharge cases. Figures 7.3 and 7.4 show wide-angle photometer and density data at Position 1. Qualitatively comparing the results from Position 0 and 1 yields similar peak density results as well as photometer results. There does appear to be significantly more initial plasma (100-300 μs) at the probe location as well as wider photometer pulses (i.e. longer plasma containment and heating) during the subsequent discharge cycles. Figures 7.5 and 7.6 show the current collected at the triple probe for various discharge parameters as compared to the wide-angle photometer. Again, qualitatively (a more thorough quantitative analysis is located in Sections 7.3 and 7.4) there are distinct correlations,

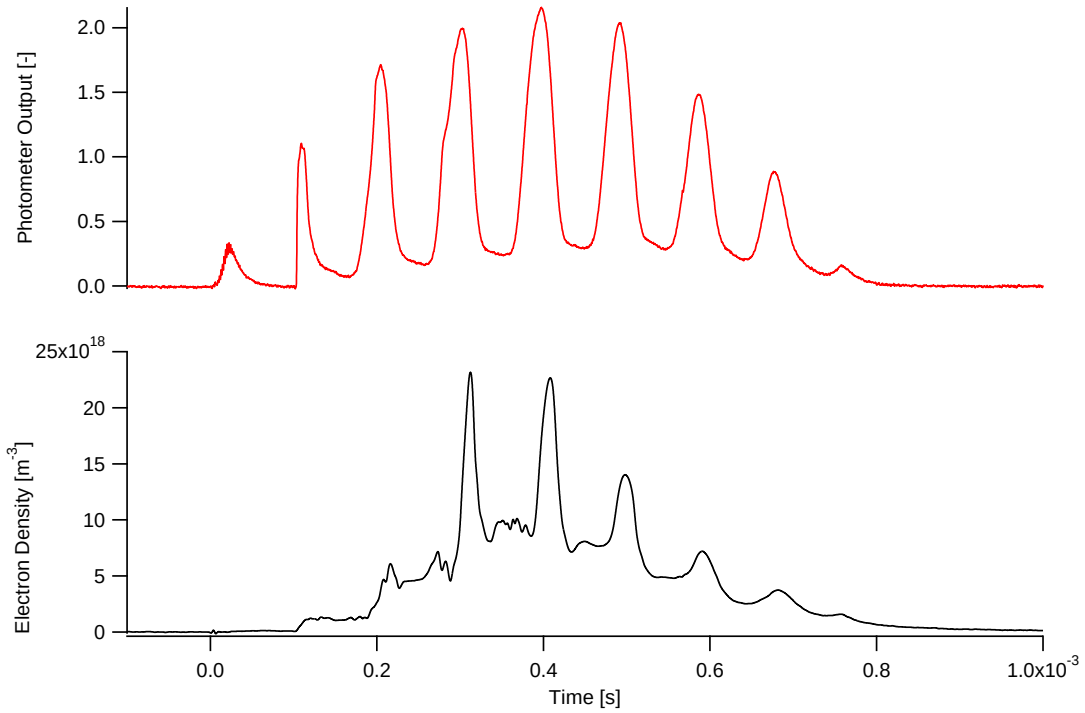

Figure 7.3: An 850-V, 185-μs, 14-mTorr argon discharge showing detailed photometer and electron density at Position 1

as expected, between the current collection and photometer emission. In fact, it is also quite clear that there are small transit time lags between the peak brightness and peak densities at probe Position 1. Also, Figures 7.5 and 7.6 relate the typical collection current and photometer magnitudes, electrical noise, and time response for the selected diagnostics.

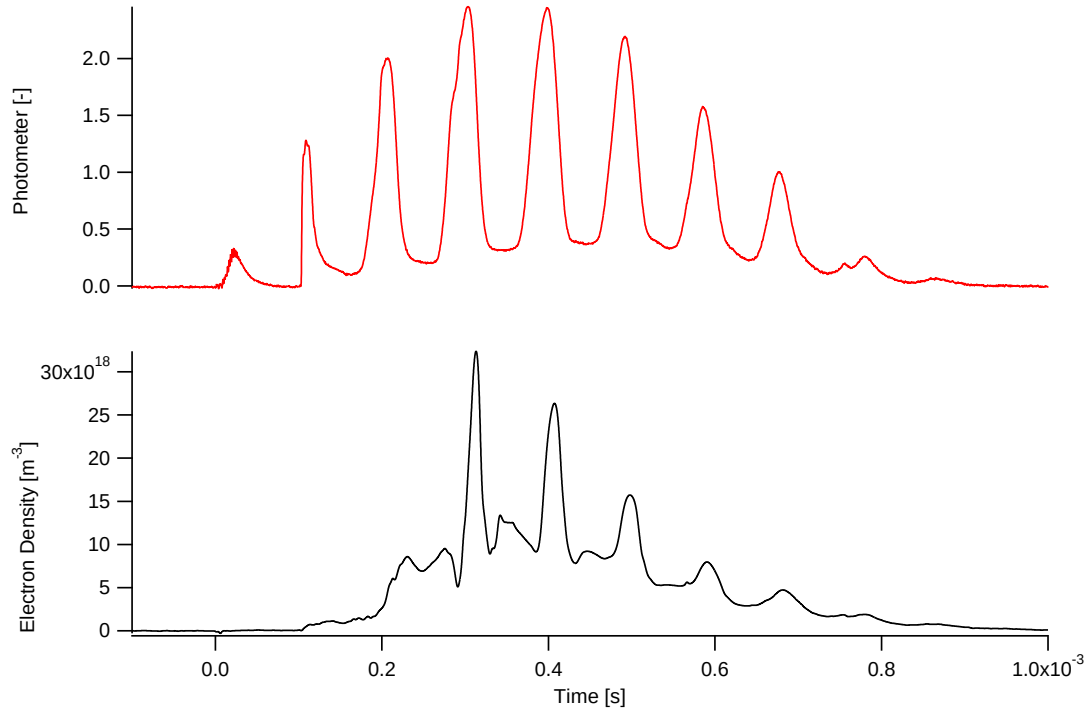

Figure 7.4: A 950-V, 185-μs, 14-mTorr argon discharge showing detailed photometer and electron density at Position 1

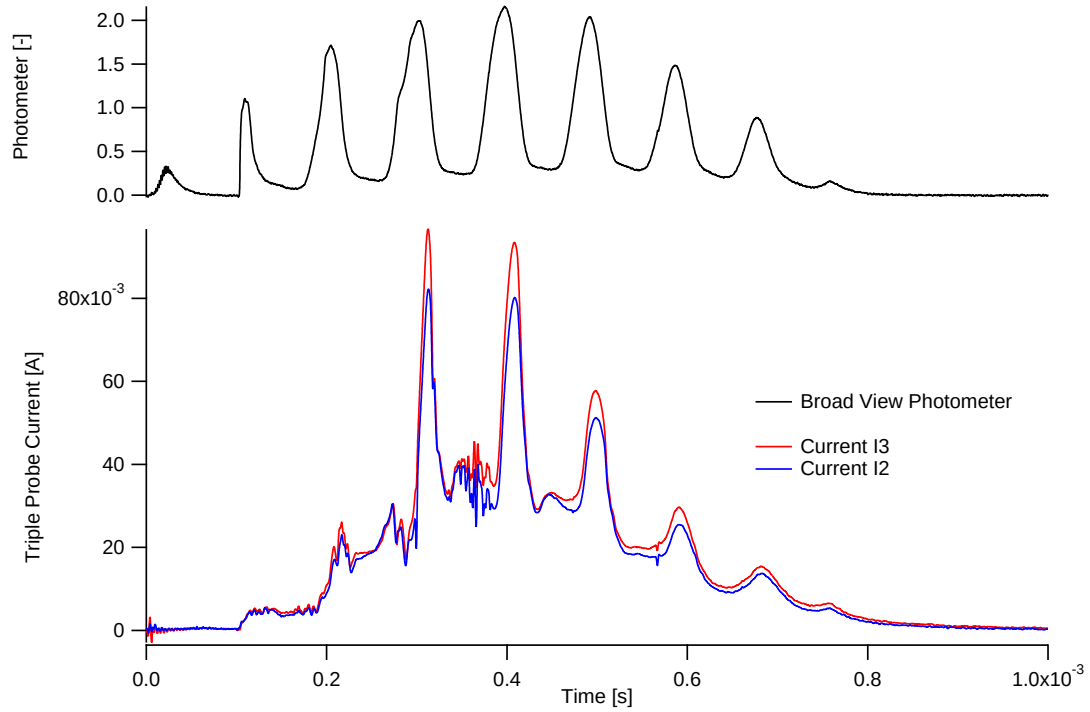

Figure 7.5: Collected triple probe current (both I_2 and I_3, see Figure 2.42) for a typical 850-V, 185-μs, 14-mTorr argon discharge

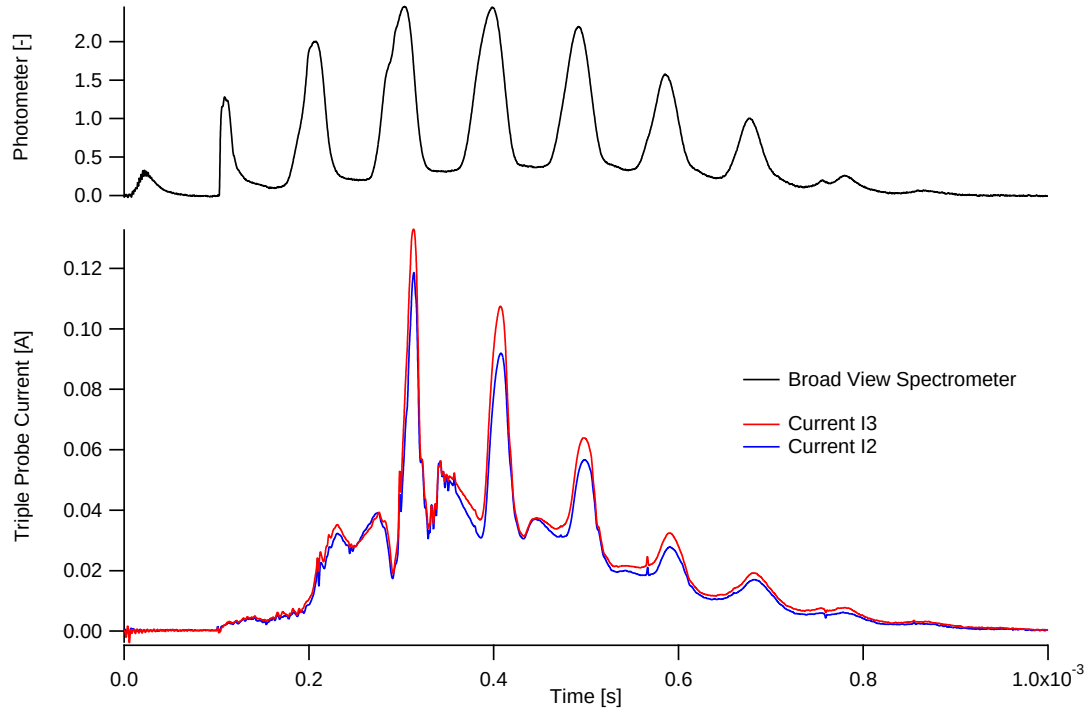

Figure 7.6: Collected triple probe current (both I_2 and I_3, see Figure 2.42) for a typical 950-V, 185-μs, 14-mTorr argon discharge

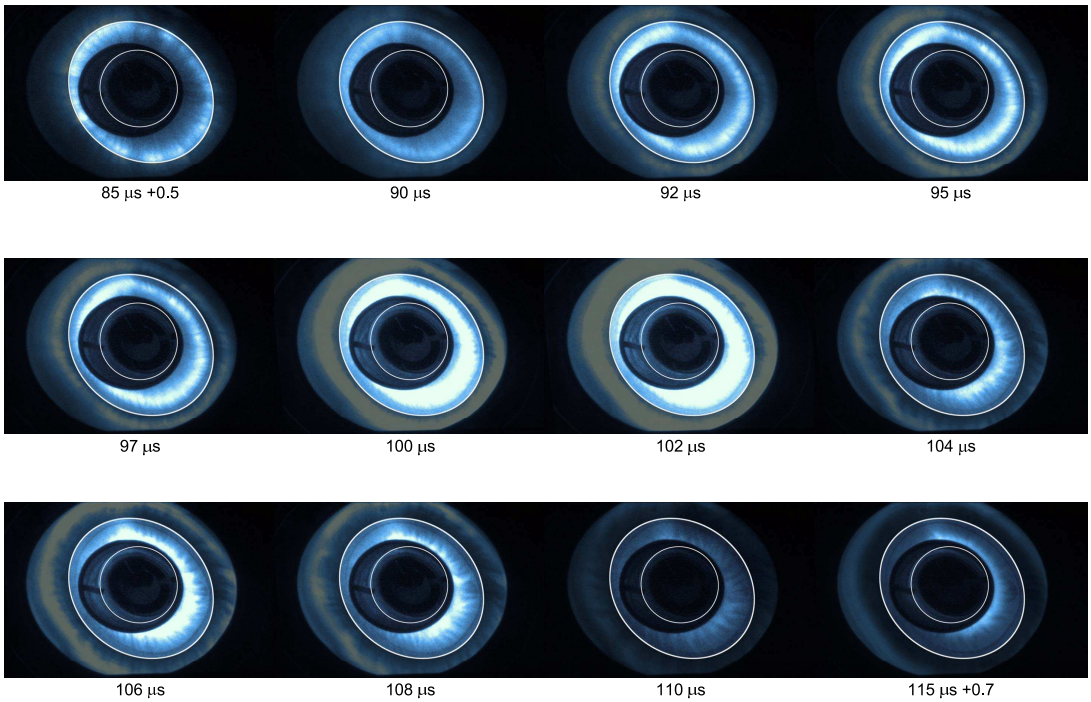

Figure 7.7: DICAM end-on visible photography for 850-V, 14-mTorr, argon cases

7.3 Argon

7.3.1 Optical Results

A 12-shot evolution of an 850-V, 14-mTorr argon discharge was created with the DICAM II, as shown in Figure 7.7. Each photograph is a 2-μs integrated image with an average DICAM exposure amplification of 5.7 [-].

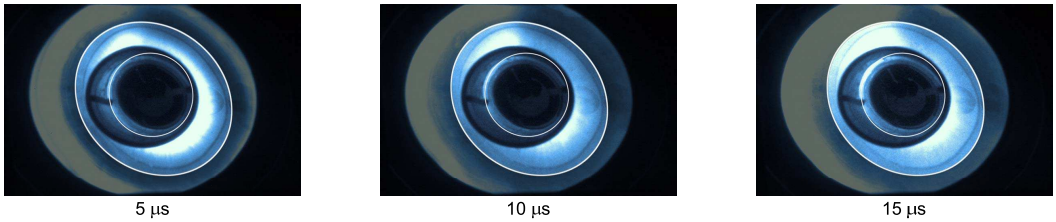

Figure 7.8: DICAM end-on visible photography for 950-V, 14-mTorr, argon cases, primary weak discharge

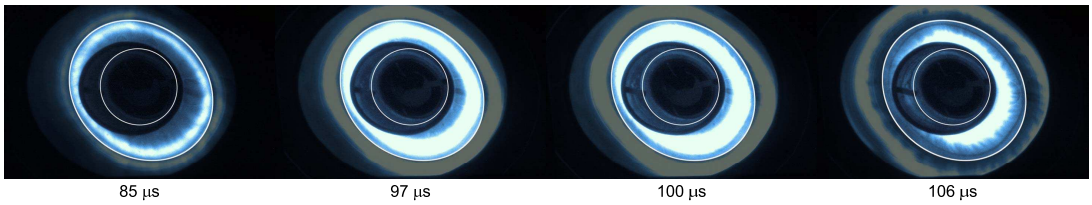

Figure 7.9: DICAM end-on visible photography for 950-V, 14-mTorr, argon cases, secondary discharge

A 3-shot evolution of a 950-V, 14-mTorr argon discharge was created with the DICAM II, as shown in Figure 7.8. Each photograph is a 2-μs integrated image with an average DICAM exposure amplification of 5.5 [-], with the aperture open two additional stops to f/5.6 from 0–20 μs.

A 4-shot evolution of a 950-V, 14-mTorr argon discharge was created with the DICAM II, as shown in Figure 7.9. Each photograph is a 2-μs integrated image with an average DICAM exposure amplification of 5.0 [-] at f/11 from 85–116μs.

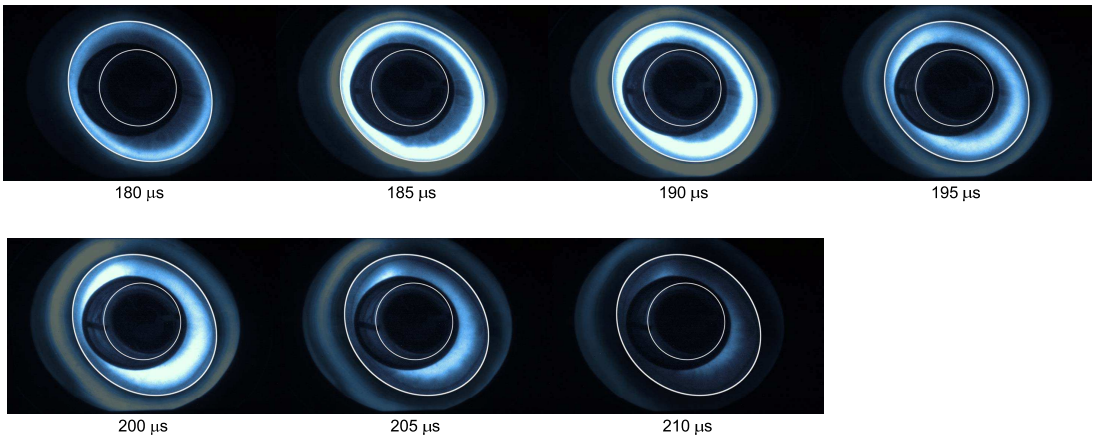

Figure 7.10: DICAM end-on visible photography for a 950-V, 14-mTorr, argon case, tertiary discharge

A 7-shot evolution of a 950-V, 14-mTorr argon discharge was created with the DICAM II, as shown in Figure 7.10. Each photograph is a $2 - \mu s$ integrated image with an average DICAM exposure amplification of 5.0 [-] from 180–210 μs.

Visible are a significant background ionization, the pre-ionization edge discharge, the sharp compression edge ($t = 95$ μs), high-density plasma filling the annulus, and a compressed toroid close to the inner discharge coil ($t = 108$ μs). The optical observation of the cross section of a forming FRC gives important information to the internal plasma analysis that is only located at one location. The very initial plasma initiation (0–20 μs) is very weak (the aperture of the DICAM had to be increased to allow four times the light input and the amplification increased in order to see any plasma) and asymmetric. It appears to be only a weakly inductively coupled extension of the pre-ionization discharge. However, the subsequent discharge at 85 to 115 μs is quite bright and shows the structures that are expected from an FRC discharge. As described by the optical studies in Chapter 5 and 6, there is a clear pre-ionization and initial plasma buildup close to the external wall of the

annulus. There is a subsequent brightness increase and compression in the interior of the annulus where triple probe data would be collected. Subsequently, there is further compression and heating and the toroidal FRC plasma appears to impinge on the inner wall where it then exhibits appearance of an n=2 rotational instability. Later discharges at 190-210 μs show increased initial background ionization (the low glow across the annulus) and a more diffuse plasma during the compression phases. As seen before, increasing the discharge energy increases the ionization rate, peak brightness, and plasma lifetime.

7.3.2 Internal Plasma Properties

The following data are the results of the detailed investigation into distinct plasma properties as well as general scaling trends for a synchronous AFRC. It is important to note that the density and temperature are collected at one location (both axially, Position 1, 2, or 3 and radially, directly in the center of the annulus), and as such care must be taken in analysis to consider both temporal and geometric effects. For instance, at axial location 3 it is quite clear that there are several regimes of operation of the triple probe as the plasma forms at the outer radius (pre-ionization), heats and compresses inward, and then becomes unstable and travels axially during each of the major reversals and high-dB/dt locations in the plasma. Additionally, when comparing photometer data it is important to note the location of the bulk photometer (outside of the main discharge coil) and its shielded view of the plasma as it changes radially during compression. Finally, see Chapter 2 for more information on error analysis of the relevant diagnostics used.

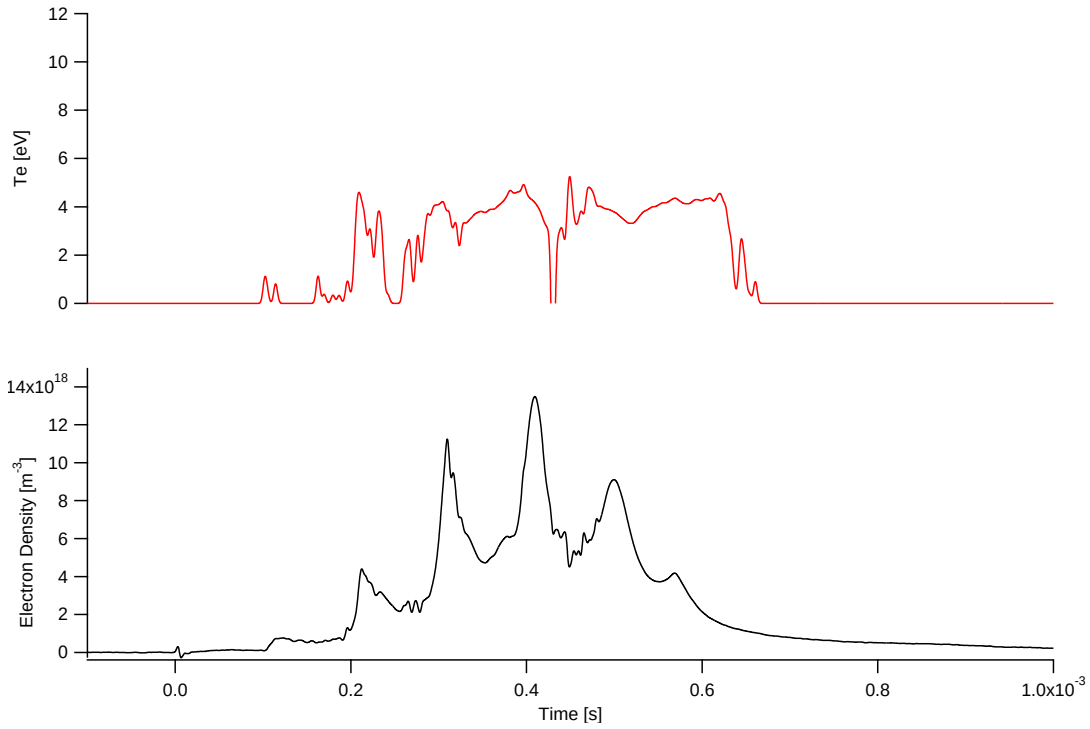

Figure 7.11: Detailed time evolution of electron density and temperature at Position 1 for an 750-V, 185-μs, 14-mTorr argon discharge

7.3.2.1 Argon Position 1

Figures 7.11, 7.12, and 7.13 detail the temporal evolution of electron temperature and density at 14 mTorr for 750-, 850-, and 950-peak-coil voltages. These data show average electron temperatures of 4.0, 4.0, and 4.1 eV though there are clear areas where the electron temperature appears to drop to zero. This is an effect of the collected triple probe current difference approaching zero, both from a true decrease in electron temperature as well as a decrease in total collected current that leads to system noise (even of a few percent) overriding the natural current differential. Also note that, as expected, the increasing applied energy extends both the plasma resonance time as well as time of residual hot plasma on the probe after main compression and heating has ceased. The collected density results will be analyzed in more detail in future charts.

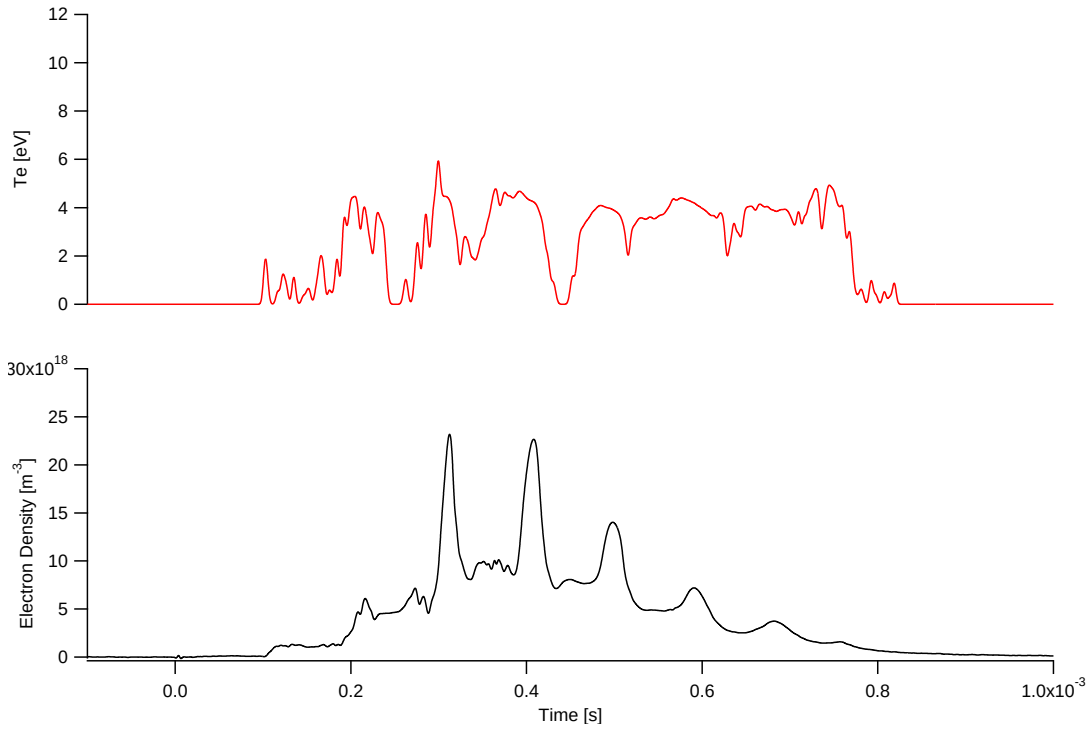

Figure 7.12: Detailed time evolution of electron density and temperature at Position 1 for an 850-V, 185-μs, 14-mTorr argon discharge

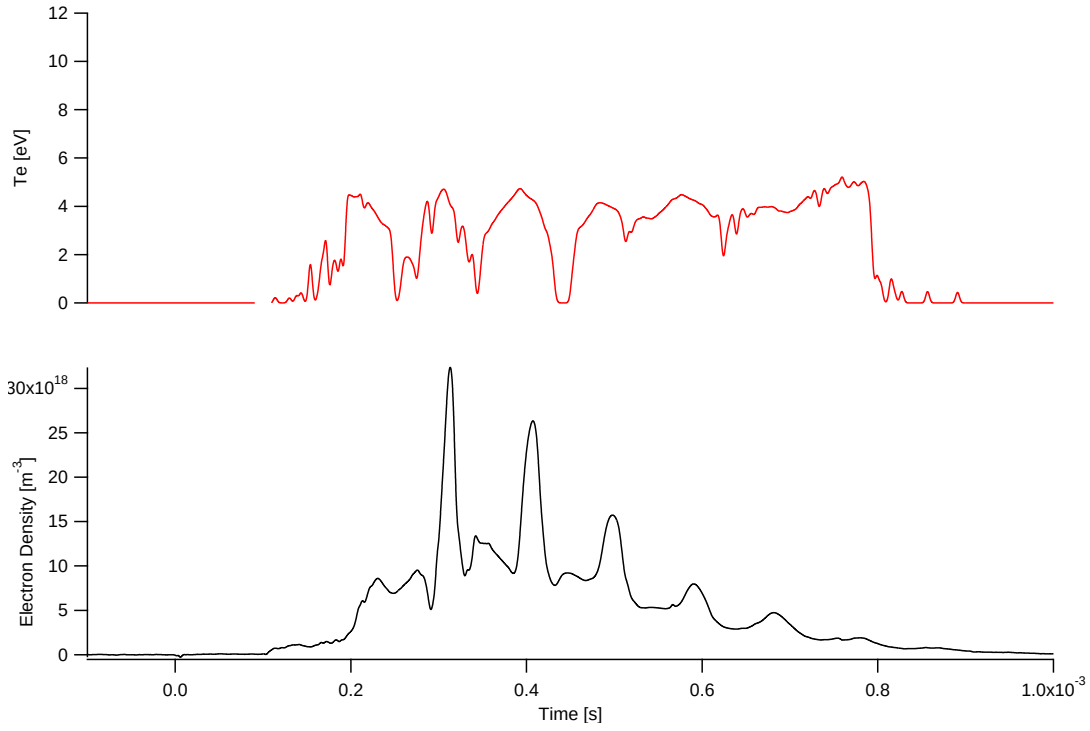

Figure 7.13: Detailed time evolution of electron density and temperature at Position 1 for a 950-V, 185-μs, 14-mTorr argon discharge

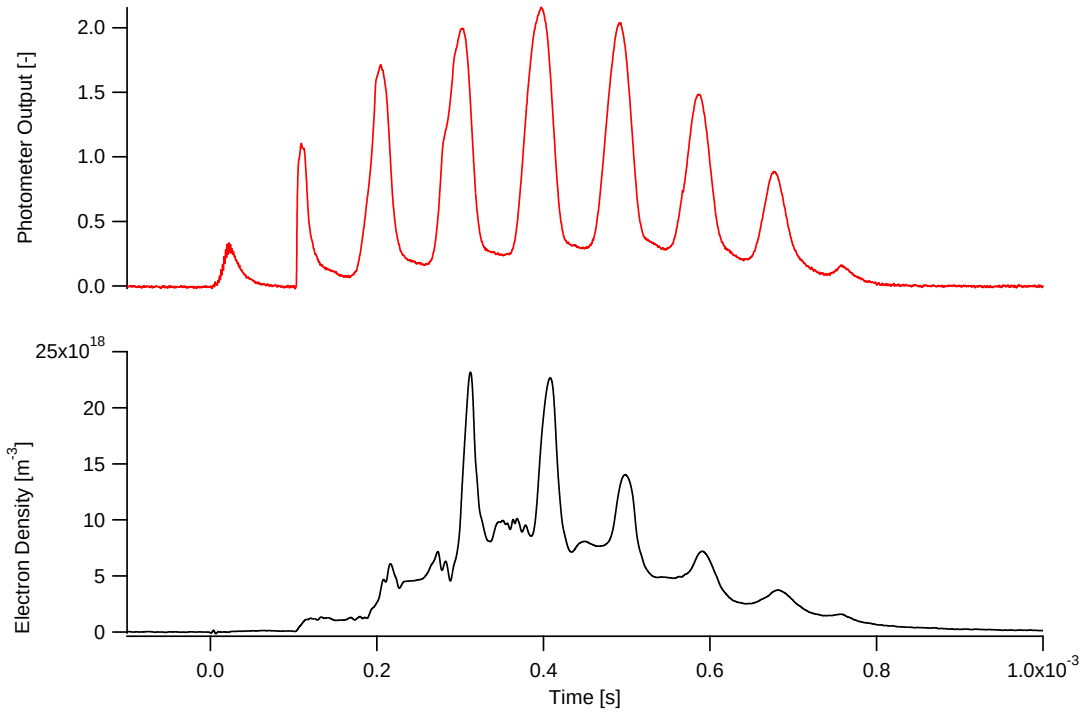

Figure 7.14: Real-time comparison of triple probe measured plasma density at Position 1 and wide-angle photometer results for an 850-V, 185-μs, 14-mTorr argon discharge

Continuing this analysis, but now analyzing the photometer response in Figures 7.14 and 7.15 more interesting trends arise. First, the primary discharge appears to have quite a weak density response ($1 \times 10^{18}\ m^{-3}$) at Position 1, and yet has a large photometer response.

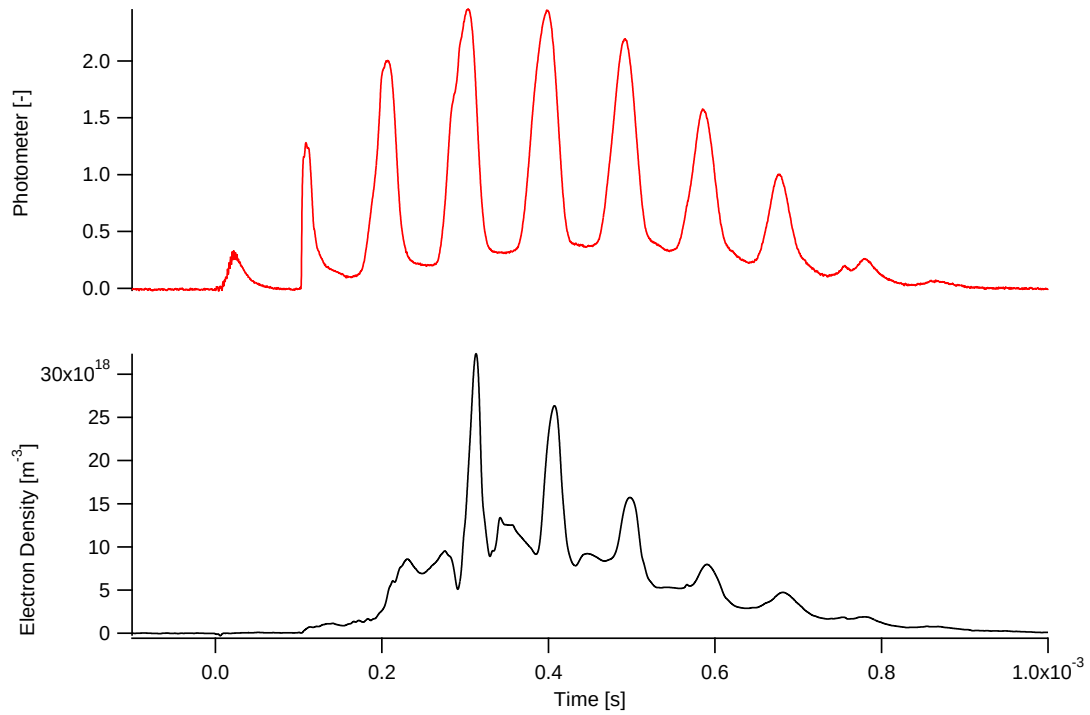

Figure 7.15: Real-time comparison of triple probe measured plasma density at Position 1 and wide-angle photometer results for a 950-V, 185-μs, 14-mTorr argon discharge

Figures 7.16 and 7.17 show density results at Position 1 for various discharge energies. In the data it is quite clear at what energies the turn-on conditions lie for the initial discharge. There is little or no plasma at Position 1 for less than 850 volts on the discharge coil for the secondary and tertiary discharges, the turn-on transition is between 750 and 850 V. Additionally, as shown with the photometer data, it appears that the initial heating and compression is outside of the plasma probes area and as the current reverses, a high density $1 \times 10^{19}\ m^{-3}$ pulse passes by the triple probe. Finally, as shown numerous times, as discharge energy increases both plasma content and lifetime increases.

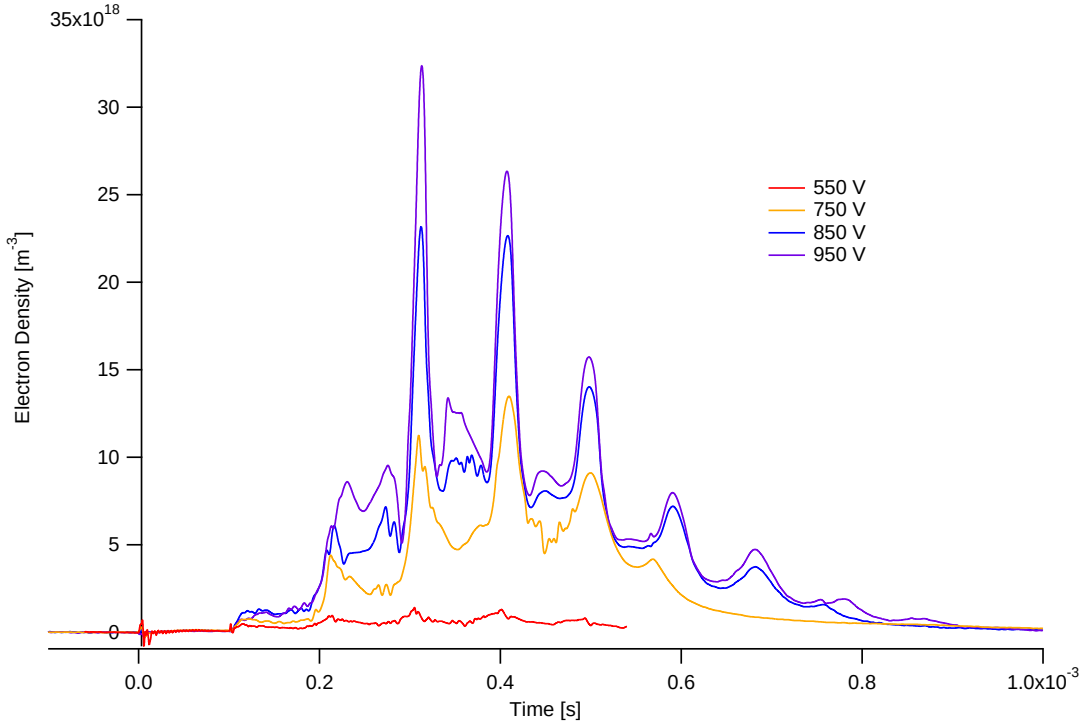

Figure 7.16: Summary of plasma density results at Position 1 for 185-μs, 14-mTorr argon discharges for various energies

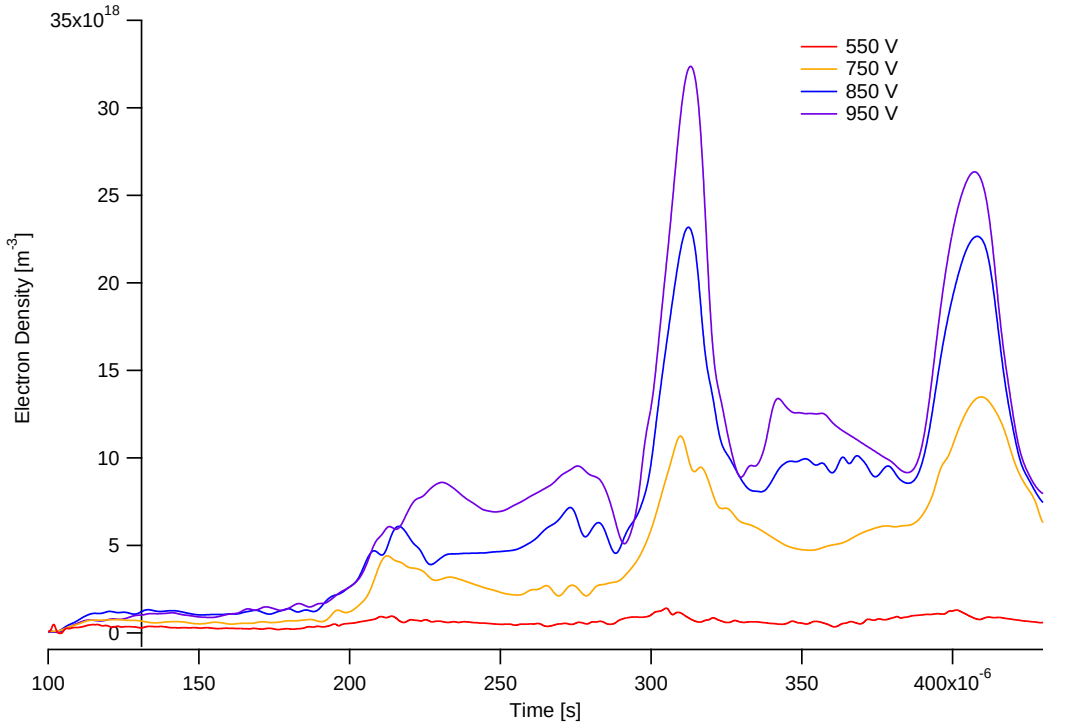

Figure 7.17: Close view of plasma density results at Position 1 for 185-μs, 14-mTorr argon discharges for various energies showing the primary and secondary discharges

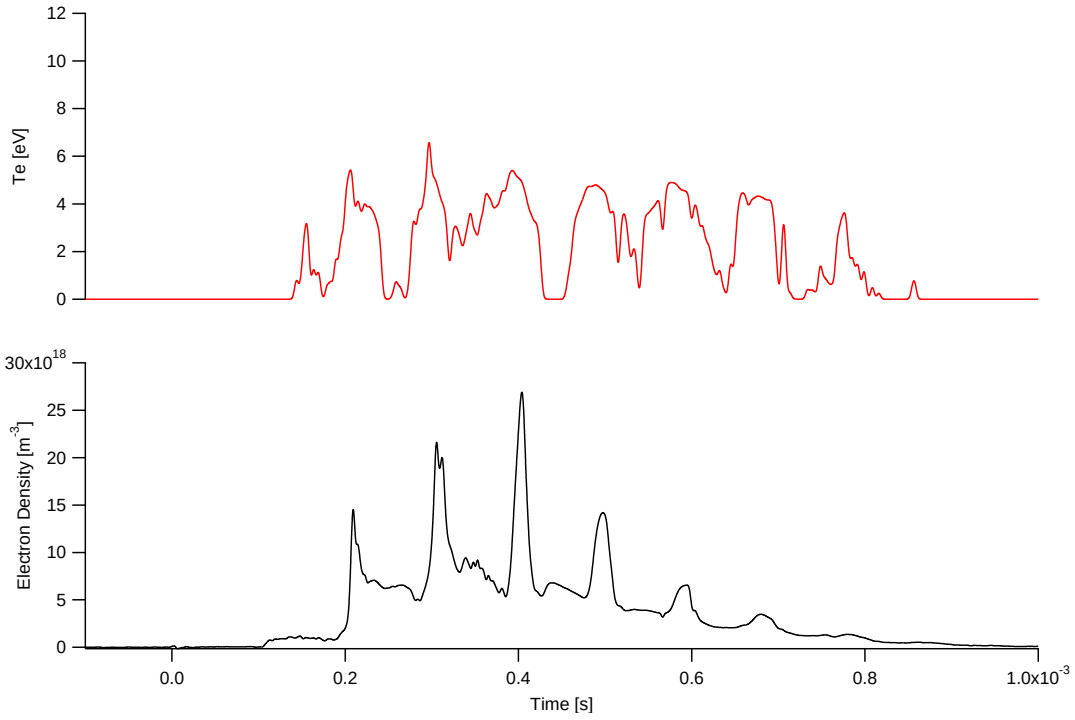

Figure 7.18: Detailed time evolution of electron density and temperature at Position 1 for a 950-V, 185-μs, 11-mTorr argon discharge

Figures 7.20–7.23 show plasma density at Position 1 as a function of background neutral pressure. Position 1 does not yield any new surprises with 14 mTorr being an optimal gas density for a given input energy. The 20-mTorr discharge case does not extend to Position 1 until some time (at approximately 300 μs) later than the primary and secondary discharges. At 950-V the initial discharge for both 11 mTorr and 14 mTorr are the same with a peak density of approximately $1 \times 10^{18}\ m^{-3}$, and the average density during the second discharge is also the same (at approximately $8 \times 10^{18}\ m^{-3}$). One important note is that at 11 mTorr the discharge plasma reaches Position 1 approximately 20 μs before the initial plasma reaches Position 1 for the 14-mTorr case. Finally, while the discharge structures are similar for all of the 14-mTorr, 11-mTorr, 850- and 950-V cases, the peak plasma densities are quite variable between 20 and $35 \times 10^{18}\ m^{-3}$.

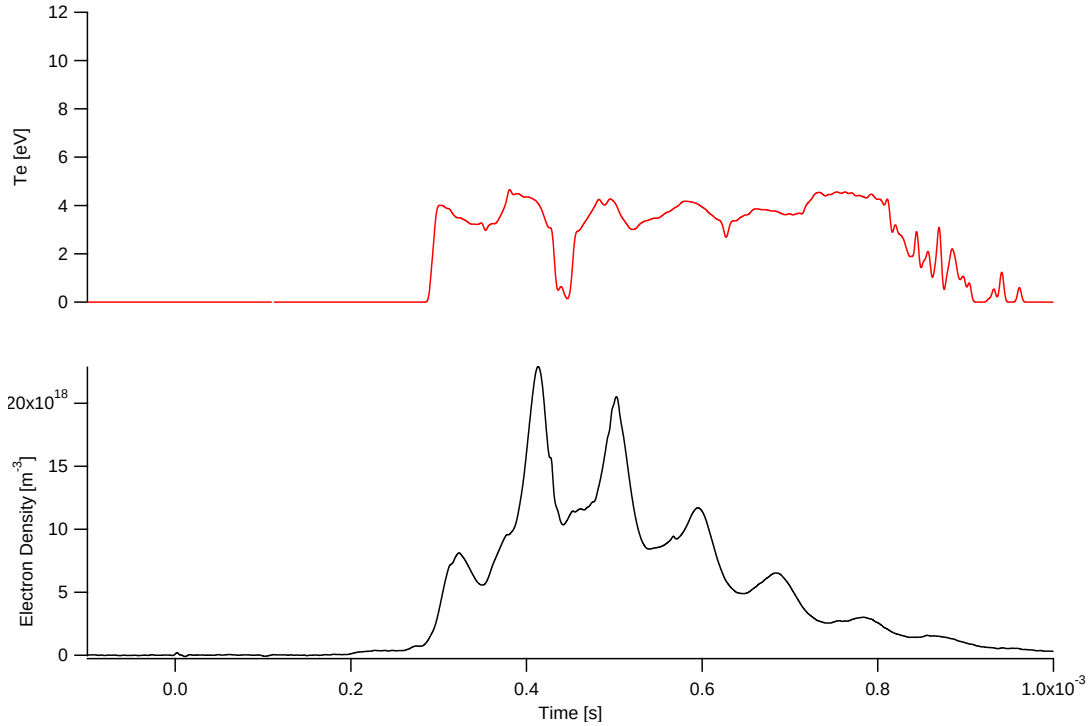

Figure 7.19: Detailed time evolution of electron density and temperature at Position 1 for a 950-V, 185-μs, 20-mTorr argon discharge

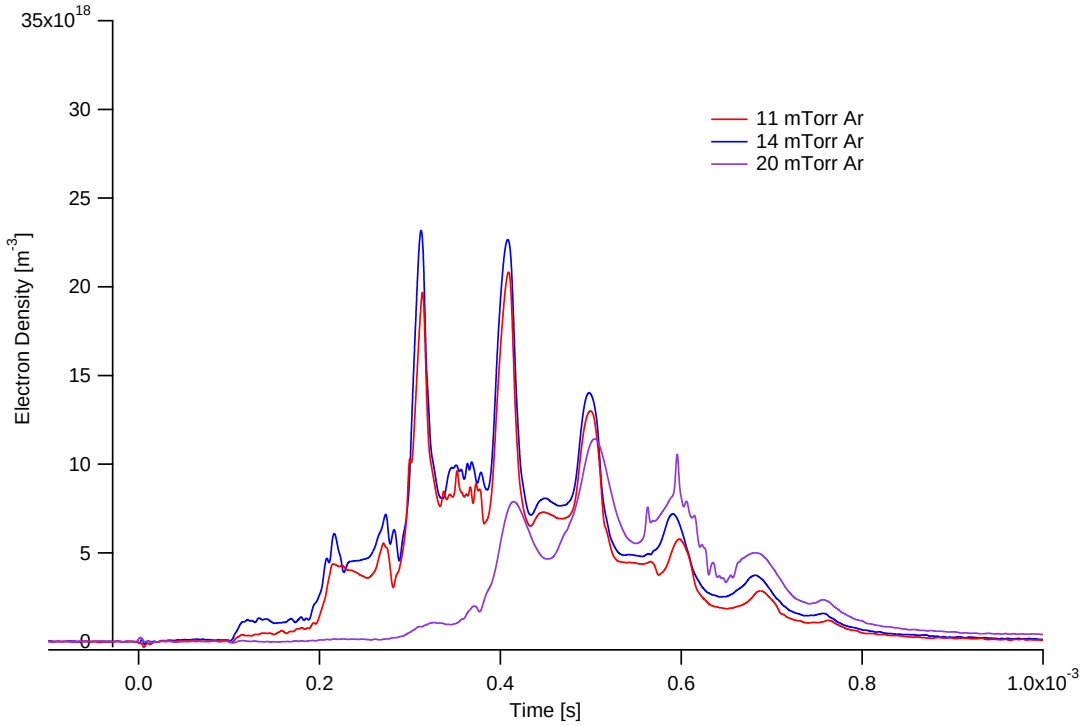

Figure 7.20: Summary of plasma density results at Position 1 for 185-μs, 850-V argon discharges for various neutral fill pressures

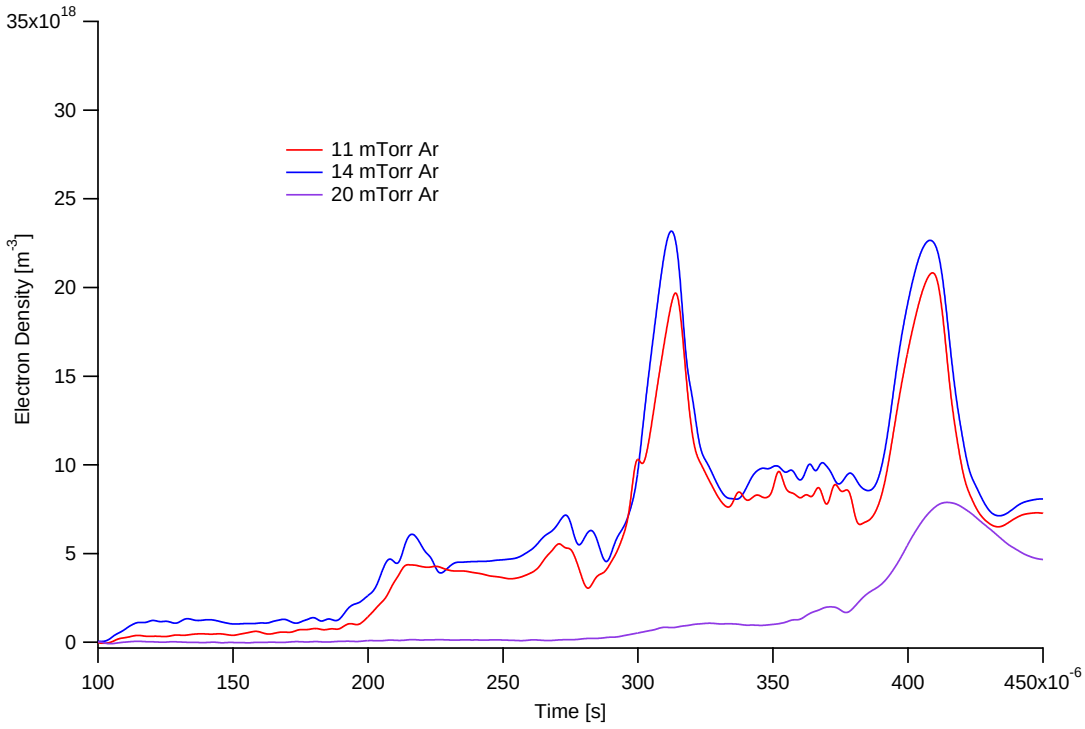

Figure 7.21: Close view of plasma density results at Position 1 for 185-μs, 850-V argon discharges for various neutral fill pressures showing the primary, secondary, and partial tertiary discharges

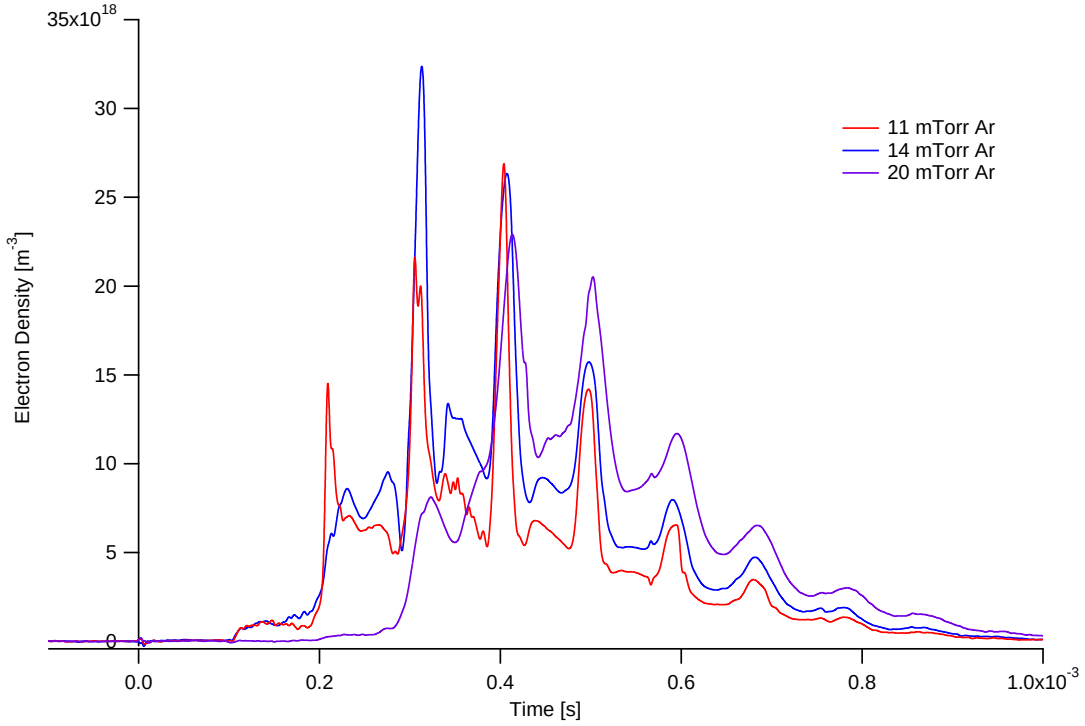

Figure 7.22: Summary of plasma density results at Position 1 for 185-μs, 950-V argon discharges for various neutral fill pressures

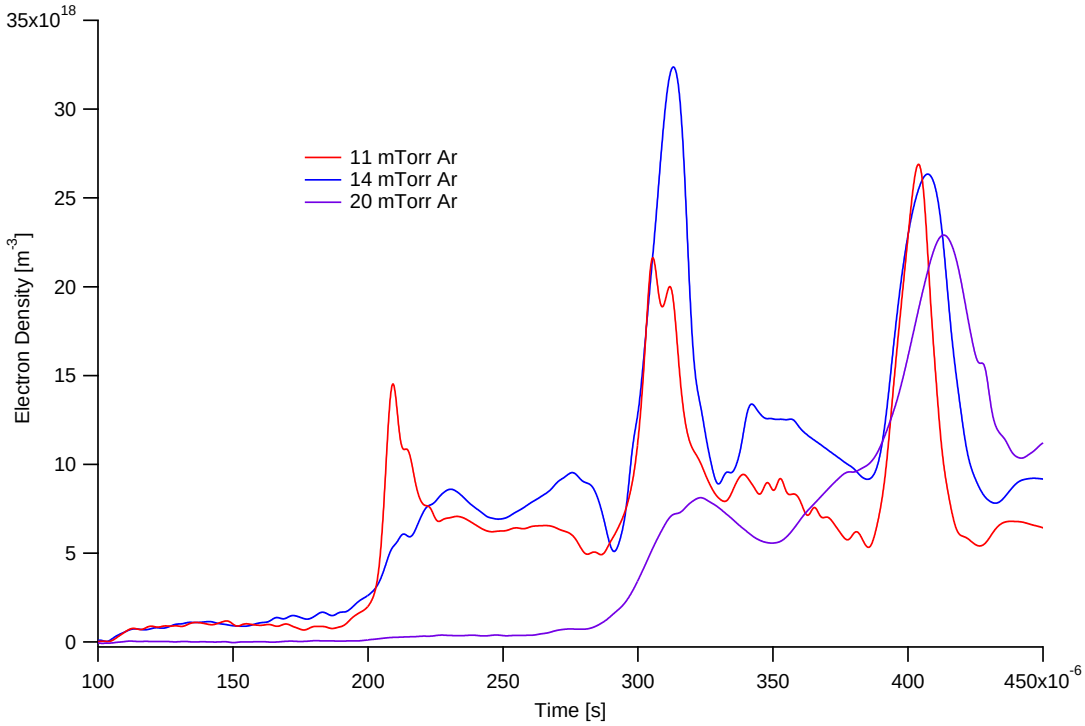

Figure 7.23: Close view of plasma density results at Position 1 for 185-μs, 950-V argon discharges for various neutral fill pressures showing the primary and secondary discharges

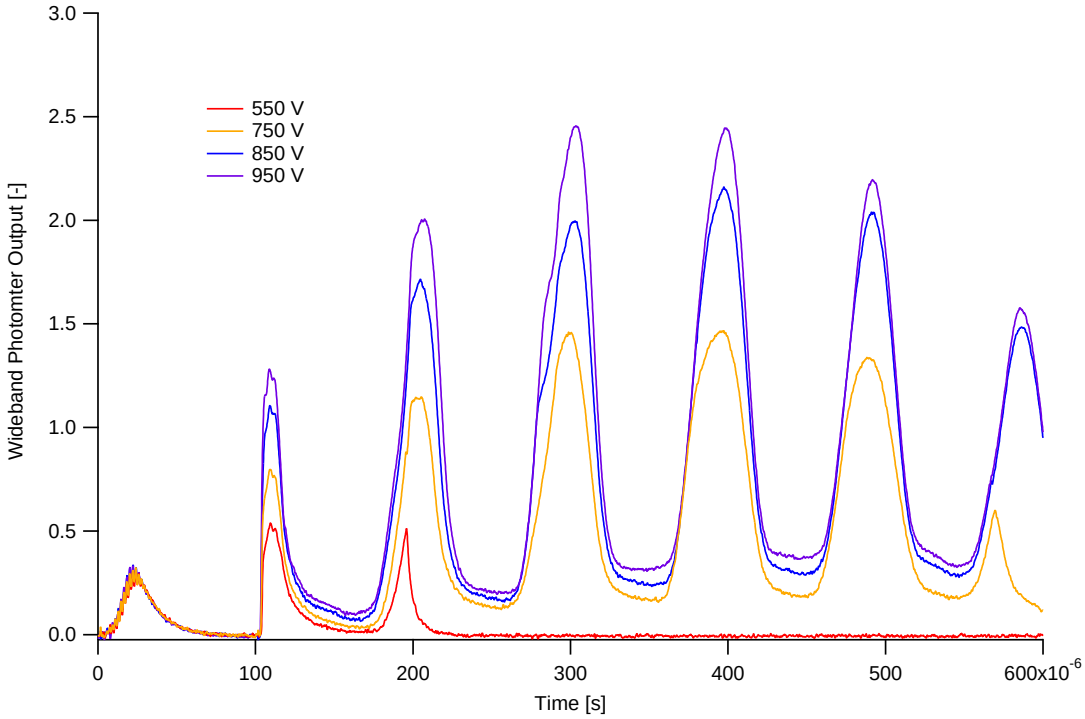

Figure 7.24: Detailed time evolution of wide-angle photometer output at Position 1 for a 950-V, 185-μs, 14-mTorr argon discharge

To verify that the findings of the previous Chapters is consistent, Figures 7.24, 7.25, and 7.26 show detailed views of a 185-μs, 950-V argon discharge at various pressures. Additionally, Figure 7.26 shows the peak photometer data as a function of neutral pressure, validating the choice of an optimal 14 mTorr pressure. In these studies the focus was no longer to investigate the finer details of pressure effects, so 3 pressure data points are sufficient.

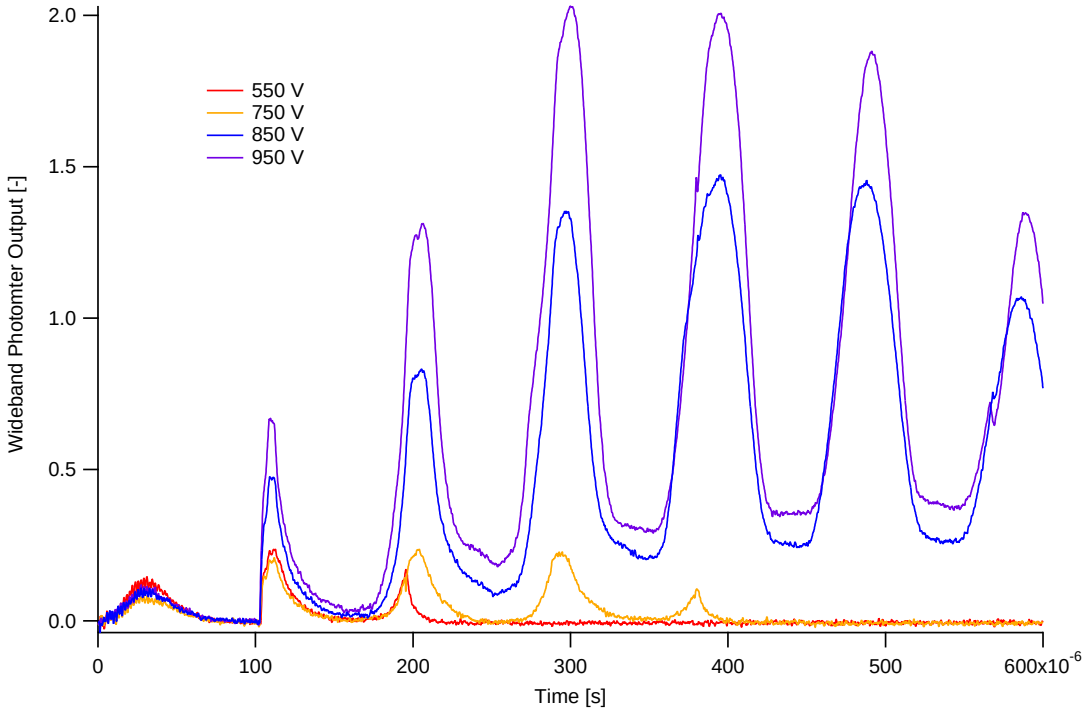

Figure 7.25: Detailed time evolution of wide-angle photometer output at Position 1 for a 950-V, 185-μs, 20-mTorr argon discharge

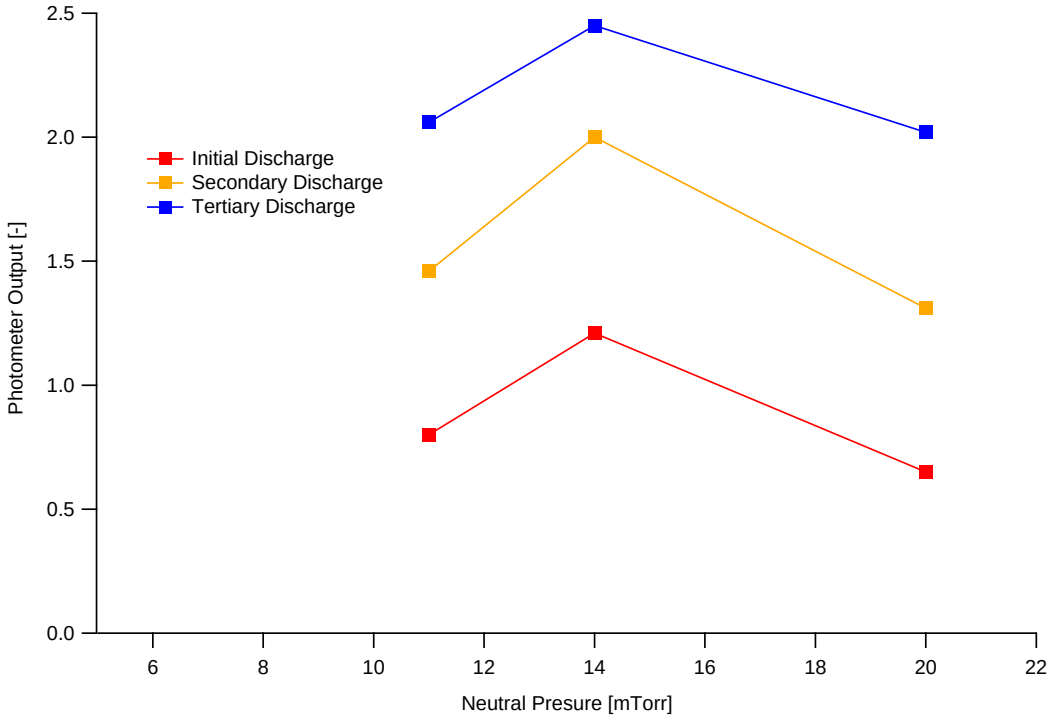

Figure 7.26: Peak photometer results as a function of background pressure for multiple discharges at 14 mTorr and 950 V

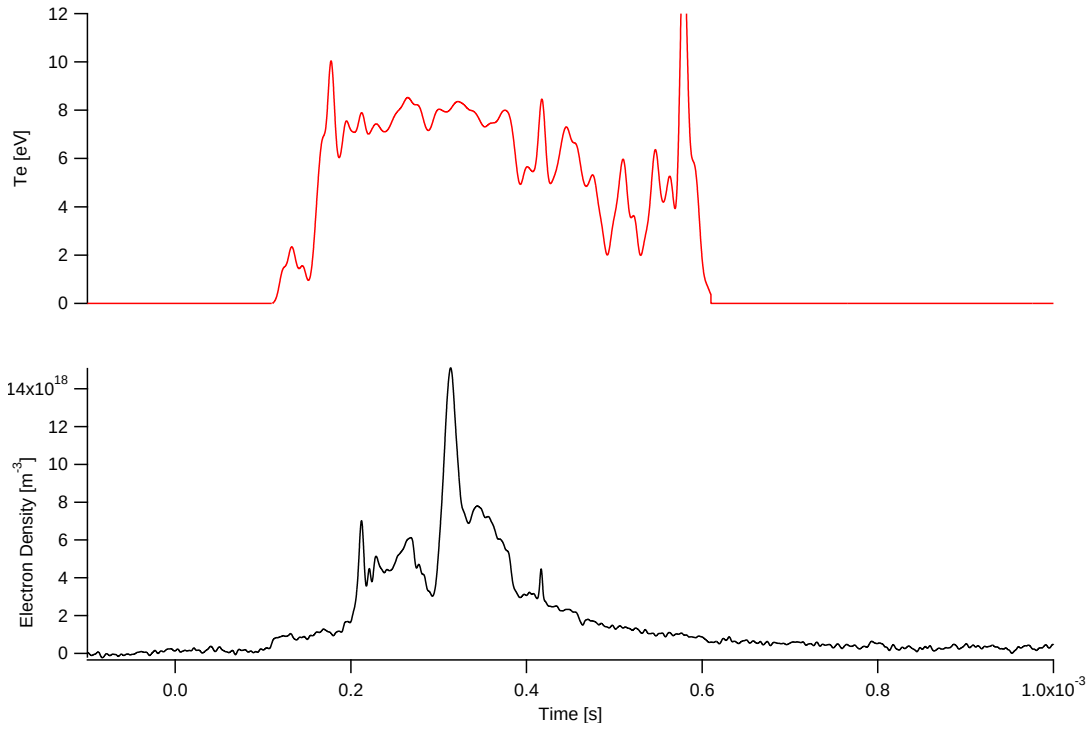

Figure 7.27: Detailed time evolution of electron density and temperature at Position 2 for an 850-V, 185-μs, 14-mTorr argon discharge

7.3.2.2 Argon Position 2

Figures 7.27–7.35 continue the exploration of the density and temperature variations at Position 2, approximately 7 cm from the bottom of the coil. At Position 2, electron temperature was measured between 8.2–8.5 eV for the various operating conditions shown here, significantly higher than Position 1. This effect is anticipated for an FRC that is centered at the midpoint on the axis. Also as expected there is a density increase from P1 for most of the neutral density and coil energy conditions. The high density turn-on delay is further seen at Position 2, indicating that it is singularly a function of input energy and E_θ and not a geometrical consequence.

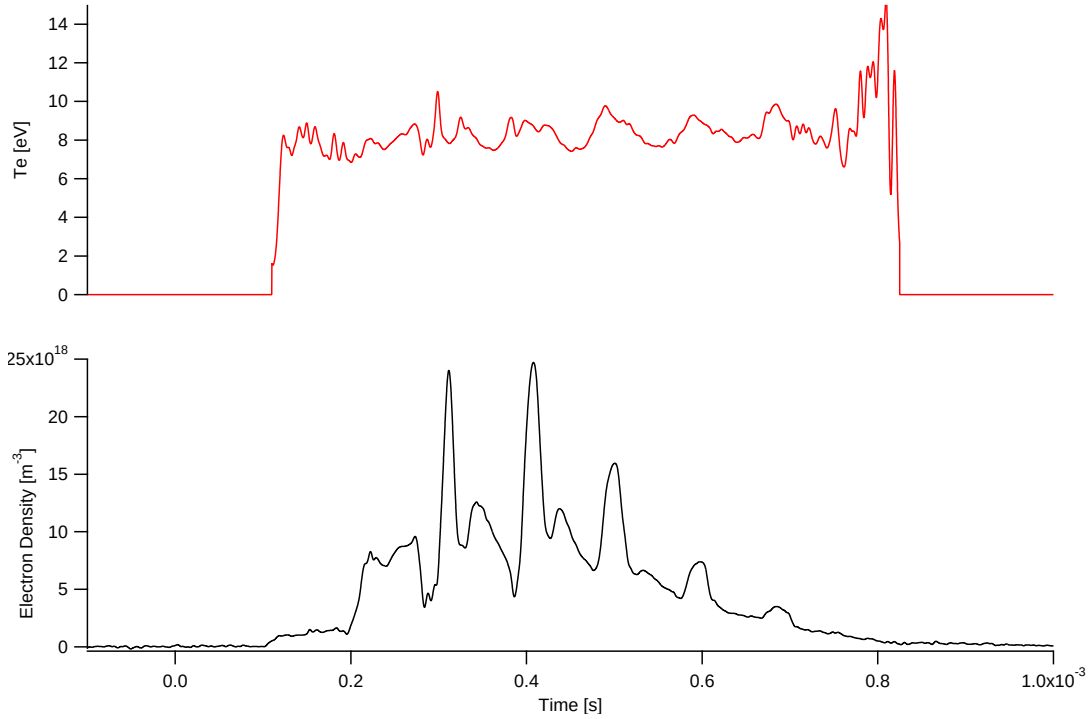

Figure 7.28: Detailed time evolution of electron density and temperature at Position 2 for a 950-V, 185-μs, 14-mTorr argon discharge

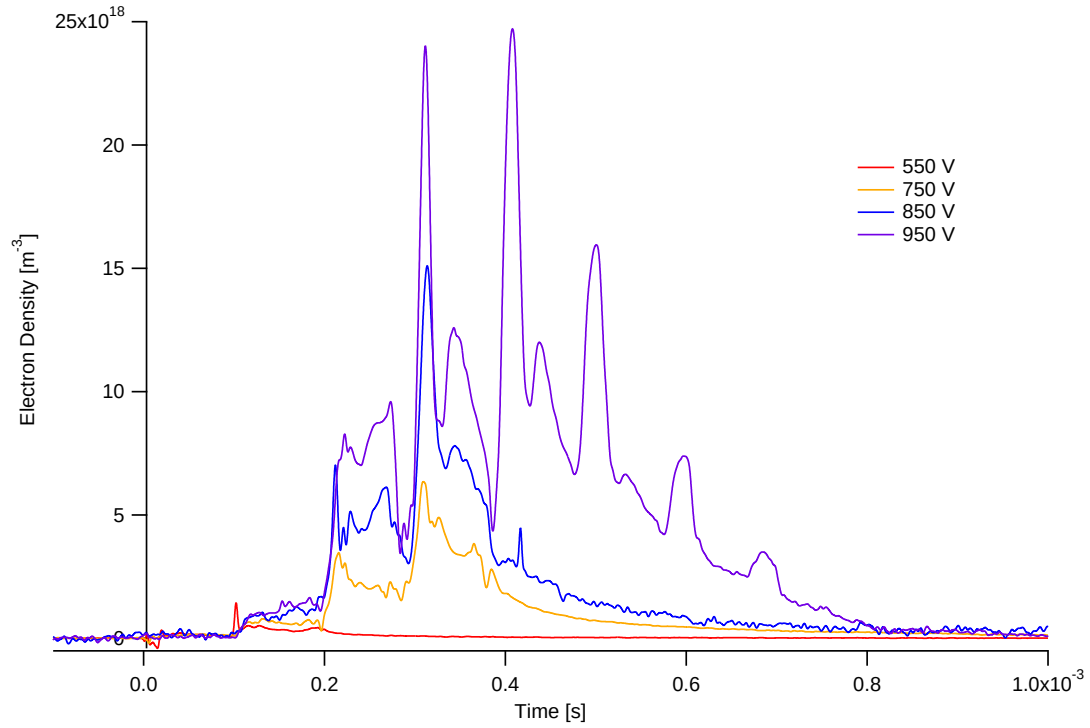

Figure 7.29: Summary of plasma density results at Position 2 for 185-μs, 14-mTorr argon discharges for various energies

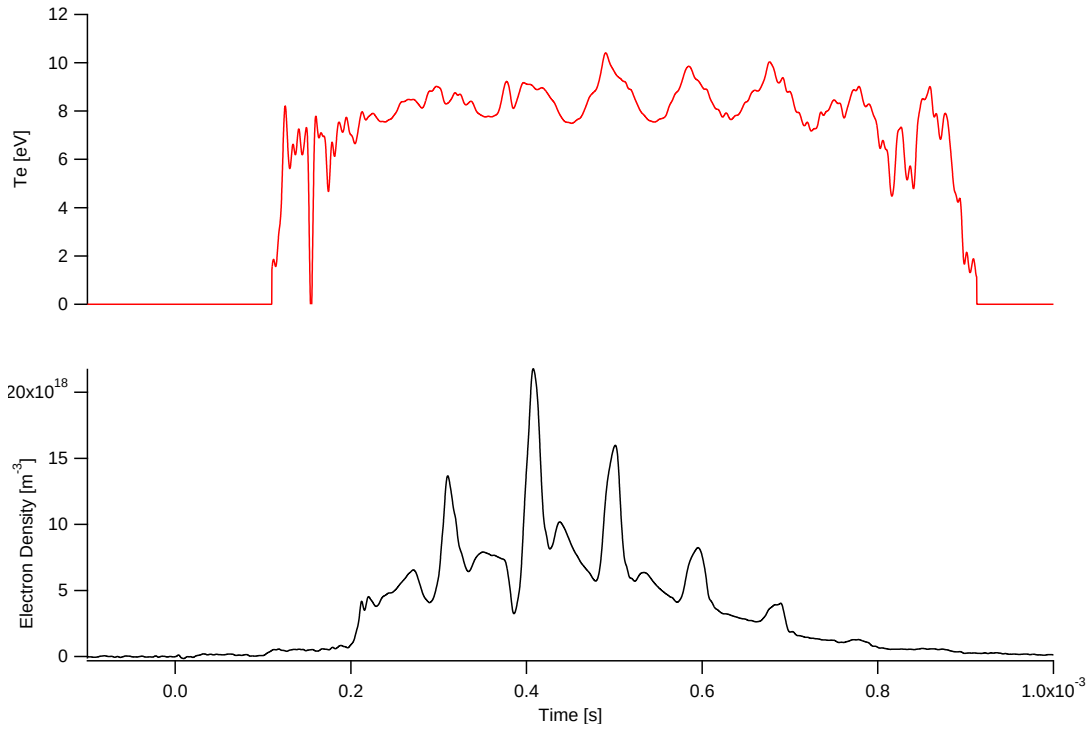

Figure 7.30: Detailed time evolution of electron density and temperature at Position 2 for a 950-V, 185 μs, 11-mTorr argon discharge

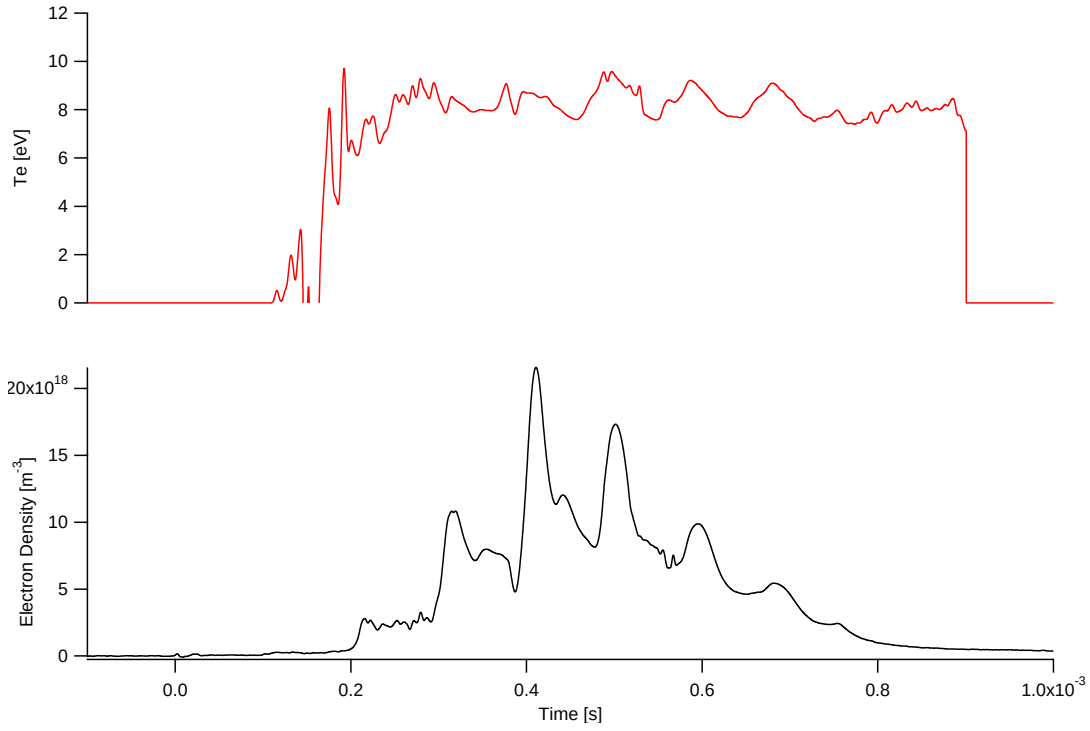

Figure 7.31: Detailed time evolution of electron density and temperature at Position 2 for a 950-V, 185 μs, 20-mTorr argon discharge

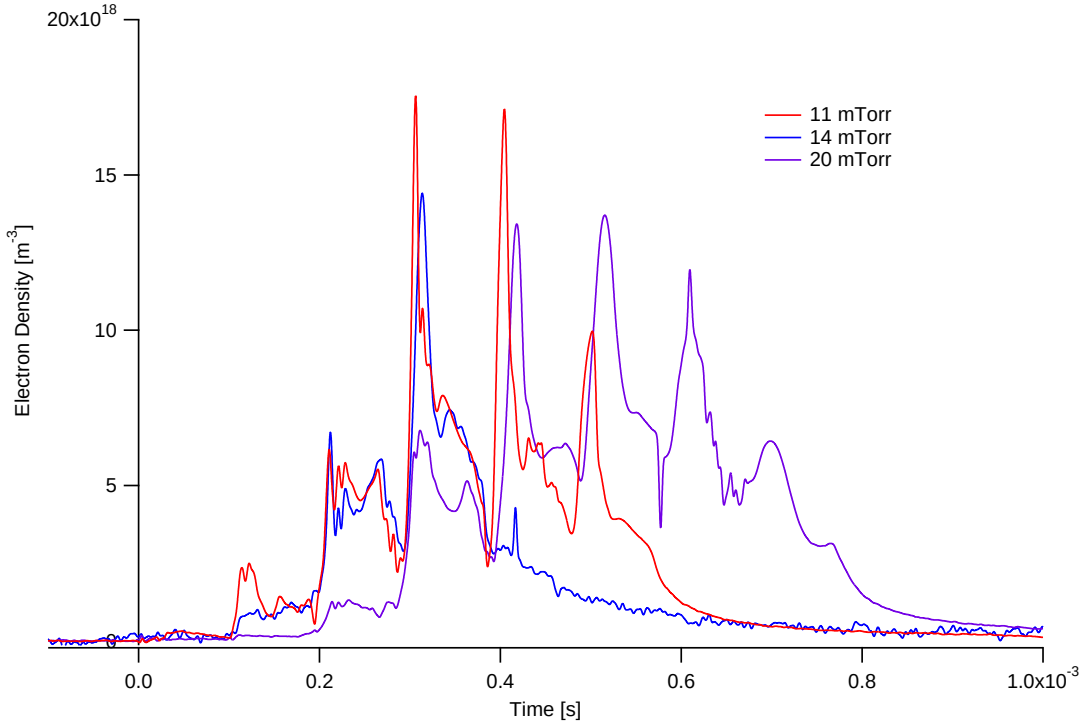

Figure 7.32: Summary of plasma density results at Position 2 for 185-μs, 850-V argon discharges for various neutral fill pressures

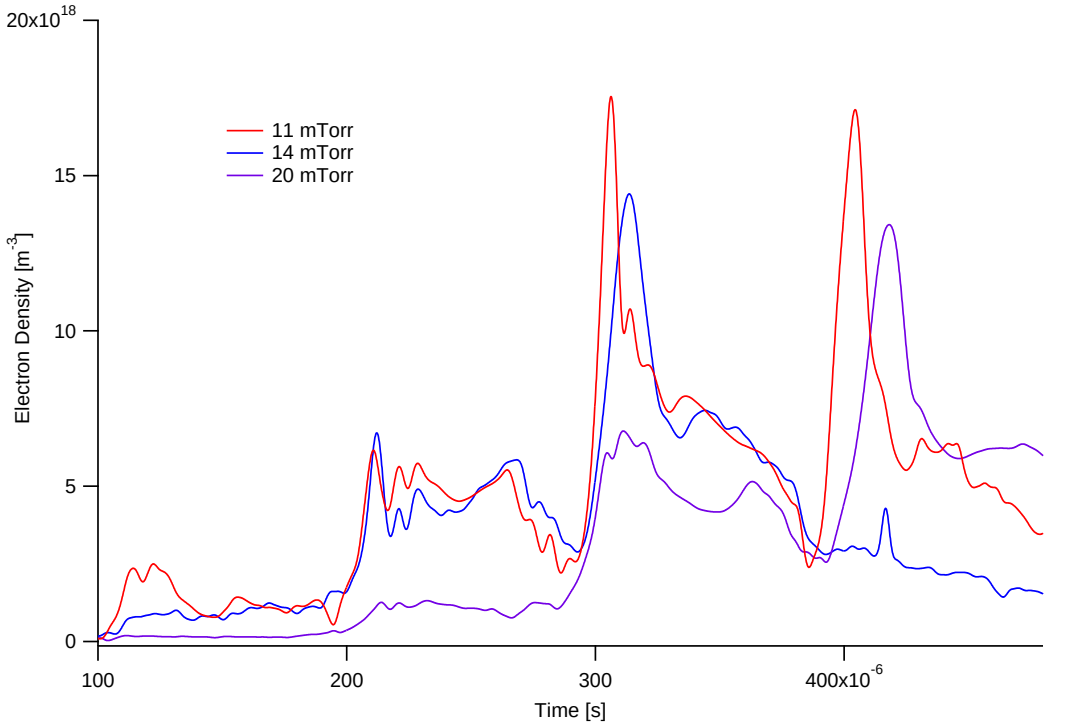

Figure 7.33: Close view of plasma density results at Position 2 for 185-μs, 850-V argon discharges for various neutral fill pressures showing the primary and secondary discharges

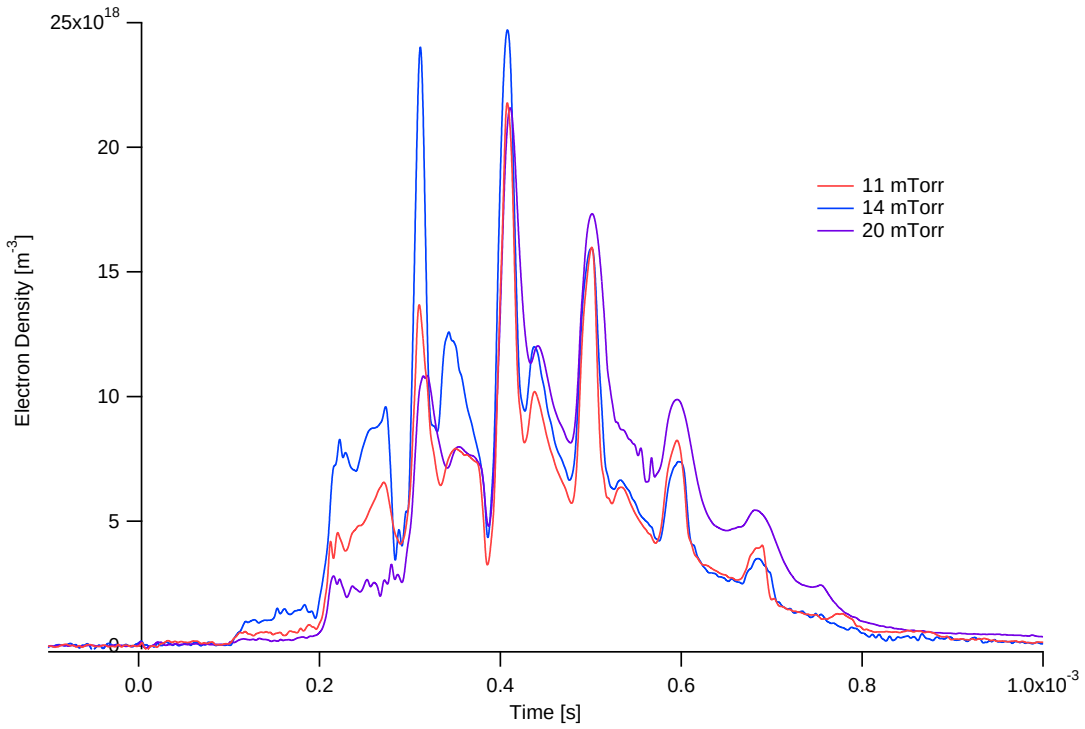

Figure 7.34: Summary of plasma density results at Position 2 for 185-μs, 950-V argon discharges for various neutral fill pressures

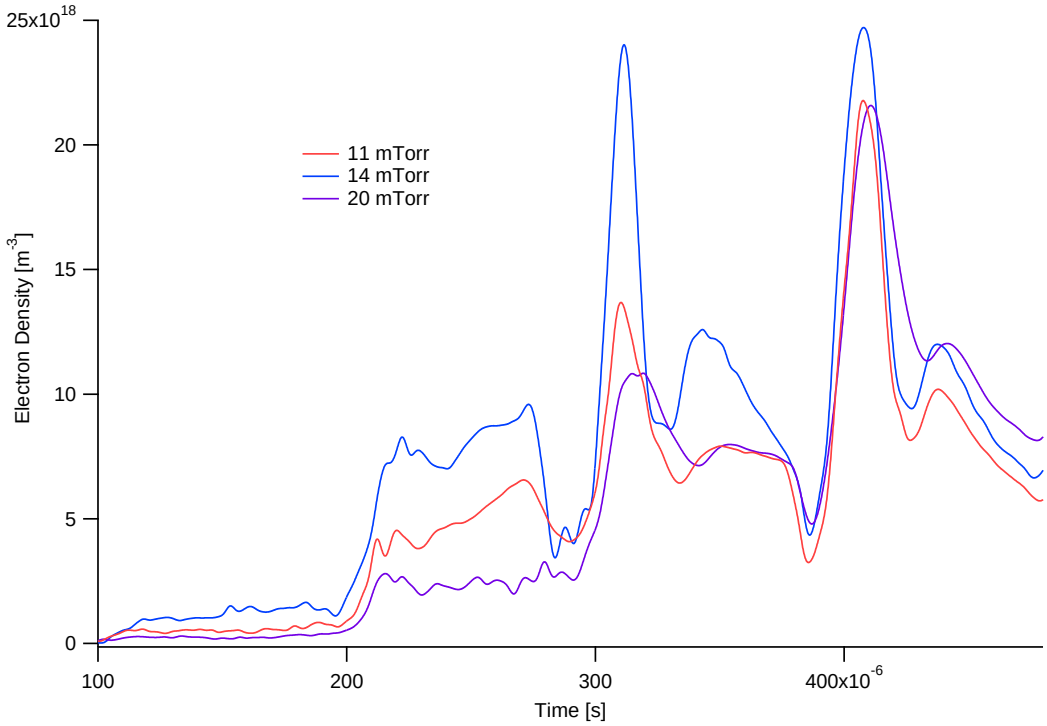

Figure 7.35: Close view of plasma density results at Position 2 for 185-μs, 950-V argon discharges for various neutral fill pressures showing the primary and secondary discharges

7.3.2.3 Argon Position 3

Position 3, approximately 13 cm inside the discharge coil yielded quite a few surprises. First, the triple probe had a significant effect on plasma formation, specifically pre-ionization initialization of the plasma. Having the cold, 0.25 in. alumina rod extending through half of the discharge coil (axially) tended to drastically reduce the pre-ionization plasma available for the main discharge. Specifically, the glow discharge voltage (and power) had to increase in order to provide sufficient electrons for the pre-ionization ringing discharge to be effective. Using photometer and density data, the glow discharge was increased in order to provide a turn-on condition as seen in the earlier glow discharge study. For these data, the glow discharge PPI voltage was increased to 7 kV (rather than 5 kV), although the power was still primarily a function of background gas density. As before, once an initial turn-on voltage is reached, changes in DC glow discharge results in minor changes in bulk plasma formation during the main discharge. Figures 7.36-7.40 detail electron temperature and density information for Position 3 as a function of coil voltage and neutral density. Electron temperatures at Position 3 were found to be 4.6–7.3 eV.

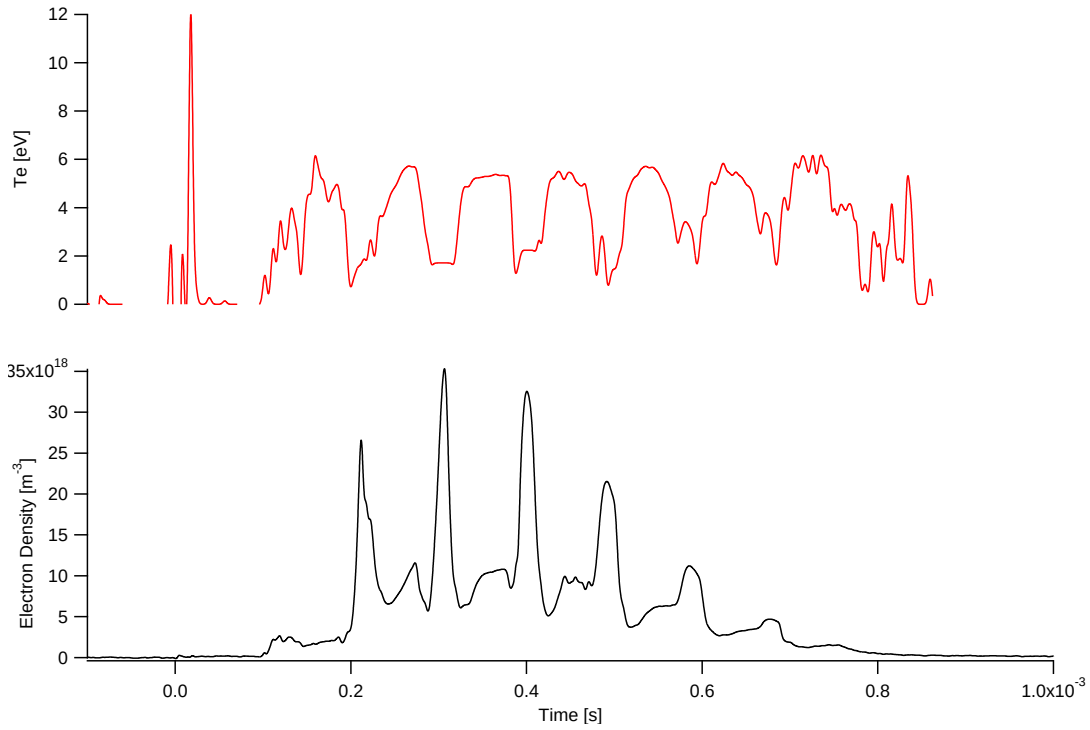

Figure 7.36: Detailed time evolution of electron density and temperature at Position 3 for a 950-V, 185-μs, 14-mTorr argon discharge

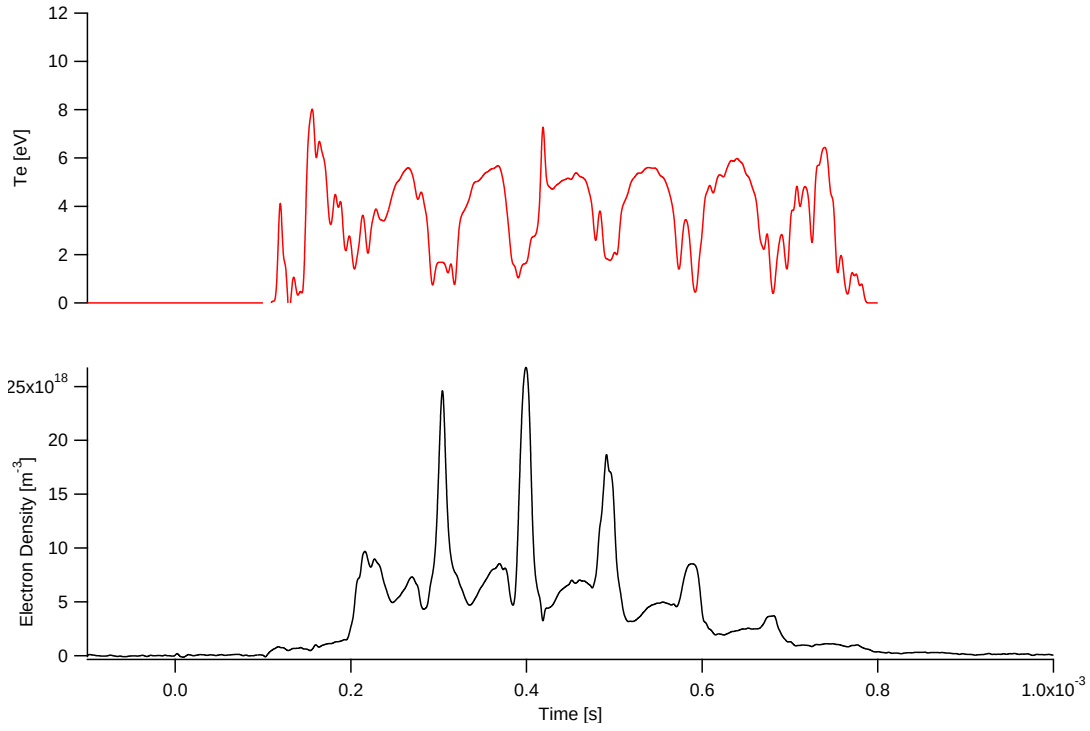

Figure 7.37: Detailed time evolution of electron density and temperature at Position 3 for a 950-V, 185-μs, 11-mTorr argon discharge

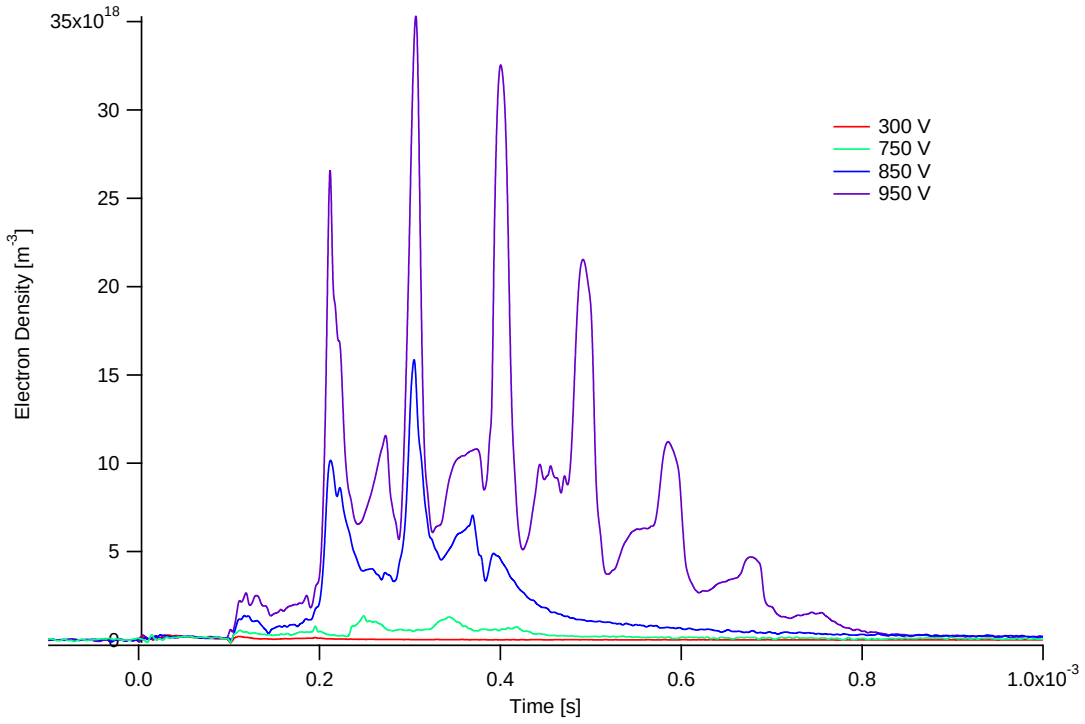

Figure 7.38: Summary of plasma density results at Position 3 for 185-μs, 14-mTorr argon discharges for various energies

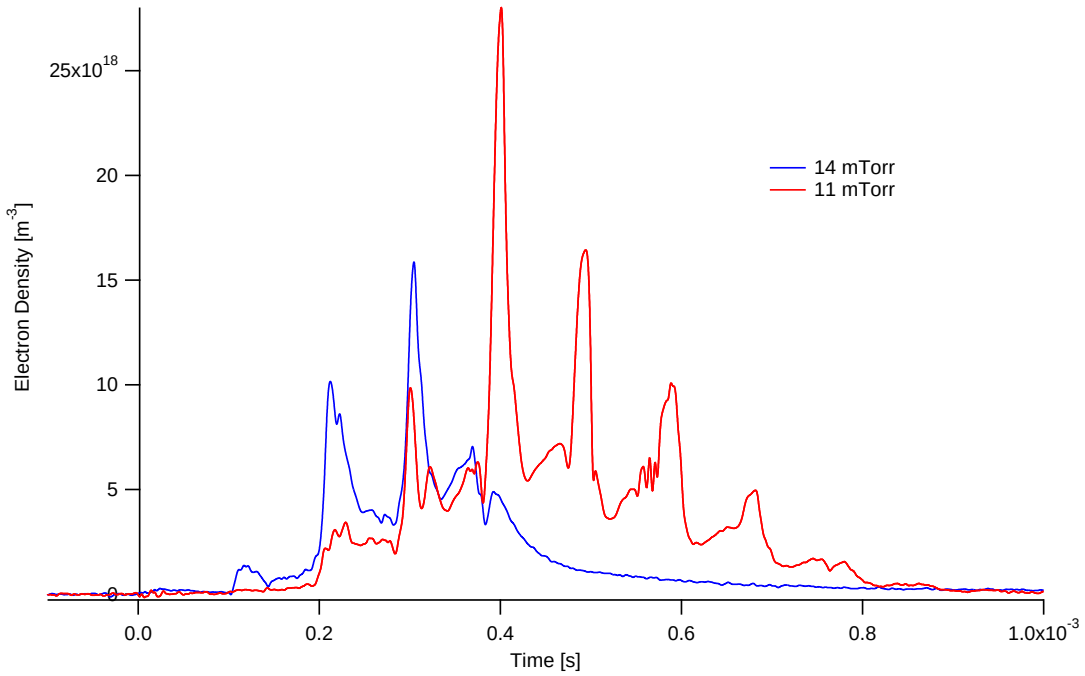

Figure 7.39: Summary of plasma density results at Position 3 for 185-μs, 850-V argon discharges for various neutral fill pressures

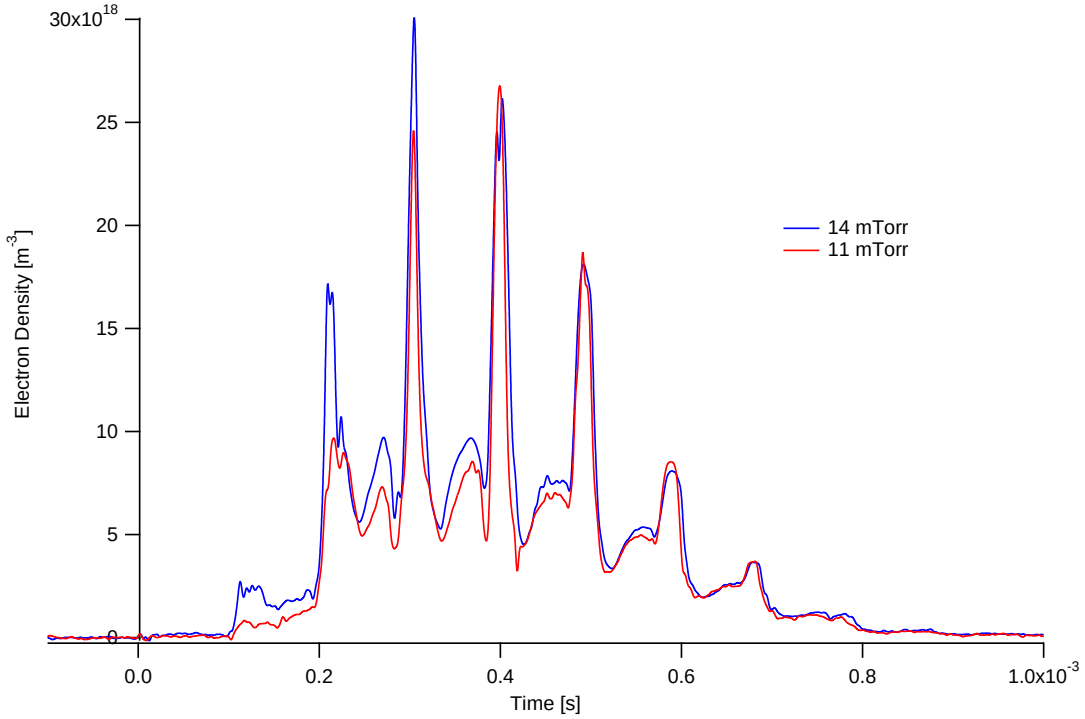

Figure 7.40: Summary of plasma density results at Position 3 for 185-μs, 950-V argon discharges for various neutral fill pressures

7.3.3 Summary of Argon Results

To summarize the above results, Figures 7.41, 7.42, and 7.43 show the 14-mTorr argon data as a function of probe location. The are some very clear trends that can be seen in the data, firstly that the bulk of the ionization and plasma density is near the center of the discharge coil and extends (in time) out to the other probe locations later in each discharge. This is shown most clearly in the contour plots which detail the early formation (in the center), the continued heating and compression in the two central probes (Positions 2 and 3), and then finally the later heating and axial expansion to the outer probe. One interesting phenomenon appears to be a function of the higher density neutral gas at the outer edge of the coil; as the first main compression event (called the secondary discharge) ends the hot, dense plasma is swept from the chamber (either as a single directional FRC or axially as the FRC destabilizes) and the next reversal and heating occurs first at the outer edges of the coil for the 850-V case, and simultaneously at the outer and central regions of the coil for the high E_θ 950-V case. As can also been seen in the end-on photography in Figures 7.7 and 7.9 the higher voltage cases are more centered (though the densities at Position 1 and 2 are still greater in both cases), compress to the location of the triple probe earlier and exist for longer (200–275 μs).

Figures 7.44 and 7.45 show graphically contour plots of density versus time as a function of axial location (at the center of the annulus) for 11 and 20 mTorr at 950 V. For 11 mTorr the effect of gas expulsion and end heating are even more prominent, while for 20 mTorr the large gas density appears to be axially centered.

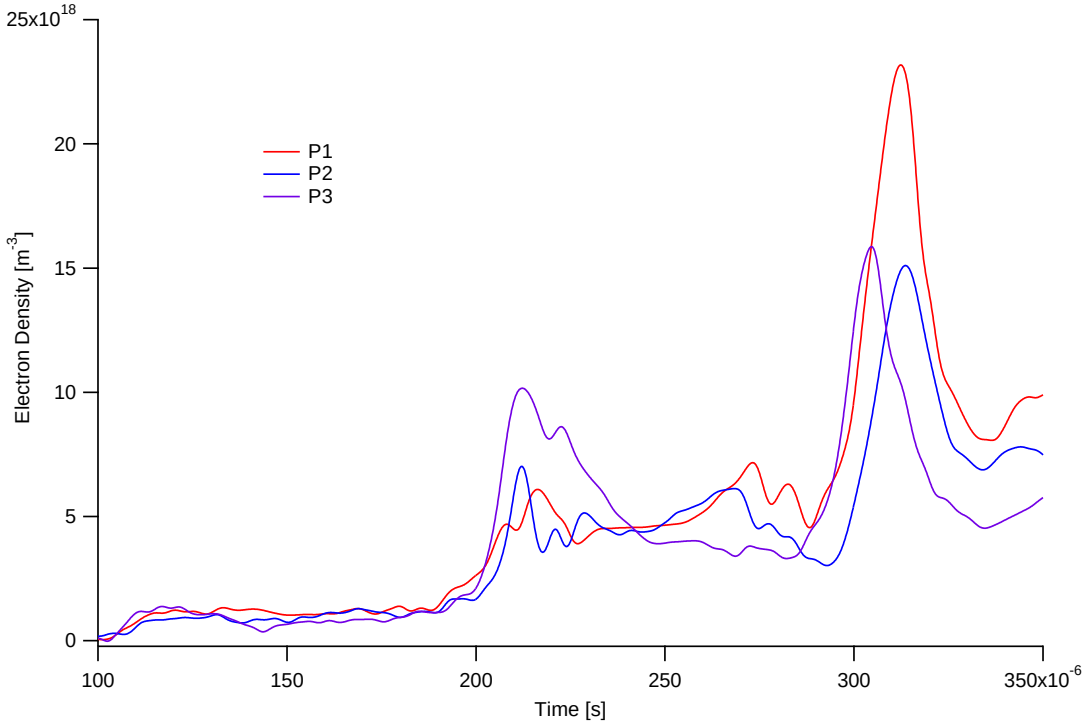

Figure 7.41: Detailed axial density scans for 185-μs, 14-mTorr, 850-V argon discharges showing initial ionization, primary, and secondary discharges

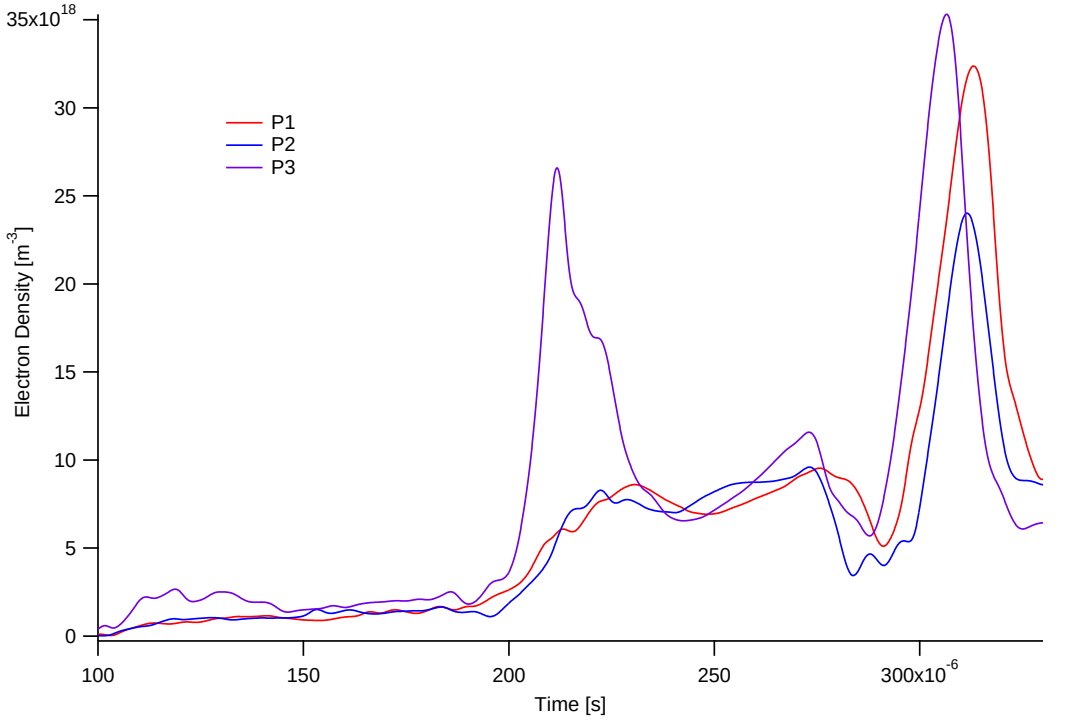

Figure 7.42: Detailed axial density scans for 185-μs, 14-mTorr, 950-V argon discharges showing initial ionization, primary, and secondary discharges

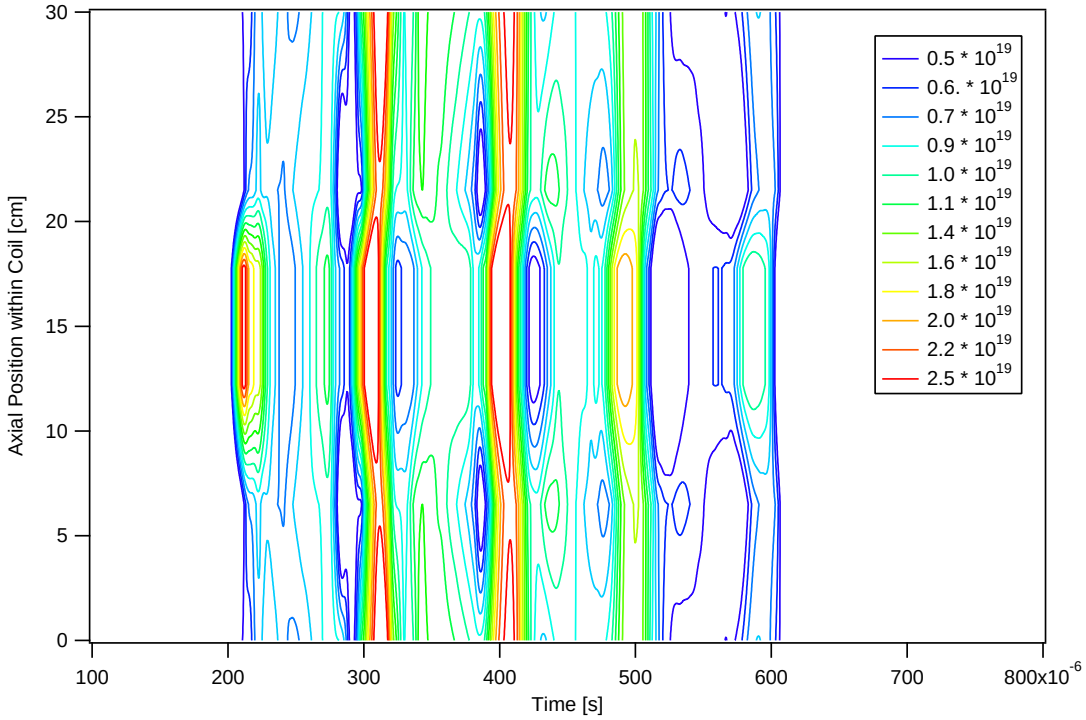

Figure 7.43: Axial density scan contours for 185-μs, 14-mTorr, 950-V argon discharges showing plasma density (axially, along centerline) as a function of time

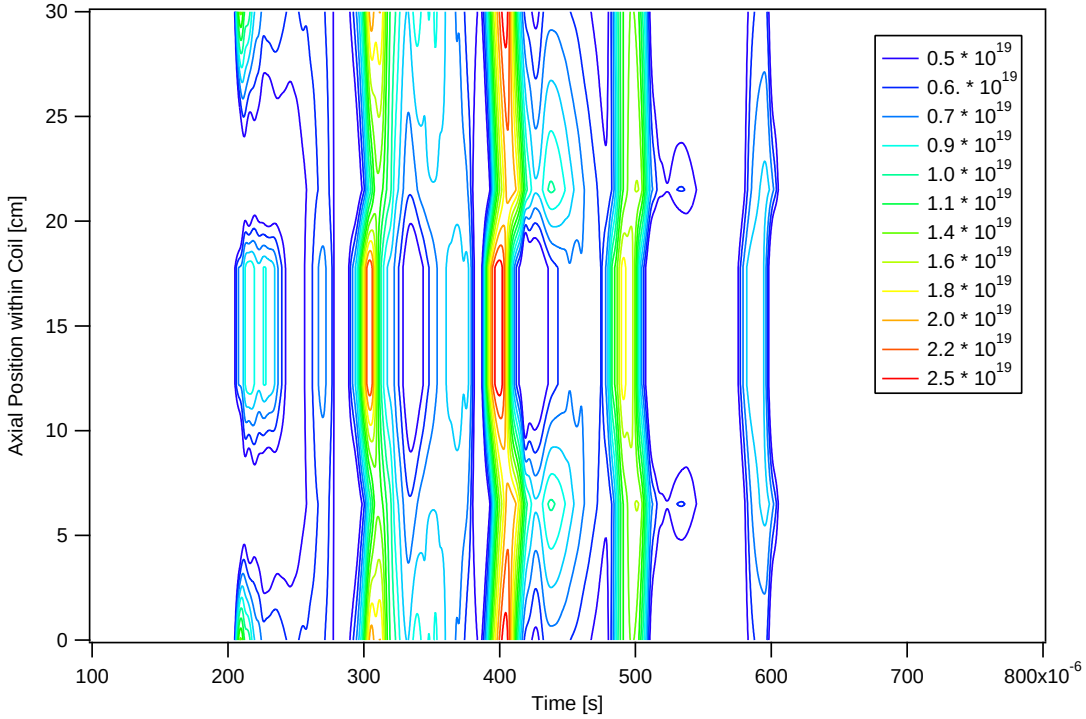

Figure 7.44: Axial density scan contours for 185-μs, 11-mTorr, 950-V argon discharges showing plasma density (axially, along centerline) as a function of time

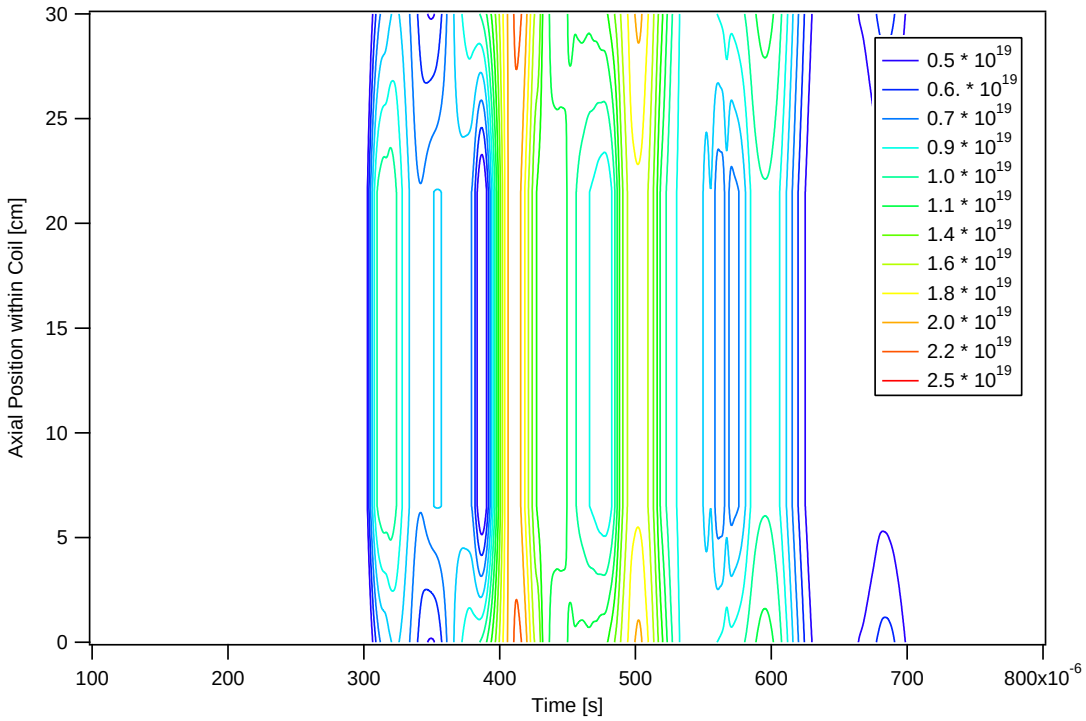

Figure 7.45: Axial density scan contours for 185-μs, 20-mTorr, 950-V argon discharges showing plasma density (axially, along centerline) as a function of time

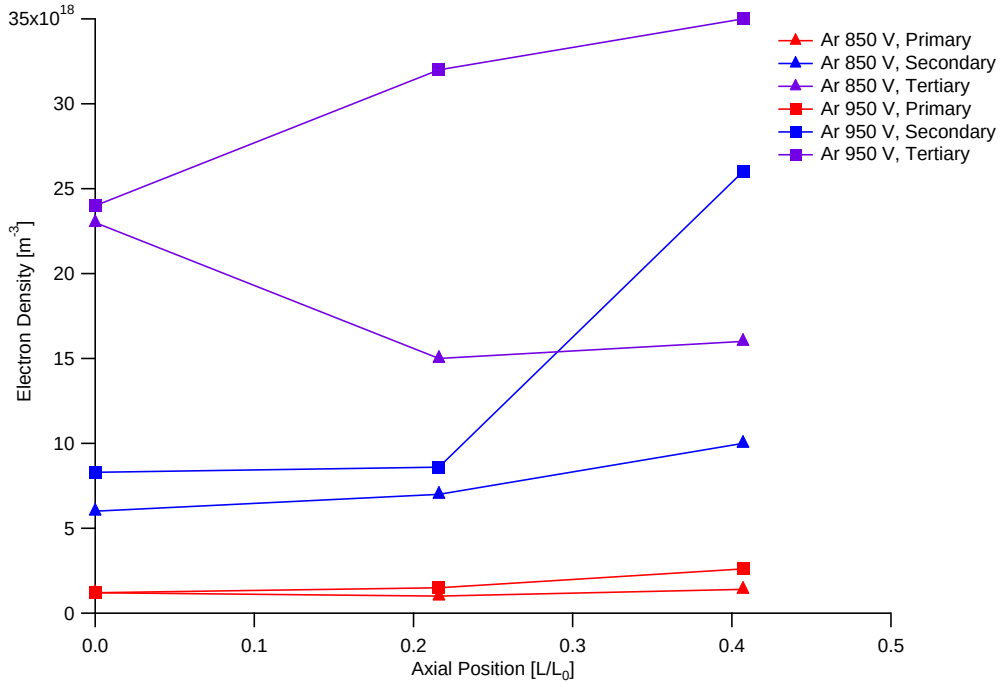

Figure 7.46: Summary of the peak densities at Positions 1, 2, and 3 for 14-mTorr discharges at 850 V and 950 V as a function of axial position

To provide an even clearer position comparison, just comparing the peak densities measured at the various points (regardless of the timing), the data were compiled into Figures 7.47 and 7.46. Again, the same general trends are shown that increasing discharge energy and pre-ionization increases the available plasma and the peak density measured. As seen in the contour plots, plasma is highly centered in the axis, suggesting low flux and plasma loss axially. Also, at higher energies, the increase in plasma density is mostly in the central region and not at the perimeter of the toroid.

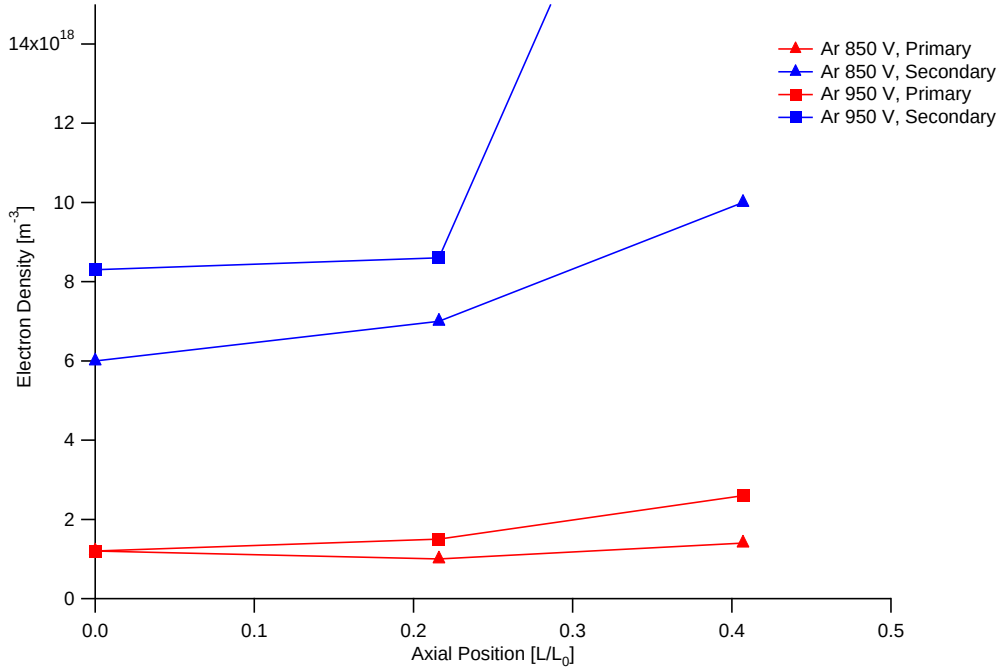

Figure 7.47: Close view of the peak densities within the first 350 μs at Positions 1, 2, and 3 for 14-mTorr discharges at 850 V and 950 V as a function of axial position

7.3.4 Argon Energy Analysis

Equations 3.5, 3.6, 3.7, and 3.8 were used with the 14-mTorr argon discharge data for Position 3 to create a complementary overview of input energy from 180–280 μs. Figures 7.48 and 7.49 show data for 850-V and 950-V discharge cases, respectively. Immediately obvious when comparing these data, the plasma input energy does not follow the input magnetic energy for very long before an instability (or translation) occurs that appears to drive the plasma to lower energies. Unfortunately, the plasma data collected is only at one point (the center of the discharge coil) and it appears that this energy analysis is failing to see the entire plasma content for the entire discharge. From the wide-angle photometer data it appears that there is a larger (and higher density) plasma just post-reversal that is outside of the collection area of the triple probe. The data collected is the formed FRC compressing inwards pass the triple probe electrodes. However, these data are quite useful for looking at plasma content and understanding energy input, though the analysis that follows will be lower than if data were collected during the main, high-energy compression that occurs outside of the probe. The energy contained in ionization verses thermal is approximately 35 % and 15 % for an 850-V, 950-V E_θ case, respectively. The triple probe sees plasma following the input magnetic energy for approximately 15 μs and bulk plasma resident on the coil for 54 μs for both cases. Peak plasma power (not shown, but simply time derivatives of the plasma energy) is approximately 150 kW and 460 kW, respectively.

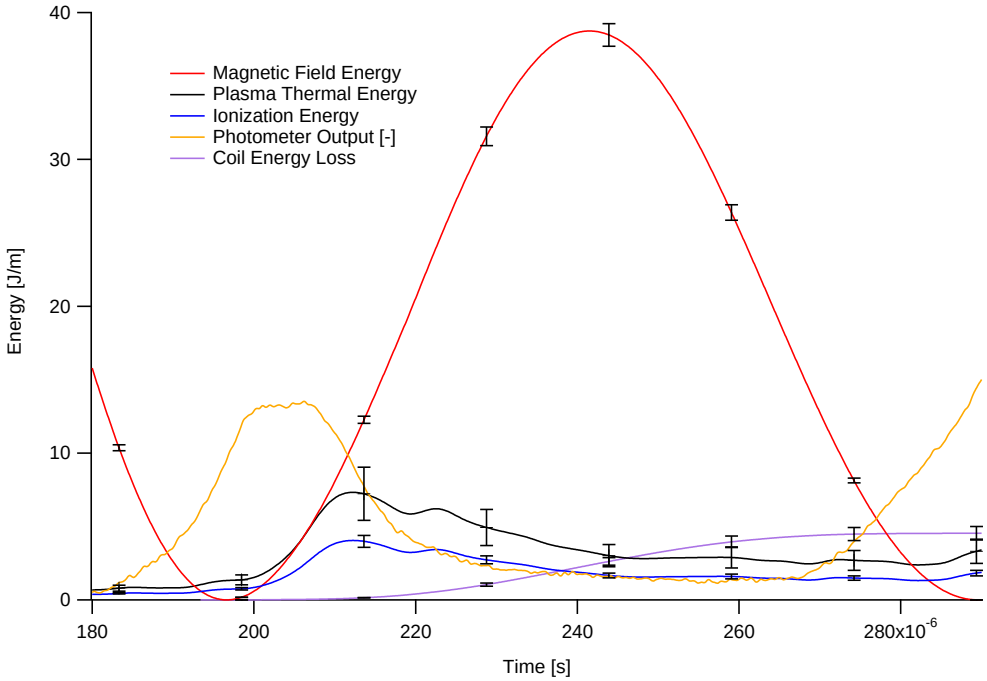

Figure 7.48: Instantaneous energy contained in the annular discharge region (per unit length) for a 185-μs, 14-mTorr, 850-V argon discharge showing plasma, ionization, magnetic, and coil dissipation energies as well as wide-angle photometer output

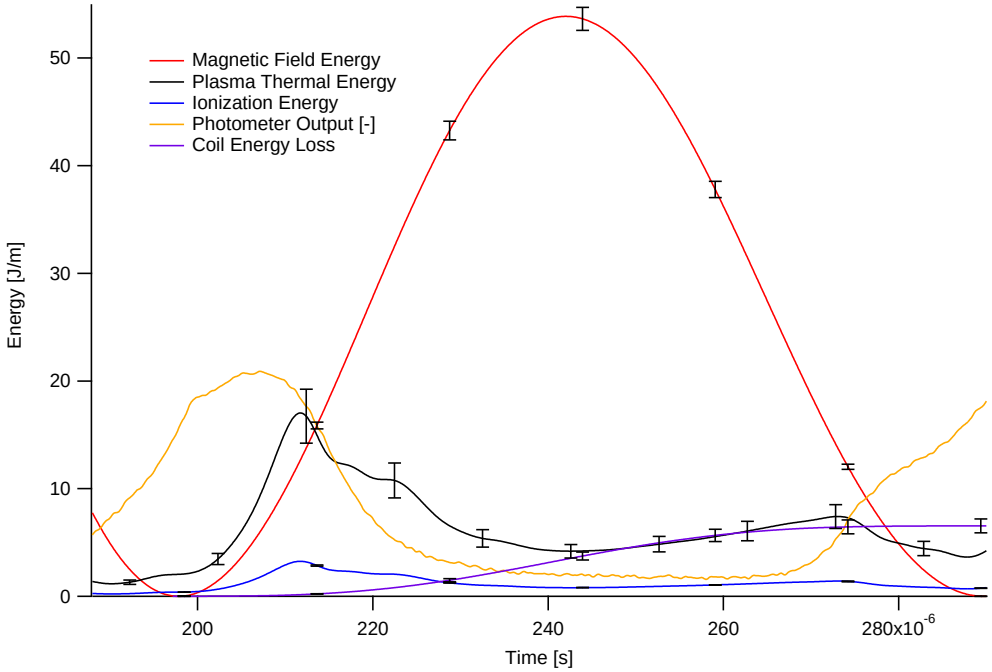

Figure 7.49: Instantaneous energy contained in the annular discharge region (per unit length) for a 185-μs, 14-mTorr, 950-V argon discharge showing plasma, ionization, magnetic, and coil dissipation energies as well as wide-angle photometer output

7.4 Xenon

The investigation into axial density distribution and operational parameters for the 185-μs discharges continued with xenon. The xenon results were similar to expected, with lower plasma temperatures and higher peak densities. Xenon appears to have significantly less instability formation, as well as less sharp compression regions than argon. Figure 7.50 shows the DICAM photos of a 3-mTorr, 850-V xenon discharge and how little rotational instability is noticed. There also appears (from the optical results) to be significantly more background ionization in the annular region (most likely foreground or background axially).

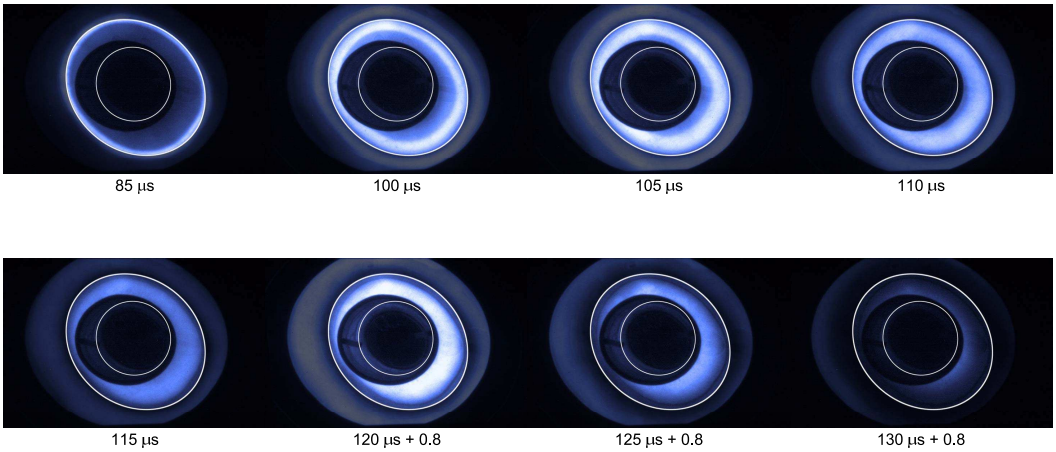

Figure 7.50: DICAM end-on visible photography for a 950-V, 3-mTorr, xenon case

7.4.1 Optical Results

An 8-shot evolution of a 950-V, 3-mTorr of xenon discharge was created with the DICAM II, as shown in Figure 7.50. Each photograph is a 2-μs integrated image with an average DICAM exposure amplification of 3.75 [-]. Visible are a significant background ionization, the pre-ionization edge discharge, the sharp compression edge ($t = 100\ \mu s$), high-density plasma filling the annulus, and a compressed toroid close to the inner discharge coil ($t = 130\ \mu s$).

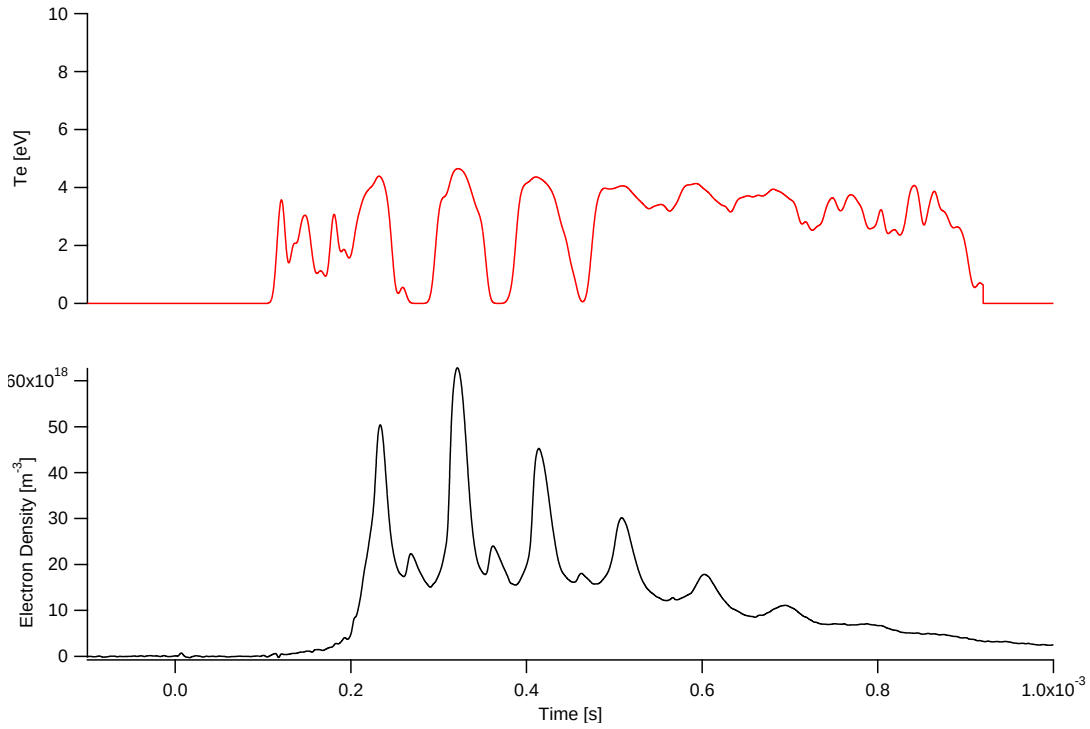

Figure 7.51: Detailed time evolution of electron density and temperature at Position 1 for a 950-V, 185-μs, 3-mTorr xenon discharge

7.4.2 Internal Plasma Properties

Figures 7.51-7.53 show samples of real-time plasma density and temperature at Position 1 at the bottom of the discharge coil. Average electron temperatures are 4 eV.

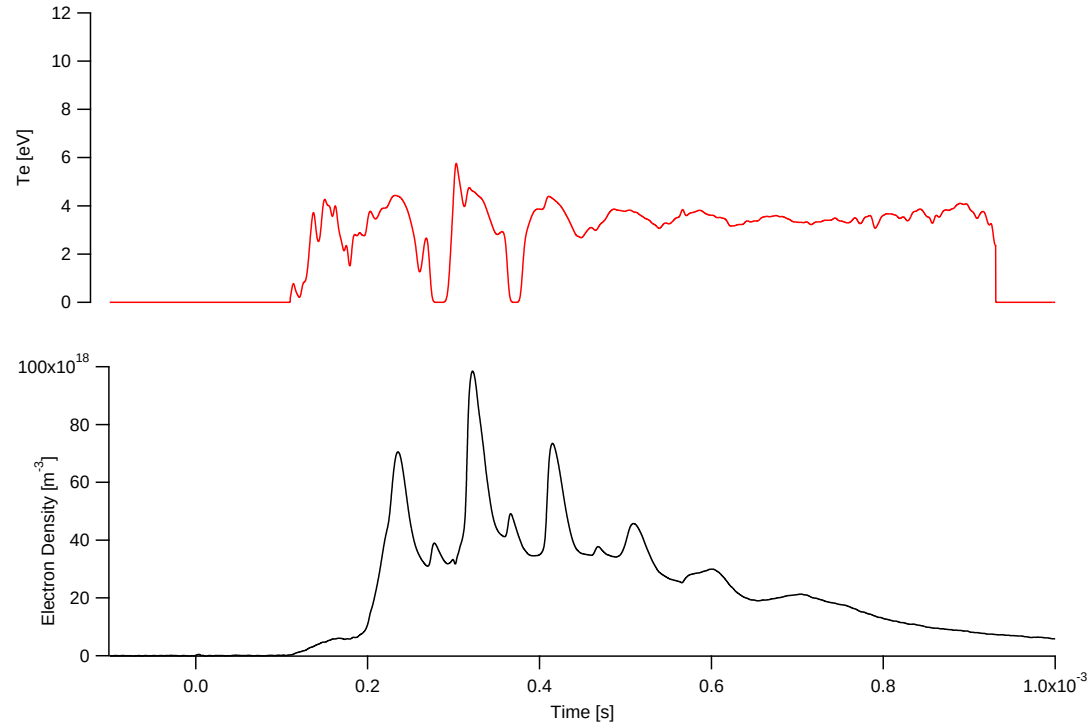

Figure 7.52: Detailed time evolution of electron density and temperature at Position 1 for a 950-V, 185-μs, 6-mTorr xenon discharge

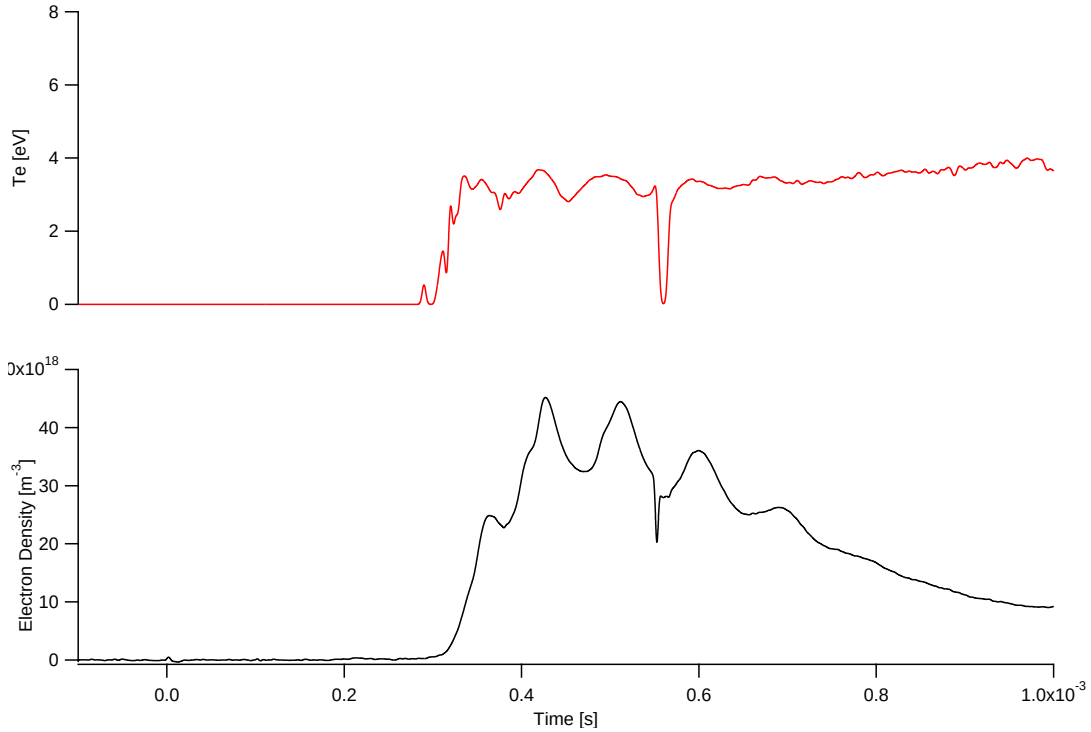

Figure 7.53: Detailed time evolution of electron density and temperature at Position 1 for a 950-V, 185-μs, 10-mTorr xenon discharge

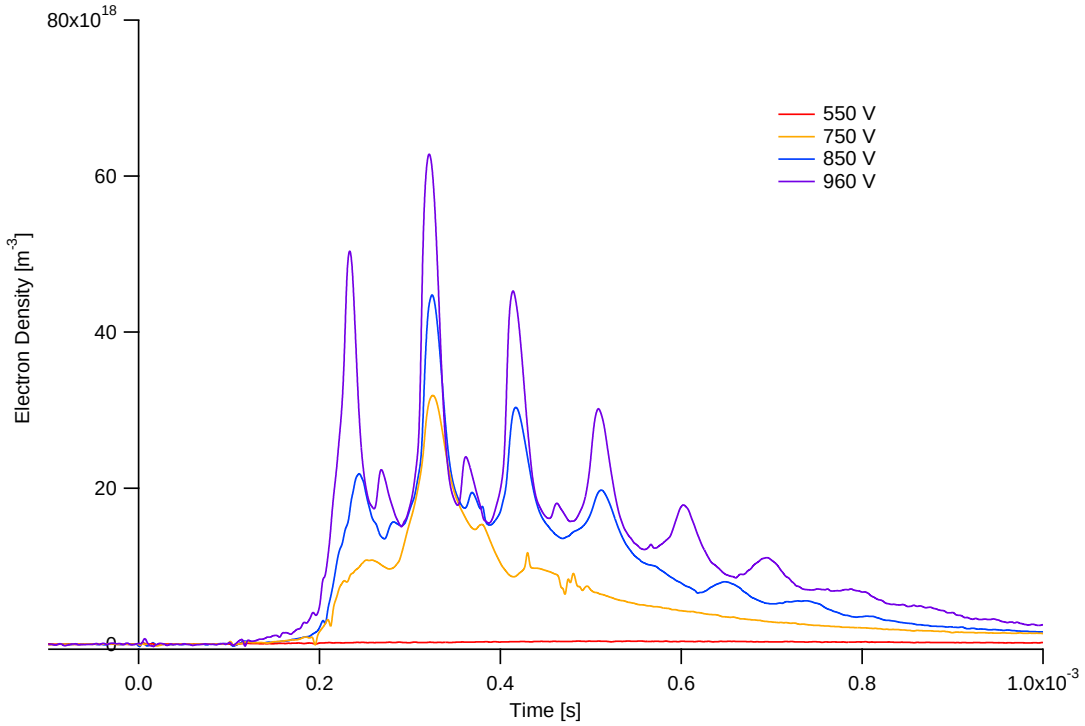

Figure 7.54: Summary of plasma density results at Position 1 for 185-μs, 3-mTorr xenon discharges for various energies

Unlike the argon results (at all positions), xenon at Position 1 does not appear to leave the discharge chamber, nor to have as clear a compression transition as it passes the triple probe. Figures 7.54–7.59 show comparisons of electron density as functions of discharge energy and neutral fill pressure. The optimal neutral fill pressure (as determined by both photometer and density results) appears to be 6 mTorr of xenon, with a 3 mTorr pressure having less available ionization populations to initiation the discharge, as well as a lower plasma density at 100 % ionization. At 10 mTorr, the applied discharge energies are not sufficient to ionize and magnetize the plasma until after 300 μs. The secondary discharge was significantly denser than the argon discharge at $5 - 7 \times 10^{19}\ m^{-3}$ for 6 mTorr and $2.5 - 5.5 \times 10^{19}\ m^{-3}$ for 3 mTorr.

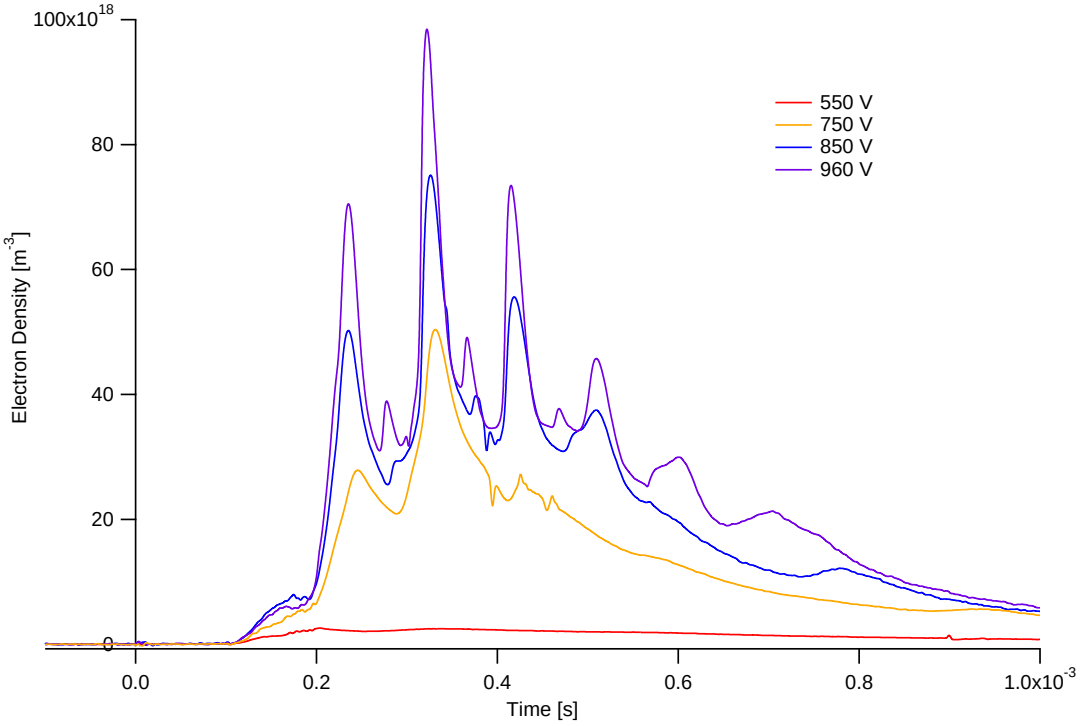

Figure 7.55: Summary of plasma density results at Position 1 for 185-μs, 6-mTorr xenon discharges for various energies

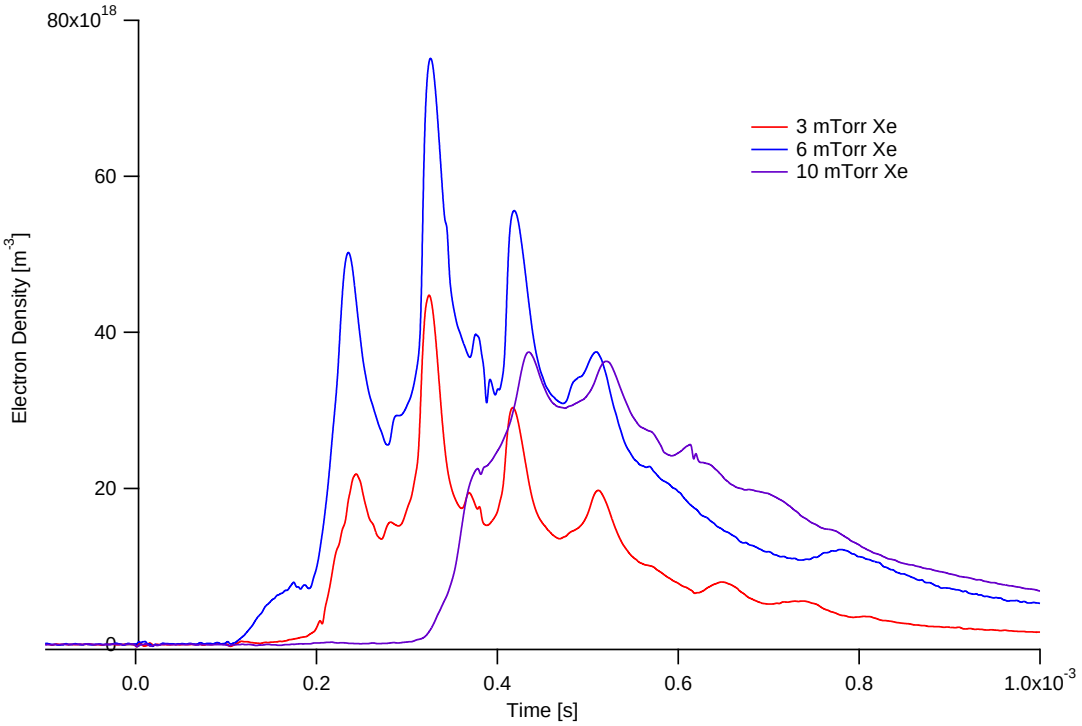

Figure 7.56: Summary of plasma density results at Position 1 for 185-μs, 850-V xenon discharges for various neutral fill pressures

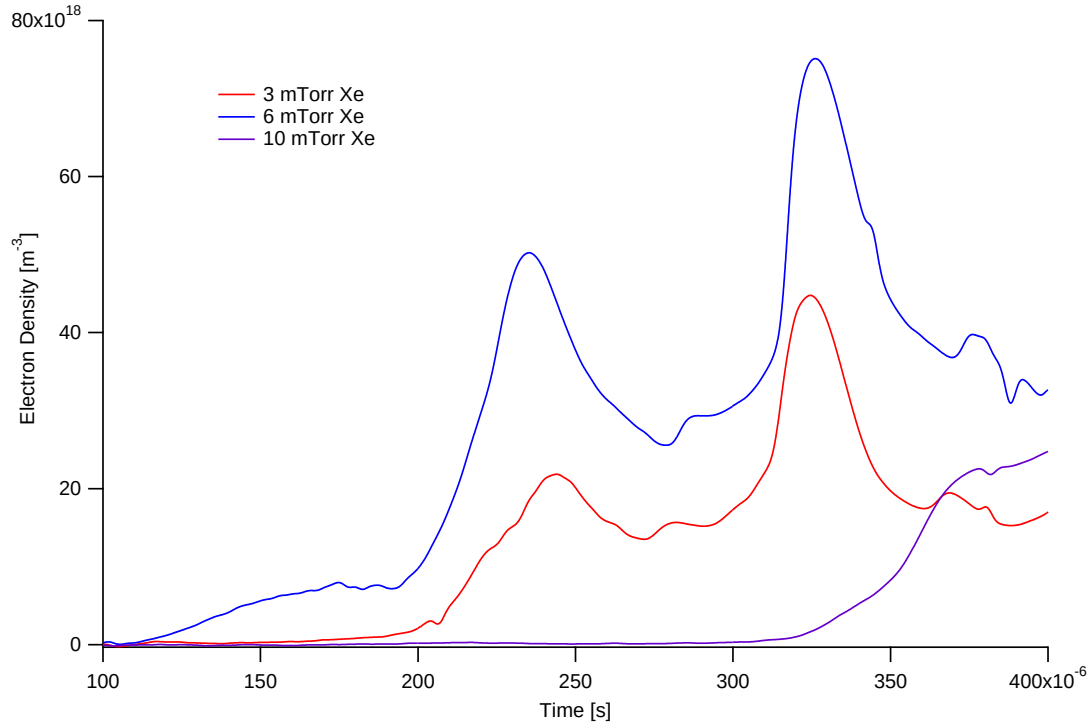

Figure 7.57: Close view of plasma density results at Position 1 for 185-μs, 850-V xenon discharges for various neutral fill pressures showing the primary and secondary discharges

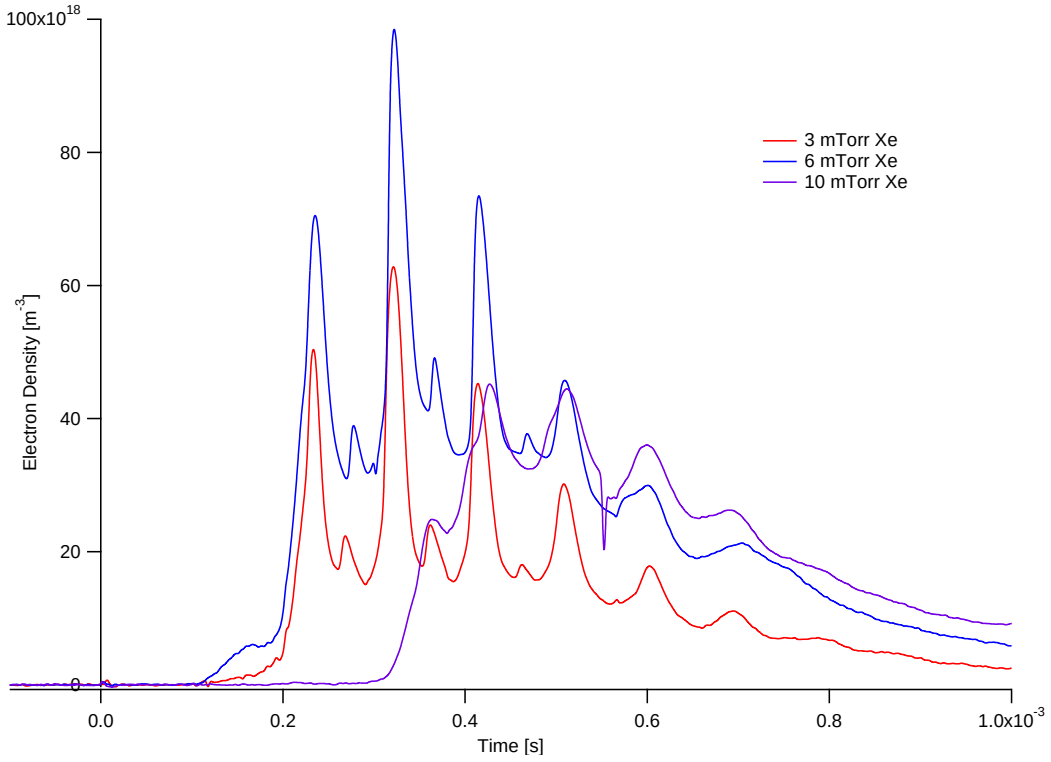

Figure 7.58: Summary of plasma density results at Position 1 for 185-μs, 950-V xenon discharges for various neutral fill pressures

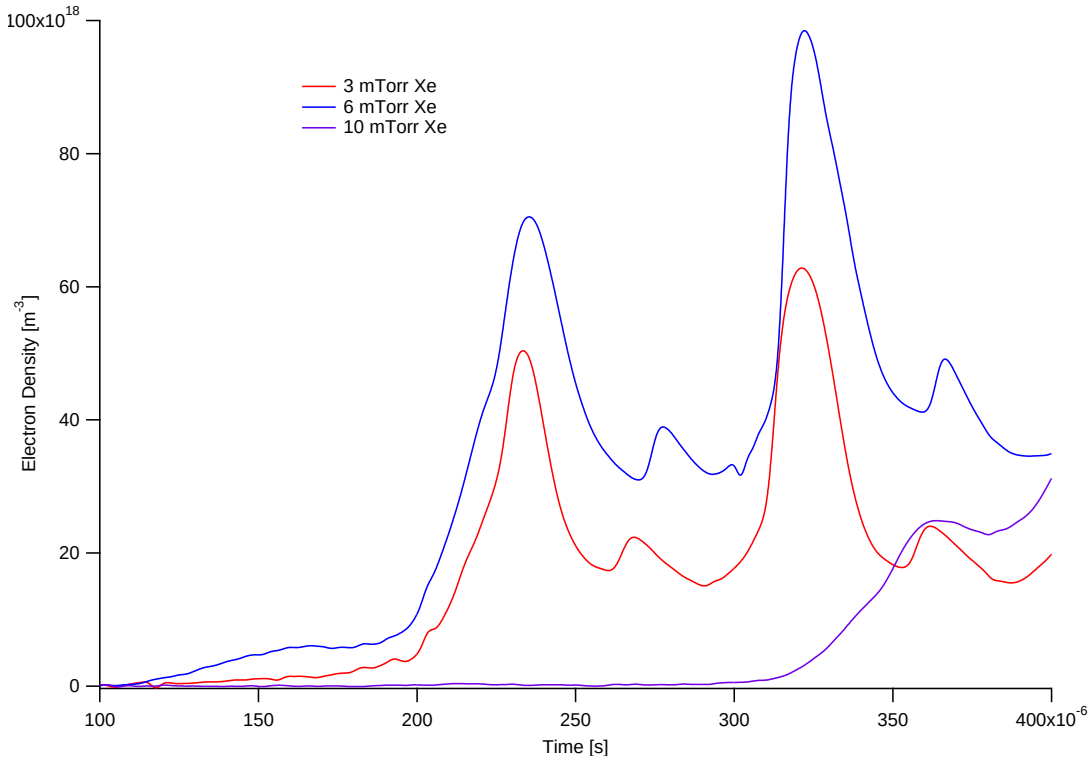

Figure 7.59: Close view of plasma density results at Position 1 for 185-μs, 950-V xenon discharges for various neutral fill pressures showing the primary and secondary discharges

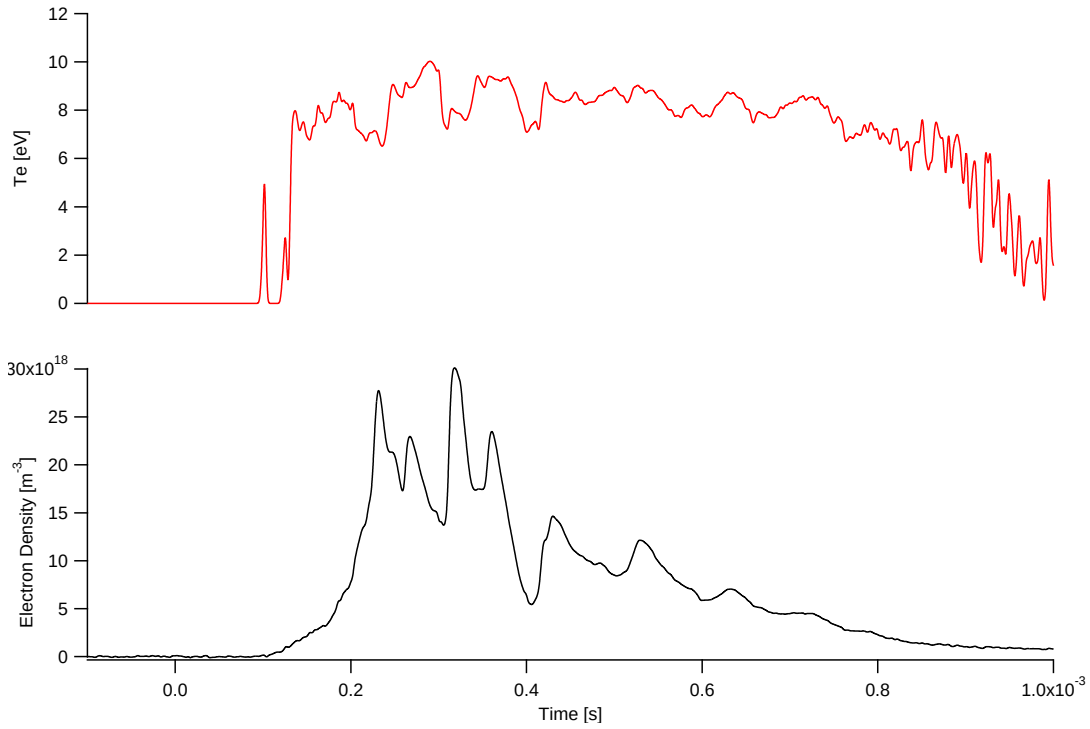

Figure 7.60: Detailed time evolution of electron density and temperature at Position 2 for an 850-V, 185-μs, 3-mTorr xenon discharge

7.4.2.1 Xenon Position 2

Position 2 saw the characteristic increase in temperature and density as in the argon densities, with average electron temperatures ($Te = 7.5 - 9.0\ eV$) as shown in Figures 7.60–7.64.

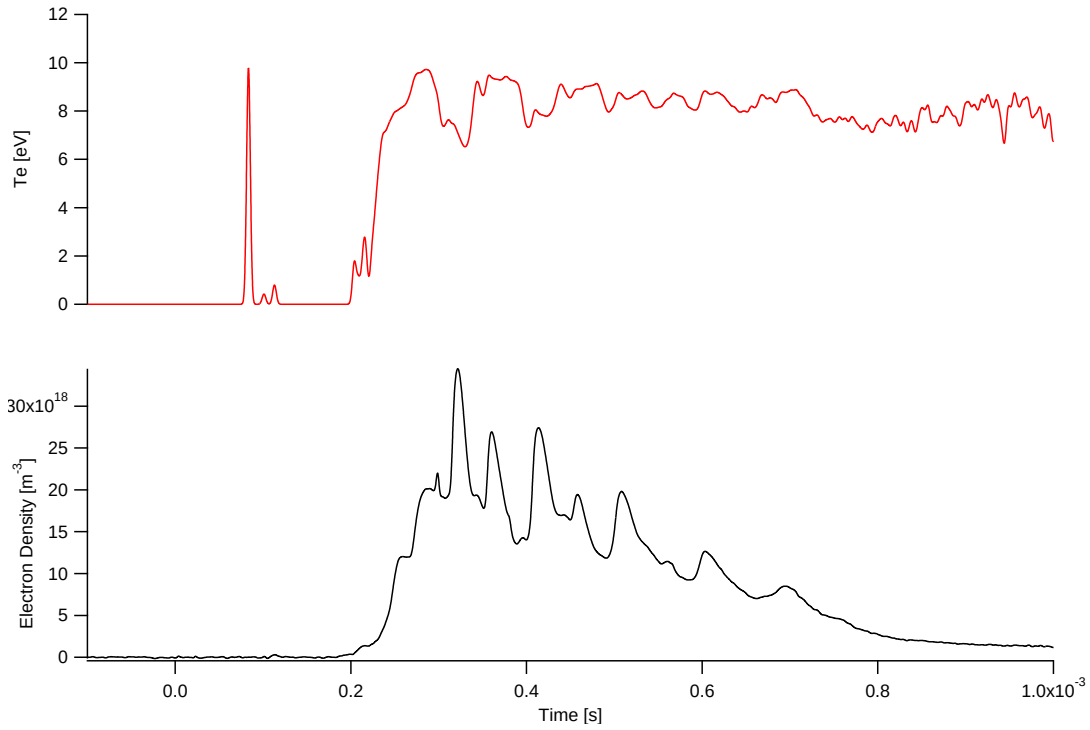

Figure 7.61: Detailed time evolution of electron density and temperature at Position 2 for a 950-V, 185-μs, 3-mTorr xenon discharge

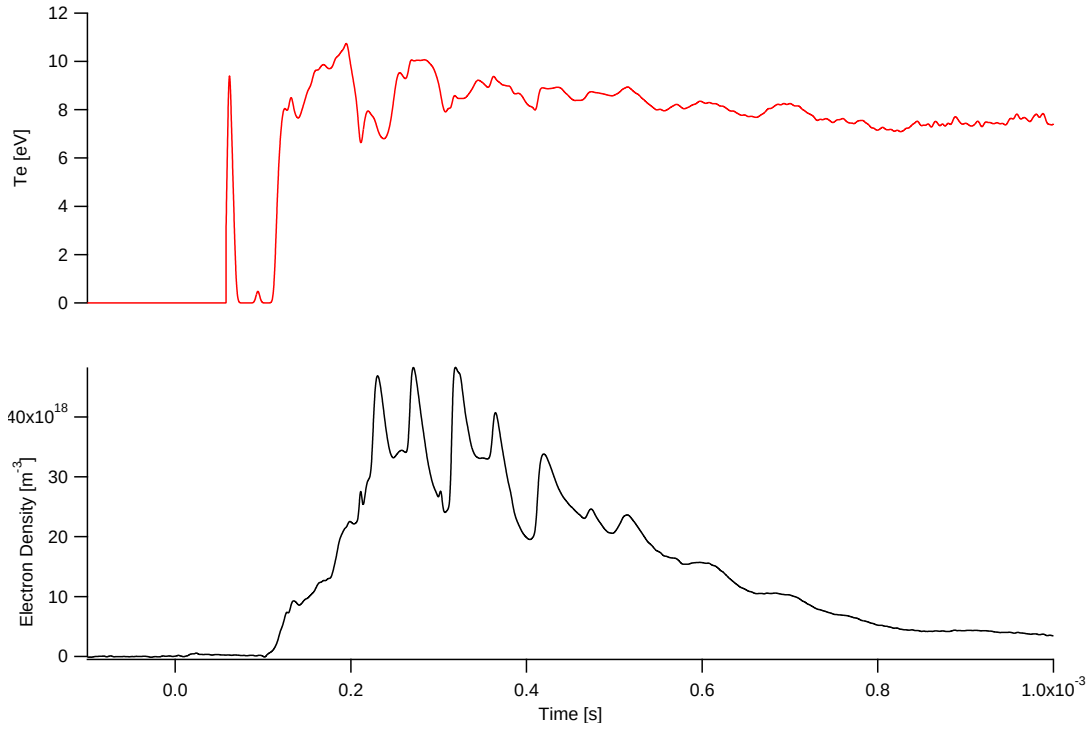

Figure 7.62: Detailed time evolution of electron density and temperature at Position 2 for an 850-V, 185-μs, 6-mTorr xenon discharge

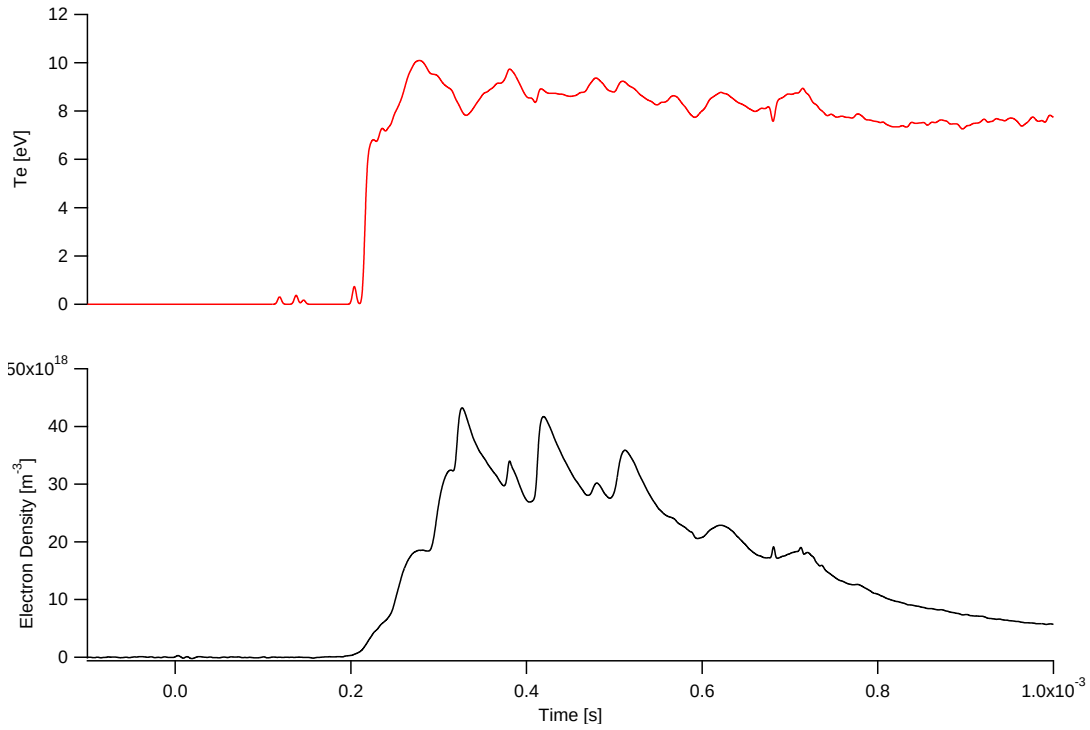

Figure 7.63: Detailed time evolution of electron density and temperature at Position 2 for an 850-V, 185-μs, 10-mTorr xenon discharge

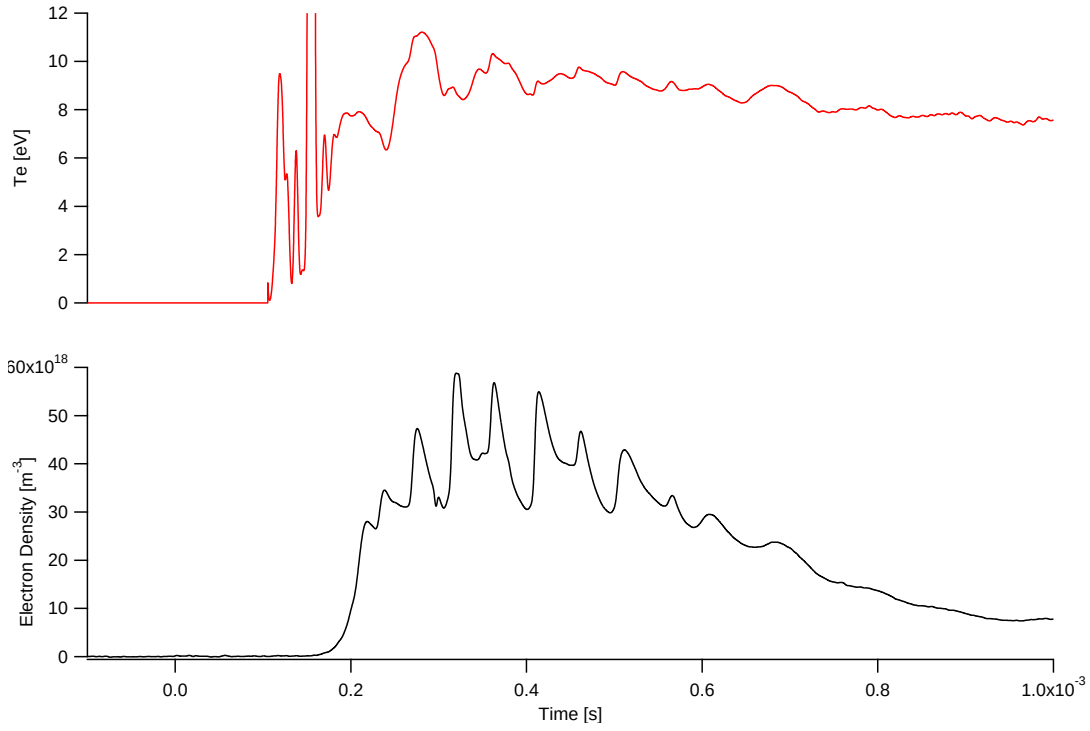

Figure 7.64: Detailed time evolution of electron density and temperature at Position 2 for a 950-V, 185-μs, 10-mTorr xenon discharge

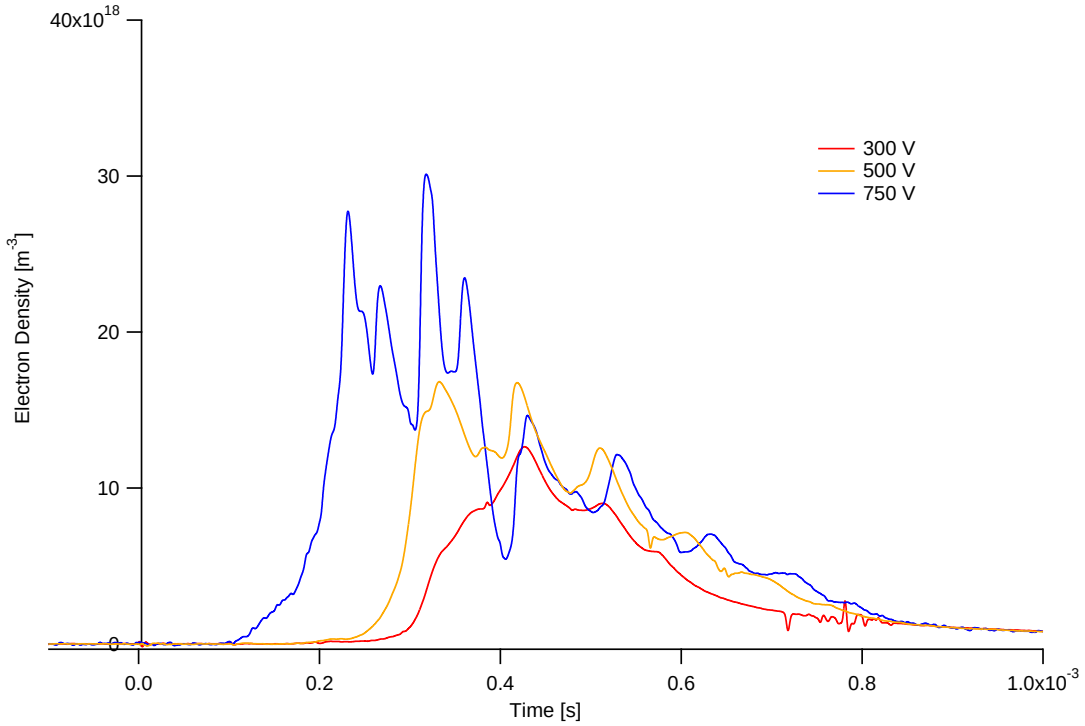

Figure 7.65: Summary of plasma density results at Position 2 for 185-μs, 3-mTorr xenon discharges for various energies

Figures 7.65–7.68 show a summary of the xenon discharge results for Position 2. Xenon's lower ionization energy and more massive ions appear to lend themselves to inductive discharges, creating more efficient and lower energy pre-ionization. Position 2 shows much more plasma density and earlier formation than Position 1. In fact, the primary discharge is quite large $3-5\times10^{19}\ m^{-3}$, with the secondary discharge at $3.5-7\times10^{19}\ m^{-3}$. As with Position 1, the plasma density remains substantial between discharges. One very interesting phenomenon that should be investigated is the difference between a 3-mTorr and 6-mTorr discharge in terms of turn-on energies and timing. The 3-mTorr discharge shows very distinct timing and energy requirement for initial magnetized plasma turn-on. Figure 7.65 shows the differences in input energies and the density response. Figure 7.66 shows that above the 550-V initial threshold, initial turn-on clearly starts and amplifies at 100 μs for all input energies.

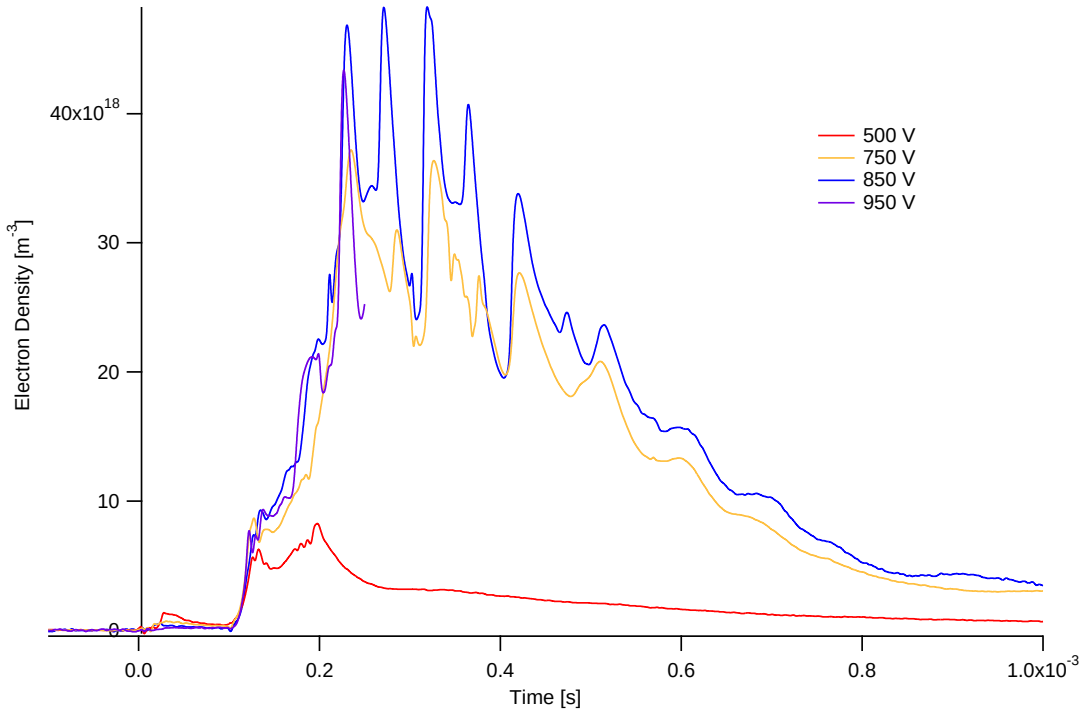

Figure 7.66: Summary of plasma density results at Position 2 for 185-μs, 6-mTorr xenon discharges for various energies. Note that the 950-V, 6-mTorr case is not complete due to a data collection error

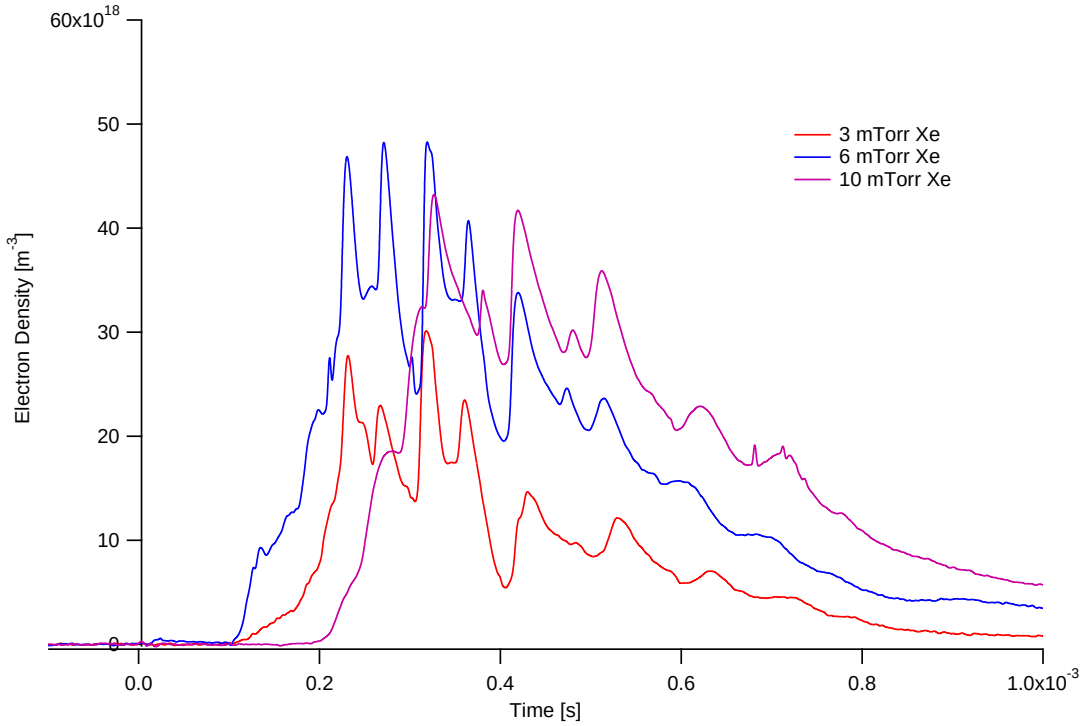

Figure 7.67: Summary of plasma density results at Position 2 for 185-μs, 850-V xenon discharges for various neutral fill pressures

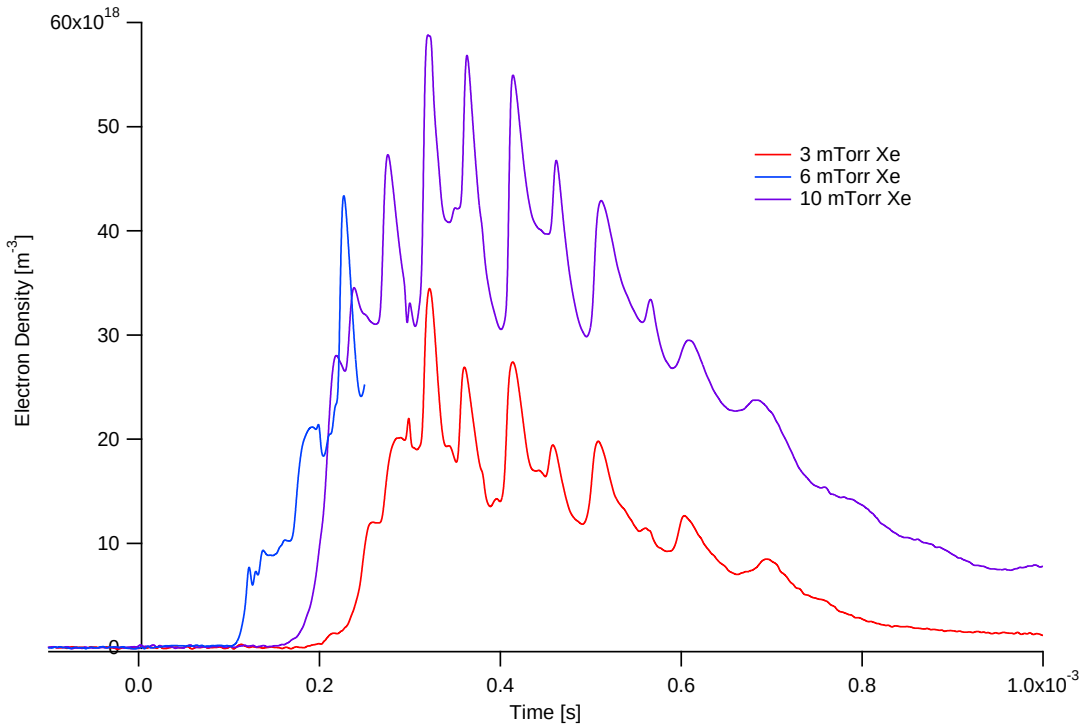

Figure 7.68: Summary of plasma density results at Position 2 for 185-μs, 950-V xenon discharges for various neutral fill pressures

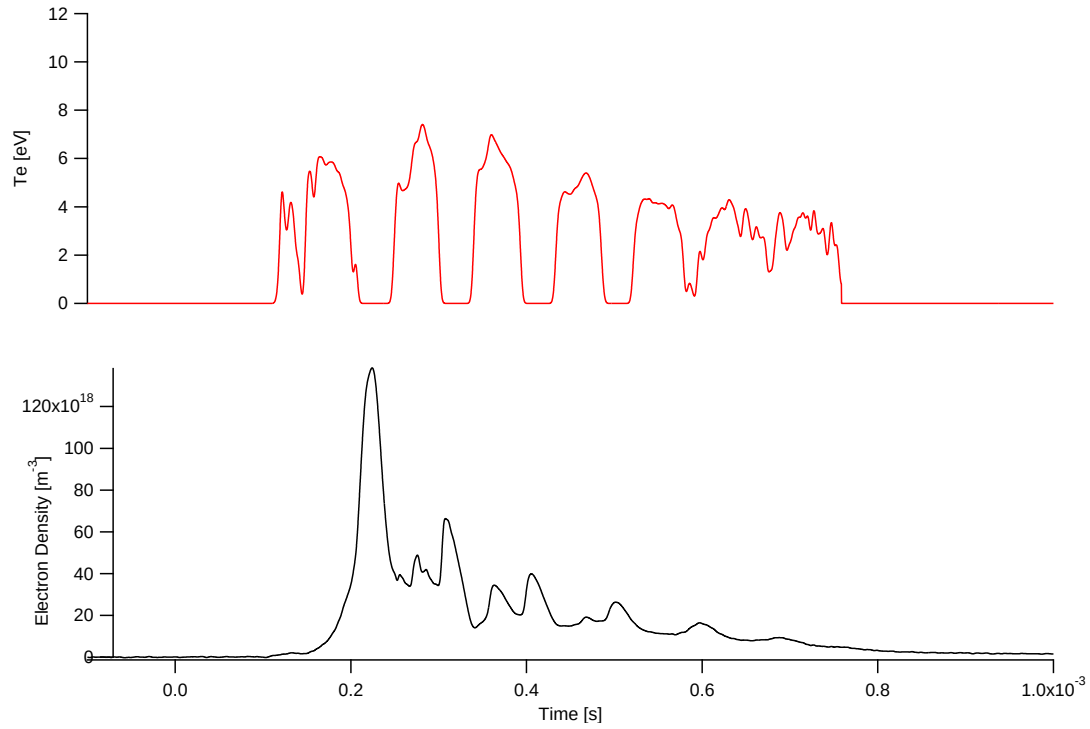

Figure 7.69: Detailed time evolution of electron density and temperature at Position 3 for a 950-V, 185-μs, 3-mTorr xenon discharge

7.4.2.2 Xenon Position 3

Figures 7.69–7.72 show plasma density and temperature for collected data at Position 3 in xenon. As with argon, plasma temperature is decreased near the core, but plasma density is significantly increased. It appears that xenon forms a more centered plasma (axially) than argon, with peak primary discharge densities of $0.4 - 1.3 \times 10^{20}\ m^{-3}$, as a function of neutral pressure. For xenon, the density response to increasing discharge energy is different than argon in that increasing discharge voltage has little effect on peak plasma density, only on plasma initiation time and electron temperature.

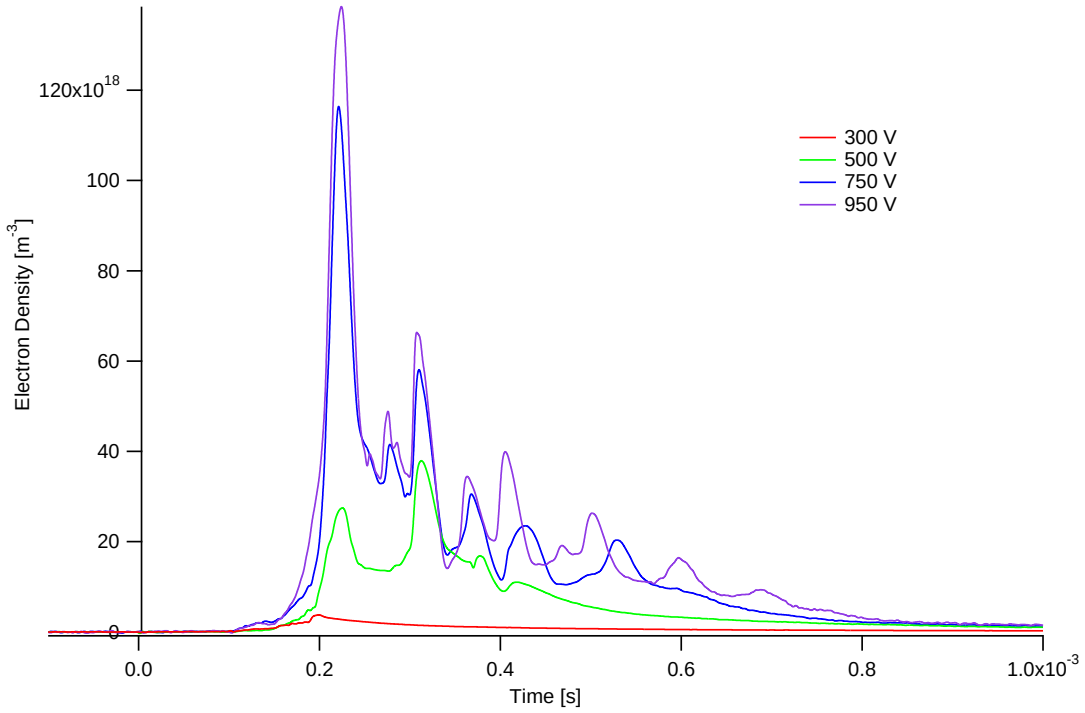

Figure 7.70: Summary of plasma density results at Position 3 for 185-μs, 3-mTorr xenon discharges for various energies

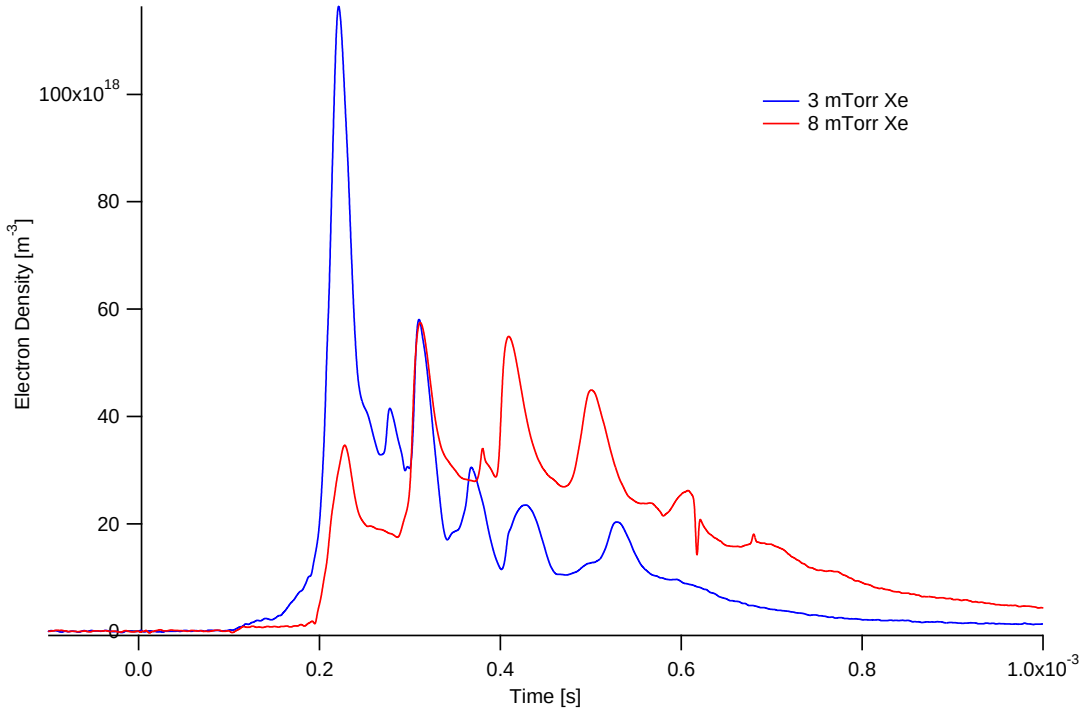

Figure 7.71: Summary of plasma density results at Position 3 for 185-μs, 850-V xenon discharges for various neutral fill pressures

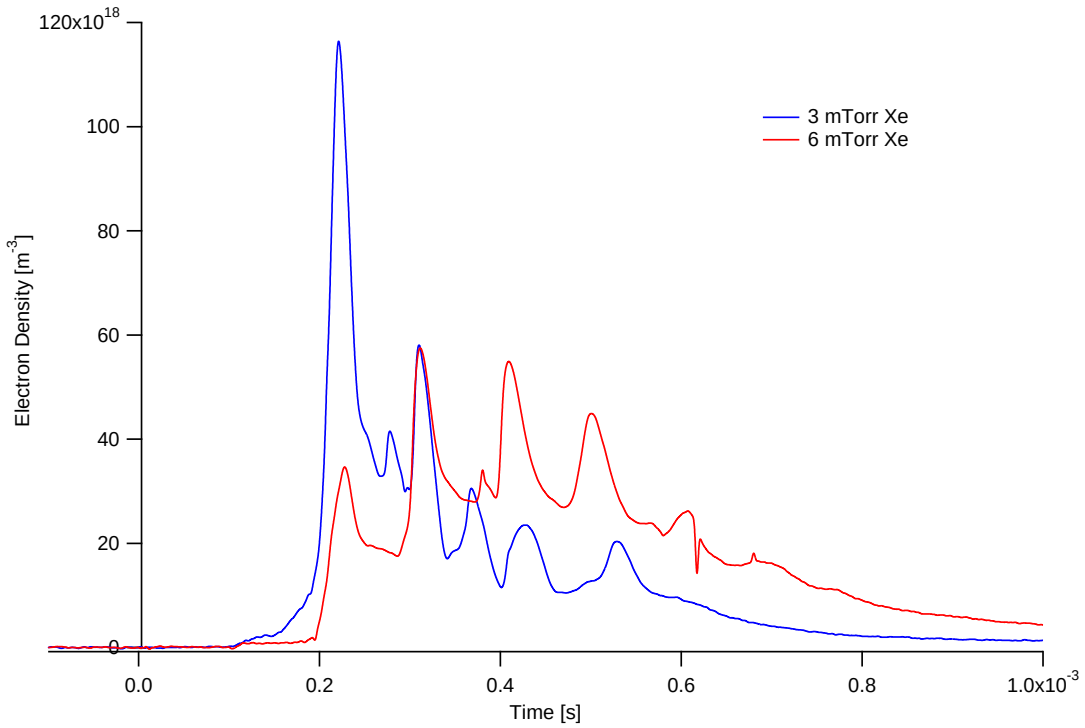

Figure 7.72: Summary of plasma density results at Position 3 for 185-μs, 950-V xenon discharges for various neutral fill pressures

7.4.3 Xenon Energy Analysis

Equations 3.5, 3.6, 3.7, and 3.8 are used with the 6-mTorr xenon discharge data for Position 3 to create a complementary overview of input energy from 180-280 μs. Figures 7.73 and 7.74 show data for 850-V and 950-V discharge cases, respectively. Not surprisingly, the results are quite similar to the collected data for argon, with delayed plasma collection at the probe and a close to 1:1 energy input into the plasma versus the discharge coil. The energy contained in ionization verses thermal is approximately 21 % and 16 % for 850-V, 950-V E_θ cases, respectively. The triple probe sees plasma following the input magnetic energy for about 24 μs and bulk plasma resident on the coil for 55 μs for both cases. Total peak plasma power (not shown, but simply time derivatives of the plasma energy) is approximately 200 kW and 250 kW respectively for the second discharge and up to 555 kW for subsequent discharges.

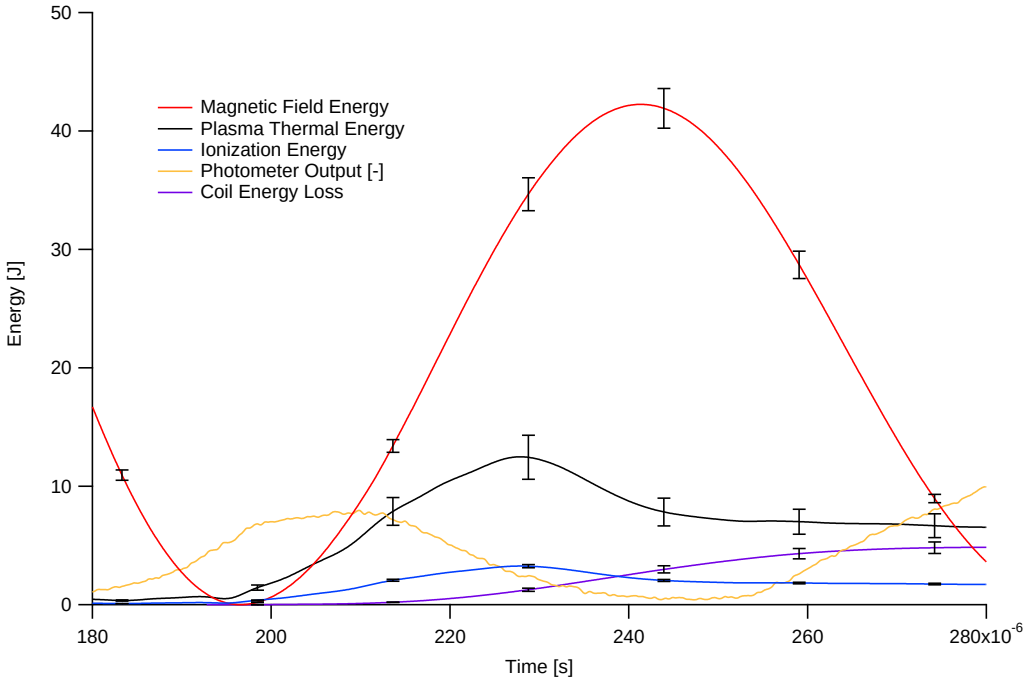

Figure 7.73: Instantaneous energy contained in the annular discharge region (per unit length) for a 185-μs, 6-mTorr, 850-V xenon discharge showing plasma, ionization, magnetic, and coil dissipation energies as well as wide-angle photometer output

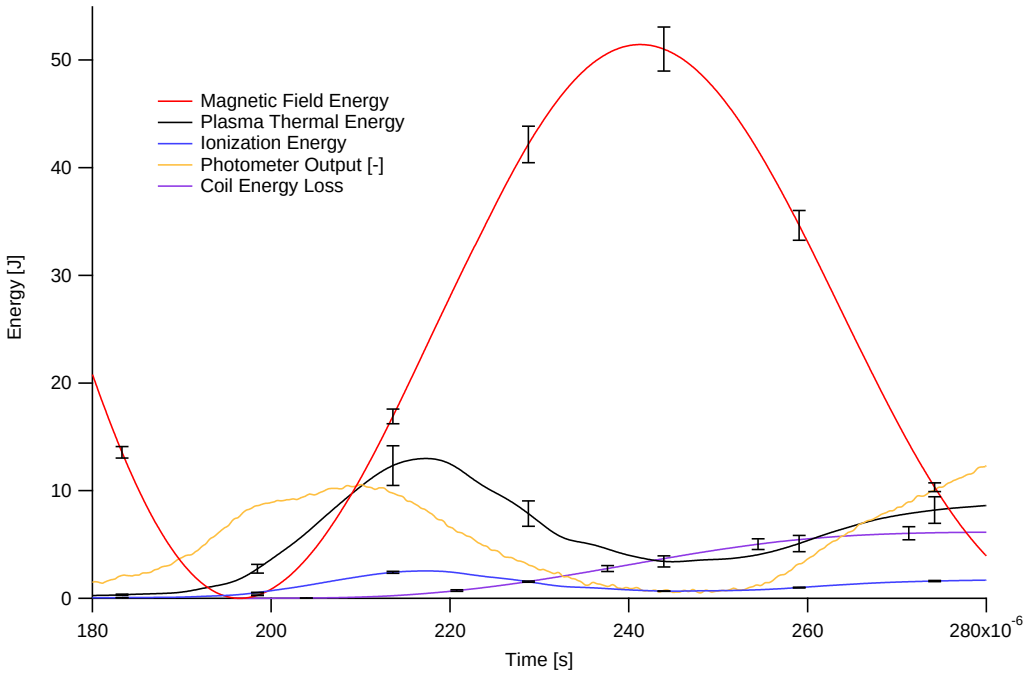

Figure 7.74: Instantaneous energy contained in the annular discharge region (per unit length) for a 185-μs, 6-mTorr, 950-V xenon discharge showing plasma, ionization, magnetic, and coil dissipation energies as well as wide-angle photometer output

7.4.4 Summary of Xenon Results

Figures 7.75–7.78 summarize the results for the axial scan study of xenon. Figures 7.75–7.78 show resolved plasma density for the 3 axial positions as well as multiple gas densities. For all cases there is a clear localized, central high-density plasma centered in the axis that then decays quickly (geometrically) that is initially created at $t = 100\ \mu s$. For the 3-mTorr discharges, this plasma is swept out of the discharge region and subsequent discharges are significantly less in magnitude. For the 6, 10-mTorr discharge cases the initial plasma density decays slightly (with time) but then is further heated and compressed by subsequent reversals, leading to very high average plasma density and energy content in the discharge region. Additionally, for the 6- and 10-mTorr cases, the primary discharge is only present in the central portion of the annulus and then diffuses/expands for subsequent reversals, a function of both physical gas diffusion as well as initial pre-ionization fraction.

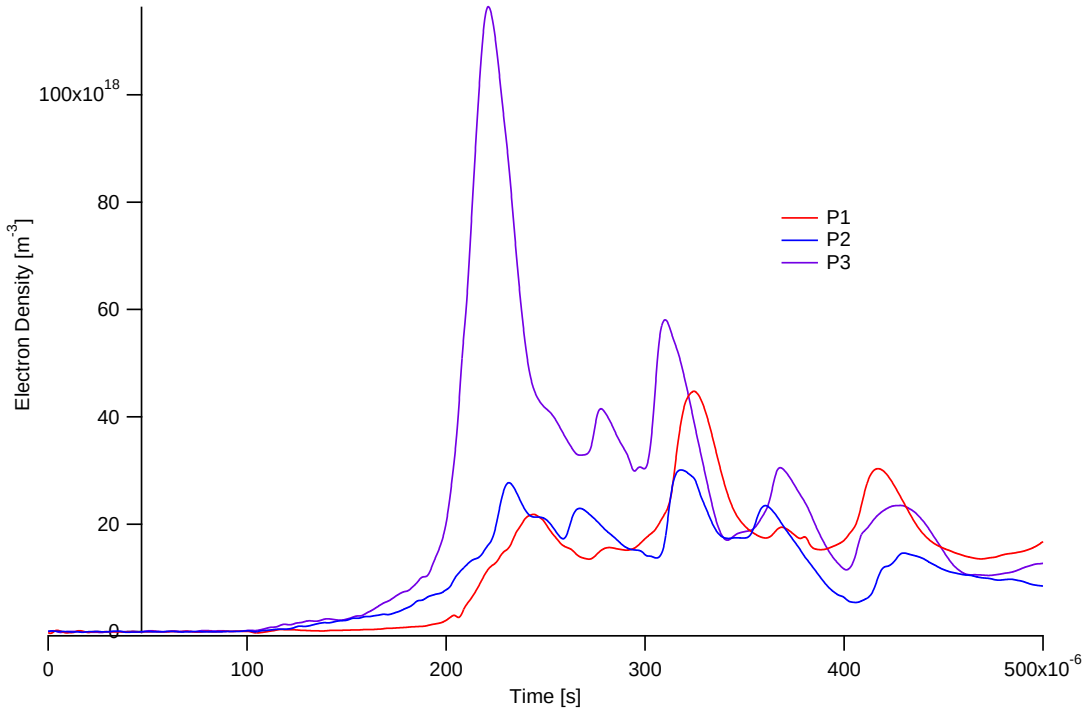

Figure 7.75: Detailed axial density scans for 185-μs, 3-mTorr, 850-V xenon discharges showing initial ionization, primary, and secondary discharges

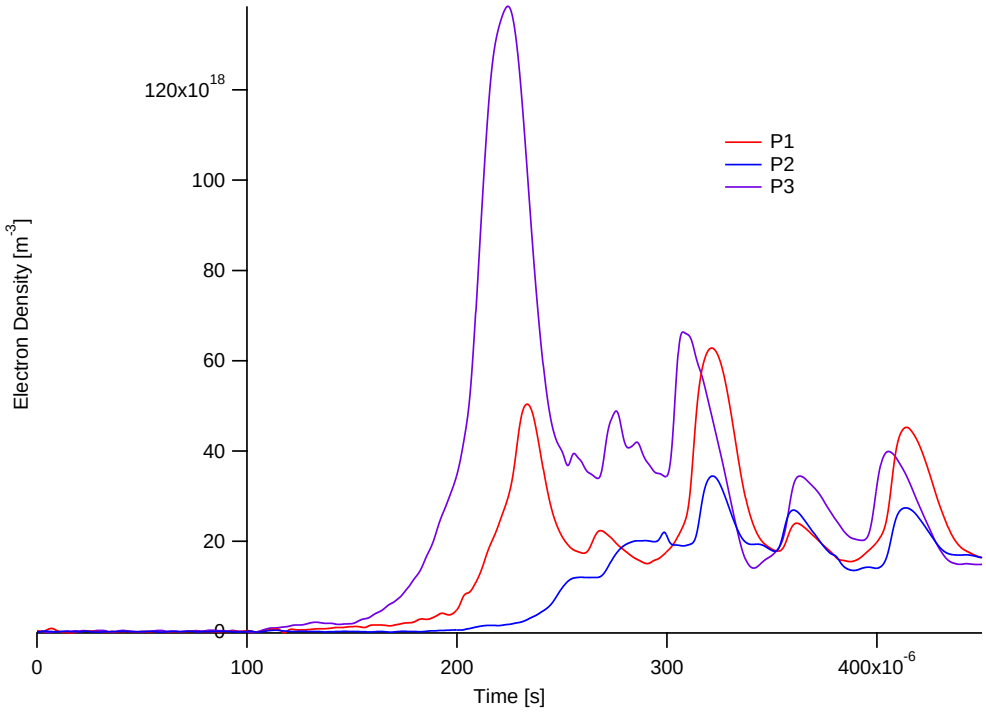

Figure 7.76: Detailed axial density scans for 185-μs, 3-mTorr, 950-V xenon discharges showing initial ionization, primary, and secondary discharges

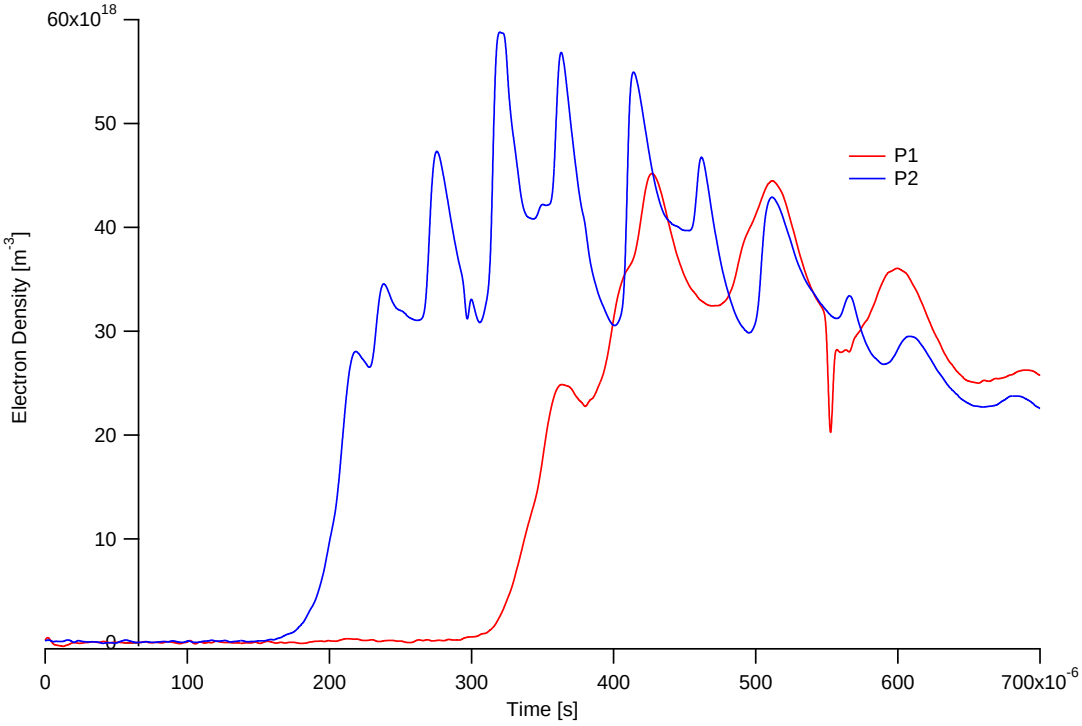

Figure 7.77: Detailed axial density scans for 185-μs, 6-mTorr, 950-V xenon discharges showing initial ionization, primary, and secondary discharges

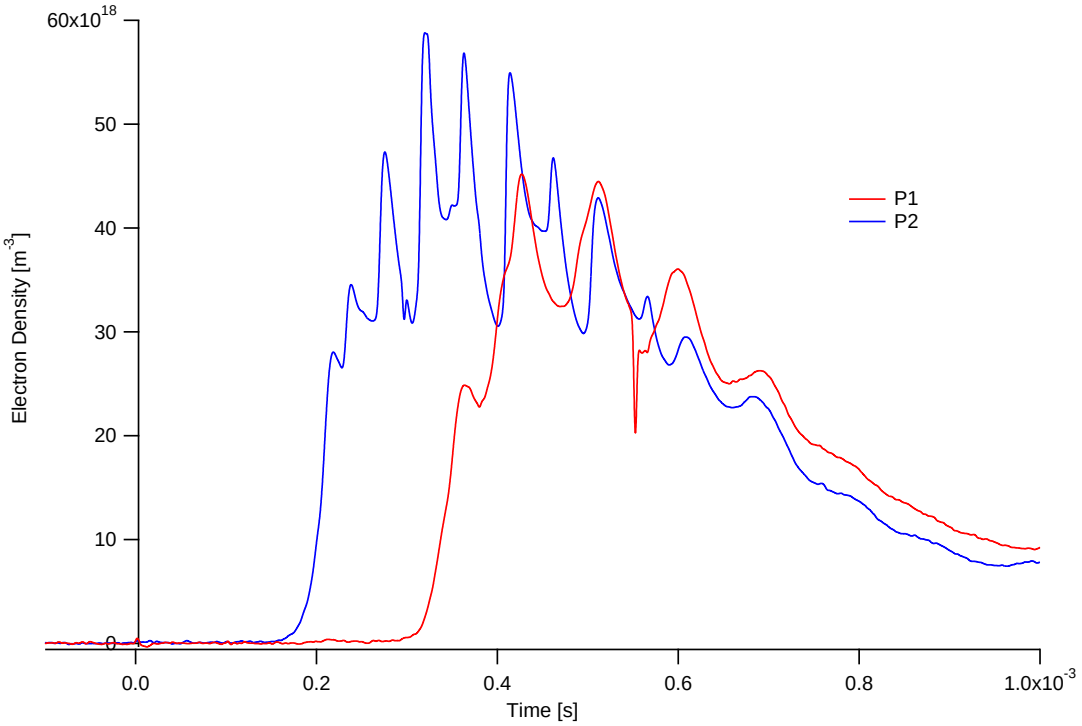

Figure 7.78: Detailed axial density scans for 185-μs, 10-mTorr, 950-V xenon discharges showing initial ionization, primary, and secondary discharges

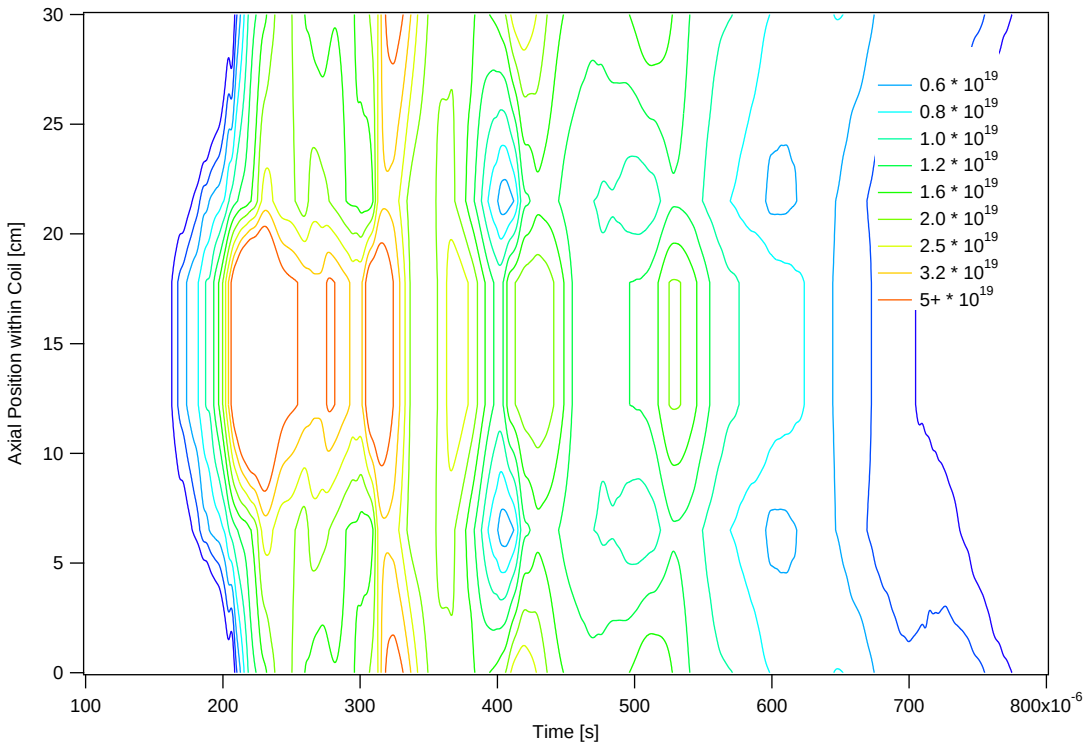

Figure 7.79: Axial density scan contours for 185-μs, 3-mTorr, 850-V xenon discharges showing plasma density (axially, along centerline) as a function of time

Visually, the plasma density formation and expansion is shown in Figures 7.79 and 7.80 in contour plots as functions of time and axial location. As with the argon contour plots, the data collected is mirrored for axial locations from 15 to 30 cm. The central plasma formation and multiple compressions are obvious ($n_e > 5 \times 10^{19}\ m^{-3}$) for both the 850- and 950-V discharge cases. Unlike argon, there is little peripheral heating due to the background neutral gas.

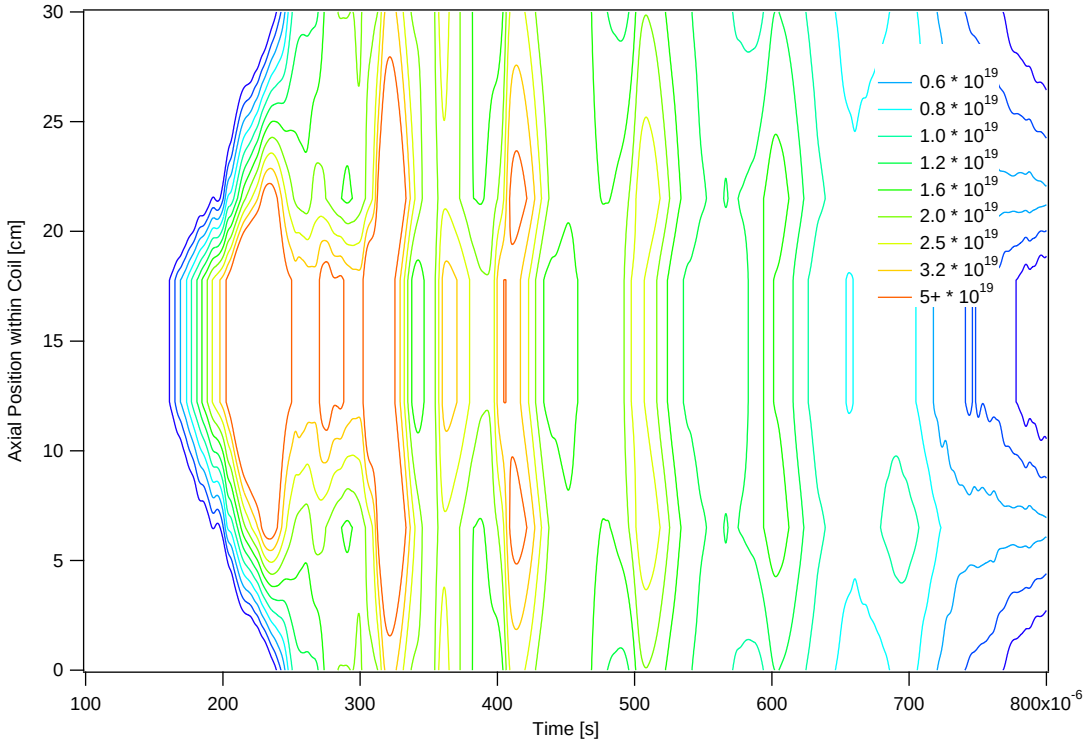

Figure 7.80: Axial density scan contours for 185-μs, 3-mTorr, 950-V xenon discharges showing plasma density (axially, along centerline) as a function of time

7.5 185-μs Discharge Conclusions

Chapter 7 was the primary focus of this study, with a detailed study of the plasma parameters of the XOCOT discharge experiment at three axial positions, two propellant gases, discharge voltages from 500 V to 1000 V and a 185-μs discharge period. While diagnostic data for magnetic field and photometer data were taken for all of the operational parameters discussed in Chapter 8, the main focus was the internal plasma parameters. The DICAM data were added in order to describe the discharge results for the 185-μs and compare with the internal triple probe plasma data. The DICAM data show that there is a clear pre-ionization and initial plasma buildup close to the external wall of the annulus. There is a subsequent brightness increase and compression in the interior of the annulus where triple probe data would be collected. Subsequently, there is further compression and heating and the toroidal FRC plasma appears to impinge on the inner wall where it then exhibits appearance of an n=2 rotational instability. The general trends observed in Chapter 5 and 6 at probe location 0 are continued with the analysis at probe locations 1, 2, and 3. Increasing discharge energy results in a higher plasma density and temperature for all axial locations. There is also clearly a relatively sensitive pressure optimum of approximately 14–15 mTorr. Large-scale magnetized discharges only occur for a narrow pressure range of 8–30 mTorr for the tested geometries and discharge energies. For the argon tests described above, there are some very clear trends that can be seen, firstly that the bulk of the ionization and plasma density is near the center of the discharge coil and extends out to the other probe locations later in each discharge. This is shown most clearly in the contour plots which detail the early formation (in the center) the continued heating and compression in the two central probes (Positions 2 and 3) and then finally the later heating and axial expansion to

the outer probe. The discharges are centered within the axis, with a significantly lower discharge density at the ends of the discharge coil (Position 1). From past FRC testing, this is expected and a highly desirable effect, both minimizing effects of the high-density background gas as well as showing that the expected axial contraction is successfully occurring. What has been clearly seen is that there is very poor initial ionization (0–20 μs) and that the anticipated high-energy discharge does not form without any reverse bias field/currents. However, with the full reversal at 200 μs a high-density (up to $4 \times 10^{19}\ m^{-3}$), efficient plasma is formed at all three positions measured. In the energy analysis performed it is quite clear that at the higher discharge energy conditions, plasmas are being created and heated to significantly higher temperatures and energies than is being lost in the ionization process or dissipated in the discharge coil. However, there is still a disconnect between the photometer data and the collected triple probe plasma data. It is expected that this is due to the initial plasma formation in a thin layer closer to the outer edge of the annulus and compressing through the triple probe location. Thus, the photometer reads a higher density plasma, earlier than the triple probe.

Xenon testing provided the same general trends as argon, a highly-centered, high-density plasma that is highly depended on input energies and background pressure. However, unlike argon, the optimal xenon pressure is approximately 6 mTorr. Additionally, xenon appears to be much more efficient in heating and compression than the argon discharges. Expectedly, xenon discharges had a lower electron temperature as xenon radiates significantly more than argon. However, the xenon discharges were significantly more compressed (starting from lower neutral pressures) and compressing to peak densities of $1 \times 10^{20}\ m^{-3}$ and to a smaller, more axially-centered plasma toroid. Additionally, the xenon discharge did not appear to suffer from the same

instability issues as did argon. These results suggest that more study, and at higher discharge energies, should be performed with the larger, more massive ion gases that suffer from less cross-field magnetic diffusion. In summary, xenon and argon were successfully tested in an AFRC at various interior locations. Presented here has been a comprehensive set of real-time plasma density and temperature information at three interior axial locations.

CHAPTER 8

Summary

A complete, 10-kJ pulsed power facility was constructed at AFRL-Edwards to explore Annular Field Reversed Configuration (AFRC) plasmas. An array of 3-axis B-dot probes, flux loops, and Rogowski coils was utilized to investigate diamagnetic behavior of the high density, magnetized plasma. A fast DICAM, wide-angle photometer, and internal high-speed triple Langmuir probe examined overall plasma content, compression regimes, downstream translation, and plasma instabilities for argon and xenon discharges ranging from 3-20 mTorr, 500-1000 V, and 185-450 μs discharge periods. AFRC devices offer the promise of low-voltage, high-efficiency, high-density plasma formation, compression, heating, and translation that have numerous uses from primary pulsed magnetic fusion, refueling for Tokamak plasmas, and advanced space propulsion. This dissertation seeks to experimentally investigate the synchronous operation of AFRC devices to explore the operational regimes, characteristics, pre-ionization effects, and minimum input energies in creating repeatable, high-efficiency, magnetized plasma discharges.

8.1 Pre-Ionization Optimization Conclusions

A complete study was done for multiple PPI pre-ionization energies, two ringing pre-ionization discharge geometries, and multiple discharge energies. Chapter 4 de-

tails this experimental study. In summary, it was found that a 5-kV glow discharge with the small thoriated tungsten electrode in Figure 8.1 was sufficient to allow for main bank plasma initiation for both xenon and argon with the current geometry. Further, as shown in Figure 8.2 increasing discharge energy into the glow ionization had little effect on final plasma content or structure for the main bank discharges. Therefore, the glow discharges utilized in Chapter 7 were a 5-kV, 1-20 W argon plasma and a 5 kV, 0.05-2.5 W xenon plasma.

The pre-ionization technique used in these experiments (and FRC experiments in general) has two stages, the low power glow seed discharge and a high voltage, low energy azimuthal ringing. The ringing pre-ionization was chosen to be 250 kHz and 3 kV (the limit of the supply) as set by earlier studies. Pre-ionization Geometry 1 was isolated (both discharge coil and discharge circuitry) at the top ($z = 30\ cm$) of the discharge coil and was found (Chapter 6) to create large non-uniformities in the plasma, decrease total plasma content, and decrease applied coil voltage. Geometry 2 utilized the primary discharge coil as the pre-ionization coil, though the switching electronics were still separated. The integrated coil geometry had similar timing and total plasma results, but a much more uniform discharge was achieved. However, joining the two circuits meant that pre-ionization initiation timing was critical to optimize plasma content while minimizing noise collection. It was found that for a 2-Joule pre-ionization the optimal delay period was 100 μs, yielding an ionization fraction of 5-10 %. See Figure 8.3.

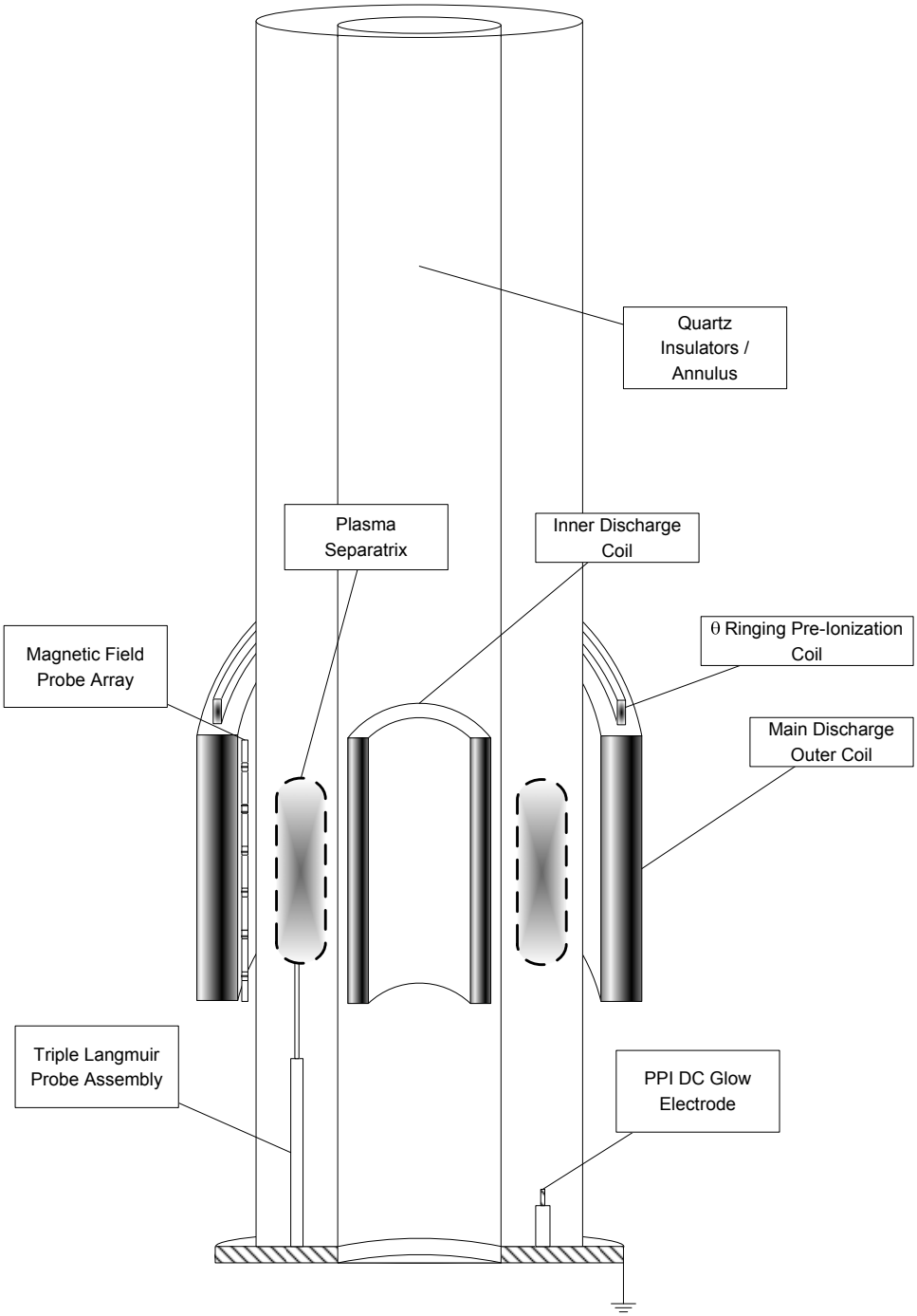

Figure 8.1: Schematic of system setup and discharge coil

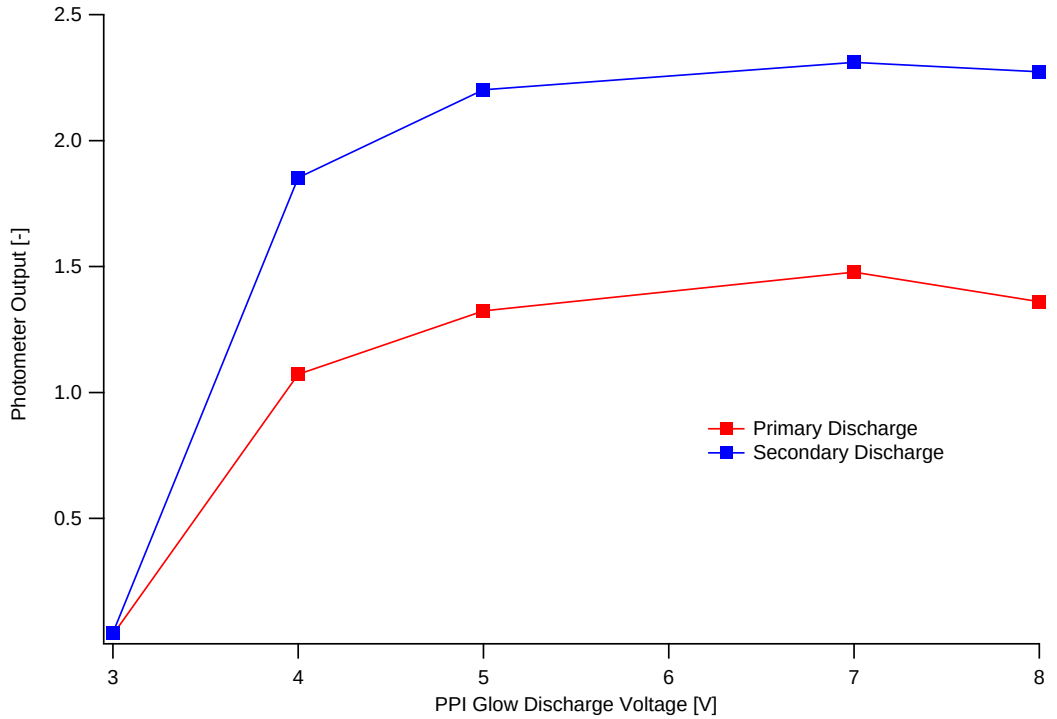

Figure 8.2: Summary of peak photometer data for various PPI glow discharge voltage and 750-V main bank discharges

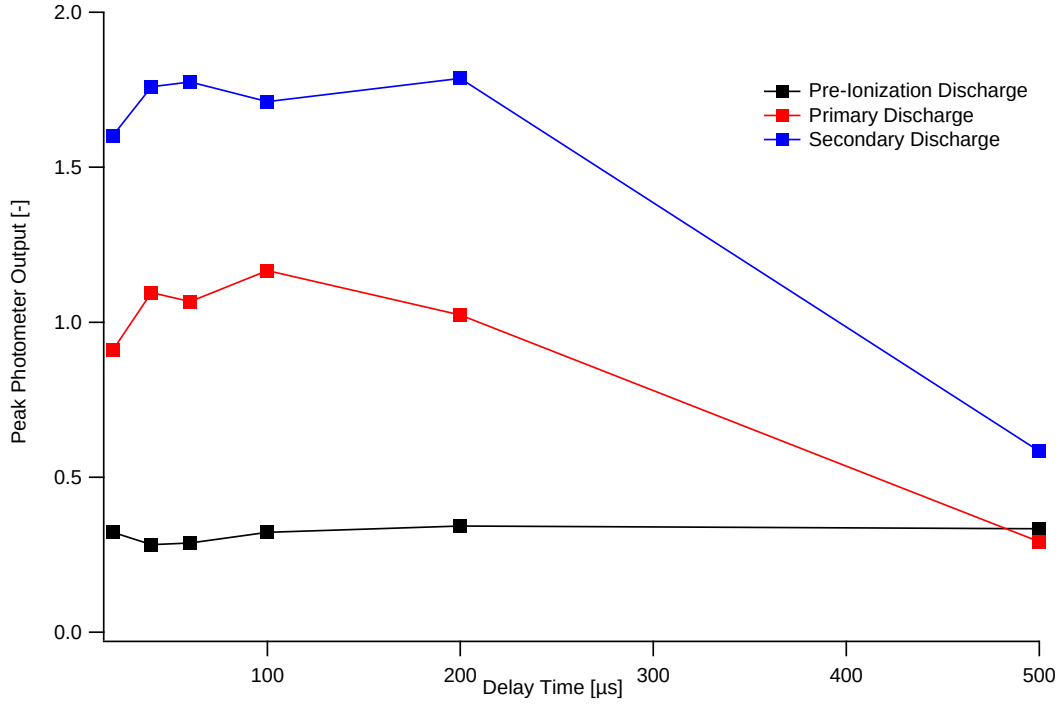

Figure 8.3: Summary of peak photometer discharge results for various delay periods

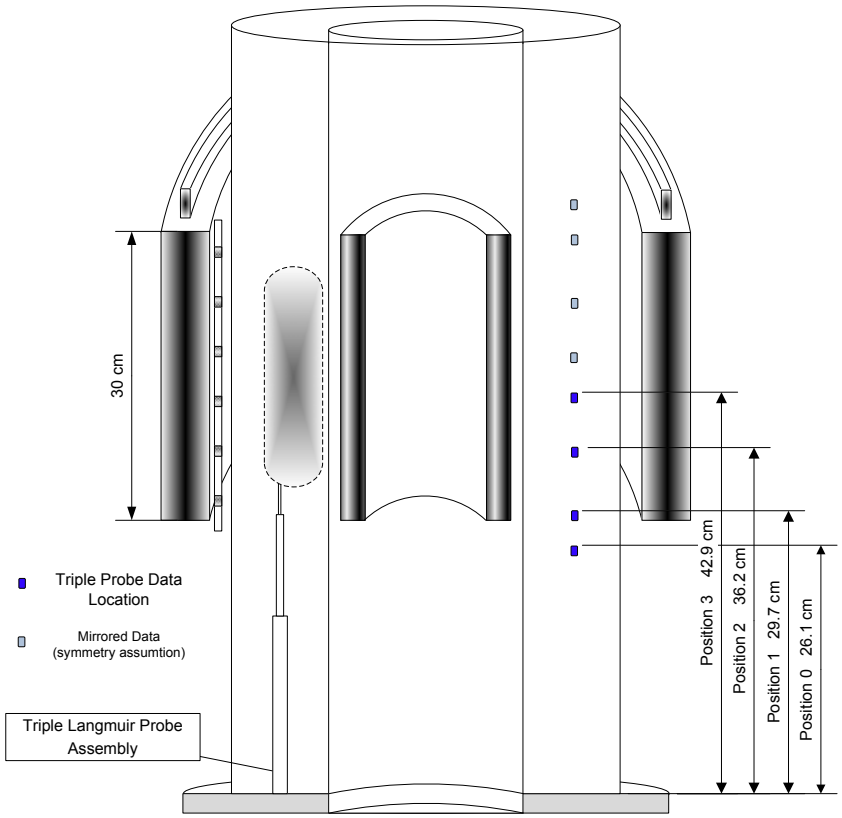

Figure 8.4: Schematic of triple probe locations for the discharge tests described in Chapters 5, 6, and 7

8.2 Internal Measurement Conclusions

Chapters 5-7 detail the investigation of the main bank discharge. Timing, discharge energy, and neutral pressure were investigated using external optical diagnostics as well as an internal scanning triple probe. Figure 8.1 shows the total diagnostics array, while Figure 8.4 shows a schematic of internal probe locations.

8.2.1 Argon

The detailed analysis of the 450-, 250-, 185-μs discharges are given in Chapters 5, 6, and 7, respectively. However, a summary is restated here for completeness. Figure

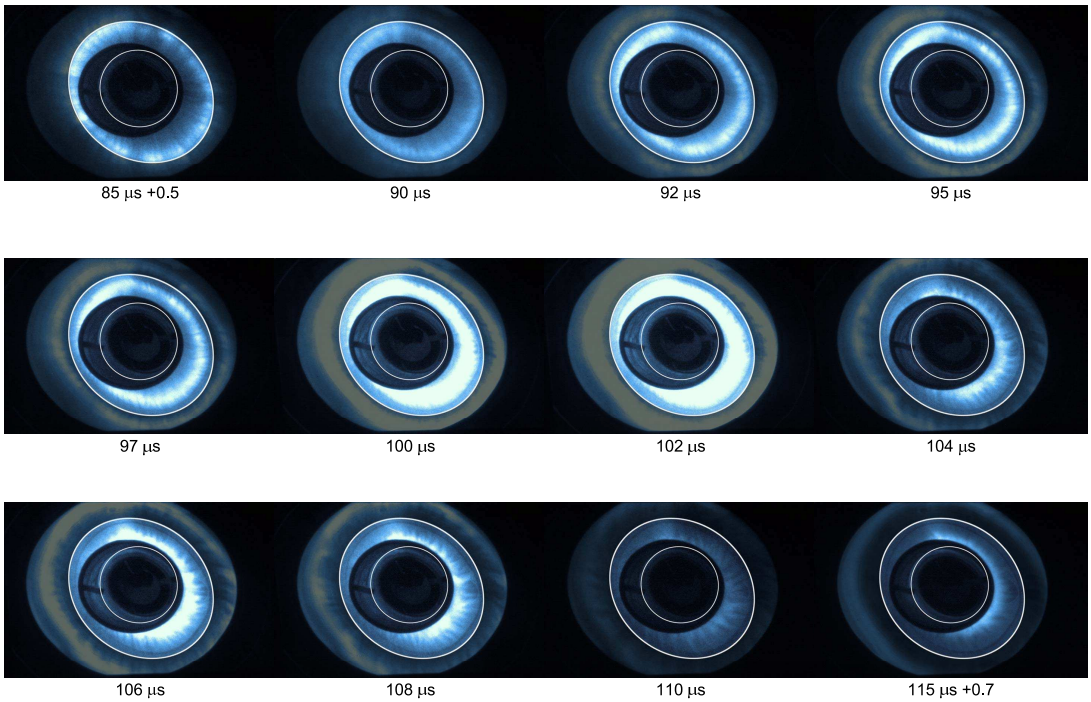

Figure 8.5: DICAM end-on visible photography for an 850-V, 14-mTorr, argon case

8.5 shows the pre-ionization, heating, compression, rotational instability, and final radial compression for a 14-mTorr argon discharge.

At 500-J, 450-μs the peak electron temperature was measured to be 15 eV and the peak density measured to be $3 \times 10^{19}\ m^{-3}$. Optimal neutral background pressure was found to be 15-20 mTorr for the various discharge energies shown in Figure 8.6. At 250-J, 250-μs the annular argon plasma was found to have a peak temperature of 8 eV and density of $3 \times 10^{19}\ m^{-3}$ for the 14-15 mTorr discharge condition. As shown in Figure 8.7, the peak neutral density was found to be between 15-20 mTorr with low-voltage discharge failure above 20 mTorr.

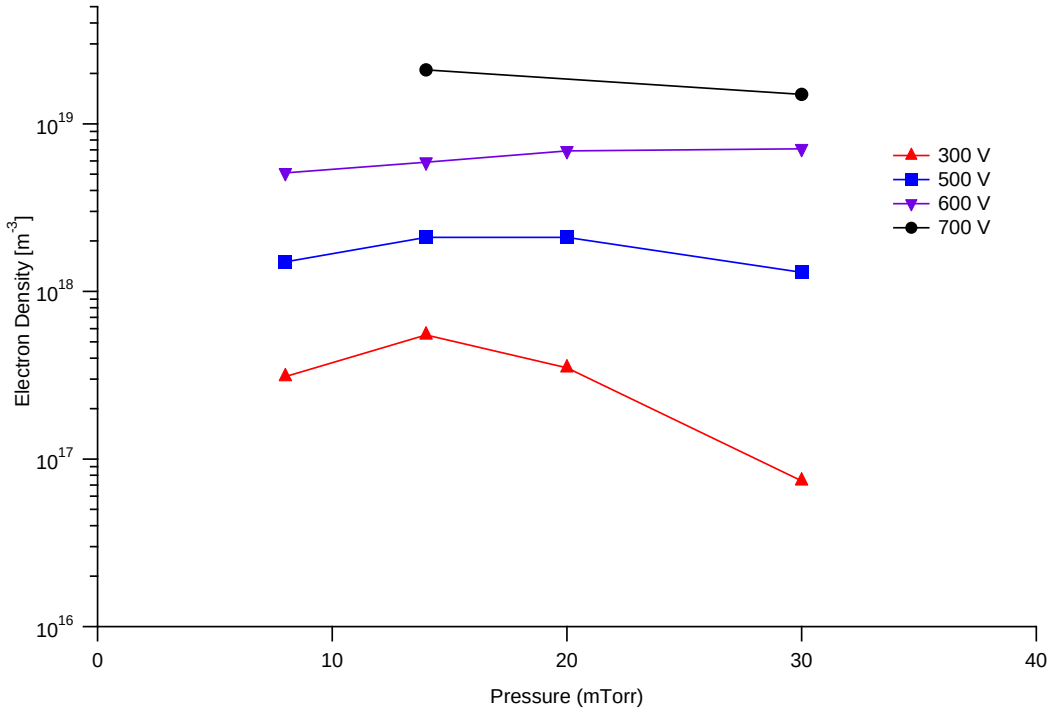

Figure 8.6: Peak Electron densities measured as a function of background pressure for multiple discharge voltages for 450-μs discharges. From 200–400 μs

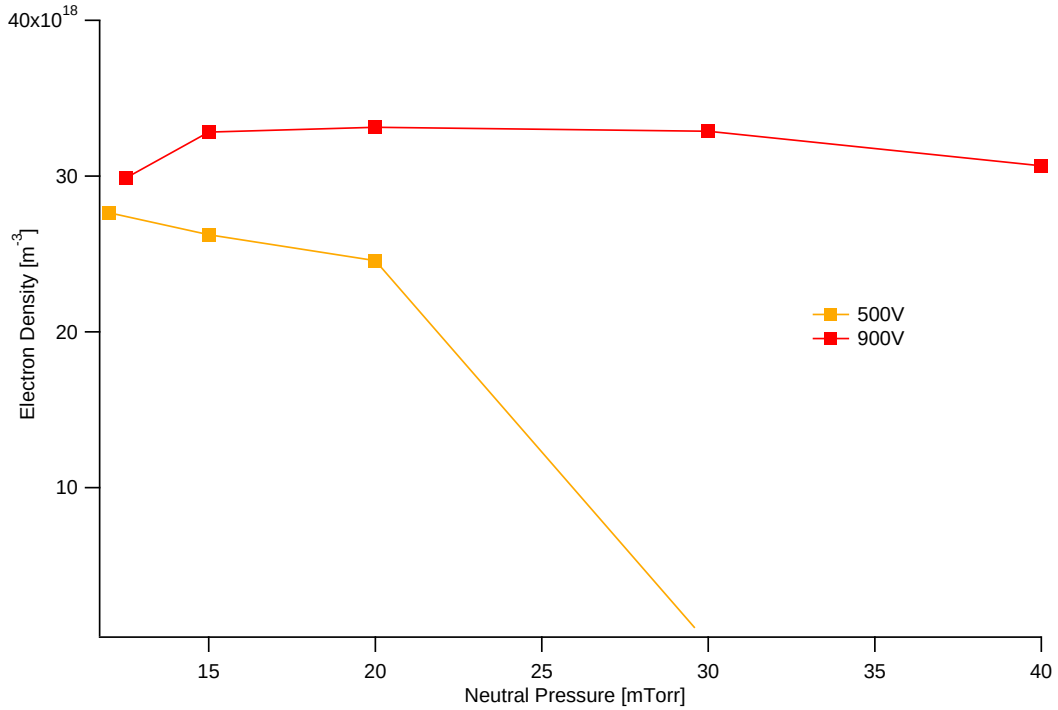

Figure 8.7: Summary of peak density results as a function of neutral pressure for the second plasma discharge at Position 0 for 250-μs discharges.

To summarize the above results, Figures 8.8 and 8.9 show the 14-mTorr argon plasma density data as a function of probe location. There are some very clear trends that can be seen in the data, firstly that the bulk of the ionization and plasma density is near the center of the discharge coil and extends (in time) out to the other probe locations later in each discharge. This effect is shown most clearly in the contour plots that detail the early formation (in the center), the continued heating and compression in the two central probes (Positions 2 and 3) and then finally the later heating and axial expansion to probe location, Position 1. To provide an even clearer position comparison, just comparing the peak densities measured at the various points, the data were compiled into Figure 8.10 that clearly shows the increasing peak densities as functions of reversal and discharge energies. Figure 8.11 shows a summary of peak plasma density for a 185-μs, 14-mTorr, 950-V discharge case. Peak argon plasma temperatures of 10 eV, and densities of $1 \times 10^{18} - 5 \times 10^{19}\ m^{-3}$ were achieved in these experiments.

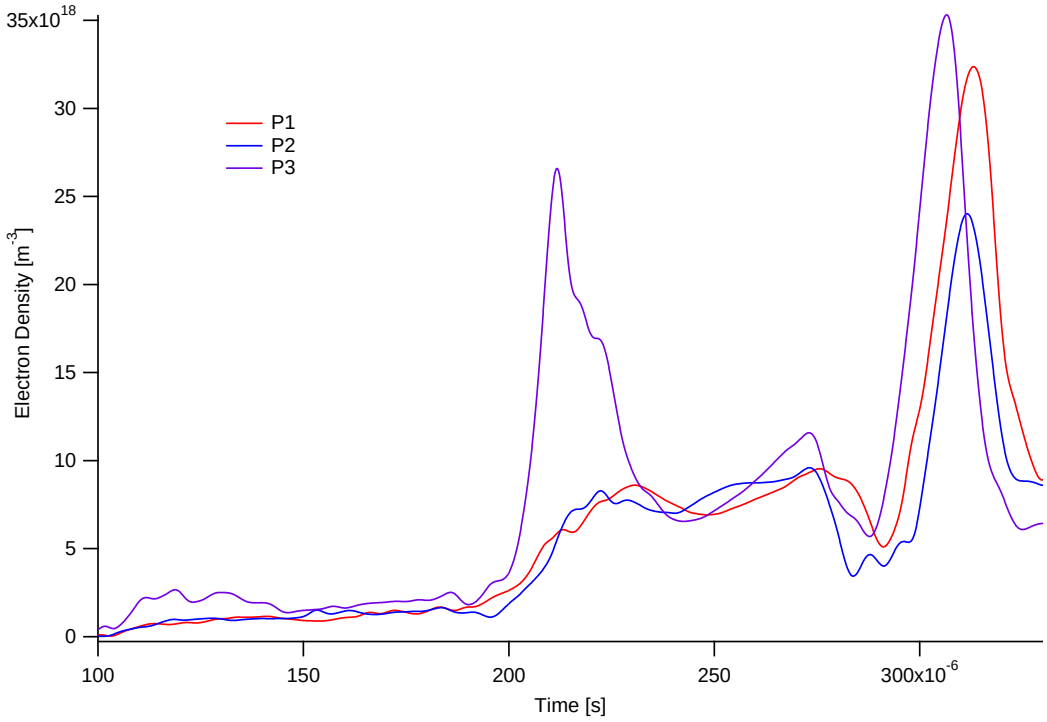

Figure 8.8: Detailed axial density scans for 185-μs, 14-mTorr, 950-V argon discharges showing initial ionization, primary, and secondary discharges

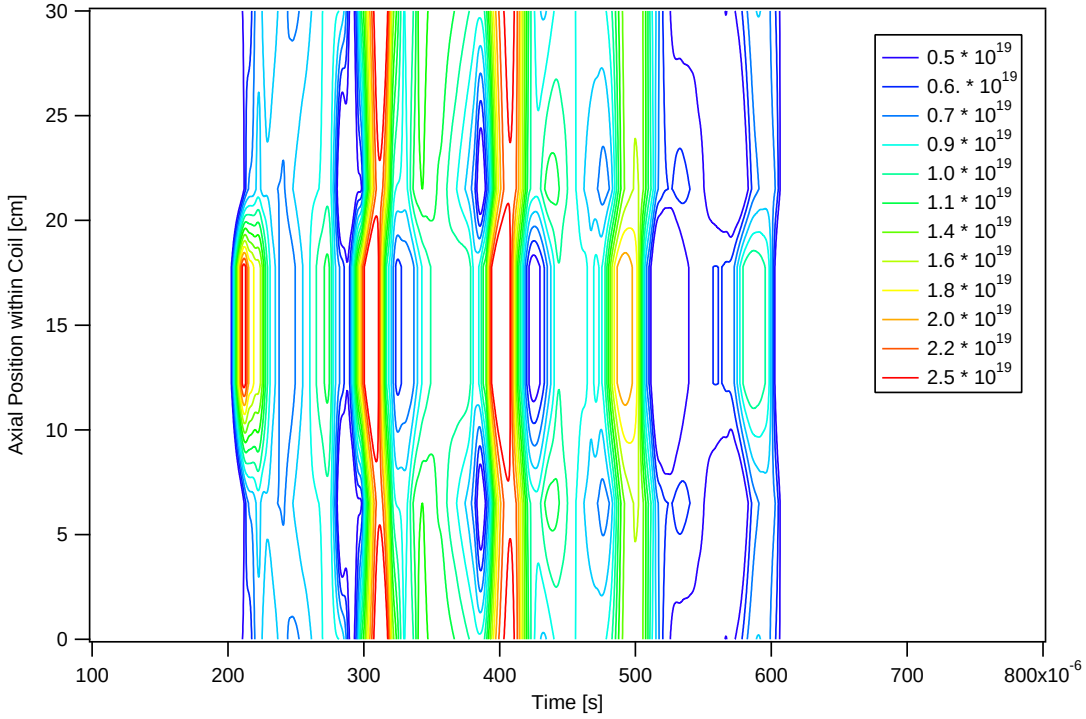

Figure 8.9: Axial density scan contours for 185-μs, 14-mTorr, 950-V argon discharges showing plasma density (axially, along centerline) as a function of time

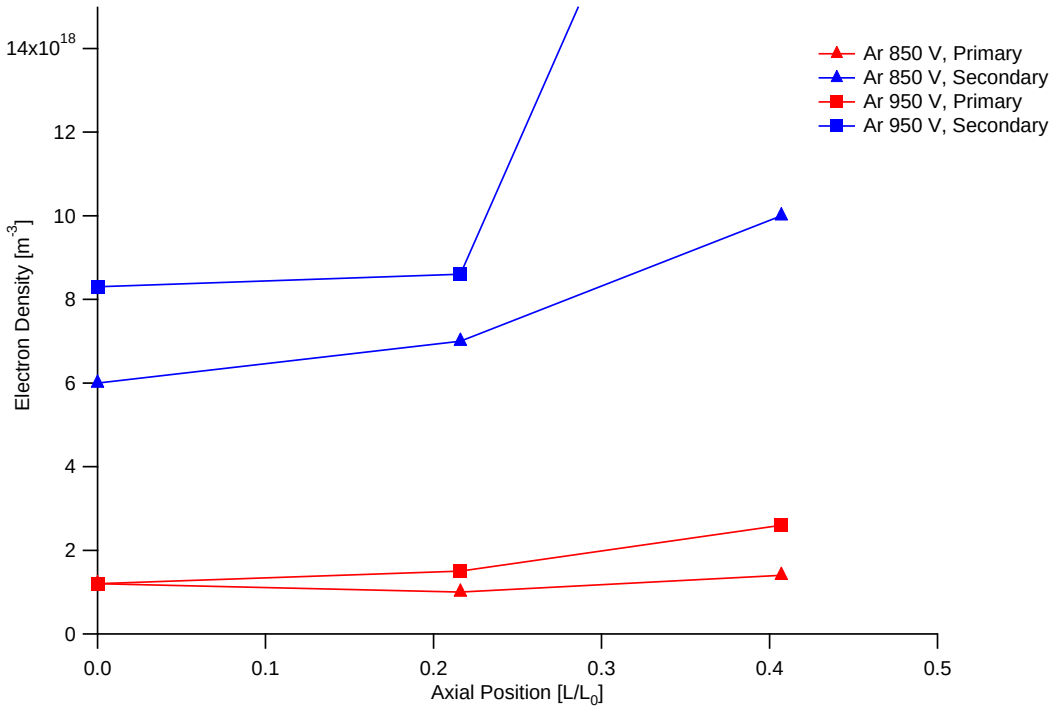

Figure 8.10: Close view of the peak densities within the first 350 μs at Positions 1, 2, and 3 for 14-mTorr discharges at 850 V and 950 V as a function of axial position

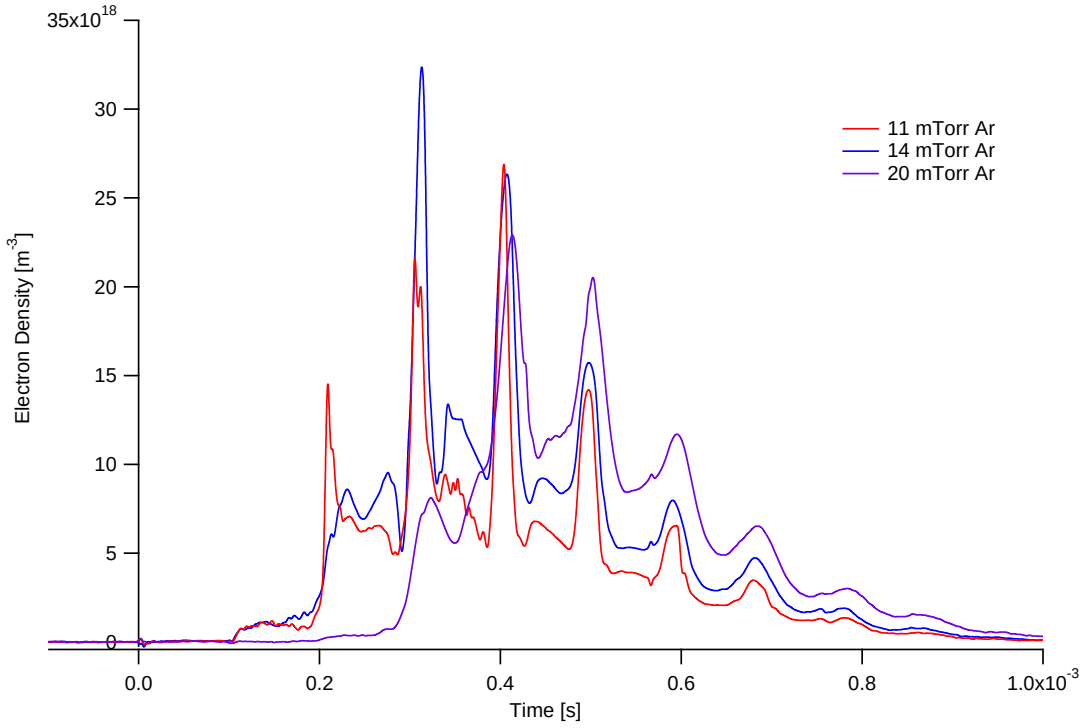

Figure 8.11: Summary of plasma density results at Position 1 for 185-μs, 950-V argon discharges for various neutral fill pressures

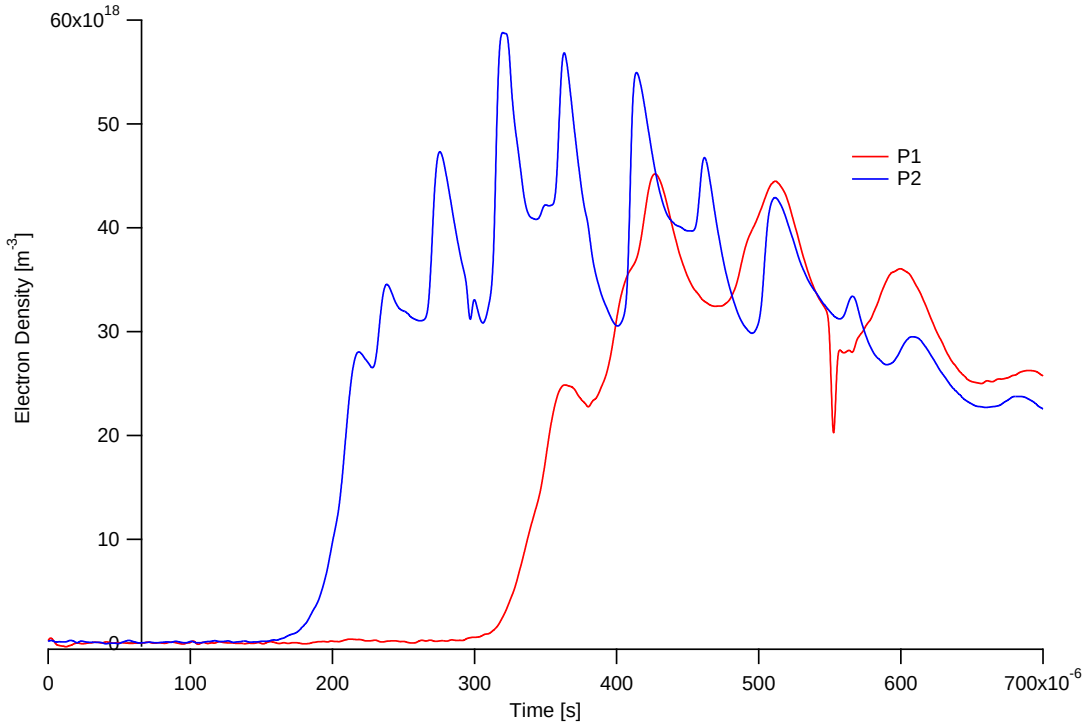

Figure 8.12: Detailed axial density scans for 185-μs, 6-mTorr, 950-V xenon discharges showing initial ionization, primary, and secondary discharges

8.2.2 Xenon

Xenon had similar results to argon, though with a significantly less distributed core, see Figures 8.12 and 8.13. Stable, longer-living xenon discharges were formed and compressed without the instabilities seen in argon. Peak xenon electron temperatures of 4-9 eV were found and peak plasma densities as high as $1.3 \times 10^{20}\ m^{-3}$ were measured. Xenon was only tested at Positions 1, 2, and 3 and for the 185-μs discharge.

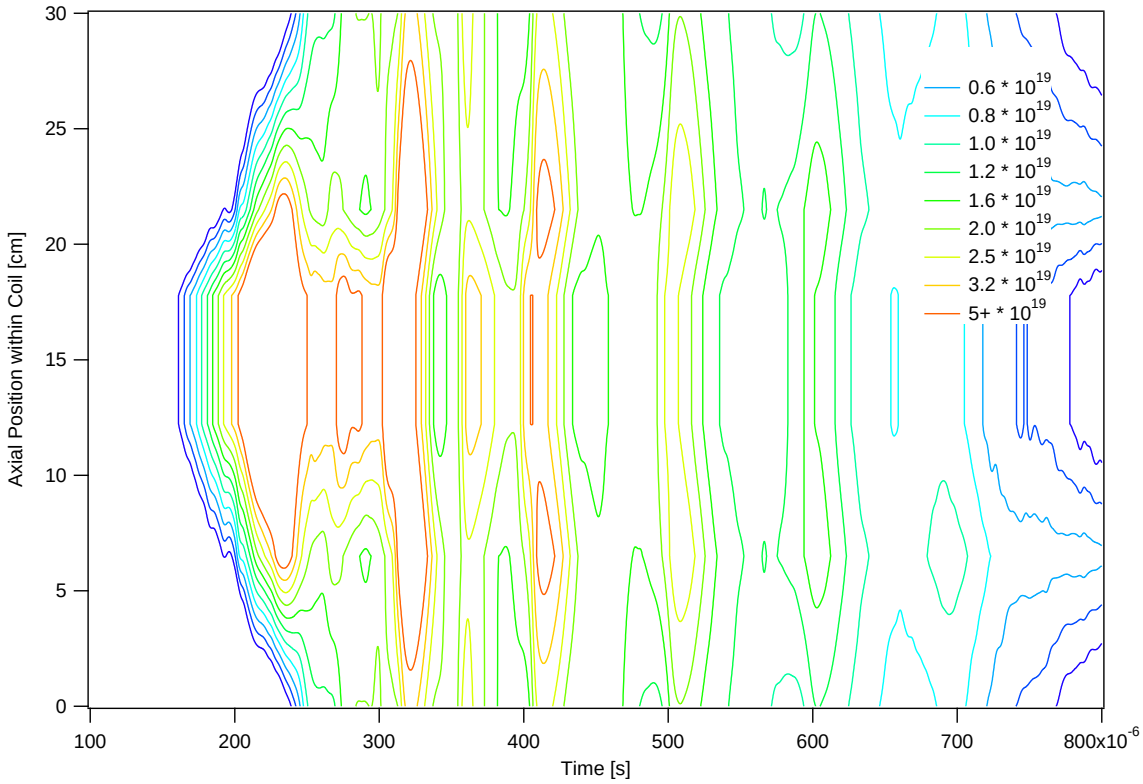

Figure 8.13: Axial density scan contours for 185-μs, 3-mTorr, 950-V xenon discharges showing plasma density (axially, along centerline) as a function of time

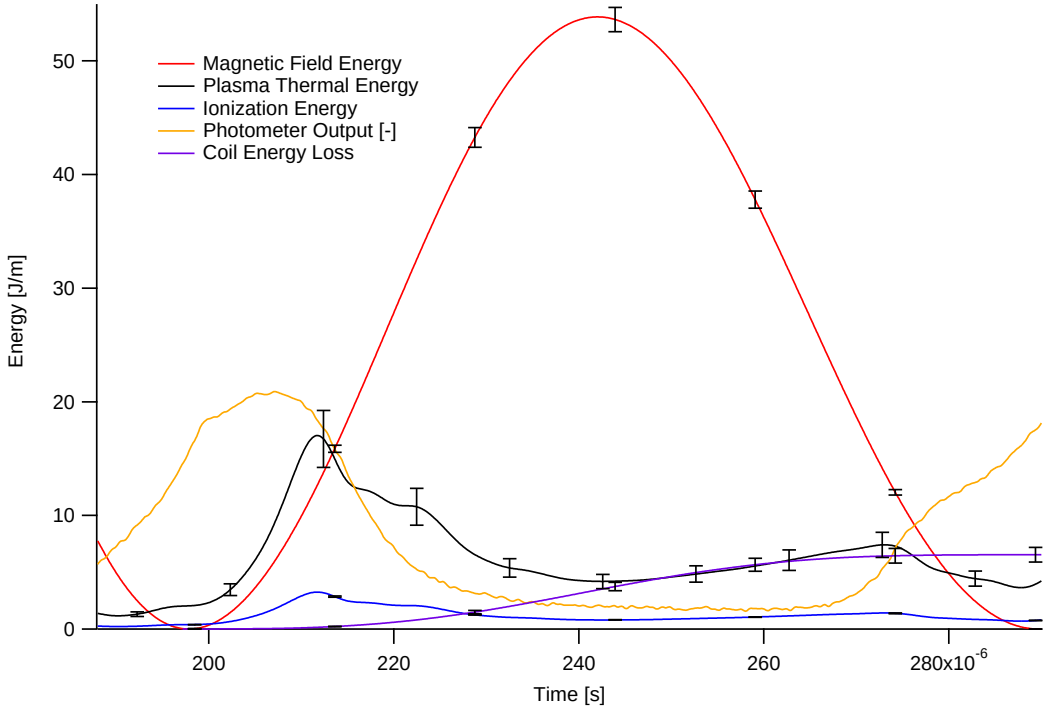

Figure 8.14: Instantaneous energy contained in the annular discharge region (per unit length) for a 185-μs, 14-mTorr, 950-V argon discharge showing plasma, ionization, magnetic, and coil dissipation energies as well as wide-angle photometer output

8.3 Energy Results

A simple energy scaling model has been developed for an annular configuration. Additionally, real-time internal plasma measurements were used to investigate the energy distribution along the center (between the coils) of the annulus. Figure 8.14 shows that for a 14-mTorr, 185-μs argon discharge, approximately 85 % of the energy input into the plasma goes into thermal energy rather than ionization. Additionally, plasma thermal energy is roughly twice the energy dissipated in the discharge coil during this plasma formation. Plasma is incident upon the triple probe for 54 μs.

8.4 Comparison With Expected Results and Past FRC Efforts

This research differs from past field reversed configuration in two main ways. First, the experiments are conducted entirely with much heavier gases than the hydrogen or deuterium that is traditional. It was expected that investigating FRC plasmas with argon and xenon will enable research into the requirements of space propulsion and advanced fusion fuels. The critical differences in using argon and xenon are the ionization energies and ion masses. Argon has a higher ionization energy than hydrogen (15.75 eV compared to 13.6 eV) so it was expected that the initial ionization and pre-ionization would be even more critical for argon. Xenon has a lower ionization energy than hydrogen and indeed it was found that the initial ionization of xenon occurred with less energy and less asymmetries. It was also expected that the much heavier ion mass would greatly reduce cross-magnetic-field diffusion rates, specifically at the earlier compression periods, increasing total plasma confinement, lifetime, and decreasing instability growth rates. Finally, radiation losses due to hydrogen are a minimal contribution to the energy losses in a traditional FRC experiment. However, a major loss mechanism for fusion experiments (with goals of > 1 keV electron temperatures) is radiation loss due to collected oxygen, carbon, and metal impurities in plasmas greater than 20 eV. The early models and expectations of this research found that using a large, highly-radiative molecule amplifies these problems for high temperatures, but by maintaining temperatures less than 20 eV, those power losses would be minimal. However, they do provide significant optical output that has been used successfully to image the plasma formation and compression.

The Coaxial Slow Source (CSS) was the first annular FRC and was tested at the University of Washington. It was tested extensively in the asynchronous discharge mode and after it was found to have significant asymmetries due to the asynchronous

coil operation flux addition. Preliminary work was done on synchronous operation at 400 J and a discharge period of 185 μs on deuterium at 15 mTorr. Additionally, the CSS device had a larger annulus (radius) and was approximately 1-m long. It was reported that the CSS yielded peak plasma densities of approximately $1 \times 10^{21}\ m^{-3}$ and temperature of 15 eV as measured by internal interferometry measurements.

In the XOCOT discharge experiment successful, high-energy, high-density magnetized plasma have been formed, compressed, and heated. Findings have been consistent with predictions laid forth in the fast formation FRCs with expected densities (100 % ionization, internal diamagnetic currents) and somewhat expected electron temperatures for these discharge energies (sub-1 kJ rather than 100 kJ). Peak densities in argon of $8 \times 10^{19}\ m^{-3}$ and peak temperatures of 10 eV in a 250-J, 185-μs discharge were found. Peak temperatures of 15 eV were found for the 1000-J, 450-μs discharge. Peak plasma densities in xenon were found to be $2 \times 10^{20}\ m^{-3}$ with electron temperatures of 8 eV at 6 mTorr. The XOCOT experiment took the ideas laid forth in the CSS design and extended them substantially to cover a range of discharge periods, pressure, pre-ionization techniques, and a shorter, prolate toroid. Pre-ionization, background gas density, and discharge circuitry have been optimized. Many of the results were found to be similar with a thin, high-compressed reversed configuration forming and collapsing inward, similar peak electron temperatures, and the ability to form FRCs at voltages and energies less than 1000 Volts and 1000 Joules. Unexpectedly, this author's investigation found difference with the results of the CSS operated in parallel/synchronous mode in that initial ionization and main bank discharge did not form the high density plasmas, and natural field reversal, immediately but instead required a full current reversal that was typically seen for the cylindrical and asynchronous annular operation. It is currently hypothesized

that an energy input into the pre-ionization (fraction, energy) was too low to allow for sufficient diamagnetic current to form during the very initial magnetized plasma turn-on in the harder-to-ionize heavy gases. However, this effect could also be a function of the backfilled geometry as well as pre-ionization geometry. One of the initial concerns with using the main discharge coil as a pre-ionization geometry is that it creates an oscillating bias field in the annulus that would directly affect the initiation of the diamagnetic drive current. This effect has been removed in the XOCOT discharge experiment with a 100 μs delay between pre-ionization and main bank discharge. Regardless, formation during the current reversal is not undesirable, and should yield significant increase in initial bias flux, and ultimately lead to better (higher-density, higher-efficiency) FRC plasmas.

Another primary difference is the configuration lifetime experience in the two devices. The CSS was unable to sustain a high-density plasma for greater than 20 μs, while the XOCOT discharge experiment had measured stable lifetimes of greater than 50 μs, with optical suggestions that lifetime was significantly higher but not measured by the internal triple probe. This difference is attributable to the heavier ion masses. The CSS was found to have a very significant, destructive rotational instability that is not seen at all in the xenon discharges. In fact, the argon discharge experiments had the appearance of the beginning of instabilities, but they did not appear to be large, destructive instabilities that collapsed the plasma toroid.

Finally, the XOCOT discharge experiment showed that there are clear pre-ionization and main bank thresholds for effective ionization and turn-on. In fact, two distinct transitions have been found both for the energy required for initial gas ionization and uniform heating by the main bank as well as the minimum energy and preionization percentage for formation of magnetized plasma. These thresholds are critical for

minimizing and optimizing energy input as well as scaling of future FRC devices.

8.5 Suggestions for Future Field Reversed Configuration Experiments

The results found in the XOCOT discharge experiment are quite exciting and suggest that a high-density, high-efficiency (greater than 50 % of the dissipated input energy is in the plasma) magnetized plasma toroid is being formed, compressed, and heated in the annular field reversed configuration. However, there have been numerous complications and data uncertainty due to the physical size and location of the internal plasma probe as well as the high-density, cold background-gas in the configuration tested. Future work must examine non-intrusive plasma temperature and density measurements along the entire radial scale of the annulus, such as two-color pulsed laser interferometry or an ion scattering diagnostic. High fidelity MHD modeling has not been performed on an AFRC geometry and should be an important component on future work, both to quantify the real-time plasma formation in areas not measured by probes as well as to aid in the scaling and design of future geometries and pulsed-discharge systems. Additionally, a complete study must be done with a pulsed neutral-gas instead of a backfilled propellant to investigate the effects of the peripheral heating and ionization losses found in the XOCOT experiments for both the synchronous and asynchronous discharge configurations. Finally, a high priority should be investigating the translational nature of the annular configuration with both asymmetric magnetic field (conical) and asymmetric neutral gas flow (pulse gas manifolds) in order to fully characterize the energy efficiency and thermal-to-kinetic conversion of input discharge current to kinetic plasma energy in an annular configuration.

APPENDIX

APPENDIX A

Data Analysis IGOR Code

```
//#pragma rtGlobals=1 // Use modern global access method.
Function Main()
Killwaves/A/Z
//initiate constants
Variable/G e_c=1.602210^-19 //MKS
Variable/G Ap=1.3710^-5 //m2
Variable/G Mi=6.69e–26 //KG
Variable/G kb=1.3810^-23 //mks
Variable Pressure=2.5//mTorr

//initiate folder loading
String FolderIteration="06"
Variable TPCondition=1
Variable Index=6

//initiate variables
Make/D/O/N=10000 V1,V2,V3,V4,Vf,I2,I3
Make/D/O/N=10000 Te,ne, Tev, Ion_Fraction
Variable Max_Pts=10000
Variable Vd2,Vd3
//LoadDocs(V1,V2,V3,V4,Vf,I2,I3, FolderIteration)
//adjust for electrical characteristics

Vd3=38
Vd2=12.7

Find_Te (I2, I3,Vd2,Vd3,Te,10000)
Smooth/B 201, Te
Tev=1/Te
Smooth/B 201, TeV
Find_ne(ne,I2,I3,Vd2,Vd3,Tev)
End


//Solve Function to find Electron temperature with given triple probe currents ratio function
Function TP_Electron_Temp(Te_Variables, Te)
Wave Te_Variables
Variable Te
return ((1–exp(–Te_Variables[1]Te))/(1–exp(–Te_Variables[2]Te))–Te_Variables[0])
End

//Primary function to find electron temperature
```

```
Function Find_Te (I2, I3,Vd2,Vd3,Te,Max_Pts)
Wave &I2,&I3
Wave &Te
//initiate variables
Variable Max_Pts,Vd2,Vd3
Variable i, CurrentRatio
//make variable storage matrix to pass to solve variables
Make /O Te_Variables

//iterate timesteps to solve Te
for(i=0;i<Max_pts;i+=1)
CurrentRatio=(2I2[i]+I3[i])/(I2[i]+2I3[i])
//Te_Variables=CurrentRatio,Vd2[i],Vd3[i] //for measured Vd2, Vd3
Te_Variables=CurrentRatio,Vd2,Vd3 //for fixed input voltages
//solve for Te
FindRoots/L=0.01/H=.1/Q TP_Electron_Temp, Te_Variables
Te[i]=V_root;

//clean data
//print CurrentRatio, V_root
//if (abs(i2[i]–i3[i])<0.00001)
//Te[i]=10000
//endif
//if (Te[i]<0) //error check
//Te[i]=0
//endif
Te[i]=1/Te[i]

//if current differential is too low, set Te=0
if ((abs(I2[i]–I3[i]))<(50e–4))
Te[i]=0
endif
//check for errant zero currents or triple probe non–uniformities
//if (((I2[i]–I3[i]))>(0))
//Te[i]=0
//endif
endfor
end

//utilize and probe dimensions to find ne
Function Find_ne(ne,I2,I3,Vd2,Vd3,TeV)
Wave I2,I3, &ne, TeV
Variable Vd2,Vd3
//reference globals
NVAR Ap, e_c, Mi
//Variable Ap,Mi,e
//initiate waves
Make/D/O/N=15000 Ji, nec, Te
Variable S=Ap
Variable Vd,TeVc,i
Vd=Vd3–Vd2//Check
//use constant Te
//Psuedo Ne
//TeVc=25
//Ji=1/S(I3–I2exp(–Vd/Tevc))/(1–exp(–Vd/Tevc))
//nec=Ji/(exp(–0.5)e_c(e_cTevc1/Mi)^(0.5))
//Real Ne
```

```
Te=TeV
//clean Te for ne. If Te is too noisy use an average Te
for(i=0;i<15000;i+=1)
if (((Tev[i])<(2e–1)))
Te[i]=10

endif
endfor
//solve for ion current
Ji=1/S(–I3+I2exp(–Vd/Te))/(exp(–Vd/Te)–1)
//solve for density
ne=Ji/(exp(–0.5)e_c(e_cTe1/Mi)^(0.5))
End


//load individual files from SIGMA 100
Function LoadDoc(xx, pathfilename)
Wave &xx
String pathfilename
String s0
LoadWave/Q/G/D/O/N pathfilename
print s_path, s_filename

s0 = StringFromList(0, S_waveNames)
Wave w0 = $s0
//output file data
xx=w0

End


//load all docs
Function LoadDocs(V1,V2,V3,V4,Vf,I2,I3,FolderIteration)
wave &V1,&V2,&V3,&V4,&Vf,&I2,&I3
String FolderIteration
//basic path
String Path="C:Data:2apr:2apr 000"
//load files 1–7
LoadDoc(V1, (Path+FolderIteration+":CH1_01h.TXT"))
LoadDoc(V2, (Path+FolderIteration+":CH2_02h.TXT"))
LoadDoc(V3, (Path+FolderIteration+":CH3_03h.TXT"))
LoadDoc(V4, (Path+FolderIteration+":CH4_04h.TXT"))
LoadDoc(Vf, (Path+FolderIteration+":CH5_05h.TXT"))
LoadDoc(I2, (Path+FolderIteration+":CH6_06h.TXT"))
LoadDoc(I3, (Path+FolderIteration+":CH7_07h.TXT"))

//Display I3,I2
//Display Vf
End

//Magnetic field processor
//input raw B and integration constants
Function BField(B1, nA1, B0, nA0,B2,B2_int)
Wave &B0,&B1,&B2, &B2_int
Variable nA0, nA1
Wave int_output
Variable i
//Smooth 500, B0,B1
```

```
//WaveStats/Q/R=(–1,–1e–6) B0
//B0=B0–V_avg/2
//rezero B–dot data
WaveStats/Q/R=(1.0e–3,1.3e–3) B0
B0=B0–V_avg
//WaveStats/Q/R=(–1,–1e–6) B1
//B1=B1–V_avg/2
WaveStats/Q/R=(1.0e–3,1.3e–3) B1
B1=B1–V_avg

B2=B1–B0
//Smooth 200, B2
//integrate B–dot data
Integrate/METH=1 B2/D=int_output
//re–zero integrated B–field
//B2_int=int_output–int_output[1900]
End

//Zero Function
Function Zero(X, ncX)
Wave &X
Variable ncX
//zero based on initial and final zero values
//Smooth 500, B0,B1
//WaveStats/Q/R=(–1,–1e–6) B0
//B0=B0–V_avg/2
//WaveStats/Q/R=(1.0e–3,1.3e–3) B0
//B0=B0–V_avg/2

//zero based on initial (pre–trigger) value
WaveStats/Q/R=(–1,–1e–6) X
X=ncX(X–V_avg)
End

//Normalize B–dot data
Function BFieldNormalize(B1, nA1)
Wave &B1
Variable nA1
B1=B1nA1
End

//Main B–field processing program
Function Process(X, NX1,X0,XVac)
string X, NX1, XVac
Wave X0
//initiate file strings
String LX1, LX2, LX3, LX4, LX5, LX6, LX7,LIX1, LIX2, LIX3, LIX4, LIX5, LIX6, LIX7,LX01, LX02,
LX03, LX04, LX05, LX06, LX07,LDX1, LDX2, LDX3, LDX4, LDX5, LDX6, LDX7

//append file iteration strings for raw data
LX1="AX1_"+X
LX2="AX2_"+X
LX3="AX3_"+X
LX4="AX4_"+X
LX5="DAX1_"+X
LX6="DAX2_"+X
LX7="AX5_"+X
//initiate waves
duplicate X0 $LX1, $LX2, $LX3, $LX4, $LX5, $LX6, $LX7
```

```
//load b–dot data from SIGMA 100
LoadDocs($LX2, $LX1, $LX4, $LX3, $LX5, $LX6, $LX7,NX1)

//normalize raw bdot data
BFieldNormalize($LX1, 1.51e3)
BFieldNormalize($LX2, –1.44e3)
BFieldNormalize($LX3, 1.37e3)
BFieldNormalize($LX4, 1.34e3)
BFieldNormalize($LX5, 1.42e3)
BFieldNormalize($LX6, –1.53e3)
BFieldNormalize($LX7, –1.38e3)

//process difference (Plasma–Vacuum) data
LDX1="D_AX1_"+X
LDX2="D_AX2_"+X
LDX3="D_AX3_"+X
LDX4="D_AX4_"+X
LDX5="D_DAX1_"+X
LDX6="D_DAX2_"+X
LDX7="D_AX5_"+X

duplicate X0 $LDX1, $LDX2, $LDX3, $LDX4, $LDX5, $LDX6, $LDX7

//process integrated data
LIX1="DI_AX1_"+X
LIX2="DI_AX2_"+X
LIX3="DI_AX3_"+X
LIX4="DI_AX4_"+X
LIX5="DI_DAX1_"+X
LIX6="DI_DAX2_"+X
LIX7="DI_AX5_"+X

duplicate X0 $LIX1, $LIX2, $LIX3, $LIX4, $LIX5, $LIX6, $LIX7
//process vauum data
LX01="AX1_"+XVac
LX02="AX2_"+XVac
LX03="AX3_"+XVac
LX04="AX4_"+XVac
LX05="DAX1_"+XVac
LX06="DAX2_"+XVac
LX07="AX5_"+XVac


BField($LX1, 1.51e3, $LX01, 1.51e3,$LDX1,$LIX1)
BField($LX2, –1.44e3, $LX02, –1.44e3,$LDX2,$LIX2)
BField($LX3, 1.37e3, $LX03, 1.37e3,$LDX3,$LIX3)
BField($LX4, 1.34e3, $LX04, 1.34e3,$LDX4,$LIX4)
BField($LX5, 1.42e3, $LX05, 1.42e3,$LDX5,$LIX5)
BField($LX6, –1.53e3, $LX06, –1.53e3,$LDX6,$LIX6)
BField($LX7, –1.38e3, $LX07, –1.38e3,$LDX7,$LIX7)
End

//Use manually loaded ne, zero it, find Te, find ne, display graphs
//designed for a specific file number
Function Process_ne(I2_X, I3_X, X)
string X
Wave &I2_X, &I3_X
Wave X0
//initiate variables for various
```

```
String ne_X, Te_X, VC_X, V1_X, V2_X
//Wave VC_temp
NVAR Ap, e_c, Mi
Variable V_average

VC_X="Vc_"+X
V1_X="V1_"+X
V2_X="V2_"+X
ne_X="ne_"+X
Te_X="Te_"+X
//create temporary Te, ne variables
duplicate/o V1_1 $ne_X, $Te_X, $VC_X
Zero(I2_X,1)
Zero(I3_X,1)

Find_Te (I2_X, I3_X,12.7,38.0,$Te_X,15000)
//Smooth 500, $Te_X
duplicate/O $Te_X VC_temp
//use average Te for I2–I3>0
Corrected_Average($Te_X, V_average)
print "Te_avg = ", V_average, "Te_max = ",V_max
VC_temp=V_average
Find_ne($ne_X, I2_X,I3_X,12.7,38,VC_temp)
//Find_ne($ne_X, I2_X,I3_X,12.7,38,$Te_X)
//Smooth 500, $Te_X
//Smooth 500, $Te_X
//smooth50($Te_X,100)
Smooth 500, $ne_X
//create graphs for ne, Te
Display $Te_X; AppendToGraph/L=L2 $ne_X
ModifyGraph axisEnab(left)=0.55,1,axisEnab(L2)=0,0.45;DelayUpdate
Label left "Te [eV]";DelayUpdate
Label L2 "Electron Density"
Label bottom "Time [s]";DelayUpdate
SetAxis bottom –0.0001,0.001
ModifyGraph freePos(L2)=–0.00015,bottom
ModifyGraph width=648,height=432
ModifyGraph lblPos(L2)=52,lblLatPos(L2)=20
SetAxis left 0,12
end

//find an average Te for differential currents that are beyond error bars
//uses Te before and after geometric probe issues
Function Corrected_Average(Xwave, Xave)
wave Xwave
variable &Xave
variable i,counter,Xave_temp
Xave_temp=0
counter=0
for(i=3500;i<9000;i+=1)
if (Xwave[i]>(2))
Xave_temp=Xave_temp+Xwave[i]
counter=counter+1
endif
endfor
Xave=Xave_temp/counter
end
```

BIBLIOGRAPHY

Bibliography

[1] W. T. Armstrong, D. C. Barnes, and et al. Compact toroid experiments and theory. *Nuclear Fusion Supplement*, 1:481.

[2] R. E. Beverly III Associates. Application notes for aqueous-electrolyte resistors. 2004.

[3] S. I. Babic and C. Akyel. New analytic-numerical solutions for the mutual inductance of two coaxial circular coils with rectangular cross section in air. *IEEE Transactions on Magnetics*, 42(6):1661–9, 2006.

[4] D. C. Barnes, J. L. Schwarzmeier, H. R. Lewis, and C. E. Seyler. Kinetic tilting stability of field-reversed configurations. *Physics of Fluids*, 29(8):2616, 1986.

[5] V.V. Belikov, V.M. Goloviznin, and V.K. Korshunov. *Plasma Physics and Controlled Nuclear Fusion Research*, 2(IAEA, Vienna):342, 1982.

[6] H. Bodin, T. Green, and et al. Plasma containment and stability in a megajoule theta-pinch experiment. *Plasma Physics and Nuclear Controlled Fusion Research*, 1:193, 1966.

[7] H. Bodin, J. McCartan, and et al. Diffusion and stability of high-β plasma in an 8-meter theta-pinch. *Plasma Physics and Nuclear Controlled Fusion Research*, II:533, 1969.

[8] F. F. Chen. *Introduction to plasma physics and controlled fusion Volume 1: Plasma physics.* Plenum Press, 1984.

[9] F. F. Chen. Langmuir probe analysis for high density plasmas. *Physics of Plasmas*, 8(6):3029–41, 2001.

[10] F. F. Chen and R.H. Huddlestone. Plasma diagnostic techniques. *Ed. RH Huddlestone and SL Leonard, New York, Academic*, 1965.

[11] P. L. Chung, L. Talbot, and J. T. Kennell. *Electric probes in stationary and flowing plasmas: theory and application.* Springer-Verlag, 1975.

[12] B. Clarenbach, M. Kramer, B. Lorenz, and Ltzenkirchen. Electron heating and plasma production in helicon plasma. *Electron Heating and Plasma Production in Helicon Plasma*, ECA Vol.28G, 2004.

[13] Rj. Commisso, W.T. Armstrong, and J.C. Cochrane. Rep. la-87qo-c. *Physics and Technology of Compact Toroids*, Los Alamos Scientific Laboratory:184, 1981.

[14] J. H. Degnan, T. W. Hussey, and et al. Progress on formation of field reversed configurations suitable for subsequent compression to magnetized target fusion conditions. In *PPPS-2001 Pulsed Power Plasma Science 2001.*, page 594, Las Vegas, NV, USA, 2001. IEEE.

[15] A. G. Es'kov, R. K. Kurtmullaev, and et al. Principles of plasma heating and confinement in a compact toroidal configuration. *Nuclear Fusion*, suppl.(2):187, 1979.

[16] A. G. Es'kov, O. A. Zolotovsky, and et al. Plasma confinement in a pulsed system with a compact toroidal configuration. In *7th European Conference on Controlled Fusion and Plasma Physics*, volume I, page 55, 1975.

[17] R. W. Evans and I. Tec-Masters. *Design Guidelines for Shielding Effectiveness, Current Carrying Capability, and the Enhancement of Conductivity of Composite Materials.* National Aeronautics and Space Administration, George C. Marshall Space Flight Center; National Technical Information Service, distributor, 1997.

[18] N.A. Gatsonis, L.T. Byrne, J.C. Zwahlen, E.J. Pencil, and H. Kamhawi. Current-mode triple and quadruple langmuir probe methods with applications to flowing pulsed plasmas. *IEEE Transactions on Plasma Science*, 32(5):2118 – 29, 2004.

[19] T. S. Green. Plasma containment in theta pinch. *Physics of Fluids*, 6:864, 1963.

[20] R. L. Hagenson and R. A. Krakowski. A compact-toroid fusion reactor (CTOR) based on the field-reversed theta pinch. In *Fusion Reactor Design and Technology. Proceedings of the 3rd Technical Committee Meeting and Workshop*, pages 377–90, 1983.

[21] R. L. Hagenson, R. A. Krakowski, and K. I. Thomassen. A toroidal fusion reactor based on the reversed-field pinch (RFP). In *Fusion Reactor Design Concepts*, pages 337–55, 1978.

[22] J.J. Hamm, H. Knoepfel, and et al. Very-high density theta-pinch. *EPE Conf. Proceedings*, II:629, 1969.

[23] A. L. Hoffman, P. Gurevich, J. Grossnickle, and J. T. Slough. Inductive field-reversed configuration accelerator for tokamak fueling. *Fusion Technology*, 36(2):109, 1999.

[24] W. N. Hugrass, I. R. Jones, K. F. McKenna, and et al. Compact torus configuration generated by a rotating magnetic field: the rotamak. *Physical Review Letters*, 44(25):1676, 1980.

[25] I. H. Hutchinson. *Principles of Plasma Diagnostics*. Cambridge University Press, 2002.

[26] T. P. Intrator, G. A. Wurden, and et al. Physics basis and progress for a translating FRC for MTF. *Journal of Fusion Energy*, 27(1-2):57–60, 2008.

[27] T. R. Jarboe, Barnes, and et al. Introduction to the spheromak and the CTX experiment. Physics of Mirrors, Reversed Field Pinches and Compact Tori. Proceedings, page 459, Varenna, Italy, 1988.

[28] Chang Jen-Shih, G. L. Ogram, R. M. Hobson, and S. Teii. The instantaneous triple-probe method for the direct display of plasma parameters in a low density continuum plasma. *Journal of Physics D (Applied Physics)*, 13(6):1083.

[29] G. F. Karabadzhak, Chiu Yu-hui, and R. A. Dressler. Passive optical diagnostic of xe propelled hall thrusters. ii. collisional-radiative model. *Journal of Applied Physics*, 99(11), 2006.

[30] D. Kirtley and et al. Details on an annular field reversed configuration plasma device for spacecraft propulsion. *International Electric Propulsion Conference, IEPC-2005-171*, 2005.

[31] D. Kirtley and et al. High density magnetized toroid formation and translation within XOCOT: An annular field reversed configuration plasma concept. *International Electric Propulsion Conference, IEPC-2007-41*, 2007.

[32] S. Koelfgen, P. Fimognari, and et al. Magnetic and langmuir probe measurements on the plasmoid thruster experiment (PTX). In *Joint Propulsion Conference*, 2004.

[33] A. C. Kolb. Magnetic compression of plasmas. *Reviews of Modern Physics*, 32:748, 1960.

[34] J. G. Laframboise and L. W. Parker. Probe design for orbit-limited current collection. *Physics of Fluids*, 16(5):629–36, 1973.

[35] B. Lehnert. The extrap concept. *Nuclear Instruments and Methods in Physics Research*, 207(1-2):223, 1983.

[36] M. A. Lieberman and A. J. Lichtenberg. *Principles of Plasma Discharges and Materials Processing*, volume 30. 2005.

[37] ETS lindgren. Helmholtz coil manual. REV A PN 399273, 2001.

[38] G. V. Marr. *Plasma spectroscopy*. Elsevier, 1968.

[39] S. Matsumura and Chen Sin-Li. Studies on the measurement of plasma parameters by means of the RF probe method. *Japanese Journal of Applied Physics*, 18(7):1329, 1979.

[40] I.A. Phillips. Proposal to produce large compact toroids, rep. la-8711-p. *Los Alamos National Laboratory*, 1981.

[41] W. F. Pierce, R. J. Maqueda, R. D. Brooks, and R. Farengo. Initial results from parallel coil operation of the coaxial slow source field reversed configuration device. *Nuclear Fusion*, 33(1):117, 1993.

[42] Z. A. Pietrzyk, G. C. Vlases, R. D. Brooks, K. D. Hahn, and R. Raman. Initial results from the coaxial slow source FRC device. *Nuclear Fusion*, 27(9):1478, 1987.

[43] Tube products department. Ignitrons: Capacitor and crowbar service. *General Electric Publications*, 1974.

[44] R. Raman, G. C. Vlases, and T. R. Jarboe. Energy balance in the CSSU device. *Nuclear Fusion*, 33(11):1685, 1993.

[45] W F Ray and R M Davis. Wide bandwidth rogowski current transducers. *EPE Joumal*, 3(1), 1993.

[46] W F Ray and K D Murray. The use of rogowski coils for current waveform measurement in power electronic circuits. *EPE Conf. Proceedings*, 3:379, 1991.

[47] D. J. Rej, W. T. Armstrong, and et al. Experimental studies of field-reversed configuration translation. *Physics of Fluids*, 29(3):852, 1986.

[48] W Rogowski and W Steinhaus. Die messung der magnetischen spannung. *Arch. Electrotech*, 1:141, 1912.

[49] J. E. Sansonetti and W. C. Martin. Handbook of basic atomic spectroscopic data. *Atomic Physics Division, Physics Laboratory*, National Institute of Standards and Technology.

[50] L. Schott. Plasma diagnostics. *edited by W. Lochte-Holtgreven, Wiley, New York*, 1968.

[51] S.G.Lee and J.G. Bak. Triple langmuir probe measurements in the hanbit magnetic mirror device. *Review of Scientific Instruments*, 72(1):442, 2001.

[52] A. G. Sgro, W. T. Armstrong, J. Lipson, M. G. Tuszewski, and J. C. Cochrane. Flux loss and heating during the formation of a field-reversed configuration. *Physical Review A (General Physics)*, 26(6):3564, 1982.

[53] A. G. Sgro, W. T. Armstrong, J. Lipson, M. G. Tuszewski, and J. C. Cochrane. Flux loss and heating during the formation of a field-reversed configuration. *Physical Review A (General Physics)*, 26(6):3564, 1982.

[54] Chen Sin-Li. Studies of the effect of ion current on instantaneous triple-probe measurements. *Journal of Applied Physics*, 42(1):406.

[55] Chen Sin-Li and T. Sekiguchi. Instantaneous direct-display system of plasma parameters by means of triple probe. *Journal of Applied Physics*, 36(8):2374.

[56] J. Slough, S. Andreason, H. Gota, C. Pihl, and G. Votroubek. The pulsed high density experiment: concept, design, and initial results. *Journal of Fusion Energy*, 26(1-2):199–205, 2007.

[57] J. Slough and G. Votroubek. Magnetically accelerated plasmoid (MAP) propulsion. *Joint Propulsion Conference)*, AIAA-2006-4654, 2006.

[58] J. T. Slough and A. L. Hoffman. Penetration of a transverse magnetic field by an accelerated field-reversed configuration. *Physics of Plasmas*, 6(1):253, 1999.

[59] Brian A. Smith and Lawrence J. Overzet. Improvements to the floating double probe for time-resolved measurements in pulsed rf plasmas. *Review of Scientific Instruments*, 69(3):1372–1377.

[60] L. C. Steinhauer. Magnetic flux trapping during field reversal in the formation of a field-reversed configuration. *Physics of Fluids*, 28(11):3333, 1985.

[61] R. A. Stubbers, B. E. Jurczyk, J. L. Rovey, M. D. Coventry, D. A. Alman, and M. L. R. Walker. Compact toroid formation using an annular helicon preionization source. *43rd AIAA/ASME/SAE/ASEE Joint Propulsion Conference*, (AIAA-2007-5307), 2007.

[62] J. A. Taccetti, T. P. Intrator, and et al. Pre-ionization experiments on a high-density field reversed configuration suitable for magnetized target fusion. PPPS-2001 Pulsed Power Plasma Science 2001, page 535, Las Vegas, NV, USA, 2001. IEEE.

[63] D.L. Tilley, A.J. Kelly, and R.G. Jahn. The application of the triple probe method to MPD thruster plumes. *International Electric Propulsion Conference*, AIAA-90-2667(1), 1990.

[64] M. Tuszewski. Field reversed configuration plasmas. *Nuclear Fusion*, 28:2033, 1988.

[65] M. Tuszewski and W. T. Armstrong. Simplified diamagnetic techniques for a field-revered theta-pinch plasma. *Review of Scientific Instruments*, 54(12):1611, 1983.

[66] George C. Vlases, D. S. Rowe, R. Raman, and et al. Design of a translating field-reversed configuration reactor. *Fusion Technology*, 9(1):116, 1986.